MONASH University

Preparation, characterization, and applications of VO_2 nanocomposites

Song Li

Ph.D. Candidate

A thesis submitted for the degree of *Doctor of Philosophy* at

Monash University in *2018*

Laboratory for Simulation and Modelling of Particulate Systems

Department of Chemical Engineering

Faculty of Engineering

Copyright notice

Abstract

From the start of the 21st century, all the energy resources of the whole world have been reduced by a large scale. Based on the research data, more than 40% of the primary energy is used by the energy consumption in buildings. Effective strategies should be considered to diminish the heat transfer from indoor to outdoor atmosphere, and the energy-efficient window coatings or walls are some meaningful approaches. Vanadium dioxide (VO_2) smart window is a representative product to solve the above energy problem. The VO_2 is a kind of smart material which can reversibly switch between two different states according to external stimuli. With the special property, the vanadium dioxide smart window can regulate the near-infrared (NIR) irradiation once the temperature is over the critical temperature, meanwhile maintain visible transmittance. Meanwhile, the critical temperature can be modulated by doping other elements which make VO_2 a very potential material for smart window application. F and W dopants have been widely used in this research area, and they show that fluorine and tungsten can affect the switching behavior at the semiconductor-to-metal phase transition.

However, there are still many problems regarding to the properties of the smart window, such as good stability in the moisture air environment, high luminous transmittance (T_{lum}), good solar regulation efficiency and reasonable critical temperature (T_c). Some research has been done to deal with the stability problem by synthesizing different VO_2 nanostructures. Core-shell structure has been meaningful method among them.

Gao and his co-workers have done some work in synthesizing VO_2@SiO_2 core-shell nanoparticles. They prepared transparent, stable and flexible VO_2-based composite film. And it shows that the film gives out good UV-shielding properties and temperature-responsive thermochromism in the near infrared region. However, they did not show many details of the stability, which are very crucial property of the VO_2 smart window application. Yamei and the co-workers synthesized some VO_2@TiO_2

core shell nanoparticles. It exhibits that the TiO_2 overcoating not only increased the luminous transmittance of VO_2, but also modified the intrinsic colour of VO_2 films.

In this thesis, the research target is improving the stability of VO_2 nanoparticles by synthesizing core-shell nanostructure. Before that, a new hydrothermal method was used to synthesize the VO_2 nanoparticles. Relative studies, such as the optical concentration of chemicals and annealing temperature were done to make sure the quality of the final VO_2 nanoparticles. After that, the VO_2 core-shell nanoparticles were synthesized to try to prevent the oxidation of VO_2 nanoparticles. Different materials were used to coat the VO_2 core material, which includes VO_2@SiO_2, VO_2@TiO_2 and VO_2@ZrO_2 core-shell structures. Moreover, optical experimental parameters were studied to get the best results. And SEM, TEM, XRD test were done to prove the final successful synthesis of core-shell structure.

The result shows that SiO_2, TiO_2, and ZrO_2 are successfully coated on the VO_2 nanoparticles. The final nanocomposites are characterized to check if they are stable in different atmosphere such as acid, alkali and oxidation environments.

Declaration

This graduation thesis contains no material which might been used for the award of any other diploma or degree at other university or equivalent institution. Moreover, as far as my knowledge, there is no material in this graduation thesis has been published previously or written by other people, except the reference of the thesis.

Signature: ……

Print Name: …….

Date: ……

Acknowledgments

Firstly, I would like to express my sincere appreciation to my supervisor Associate Professor Xuchuan Jiang for accepting me to his research group. Moreover, he gave me a lot of help and guidance in my Ph.D. study period. He always gives me valuable suggestions and idea support in my research. And we often have face-to-face talking about the project, which helps me a lot in processing my research. I also thank my co-supervisor Professor Aibing Yu for leading me and providing financial assistance until the completion of my Ph.D. degree. I appreciate every word he talks in the group meeting which gives me a direction for my future career.

Secondly, I would also like to express my appreciation to the staff in Department of Chemical Engineering, particularly Ms. Lilyanne Price, Dr. Ruiping Zou and Ms. Kim Phu, as they provided me a lot of academic or administrative assistance in my Ph.D. process. I would also like to express my appreciation to the technical staff in the Monash Centre for Electron Microscopy (MCEM), particularly Xiya Fang, Emily Chen and Tim Williams, as they supported me a lot in SEM, TEM, and HRTEM samples analysis. I also thank my colleagues and friends of SIMPAS, especially Professor Weifan Chen, Dr. Yue Tang, Dr. Shufen Wang, Dr. Bin Su, Mr. Minsu Liu, Mr. Yuan Feng, Mr. Weiren Fan, Mr.Zichuan Liu and Miss. Linghui Peng for their help in discussing experimental details and their valuable suggestions.

Most importantly, I want to thank my family members in China who has been always with me and supporting me. Last but not least, I want to thank my wife Min Liu for supporting me and helping me to get through the difficult times I experienced during my Ph.D. candidature.

Table of Contents

List of Abbreviations

Abbreviation	Full name
MIT	Metal-insulator transition
SMT	Semiconductor-to-metal transition
CVD	Chemical vapor deposition
APCVD	Atmospheric pressure chemical vapour deposition
AACVD	Aerosol assisted chemical vapour deposition
RF	Radio frequency
PLD	Pulsed laser deposition
SPR	Surface plasmon resonance
SEM	Scanning electron microscopy
TEM	Transmission electron microscopy
XRD	X-ray diffraction

List of figures

List of tables

Chapter 1 Introduction

1.1 Background

Vanadium dioxide (VO_2) is a typical binary compound characterized because of its rich polymorphs. Different kinds of polymorphs such as VO_2 (B) and VO_2 (A) phase were found by researchers. Among them, only VO_2 (M) undergoes a reversible metal-insulator transition (MIT) at near room temperature (340K). In the phase transition process, VO_2 (M) with a monoclinic crystal structure will change to VO_2 (R) with a rutile-type tetragonal structure. At the same time, an obvious change will occur in optical properties from infrared (IR) transmitting to highly IR (infrared light) reflecting, which makes VO_2 a potential candidate for smart window.

With the help of VO_2 nanoparticles coating film, the window can regulate the IR transmission automatically according to the environmental temperature. When the environmental temperature is high, the smart window will change to rutile phase, which has a low IR light transmission, then less heat will be transferred into the room. On the contrary, when the temperature is low, the VO_2 material will maintain its monoclinic phase, which has a higher IR light transmission. Therefore, the window can regulate the heat from sunlight which will affect the room temperature. It is very meaningful to use this sort of window in the buildings to save the energy consumption.

Usually, pure phase VO_2(R) nanorods can be synthesized by the reduction of V_2O_5 via reduced agent. And it can be completed by a one-step hydrothermal treatment. There are also some other methods to synthesize a VO_2 with good crystal structure. The details of the synthesis methods will be talked the in the following chapter.

The property of VO_2 film can be adjusted by doping other elemental material. For example, critical temperature for VO_2 metal-insulator transition (MIT) can be reduced by W-doping. It was found that W dopant can change the local structure around W atom which can lead to a distortion of VO_2 lattices. Much research has been done to

synthesize VO_2 nanoparticles and improve its optical properties. However, not much research was done to enhance its stability.

VO_2 has a lot of applications, and the ability to achieve energy saving in architectures and optical solar energy utilization have attracted the researchers. It can be used in the thermochromic smart window applications. The VO_2 in energy-efficient windows is hindered by high transition temperature, low luminous transmittance, small solar modulation efficiency, the uncertainty of durability, and the lack of color change.

Especially, the VO_2 is not stable in ambient temperature. It is easier for the VO_2 particles to be oxidized to other vanadium oxides, which will lose the thermochromic property. Thus, the protection of VO_2 will be important for the application of VO_2 smart window. Different strategies have been used to tackle this problem. Composite structures (core-shell nanostructure, hybridization, multilayer structure, etc.) Gao and his co-workers have done some work in synthesizing $VO_2@SiO_2$ core-shell nanoparticles. They prepared transparent, stable and flexible VO_2-based composite film. And it shows that the film gives out good UV-shielding properties and temperature-responsive thermochromism in the near infrared region. However, they did not show many details of the stability, which are very crucial property of the VO_2 smart window application. Yamei and the co-workers synthesized some $VO_2@TiO_2$ core shell nanoparticles. It exhibits that the TiO_2 overcoating not only increased the luminous transmittance of VO_2, but also modified the intrinsic colour of VO_2 films.

The synthesis of VO_2 composites such as core-shell nanoparticles is a valid method for the protection. In this thesis, different types of VO_2 nanocomposites (core-shell structures) were synthesized to check if they are valuable and effective in the practical application. $VO_2@SiO_2$, $VO_2@TiO_2$, and $VO_2@ZrO_2$ were all tried to synthesize. The tests of stability were also performed to check the stability of core-shell structures .

1.2 Scope and objectives

The research objectives of this thesis are demonstrated as below:

- Synthesis of VO_2 (M) nanorods which includes the study and exploration of optimized parameters of the synthesis.
- Synthesis of VO_2 (M) nanocomposites, such as $VO_2@SiO_2$ core-shell nanoparticles, $VO_2@TiO_2$ and $VO_2@ZrO_2$ core-shell nanoparticles.
- Characterizations of VO_2 (M) nanorods and nanocomposites via advanced analytical techniques, such as Scanning Electron Microscopy (SEM), X-Ray Diffraction (XRD), Transmission Electron Microscopy (TEM), and Ultraviolet-Visible light (UV-Vis) spectroscopy.
- Investigations of protective properties of VO_2 nanocomposite such as its anti-oxidizing, anti-acid, and anti-alkali properties.

The detailed contents of each chapter in this thesis are demonstrated as following:

I. Chapter 1 introduces the background knowledge and the objectives of this research.
II. Chapter 2 gives an in-depth review of the properties of VO_2 and its synthetic methods and applications. Moreover, the application of VO_2 film as smart window coating is also discussed in details.
III. Chapter 3 focuses on the synthesis of VO_2 (M) nanorods by hydrothermal method. Optimized experimental parameters are studied. Relative characterizations are performed to prove the successful synthesis.
IV. Chapter 4 mainly talks about the synthesis of $VO_2@SiO_2$ core-shell nanocomposites. Its relative characterizations and properties are also talked. The protective performance of SiO_2 shell structure is studied due to its chemically stable property and high visible light transmittance.

V. Chapter 5 furtherly tries to synthesis VO_2@ZrO_2 core-shell nanoparticles and VO_2@SiO_2@ZrO_2 multilayered structure. It talks about the optimal synthesis parameters of VO_2@SiO_2@ZrO_2 nanocomposites. Its chemical stability is also studied.

VI. Chapter 6 shows the research of VO_2@TiO_2 core-shell nanoparticles and VO_2@SiO_2@TiO_2 multilayered structure. As the TiO_2 is an interesting material which has a photocatalytic property. The TiO_2 shell can not only protect the VO_2 nanorods from oxidizing but also provide some other functions such as self-cleaning.

VII. Chapter 7 concludes the research in the thesis and figures out the future research directions.

Chapter 2 Literature review

2.1 Vanadium dioxide

Vanadium dioxide[1-3] is a kind of semiconductor, which has been theoretically and experimentally studied by the materials researchers for more than 60 years according to its special behaviors, such as superconductivity at high temperature, magnetoresistance, and insulator-to-metal transitions.

2.1.1 Structure of vanadium dioxide

The research of vanadium dioxide[4-6] has been done in theory and experiment for more than half a century[7]. There is a semiconductor-to-metal transition (SMT) for the vanadium dioxide crystals, it is also known as the metal-insulator transition (MIT), and the transition happens at a critical temperature which is 68 ℃. Accompanied with the transition, a first-order structural phase transformation from a monoclinic ($P2_1/c$) to tetragonal rutile ($P4_2/mnm$) structure will occur at the same time, it has been characterized by a small lattice distortion along the *c*-axis.

The rutile structure of metallic VO_2 will exist at high temperature, which is based on a simple tetragonal lattice (space group $P4_2/mnm$) (Fig.1). The vanadium atoms are situated at the equidistant Wyckoff positions (4f), (0, 0, 0) and (1/2, 1/2, 1/2), moreover, each V atom is encircled by an edge-sharing octahedron of oxygen atoms, VO_6, which take up the positions at± (1/2+u, 1/2- u, 1/2). and ±(u, u, 0). When the temperature is low, another phase of VO_2-semiconducting phase will occur, which belongs to the monoclinic crystal system (space group p21/c) (Fig.2). When the temperature is 25 ˚C the unit cell parameters of the lattice are: a=5.75 Å, b=4.52 Å, c=5.38 Å and β =122.60°. The doubling and distortion in the size of the metallic tetragonal phase in high temperature will lead to this lattice result. The V^{4+}-V^{4+} pairing with alternate shorter (0.265 nm) and longer (0.312 nm) V^{4+}–V^{4+} distances

along the monoclinic *a* axis are involved in this structure, and it also tilts in regard to the rutile c-axis. The pure VO_2 phase is referred to as M_1, as doping of vanadium(IV) oxide leads to another monoclinic arrangement, M_2 (space group $C_{2/m}$).

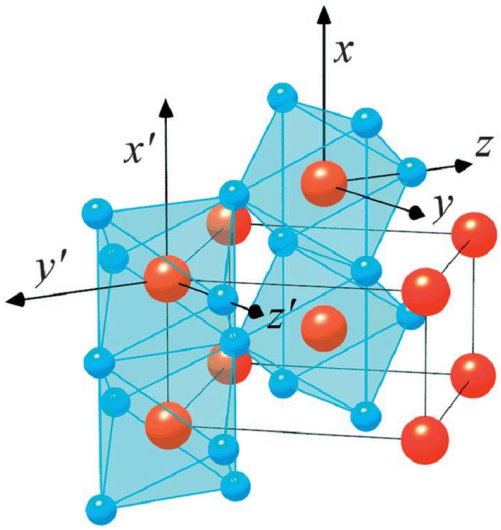

Figure 1. The rutile structure of VO_2 when $T>T_c$.

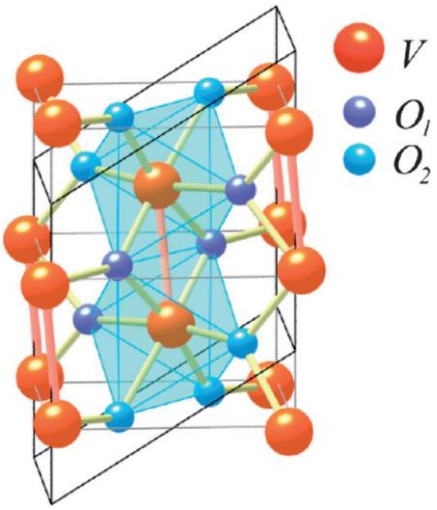

Figure 2 The monoclinic structure of VO_2 when $T<T_c$.

2.1.2 Mechanism of the phase transition

Since Morin[7] reported a first-order semiconductor-to-metal transition in VO_2 at a transition temperature $T_t \approx 340°K$, the mechanism of the phase transition was studied by the researchers. In 1971, Goodenough[3] came up with two distinguishable mechanisms of VO_2 phase transition, which are identified as: an antiferroelectric-to-paraelectric transition at a temperature T_t as well as a change from homopolar to metallic V-V bonding at a temperature T_t'. For pure VO_2, at atmospheric pressure, the two transitions happen at the same temperature, which means $T_t = T_t' \approx 340°K$. It can be explained by the molecular orbitals and band structure diagram (Fig.3).

By going through the transition temperature, the electrical conductivity changes dramatically. It is accompanied with a vital increase in infrared reflectivity, however, there is no change in the visible region. When the temperature is higher than T_c, the material reflects infrared radiation, while its temperature is lower than T_c, it is transparent in infrared range.

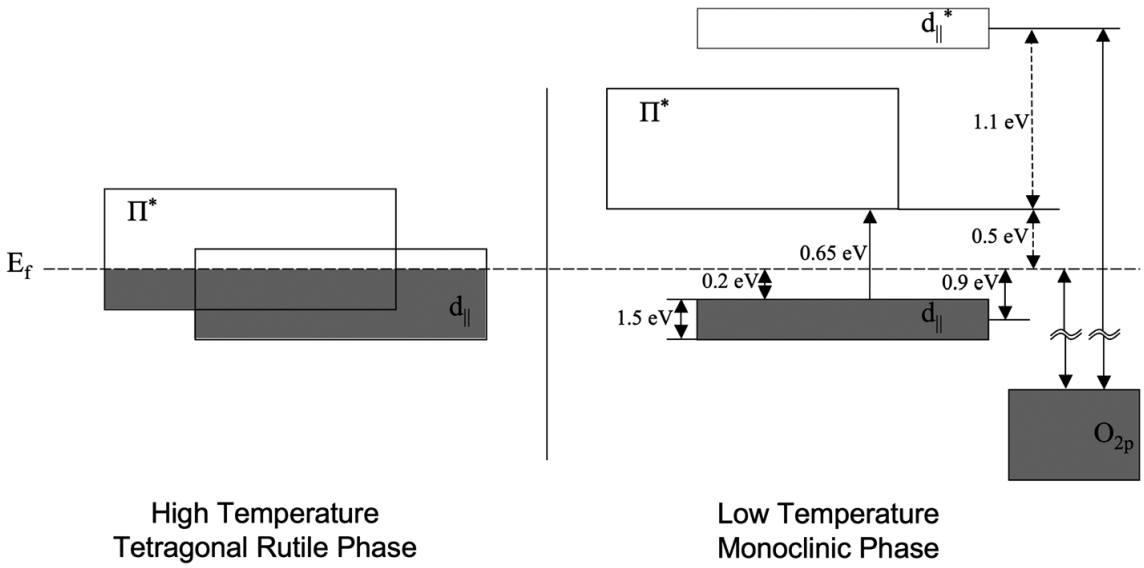

Figure 3.Schematic band structure diagram of VO_2

2.2 Synthetic methods

The valence state of vanadium dioxide is 4^+, it is not the highest one and not the lowest one. Therefore, it is difficult to control the oxygen content in the synthesis process. A range of methods have been used to synthesis VO_2 thin film successfully. Generally, these approaches can be divided into solution based synthesis and gas based synthesis.

2.2.1 Gas-based synthesis

2.2.1.1 Chemical vapor deposition method

In industries, chemical vapor deposition (CVD) method[8-11] is very popular to deposit high-quality and high-performance thin films. In 1967, VO_2 film was initially deposited using CVD method[12]. The method has been used broadly from that time[13]. There are some unique CVD methods which were used widely. They are atmospheric pressure chemical vapor deposition (APCVD) and aerosol assisted chemical vapor deposition (AACVD).

A comprehensive research with APCVD was processed to deposit TiO_2-VO_2 films with a transitional phase gradient[14]. Through a reaction of $TiCl_4$, VCl_4, ethyl acetate and H_2O at 550 °C, a film was grown on a glass substrate. The concentration of the gas mixtures varied during they going across the reactor to induce compositional film growth. The method is beneficial for the formation of films which have multifunctional properties, such as photocatalysis, photoinduced hydrophilicity, a decreased bandgap and a smaller T_c number (about 18 °C).

There is a new enhancement of CVD method which is called the electric-field chemical vapor deposition (EACVD). The electric fields have a profound effect about the crystallographic orientation, making the particle size smaller and decrease T_c of VO_2 films[15]. Binions et al.[15-16] have studied several parameters systematically which

include the strength of electric fields, effects of types of electric fields and deposition time. They published the application of electric field in the process of growth of VO_2 films by using a persistent positive bias to the substrate too. The test was conducted in a cold wall reactor (Fig. 4). At the center of the top plate and the substrate of the reactor, there is an electric field which was generated via using a potential difference. VO_2 films were deposited on glass substrate at 530 °C from vanadyl acetylacetonate solution in ethanol under the use of electric fields through using the AACVD. The electric fields were found had a dramatic influence on the properties and microstructure of the VO_2 films. The increased strength of electric field can lead to a decrease in particle size and enhance the porosity and surface area.

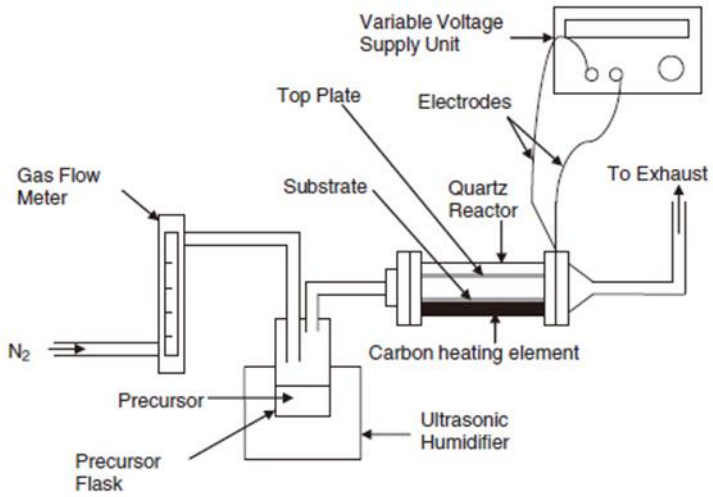

Figure 4. The schematic diagram of the cold wall reactor

Sometimes, the use of the electric field can also affect the microstructure and growth of VO_2 films (Fig.5). Under the electric fields, some changes of orientation and growth can be more easily found. Fig. 5 shows the SEM images of VO_2 films at different deposition times. In the image, it was found that a rodlike structure can be formed by a deposition time of two minutes. That is because the growth of the nanoparticles in one-dimension (Fig. 5b). When the deposition time was increased to five minutes, films began to grow along rod structures and spread to a two-dimensional structure (Fig. 5c). After the increase of the deposition time to ten minutes, there was a porous structured films which is consist of spherical particles of

200 nm in diameter (Fig. 5d). Twenty minutes later, there were large porous islands on the films which has the size between one to two micrometers. Even though no dramatic thermochromic properties were observed, the influence of electric fields on the structure of VO_2 films was significant. Moreover, porous and good structured surface structure can be got, and they can be potentially useful to a lot of applications. They can be used as chemical sensors or supercapacitor electrodes.

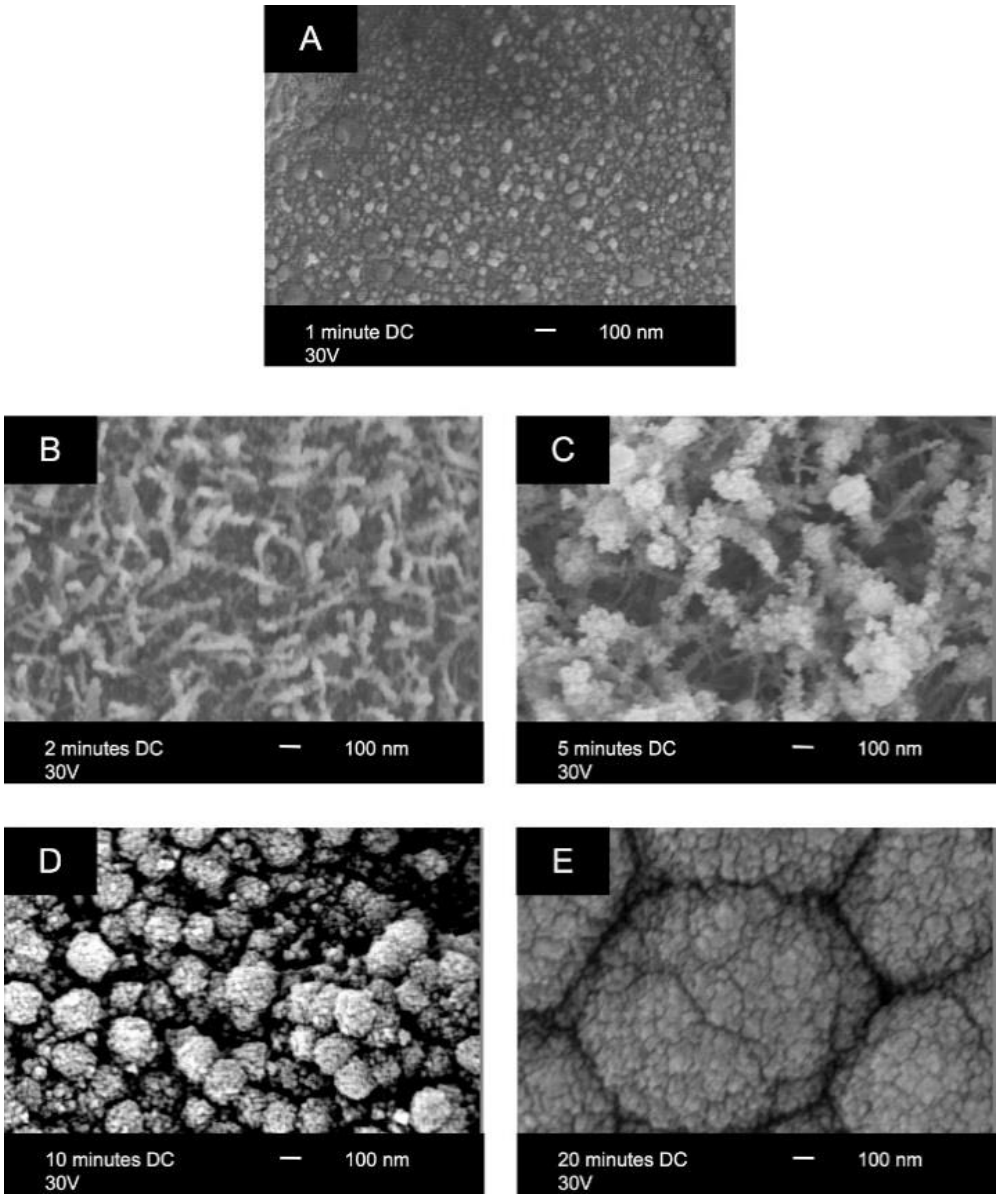

Figure 5. How the electric field affect the growth and structure of VO_2 films

2.2.1.2 Physical vapor deposition method

Physical vapor deposition (PVD) [17-21] is another significant technology to fabricate thin films by gas[22-24]. Usually, there are four steps in a PVD method: evaporation, transportation, reaction, and deposition. The deposited materials are called targets, which are often solid-state metals. The target materials are bombarded from a high-energy source via reduced pressures. PVD methods can be used as a better method to synthesize ultrathin films to meet the demands of environment-friendliness, low temperatures, compatibility to a lot of substrates and contribution to a range of multi-layer thin films[25].

One of the most commonly used PVD process to synthesize VO_2 films is reactive sputtering[26]. In 1967, VO_2 films were synthesized at the first time by applying ion-beam sputtering from a vanadium source to an argon-oxygen atmosphere[27]. From that moment, it has been broadly used to synthesize VO_2 films by this method. Usually, the sputtering methods are consist of radio frequency (RF), direct current, and magnetron. There are several advantages for these sputtering process, such as good homogeny of products, fine expansibility to bigger substrates and good efficiency for deposition.

In terms of the thermochromic property of VO_2 films, Batista et al. published a relative paper, which is about the deposition of Nb-doped VO_2 by using pulsed-DC magnetron sputtering method. In terms of this method, a high purity metallic vanadium target was used in an oxygen/argon atmosphere. Two gas mass flow controllers were used to provide and control the flow of oxygen and argon gases into the chamber separately. Compared with the VO_2 films synthesized by traditional DC sputtering, the VO_2 film deposited by this method gives a better thermochromic performance. VO_2 films can also be synthesized on the float glass with SiO_2-coating layer via reactive or pulsed-DC magnetron sputtering in an atmosphere which contains fixed ratio of oxygen and argon[28]. Before the deposition in an oxygen-free atmosphere, conditions need to be make sure to get metallic surface without oxide atoms, a pre-sputtering of the metal target was carried out. The relations between

oxygen partial pressure and its effects on the optical properties and electronic transition properties of VO_2 films were studied[29]. The study showed that the oxygen partial pressure can affect the resistivity transition and the structural performances of VO_2 films. The transmittance and optical absorption spectra below T_c were much related to the oxygen to argon content. And the T_c was decreased from 66.4 to 46.2 °C which follows the ratio of oxygen/argon from 2:48 to 1:49. With the reduction of the oxygen/argon ratio, there will be an increase of near-infrared extinction coefficient k and optical conductivity.

Some other development in the sputtering technology is also studied. There is a two-step procedure which is consist of the sputtering procedure and another condition, which might be oxidation or post-annealing. Xu et al. published an easy but new sputtering oxidation combination procedure to synthesize good quality VO_2 films. Regarding to their approach, it is the first time to fabricate the VO_2 film by DC-magnetron sputtering procedure, after that, it can be oxidized by a high temperature in with the help of oxygen. The results showed a potential phase transition at room temperature. By using DC magnetron sputtering method and a post-annealing procedure, VO_2 films which has a low T_c of 45 °C were synthesized. The transmission spectrum of the VO_2 film exhibited a good switching performance within IR range when the temperature is at the critical transition temperature, and the switching efficiency is about 52% at 3.39 μm. Through changing the experimental parameters, VO_2 films can also be fabricated by applying reactive ion sputtering, along with the help of a post-annealing process[30]. Nanostructured VO_2 films showed a good phase-transition performance. The T_c value was also reduced from 35°C to about 33°C, which is much better than the traditional VO_2 films. In 2014, an argon ion beam relative non-reactive AC dual magnetron sputtering has been published, this research studied how to prepare VO_2 films in substrates of bare glass and glass with ITO coating[31].

Some other approaches can be treated as important parts of PVD techniques. Pulsed laser deposition (PLD) can be seen as a PVD method, that is very suitable for the growth of oxide film[32]. A strong power pulsed laser beam is used in this

research. And the beam is devoted to a target with particular components inside a vacuum chamber. The evaporation progress of electron beam could be treated as a PVD method. By applying evaporation of reactive electron beam from a vanadium target in high oxygen atmosphere, high-quality VO_2 films can be synthesized[33]. The fabricated films display monoclinic VO_2 phase. Some experimental parameters about the properties of VO_2 films were studied. The VO_2 films were synthesized at a radio frequency incident power which is 50W. The VO_2 films synthesized in optimized conditions have excellent changes in optical and electrical performances along with the phase transition. The resistivity difference can be up to 10^4 and the transition width can be down to 3˚C in the heating/cooling hysteresis measurements.

2.2.2 Solution-based deposition

Even though the gas-deposition method is very useful in synthesizing VO_2 films, the facilities used in the gas-deposition is mainly expensive. In contrast, it is more cost effective to use the solution-based deposition. It has the property of high-yielding and agile. It gives an optional choice for the synthesis of smart window coatings. Some traditional solution-based methods will be talked below.

2.2.2.1 Sol-gel method

Sol-gel method[34-38] is a traditional wet-chemical method to fabricate different kinds of materials. The reaction usually starts from a chemical solution which contains colloidal precursors. It is commonly used to fabricate VO_2 films, especially for films doped with other metals. As it can control the chemical components, even though the quantity is small[39]. In 1983, Greenberg et al.[40] is the first person who used sol-gel method to deposit VO_2 films. He used $VO(OC_3H_7)_3$ as the source of vanadium. In a sol-gel procedure, the first step is to establish an oxide network by a polymerization reaction with chemical precursors, which is always dissolved in a liquid solution. Tetravalent alkoxide can be treated as the most commonly used

precursor, such as vanadium tetrabutoxide. But the price of it is high and it always need a high annealing temperature with a low oxygen atmosphere. Moreover, more research has been done to fabricate different vanadium precursors to form sol-gel derived VO_2 films.

An inorganic sol-gel progress has been published by Huang's group[41]. They focused on the synthesis of VO_2 films and elemental cerium (Ce)[42] and/or W[43] doped VO_2 films. The vanadium sol solution can be made by mixing vanadium pentoxide (V_2O_5) powder into water. With this precursor, VO_2 crystal structure can be got at relatively low calcination temperatures, which is about 400-600 °C. The thermal stability of VO_2 films through this method was also studied. The VO_2 films were deposited on muscovite (011) substrate and annealed in air at different temperatures. The VO_2 films were very stable in air when the temperature is lower than 200 °C. And it maintains its steady phase transition performances. When the annealing temperature was higher than 200 °C, there will be an increase in T_c according to the larger grain size of VO_2 film. Moreover, when the annealing temperature is increased to about 300 °C, the VO_2 will be oxidized to V_2O_5, with an increase in T_c and a decrease in the phase switching efficiency of VO_2 film. Phase transition property of VO_2 can be damaged if the annealing temperature is higher than 400 °C. Besides, an organic sol-gel method was also used to synthesize the VO_2 film[44]. The organic vanadium sol can be made by adding V_2O_5 powder in a mixture of $C_4H_{10}O$ and C_7H_8O at a particular molar ratio (V_2O_5: C_7H_8O: $C_4H_{10}O$= 1: 8: 80). Then the mixture will be refluxed at 110 °C for 4h. The VO_2 films can be grown on the mica substrate with spin-coating method. Additionally, VO_2 films will be annealed in static N_2 atmosphere from 440 to 540°C. In terms of the sample which is heated up to 500°C, the biggest TIR transformation during the transition was 73%. While the narrowest temperature hysteresis width was 8°C.

2.2.2.2 Hydrothermal synthetic method

Nanostructures are usually synthesized by hydrothermal synthesis[45-49] since unique nanoscale morphology can be generated by this method. It makes the control of structure possible, which can be completed through the typical high-temperature solid-state reactions[39]. Hydrothermal method have features like low cost and sensitive to synthesis atmospheres. The parameters such as time, pH, temperature, concentration, reducing agents and pressure can be very significant to affect the results and exploration of new phases. Hydrothermal method has been a possible method to synthesis VO_2 nanoparticles as it has such special features. Some pressure-dependent phase formation and pH-dependant morphologies have been studied in the case of VO_2 polymorphs[50]. However, in most cases, the results are non-thermochromic phase VO_2 (B) or a combination of VO_2 (M) and VO_2 (B) [40-41]. Recently, the research about hydrothermal processing of VO_2 has been focused on the synthesis of pure monoclinic phase VO_2 with particular morphology which has improved thermochromic properties.

Not only VO_2 nanoparticles, hydrothermal method can also be applied to the synthesis of VO_2 nanocomposites successfully. A TiO_2 seed-assistant hydrothermal method has been reported to synthesize molybdenum (Mo)-doped VO_2 (M)/TiO_2 composite nanoparticles[51].

Usually, a specific amount of rutile TiO_2 nanoparticles which is about 15 nm was added to the solution with oxalic acid ($C_2H_2O_4$), vanadium pentoxide (V_2O_5) and molybdic acid. Then the mixed solution will be heated in a sealed autoclave by 220 °C within 2 days. Through this research, more Mo doping can lead to the formation of VO_2 (M), and rutile TiO_2 seed is helpful to control the morphology, size distribution and infrared modulation of Mo-doped VO_2 (M) nanoparticles. The morphology changed from asterisk-like shape to quasi-spherical shape. For the asterisk-like particles, the size is around 1 um for Mo-doped VO_2 (M) without TiO_2 seeds, however, for the quasi-spherical one, the size will be reduced to 20 nm for Mo-doped VO_2 (M)/TiO_2 nanocomposites. Moreover, with the increase of TiO_2 seed

contents, the size of the composite nanocrystals will be decreased, and Tc can be modulated to room temperature.

The VO_2 (M)/SiO_2 nanofibers were made into self-supporting thermochromic films, it has been reported by Gao et al. [52] By their method, it is the first time to obtain the VO_2 (M) nanofibers by annealing VO_2 (A) nanofibers which are synthesized by hydrothermal method with the assistance of acid. For this method, it is by reducing NH_4VO_3 with 1, 3-propylene glycol in an acidic solution. Some parameters such as reaction time, temperature, and types of reducing agents were changed to study their effects on the last products. The final results keep its primary fibrous morphology, which has a great thermochromic properties. Through filtration, the VO_2 (M)/SiO_2 nanofibers were then deposited into a self-supporting film. It can display great thermochromic properties. At the same time, the VO_2/TiO_2 core-shell structure was also synthesized through VO_2 nanorods core from the hydrothermal method.[53]

2.2.2.3 Film deposition with the assistance of polymer

Polymer-assisted deposition (PAD) is a commonly used method to synthesize high-quality polycrystalline, particularly the metal oxide films. The method used relationships of polymers and metal ions to improve the homogeneous distribution of the metal ions and then the deposition of uniform metal oxide films. It can be treated as a cheap and scalable alternative approach for sol-gel method[54].

Recently, Gao's group[55] has developed this method to prepare some VO_2 films, it mainly enhanced the synthesis of nanostructured VO_2 films. By a standard PAD procedure (Fig.6), this is the first time vanadium solution was made with particular soluble polymers and doping chemicals. After that, the VO_2 film was deposited through dip-coating and spin-coating technique after annealing process. In 2009, Gao et al. published the synthesis of M/R –phase VO_2 films through PAD progress. In that research, the vanadium resource was provided by V_2O_5 and hydrazinium chloride (N_2H_4.HCl), it is used to form a $VOCl_2$ solution.

Poly (vinylpyrrolidone) (PVP) or poly (ethylene glycol) (PEG 6000) were put into the solution to work as a film forming promoter. In this research, it showed that PVP not only help to form the film but also improve the synthesis of M/R- phase VO_2. From Fig 7, we can see the SEM figures and optical transmittance images of the films, which has specific and porous structures. Even though the size of the particles with PVP (about 100 nm in diameter) was smaller than that of non-PVP samples, the porosity of non-PVP films (63.5%) was significantly bigger than the PVP added samples (17%). For all the above samples, a transition of semiconductor to metal state can be observed clearly (Fig.7 c and f). For the films with PVP, the optical

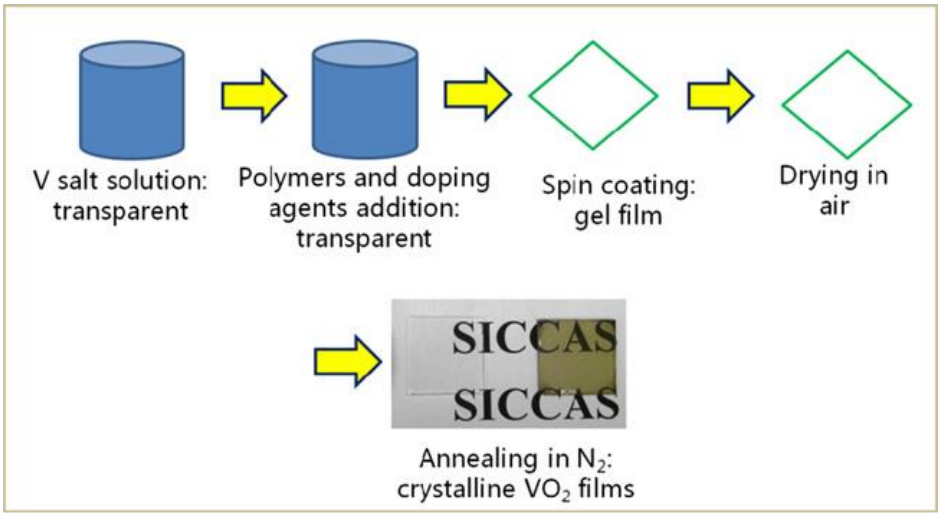

Figure 6 Process of VO_2 film deposition with the assistance of polymer.

properties were prominent in both visible range and IR range. It was also studied in details about how the microstructure affect the feature of the phase transition. The results showed that the grain sizes and boundary conditions can enormously affect the widths and slopes of the hysteresis loops.

Many researchers synthesized a lot of different VO_2 films with the PAD method, such as nanoporous VO_2 films[56], titanium doped VO_2 films[57], and VO_2 films with TiO_2 as a buffer layer[58]. For the PAD process, some polymers are need and PVP is the most commonly used one. In terms of investigating the role of polymer, a research of thermogravimetric/differential thermal analysis-mass spectrometry (TG/DTA-MS) has been conducted. According to the TG/DTA-MS analyses, the PVP can improve the formation of cross-linked high-quality gel with high quality, and this happens after the

evaporation of the solvent through the interactions of charged metal ions and amide groups. Moreover, PVP can also stop the segregation in the precursor solution by the space between the metal ions and the polymer. Furtherly, the molecular weight of the polymer also plays a great role in the decomposition sequence.

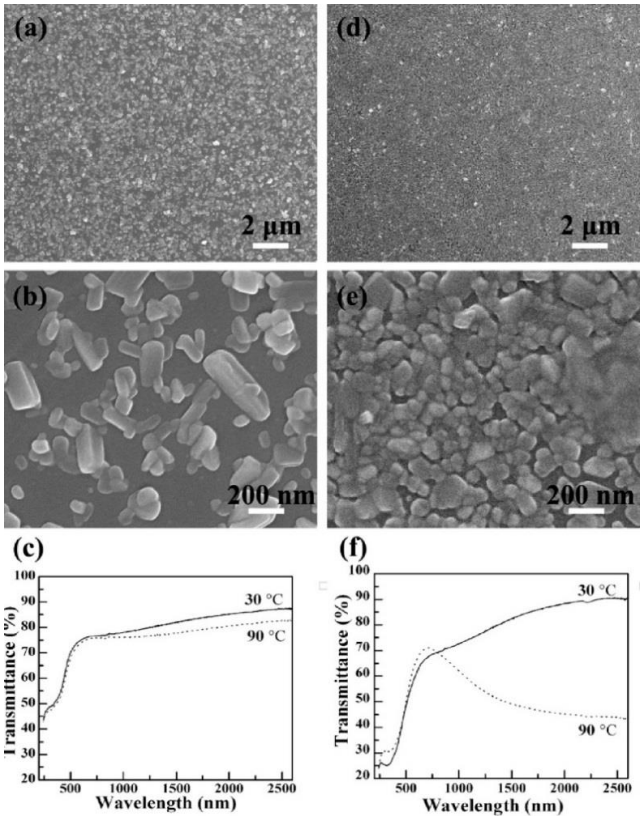

Figure 7 SEM figures and UV-Vis light transmittance spectra of VO_2 films synthesized by polymer-assisted deposition

Besides PVP, Miao et al. used another surfactant Pluronic F-127 (EO_{100}-PO_{65}-EO_{100}) to synthesize VO_2 films. They fabricated VO_2/SiO_2 composite films by a solution-processed deposition approach. In terms of the synthesis of VO_2/SiO_2 composite solution, a SiO_2 sol was firstly made before mixing with $VOC_2O_4.xH_2O$ solution to make a uniform, transparent and blue solution. The function of Pluronic F-127 was added to improve the film porosity as a pore-forming chemical. With the help of spin coater, the composite films can be deposited on a series of substrates. For the composite films synthesized by this method, all showed pore monoclinic phase structure and had great crystallinity. Moreover, the composite films have a better chemical stability, especially against oxidation. And both the T_{lum} and ΔT_{sol} were

improved. The film which has a molar ratio of Si/V which is 0.8 exhibited an enhancement of 18.9% (increase from 29.6 to 48.5%) in T_{lum} and an improvement of 6.0% (increase from 9.7 to 15.7%) in ΔT_{sol}, the result is much better than the VO_2 film. The reason is the addition of SiO2 in the films. SiO_2 addition was beneficial of increasing the stability of VO_2 and stop the aggregation of VO_2.

In summary, the comparison was given in the following table for the synthesis of VO_2 nanoparticles with different methods.

	Advantages	**Disadvantages**
Gas-based synthesis		
Chemical vapor deposition	• High growth rates possible • Good reproducibility • Can deposit materials which are hard to evaporate • Can grow epitaxial films	• Run in high temperature. • Safety issues, some precursors and by-products are toxic, pyrophoric or corrosive.
Physical vapor deposition	• Atomic control of chemical composition, film thickness and transition sharpness. • No toxic by-products • Flexibility of material • Simplicity of process	• Run in low temperature. • High cost

Solution-based synthesis		
Sol-gel method	• Simple technique • Cost effective • A large range of material can be used in this procedure • High purity • Precise control of doping level	• Cost of precursors • Shrinkage of a wet gel upon drying. • Preferential precipitation of a particular oxide during sol formation. • Difficult to avoid residual porosity and OH groups.
Hydrothermal method	• The ability to create crystalline phases which are not stale at the melting point. • Materials which have a high vapour pressure near their melting points can be grown by the hydrothermal method.	• Sensitive to atmosphere • Expensive autoclaves • Impossibility of observing the crystal as it grows.
Polymer assisted method	• Low-cost • scalable	• Complicated operation

Table 1 Summary and comments of method to synthesize VO_2 nanoparticles

2.3 Methods to enhance thermochromic properties of VO_2

2.3.1 Dope with other elements

In terms of the application of smart window industry, the T_c value should near to common room temperature, which is between 20-30°C[59]. There are some methods to deal with this problem, doping other elements[60-64] is one of the efficient approach. Elemental doping has been used broadly to decrease T_c and improve hysteresis loop width performance of VO_2 films[65]. It has been studies that T_c can be decreased by doping with high valence cations, such as Nb^{5+}, Mo^{6+}, W^{6+}, and Ta^{5+}. On the contrary, it can be increased by doping with low valence cations, including Ti^{2+}, Ga^{3+} and Cr^{3+} [66]. However, there are still much work need to do for the synthesis of elementally doped VO_2 films. Except different kinds of doped ions, the doped samples' thermochromic properties can also be affected by synthetic processes and types of ionic precursors. Besides, doping with other elements can also be treated as a method to modify the transmittance and the solar modulation ability of VO_2 films. How the dopants will affect the T_c and optical properties of VO_2 films will be talked here.

2.3.1.1 Decrease of T_c

Among all the ions, metallic W was treated as the most effective ions to decrease T_c of VO_2 films[67]. Many methods have been used to study the mechanism of decrease of T_c of VO_2 phase transition by W-doping. Synchrotron radiation X-ray diffraction spectroscopy was applied to look for the reasons of atomic structure evolutions of W dopant and its help in adjusting T_c. It is also helpful to use some first principle calculations to study this[68]. It is intrinsically symmetric for the local structure around the W atom. It usually shows an evolution which is related to the concentration, including repulsion, distortion and final stabilization according to a significant interference between doped W atoms and VO_2 lattices during the transition of the phase. It is obvious that the symmetric W core can drive the asymmetrical

monoclinic VO_2 lattice to be rutile-like VO_2 core, furtherly decrease the energy used in the phase transition.

Cho et al. studied the VO_2 films synthesize by inorganic sol-gel method, mainly on the effect of W on thermochromic performances and electrical performances of VO_2 film. They showed that doping with WO_3 can lead to an important change of the grain size of the VO_2 films. It can also adjust the pore size of the final VO_2 films. The T_c was also decreased to be 15.5 °C/mol.

It is possible that the T_c can be turn to room temperatures when 2.7 mol% WO_3 was used. Moreover, a spread phase transition and a weal change in the electrical resistance can be achieved by adding W toVO_2.

A hydrothermal method was used to synthesize VO_2 (A) and W doped VO_2 (M) nanobelts by Zhang et al[69]. It was showed that the dopant W was very important to control the VO_2 polymorph. Without dopant, the VO_2 (A) can be synthesized, however, VO_2 (M) can be got with tungstenic acid. The reason for this difference is given in the research. A small amount of vanadium atoms are substituted with tungsten atoms, which can induce the distortion of the VO_6 octahedral structure. It is helpful to separate the interconnections between octahedral structure and lead to the transition from VO_2 (B) to VO_2 (M). With the doped tungsten atoms into the VO_2 (M) matric successfully. T_c of VO_2 (M) was decreased to about 50 °C with a heating cycle at 2 at% tungsten doping and T_c can be changed to different temperature with the adjustment of tungsten atomic percent.

2.3.1.2 Enhancement of optical properties

To deal with some problems in practical application[70], such as the dark color of the glass which can affect the transmittance and lead to a low solar modulation ability. The application of VO_2 films in smart window need to increase the T_{lum} and $\Delta T_{sol.}$ Moreover, the yellow color of the films are not pleasant for human eyes[71]. The

optical properties have important relationships with film thickness, microstructure, and optical constants. Until now, a lot of methods have been tried, and among them, element doping is a very useful method to improve the visible light transparency and decrease the original yellow color of the VO_2 films. The typical dopants include fluorine (F)[72], Mg[73] and Ti[74].

The doping of fluorine was firstly studied from 1989. Khan and co-workers. synthesized films of vanadium oxyfluoride and it shows that the doping of fluorine is beneficial to increase the transmittance and modify the structural transformation temperature[75]. It showed a very good thermochromic properties in the near-infrared region for the VO_2 films doped with F. Not like pure VO_2 films, F-doped VO_2 films shows a better solar-heat shielding ability (35.1%) and an accurate T_{vis} (48.7%). The doping of fluorine for the VO_2 films deal with the reduced Tc problem, it also dilute the color and gives out a great thermochromic property.

Mg is another well-studied doping material. In 2009, the Tc has been reported that it is reduced by 3°C per 1 at% Mg. At the same time, the optical transmittance was also modified[76]. Particularly, if the Mg amount was increased to 7at%, Tc will drop to 45°C, and T_{vis} and T_{sol} will be increased by 10%. Li et al. synthesized Mg-doped VO_2 films, with various of atom ratio z (z=Mg/(Mg+V)), on carbon substrates and heated glass. Films doped with My have a much better T_{lum} and ΔT_{sol} as a contrast to pure VO_2 films.

Some other research about earth metals (AEM) doping was conducted by Dietrich et al[77]. The alkaline earth metals include Mg, Calcium (Ca), Strontium (Sr) or Barium (Ba). AEM doping can make a big improvement of thermochromic properties. Moreover, the appearance of the films can be modified with an AEM doping. The problem of the brownish coloration of pure VO_2 can be overcame by AEM doping.
Zinc (Zn) can be treated as another interesting dopant, it is found that zinc doping can be used to adjust optical properties of VO_2 films. Usually, the zinc doped VO_2 films were synthesized by a PAD method. In that method, $ZnCl_2$ was put into the precursor solution to adjust the microstructure of the last films[78]. It is found that $ZnCl_2$

can be used to enhance the micro-roughness of the final films which will be helpful to increase the T_{lum} and ΔT_{sol}. Zinc doping will be important to control the structure, average particle size and surface roughness of VO_2 films. It will lead to the enhancement of optical performances. Compared to VO_2 films without doping, the absorption edge of the $V_{1-x}Zn_xO_2$ (x = 0.077) film shows a shift to UV light side by 80 nm. As we can see from Fig. 8b, T_{lum} was increased by 30%. When the $V_{1-x}Zn_xO_2$ film has an x = 0.077, the color of VO_2 films will change from yellow to a better color. It is because it has a blue shift of the absorption edge (Fig. 8a).

In a nutshell, it has been found that element doping is a very useful strategy to modify thermochromic properties and optical properties of VO_2 films. The addition of other elements can lead to change in thermochromic transition, optical properties and electrical performance of VO_2 films. The most effective dopant for reduction of Tc to lower temperature is W. The doping content of W can not only reduce the Tc but also control the VO_2 polymorph. Elements doping is also a helpful way to enhance the optical properties of VO_2 films, it can improve the visible light transmittance and decrease the yellow color validly. In the case of F doping, a better ΔT_{sol} (10.7%) and T_{vis} (48.7%) can be got with an F doping, the color of the VO_2 films also gets a big improvement. Not only the traditional dopants, some new dopants are also in the research, which includes Zn, Zr, and alkaline earth metals. Especially, many dopants can decrease transition temperature (T_c), improve T_{lum}, increase ΔT_{sol} and change the appearance of VO_2. That is very meaningful for practical application of VO_2 films.

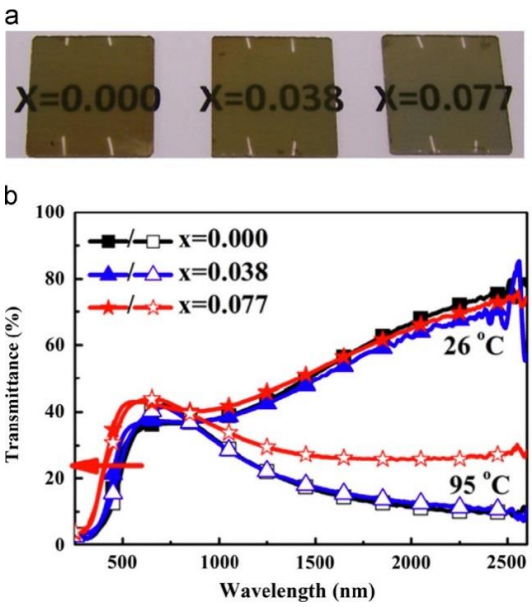

Figure 8 (a) Photograph of $V_{1-x}Zn_xO_2$ films of different concentration of Zn. (b) UV-Vis Transition spectra of the $V_{1-x}Zn_xO_2$ films.

2.3.2 VO_2 multilayer structures

Another problem for practical application is the stability of VO_2 films.VO_2 films are not stable in moisture air atmosphere. Sometimes, the single layer VO_2 on a substrate is not enough for practical using. Many methods have been used to stabilize the VO_2 films. One of them is to combine other layers of materials to provide new functions to the performance of VO_2 films. It can be treated as a highly potential method to modify the VO_2 smart window. As we can see in Fig.9, a multilayered structure was made and deposited by using a combined nanostructured VO_2 films with a low T_c value which is about 35°C. Visible light can go through the multilayered structure at different temperature. However, for the infrared light, it is transparent at low temperature and opaque at high temperature. As a result, it can adjust the transmittance of infrared light as a smart material.

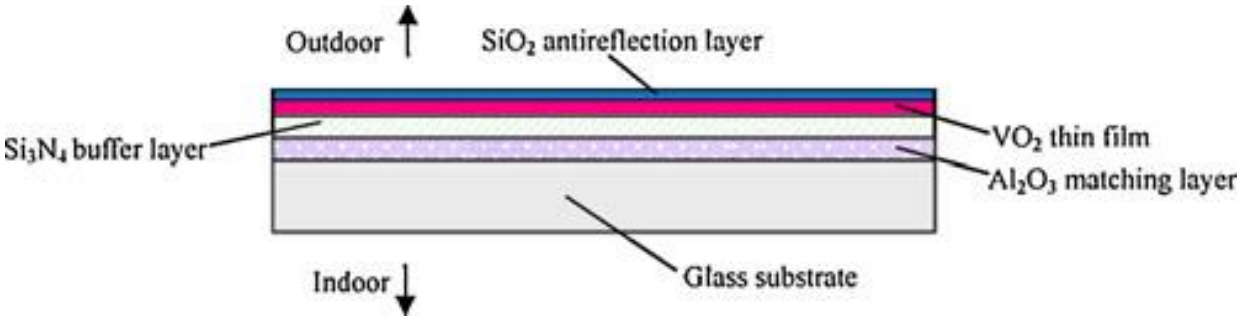

Figure 9 Schematic multilayer structure for smart windows.

2.3.2.1 Buffer layer of metallic oxide

Different kinds of metal oxide, such as ZnO, TiO_2, SnO_2, and CeO_2 were used to work as a buffer layer for VO_2, as they have structural similarity to VO_2. Park et al.[79] studied the phase formation and thermochromic functions of these layers to VO_2 films. As we can see, the buffer layers play an important role on the growth of VO_2 films. Though the use of TiO_2, ZnO, and SnO_2 as buffer layers, we can synthesize

the VO_2 (M) films at around 370 °C. However, if the CeO_2 buffer layer was the substrate, the VO_2 (B) will be formed. Moreover, the buffer layers can also influent the thermochromic performances of VO_2 (M) films. When VO_2 films were combined to ZnO, SnO_2, and TiO_2 buffer layers, they can show great thermochromic properties. The synthesized VO_2 film on ZnO buffer layer shows a much bigger transition amplitude and a much smaller hysteresis width. The reason is that the ZnO film which is grown on a soda line glass usually had preferred orientation at 370 °C. Gao and co-workers [58] also published that the incorporation of TiO_2 as a buffer layer. It can be used to increase the oxidization resistance property of solution-deposited VO_2 films in an atmosphere of high-level oxygen content. VO_2 can be turned into V_2O_5 by an oxidization treatments when it is deposited on the surface of fused quartz substrates, however, oxidation progress can be decreased by the TiO_2 buffer layer, particularly at the VO_2/TiO_2 interface.Buffer layer can not only enhance the crystallinity performance and the oxidization resistance property of VO_2 films, it can also optimize the optical properties of VO_2 films. Usually, the VO_2 films have a weak function of low radiation. It means that it has small reflective property for far-infrared light, particularly when the wavelength of the light is 3μm and the wavelength range of 3-50μm from the objects inside and outside the room from the environmental radiation[80]. In terms of improving the optical performances of VO_2 films, an Al-doped ZnO which is also known as AZO top layer has been applied to deposit on the VO_2 films[81]. In fact, AZO/VO_2 films has a low emissivity of 0.31-0.32, it also has a potentially property of T_{lum} (> 46%) and ΔT_{sol} (> 4.1%). The phase transition temperature also has a decrease (Fig. 10) because of the AZO layer, which makes an attribution to the formation about surface non-stoichiometry, for example, some deficiency of oxygen. Moreover, VO_2 films also have an increased anti-oxidization ability. As we can see in Fig. 10b, after the oxidization experiments, the thermochromic properties of single-layered VO_2 films disappeared. However, the AZO /VO_2 films still shows strong thermochromic properties with an outstanding increase in T_{vis}, as we can see in Fig 10c. The increase of T_{vis} is according to the result of $Zn_2V_2O_7$ after oxidization (Fig. 10d).

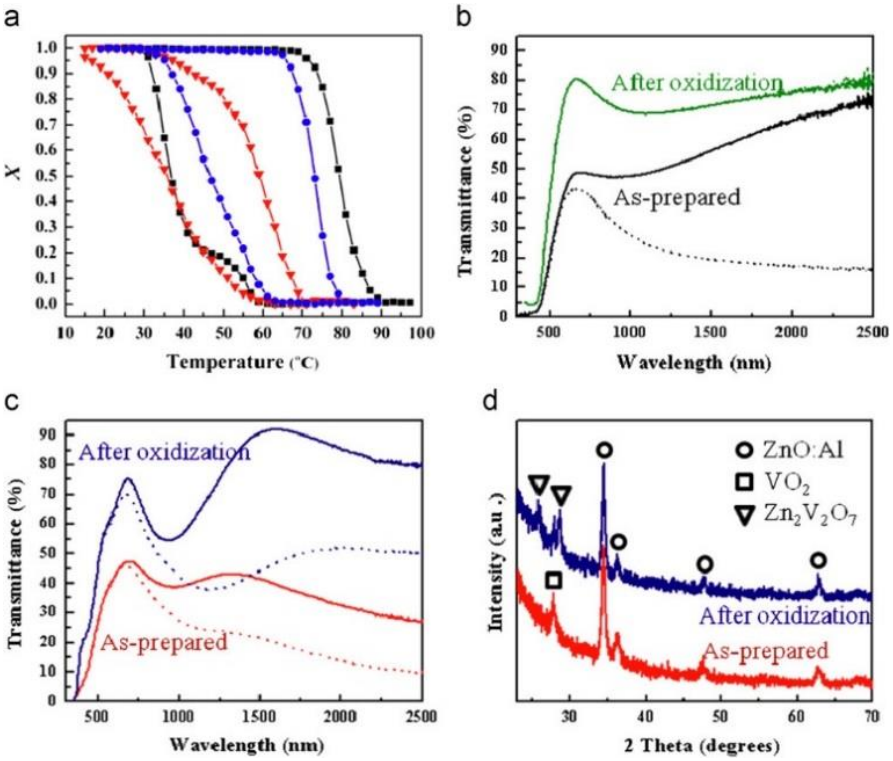

Figure 10 (a) Normalized thermal hysteresis loops of optical transmittance at 2.0μm for bare VO_2 (lines with squares) and AZO/VO_2 double-layered films before (lines with triangles) and after oxidization experiments (lines with circles). (b) Transmittance.

2.3.2.2 Layers with antireflection ability

Antireflection coating is a sort of layer structure prepared in VO_2 films. Usually, the function is to enhance the optical performances of VO_2 films. It has been reported that Long et al. found that Si-Al based antireflection coatings can improve the thermochromic properties of VO_2 films. By the usage of Silicon-Aluminium coatings, the transmittance can be enhanced and the IR contrast can be maintained at 2500 nm with 18% increase in ΔT_{sol}. When it is in low-temperature phase, it gives more obvious antireflection effect. At optimized conditions, both promising T_{lum} (47.5%) and ΔT_{sol} (7.7%) can be got. VO_2 films can also alter it hydrophilic property, and the contact angle (θ) can be changed from 25˚ to above 100˚, with the assistance of fluorination. The F-Si based antireflection layer exhibit improvement to an enhancement in T_{lum} by 14% without affecting ΔT_{sol}[82]. By using a solution process, VO_2 based double-layered films have been synthesized which contains SiO_2 and

TiO_2 antireflection layers. Through modifying the antireflection coating and the thickness of the film, the T_{lum} of TiO_2/VO_2 double coating structures was improved to 84.8%. The ΔT_{sol} has the potential possibility to be increased to 15.1% by changing the position of antireflection peaks. It has been successfully obtained the sample which has a balanced T_{lum} of 58% and ΔT_{sol} of 10.9%.

Recently, according to a medium frequency reactive magnetron sputtering method[83], a large a large-scale (400×400 mm^2 area) multifunctional TiO_2 (R)/VO_2 (M)/TiO_2 (A) multilayer film has been successfully synthesized. The mixed films have a lot of functions. Firstly, its middle VO_2 (M) layer has thermochromism. Secondly, the top layer TiO_2 (A) has photo-induced hydrophilic performances and photocatalytic property. Finally, it also has functions such as self-cleaning or anti-fogging. The TiO_2 at the bottom has a rutile phase, and it is significant in the formation of monoclinic phase of VO_2 layer and works as an antireflection layer. Moreover, if the TiO_2 layer has a proper thickness, the T_{lum} and ΔT_{sol} of the film can be increased. The multilayer film had a satisfactory optical abilities with great ΔT_{sol} (10.2%) and applicable T_{lum} (30.1%) when the temperature is low. The multilayer coating with multifunction has an excellent performances application for smart windows.

2.3.2.3 Assistance of layers of noble metal

Except antireflection layer, noble metal films can also be used extensively to minimize the thermal exposure while maintaining proper visible transmission of glass substrats[80]. It has showed that the integration of noble metals, such as Au and Ag, has a significant effect in modifying optical properties of VO_2 films. Especially, when the wavelength region is between 500 to 1500nm. Recently, by using PAD process and sputtering, Pt/VO_2 composite films were grown on fused silica substrates[84]. The use of Pt layers significantly increase the infrared reflection of VO_2 films. The transmittance can be increased from 25.1 to 37.9%% at 0.55 μm with the addition of antireflection coating. At the same time, the Tc of Pt/VO_2 films was decreased to 9.3 ˚C if the Pt layer has a thickness of 9 nm. The T_{vis} can also be diminished by the Pt

layer, and it can be significantly boosted with the addition of SiO_2 antireflection coating.

In a nutshell, it has been treated as a valid method to improve thermochromic properties of VO_2 films by designing and construction of VO_2 multilayers. A large amount of layers are used in the multilayer system, and they are playing different roles. Among them, metal oxide buffer layers can enhance the crystallinity property and oxidization resistance ability of VO_2 films. Particularly, oxide layer could improve the optical performances of VO_2 films too. For instance, with the addition of AZO top layer, the emissivity will be decreased and a promising optical performance can be got [T_{lum} (>46%) and ΔT_{sol} (> 4.1%)]. Besides that, T_{lum} and ΔT_{sol} values of VO_2 films can be also improved by introducing antireflection coatings such as Silicon-Aluminium based coatings or TiO_2 coatings. The noble metal layers usually have a lot of functions to improve the optical performances of VO_2 films, such as modifying the light property in the medium infrared radiation region, changing the colour or reducing T_c of VO_2 films. Moreover, many special results can be got by synthesizing multilayer structure. Representatively, by using VO_2/Al_2O_3 based metal/Vanadium dioxide/semiconductor equipment, the semiconductor/metal transition can occur.

2.3.3 VO_2 microstructures

In terms of improving thermochromic properties[56, 103] of VO_2-based materials for energy conservation, many nanotechnology methods can be used. In recent years, more researchers feel interested in VO_2 nanoparticles, as they could be applied to achieve the clear-cut thermochromic functions. Fig.16 shows temperature resistant spectrum of VO_2 films with VO_2 particles in small and large size. For the VO_2 film with nanostructure, when the grain size is 8 nm, the T_c is 35 ˚C (Fig.17b). When the size is about 1-2μm (Fig.17a), the T_c can be increased to about 68 ˚C.

For the research of the relationship of the grain size and hysteresis width about VO_2 films. Zhang and co-workers.[104] synthesized VO_2 films with spherical nanoparticles in

various sizes with DC reactive magnetron sputtering method. As we can see in Fig. 13 a-d, through changing the annealing time, the size of the VO_2 nanoparticles can be controlled.

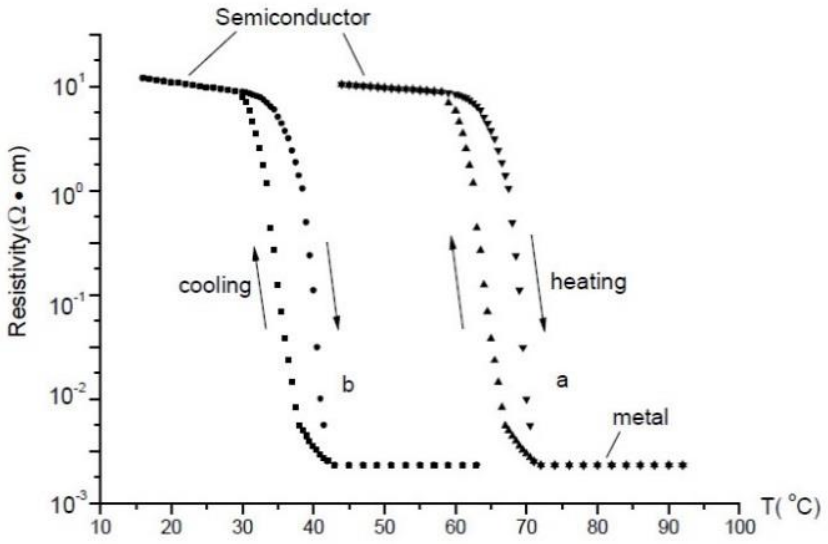

Figure 11 Resistance-temperature (R-T) spectrums of microstructure (a) and nanostructured (b) VO_2 films.

By increasing the annealing time up to 45 min, the porosity of the film can be decreased dramatically. After that, the porosity improved again. Fig. 13e exhibits optical transmission spectrum of results with different calcination times, and they have been tested at the wavelength about 1100nm. The results showed that the hysteresis width will be increased with the smaller average grain sized VO_2 films.

2.3.3.1 Porous nanostructures for VO_2

It has been a meaningful method to enhance the thermochromic properties of smart windows by synthesizing the porous nanostructures.

Gao et al. [105]has reported that the crystallized mesoporous TiO_2-VO_2 films can be synthesized by dispersing VO_2 nanoparticles into TiO_2 sol. In that case, a two-step

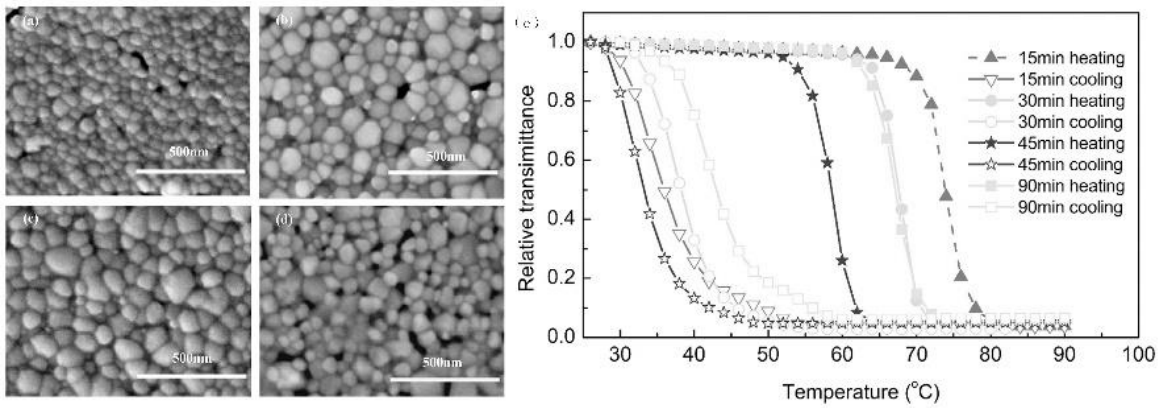

Figure 12 SEM images of VO_2 films annealed for different times: (a) 15 min, (b) 30 min, (c) 45 min and (d) 90 min. (e) Optical transmittance curves of VO_2 films annealed for different time durations.

calcination procedure was employed. A coupling chemical has been employed to treat the structure of the specimen. With the appearance treatment, the VO_2 nanoparticles can dispersed in the TiO_2 sol well, and the sols shows great film-forming property. The porosity can be controlled by changing the annealing rate, then the optical performance can be affected. The optimized sample had T_{lum} values of 62.0% at 20 ˚C and 60.5% at 90 ˚C, as well as ΔT_{sol} of 14.6%. Moreover, as the presence of crystallized TiO_2, a self-cleaning function can also been seen in the composite films.

Unlike the disordered structures, there are some special advantages for the ordered nanostructures. The reason is that the ordered nanostructures often has much bigger appearance space and potential nano-size effects which has the possibility to be affected by the high directionality. A method used to synthesize nanoporous/nanotubular VO_2 layers was studied by Schmuki et al. [106]and the layers were got by an optimized anodization/annealing progress. By using self-ordering anodization treatment in a heat atmosphere at suitable environments, self-assembled VO_2 layers with different kinds of good ordered nanostructures can be synthesized. In the warming and cooling progress in the alteration of phase, an obvious reversible super-cooling effect can be seen. The defects of the grains can be treated as a center of pinning for tetragonal phase, and it can lead to the fast-cooling effect and increased hysteresis loop width in the nanoporous VO_2 layers.

In summary, nanotechnology is very significant to develop high-performance thermochromic. In order to balance the performance between T_{lum}, ΔT_{sol} and thermochromic effects, nanostructure film can be demonstrated as a good model. Moreover, core-shell nanostructures can be treated as a very potential materials to create smart window with many functions. For example, VO_2 smart solar cells were synthesized by VO_2/SiO_2, VO_2/TiO_2 and VO_2/polyurethane core-shell structure. And it has thermochromic and energy-saving properties. The preparation of porous nanostructures have been a new method to get great thermochromic performances as both T_{lum} and ΔT_{sol} can be improved by simply increasing the porosity. Particularly, additional advantage can be given through ordered porous nanostructures according to the high directionality and large surface area. High T_{lum} (76.5%) and ΔT_{sol} (14.0%) can be got from VO_2 films with orderly patterns.

2.4 Some synthesized VO_2 and VO_2 composites

2.4.1 VO_2 nanoparticles

Gao et al. have synthesized pure single-crystal rutile VO_2 powders by a one-step hydrothermal reactions at 240 ˚C for 7days[85].V_2O_5 powder was used as vanadium source, and oxalic acid was used as reduced agent.

W-doped rutile-type VO_2 has been assembled by a hydrothermal reaction without subsequent thermal treatment. The VO_2 rods and the snowflake powders have a monoclinic structure with [110] directional preferential orientation growth. And it shows that the addition of tungstenic acid affects the phase of the as-grown VO_2 nanostructures significantly.

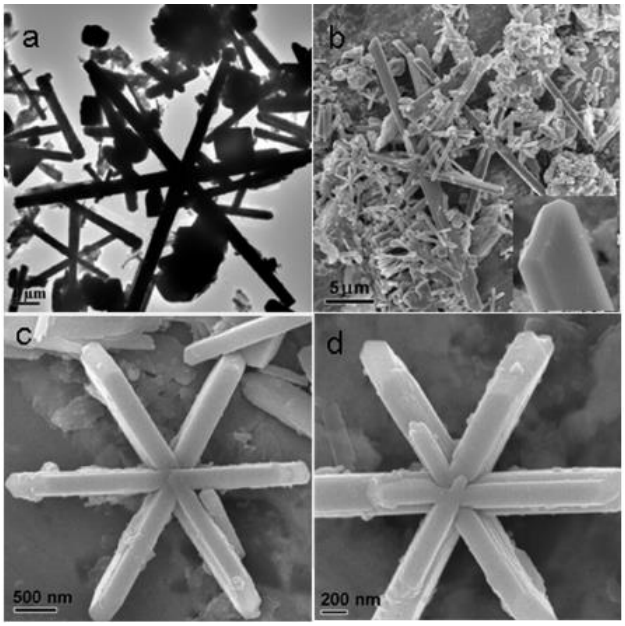

Figure 13 (a) Typical low-resolution TEM and (b) field-emission SEM images of the VO_2 powders. (c) Snowflake-shaped VO_2 structures with perfect crystallinity, and (d) the "growing" snowflake-shaped VO_2.

Whittaker et al. prepared VO_2 nanobelts (Fig.12) from solvothermally exfoliate bulk V_2O_4 by different aliphatic alcohols[86].With the exfoliation, the synthesized VO_2 nanobelts give a different thermal behavior, a wider hysteresis loop, and a broadened differential scanning calorimeter (DSC) peak according to the size effects. The reaction time can affect the morphology of nanobelts and its size.

This research group also hydrothermally synthesized star-shaped VO_2(M) nanocrystals(Fig.13)[87] and W-doped VO_2(M) nanobelts and nanobeam by one step[88].

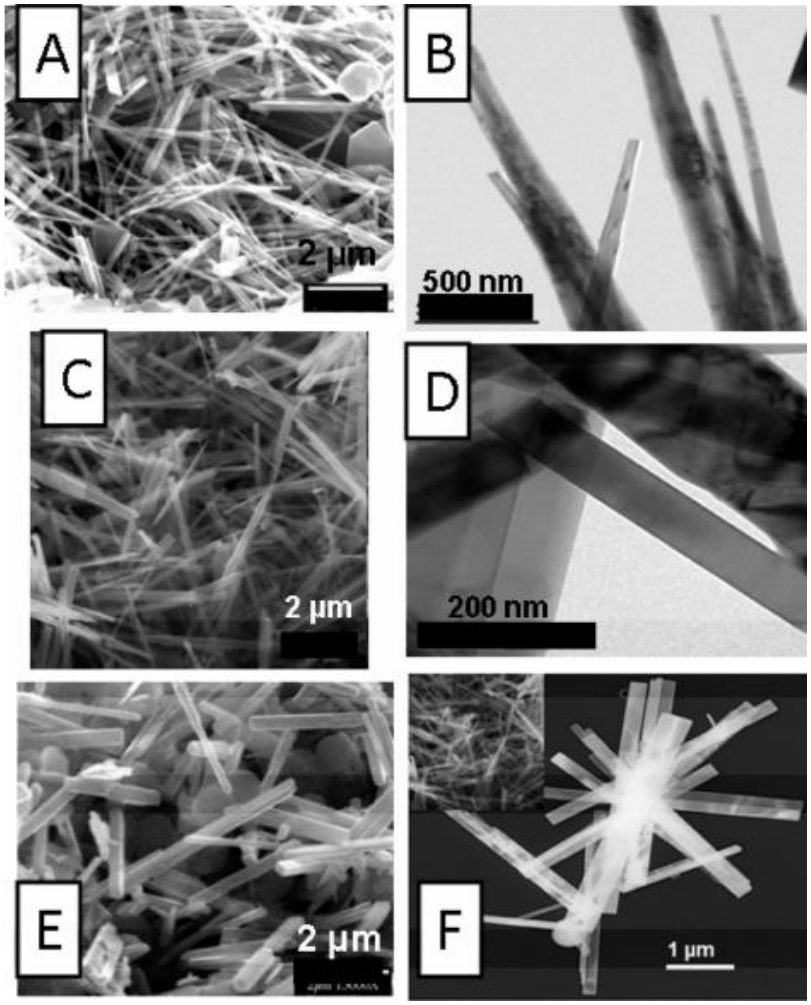

Figure 14 SEM (left) and TEM (right) pictures of VO_2 nanostructures synthesized by the solvothermal reaction of bulk V_2O_4 with (A,B) 2-propanol for 3 days, (C,D) methanol for 7 days, and (E,F) 1,3-butanediol for 7 days.

Wu and his coworkers synthesized VO_2(M) single-domain nanorods at 200 ˚C, and this is the lowest hydrothermal temperature to one-step VO_2 (M)[89].And it gives new light on deeper investigation of VO_2(M) single-domain structure by the large-scale synthesis of monoclinic VO_2 (M) nanorods.

There are also some research reports of one-step hydrothermal synthesis of undoped[90], W-doped[91-93], and Mo-W co-doped VO_2 (M)[94].Some published results of one-step hydrothermal synthesis of VO_2 (M) and the details of the experiment parameters, $T_{lum,}$ and ΔT_{sol} (Table 1).

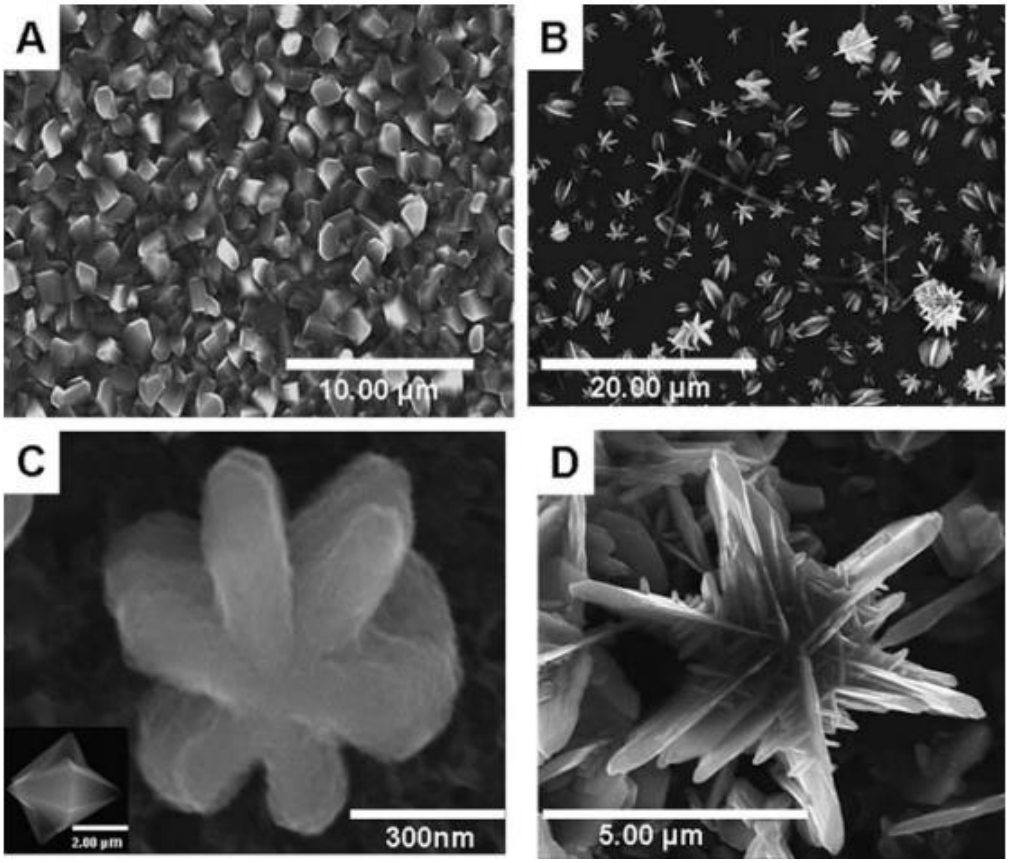

Figure 15 SEM images of the deposited V_2O_5 layers and nanostars. (A) Polycrystalline V_2O_5 film prepared by the catalytic vapor transport of bulk VO. (B) V_2O_5 nanostars formed by the combined vapor transport/ hydrothermal dissolution of vapor-deposited V_2O_5 layers. (C) High magnification of an as-synthesized V_2O_5 nanostar; inset shows a cross-sectional image. (D) Incomplete separation of the six arms indicating and unfinished reshaping of the surface-tethered V_2O_5 grains

According to the table, the value of ΔT_{sol} is up to 22.3%, which is so far the best reported thermochromic record for VO_2 system. And all the T_{lum} and ΔT_{sol} in the table is lower than the theoretical simulation value ($T_{lum} \approx 60\%$ and $\Delta T_{sol} \approx 25\%$), which means there is still a lot of performance to develop by synthesizing a high pure and high-thermochromic-property VO_2 (M) via hydrothermal method.

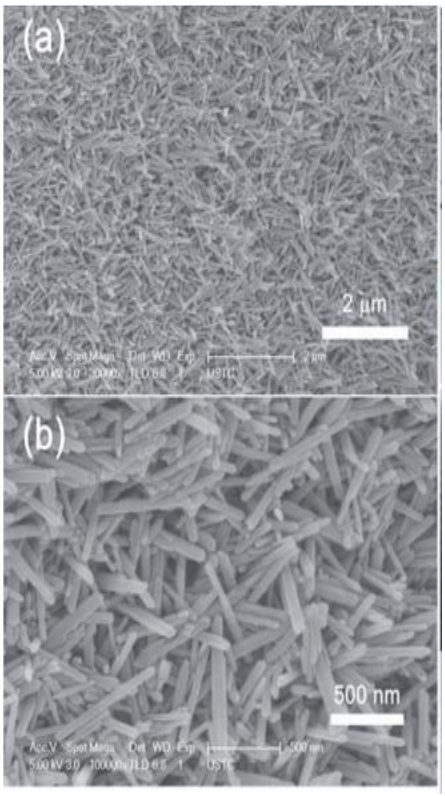

Figure 16 (a) and (b): Low and high magnification FESEM images.

Precursor	Doping	Morphology	T_{lum} and ΔT_{sol}	Ref
$V_2O_5+H_2C_2O_4+(NH_4)_5H_5[H_2(WO_4)_6]$	W	Nanorod	T_{lum}=60.6%,ΔT_{sol}=10.3%	93
$V_2O_5+H_2O_2+H_2WO_4+N_2H_4$	W	Nanobeam	T_{lum}=31.2%,ΔT_{sol}=6.4%	95
$V_2O_5+H_2C_2O_4$	N/A	Star-shape	T_{lum}> 40%	96
$V_2O_5+H_2C_2O_4+NaOH+NH_4$	W	Nanoparticle	T_{lum}=33.5%,ΔT_{sol}=16%	85
$V_2O_5+N_2H_4+H_2O_2$	W	Nanoparticle	T_{lum}=45-60%	97
$V_2O_5+Sb_2O_3+N_2H_4+HCl$	Sb	Nanoparticle	T_{lum}=35%,ΔT_{2000nm}=40.6%	98
$VOSO_4+N_2H_4+CO(NH_2)_2$	W	Nanoparticle	T_{lum}=20.6%, ΔT_{sol}=7.6%	99
$V_2O_5+N_2H_4.HCl+HCl$	N/A	Nanoparticle	T_{lum}=45.6%,ΔT_{sol}=22.3%	100
$V_2O_5+H_2C_2O_4+TiO_2+ZnO$	N/A	Nanoparticle	T_{lum}=52.2%,ΔT_{sol}=9.3%	101
$V_2O_5+H_2C_2O_4+MgNO_3$	Mg	Nanoparticles	T_{lum}=54.2%,ΔT_{sol}=10.6%	73
$V_2O_5+H_2C_2O_4+NH_4F$	F	Nanoparticle	T_{lum}=48.1%,ΔT_{sol}=13.1%	112

Table 2 Summary of some published papers about one-step hydrothermal synthesis of VO_2 (M) and related experiment parameters, T_{lum} and ΔT_{sol}.

Gao et al. have tried to synthesize the VO_2 (M) nanoparticles by transfer VO_2 (D) nanoparticles. The XRD and SEM images are shown in Fig. 29, therefore, the results

are similar to Gao's results[102]. And it seems that the two-step synthesized VO_2 (M) nanoparticles have smoother XRD peaks.

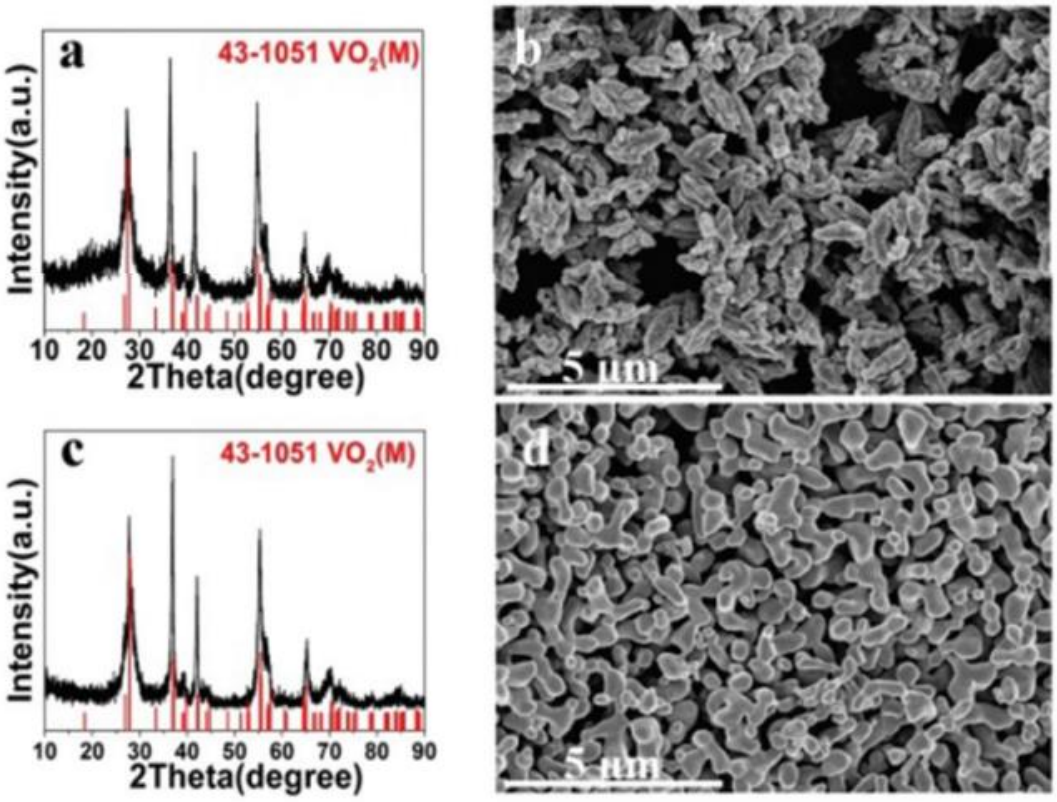

Figure 17 XRD patterns and SEM images of the as-obtained cucumber shaped VO_2 (M) (a, b) and VO_2 (M) nanoaggregates (c, d).

2.4.2 VO_2@SiO_2 core-shell structure

Meng et al. have tried to synthesize VO_2 (B)/C core-shell composites for the application of supercapacitor electrode. The core-shell structure was obtained by a facile one-pot hydrothermal method, and commercial V_2O_5 powder was used as a vanadium source[107]. The products consist of the crystal VO_2 (B) phase and the amorphous carbon phase with the VO_2 (B) core encapsulated into carbon as a core-shell nanobelts. The products shows an excellent energy density of 198.9W h Kg^{-1}at a power density of 504.5 W Kg^{-1} and a fast reversible redox Faraday response.

Chen and the coworkers tried to synthesize the VO_2@ZnO core-shell nanoparticles on the purpose of enhancing the performance and durability of thermochromic films[108]. The VO_2 nanoparticles were synthesized by a common hydrothermal method. Vanadium source was provided by commercial V_2O_5 and reduce agent was oxalic acid powders. And the VO_2 was dispersed into deionized water, with the assistance of hexadecyl trimethyl ammonium bromide (CTAB), zinc nitrate hexahydrate ($Zn(NO_3).6H_2O$),hexamethylenetetramine (HMT), a uniform solution can be obtained, then the suspension will be heated up to 85 ˚C and maintained up to 8 h. Finally, the VO_2@ZnO nanoparticles can be got (Fig 19, 20).This novel thermochromic VO_2@ZnO core-shell structure has excellent integrated performance, which has an enhanced thermochromic performance (ΔT_{sol} of 19.1% and T_{lum} of 51.0%). And the ZnO shell gives a protection for the VO_2 nanoparticles.

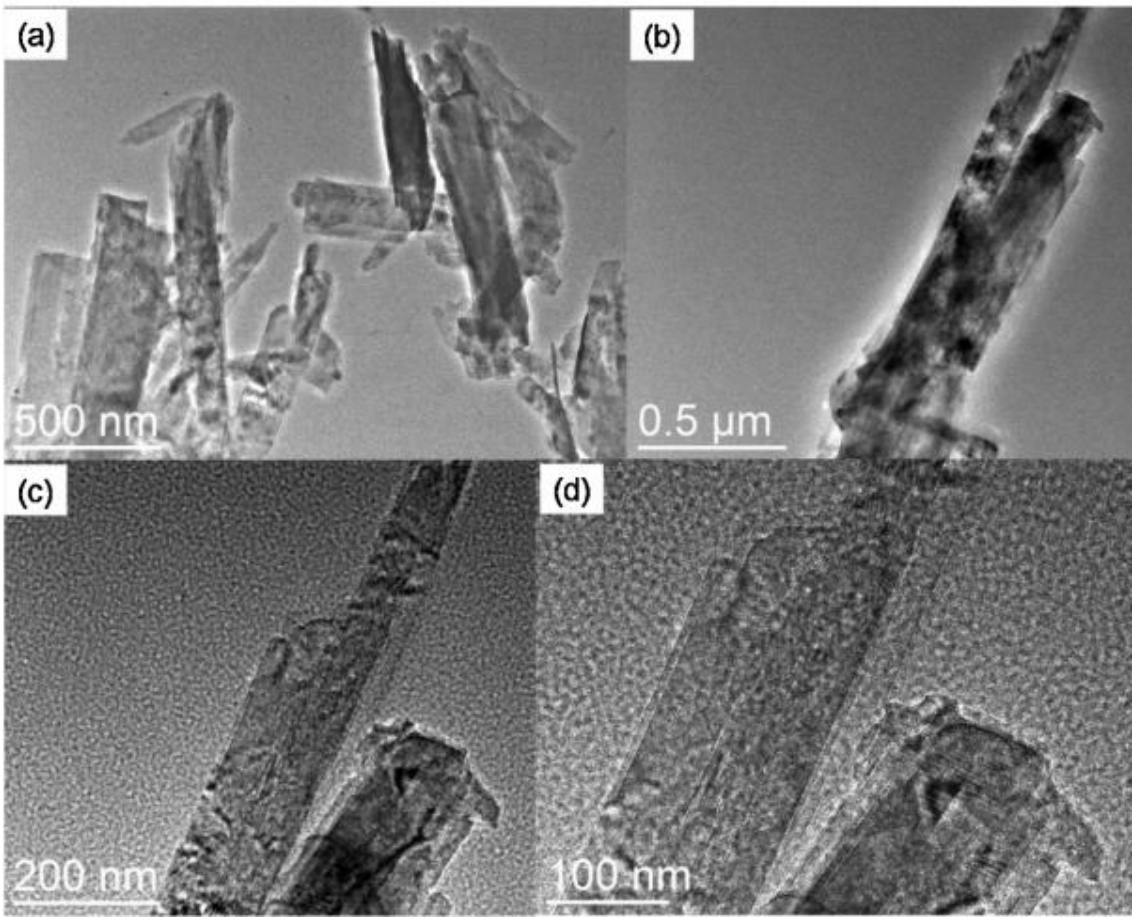

Figure 18 TEM images of the typical VO_2 (B)/C composites.

Tong et al.[109]have tried to prepare VO_2/Al-O core-shell structure with improved weathering resistance for smart window. Firstly, the VO_2 nanoparticles were synthesized via a hydrothermal treatment. Then the synthesized VO_2 nanoparticles were dispersed in deionized water by ultrasonic. The $AlCl_3 \cdot 6H_2O$ was added into the suspension as Al source. Methenamine ($C_6H_{12}N_4$) was applied to prompt the Al^{3+} to hydrolyze. As Methenamine is a kind of non-ionic amine, which can be soluble in water and release OH^- slowly. The reaction was conducted at 60 ˚C for 5 h with vigorous stirring. The final particles were dried in air at 80 ˚C. Annealed V/AO can be synthesized after the sediments were heated in vacuum at 600 ˚C for 3 h.

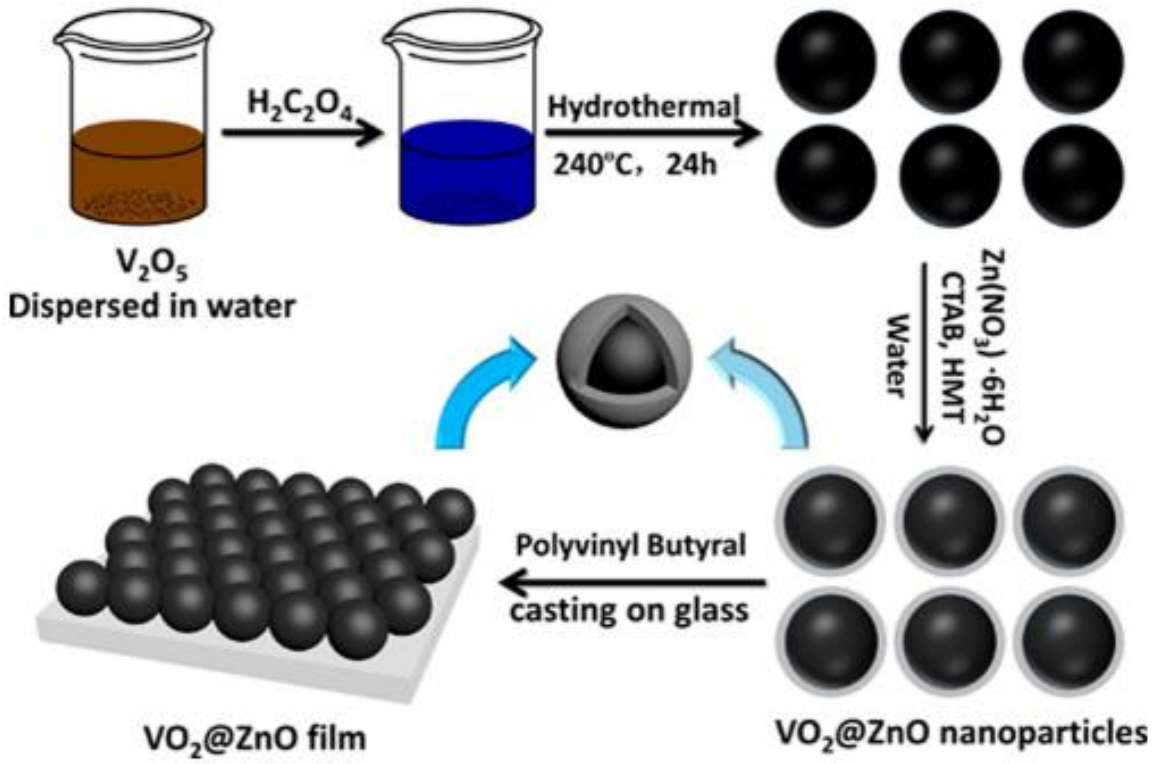

Figure 19 Process of synthesis of VO_2@ZnO core-shell nanoparticles

With the protection of the Al-O shell, the VO_2 core can be stable for high temperature (350 ˚C in air) or in the moist air heating condition. And this core-shell structure show

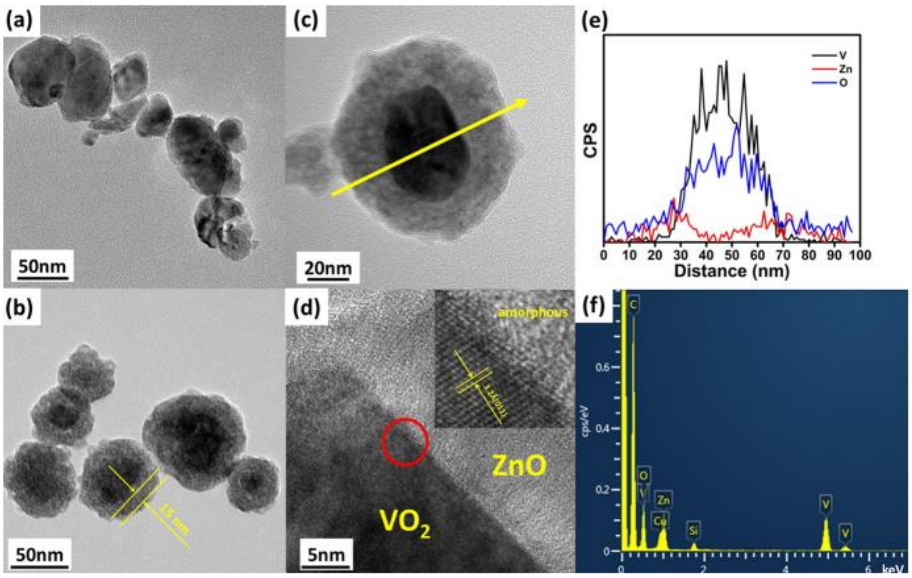

Figure 20 . (a) TEM image of uncoated VO_2 nanoparticles. (b, c) TEM images of VO_2@ZnO core−shell structure nanoparticle. (d) HRTEM image

good optical performance and well chemical stability. This work is meaningful for the application of VO_2 smart windows.

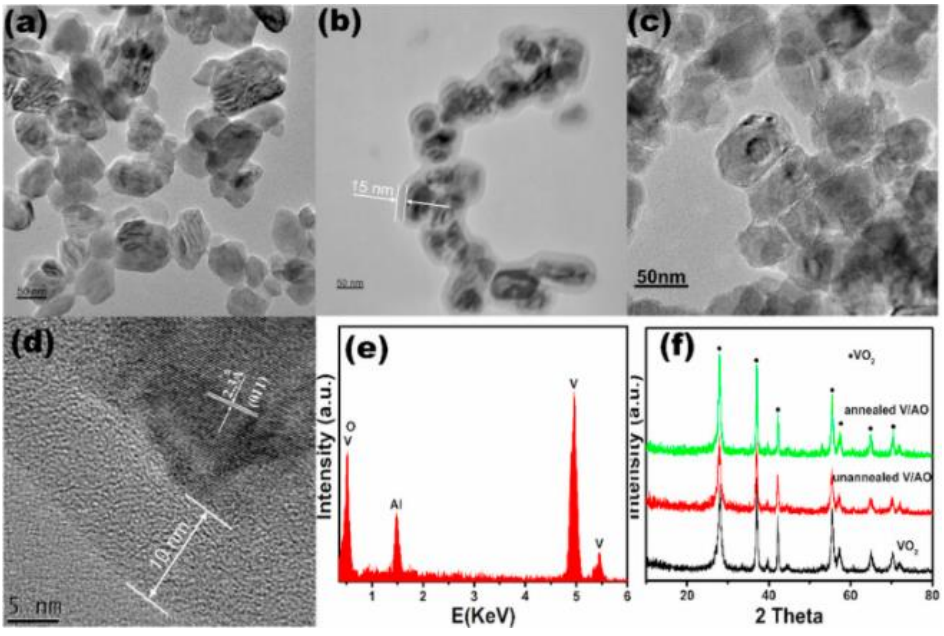

Figure 21 (a), (b), (c) TEM images of VO_2, unannealed V/AO and annealed V/AO nanoparticles (d)HRTEM image of annealed V/AO nanoparticles(e)EDS spectrum of annealed V/AO nanoparticles (f) XRD patterns of uncoated VO2, unannealed V/AO and annealed V/AO nanoparticle

Gao et al.[110]have tried to synthesize pure VO_2@SiO_2 core-shell nanoparticles to enhance the optical and anti-oxidant properties of a VO_2 film. The VO_2 nanoparticles were synthesized by a hydrothermal method, and then a new method of preparing VO_2@SiO_2 core-shell nanoparticles were used without surfactants. Firstly, the VO_2 nanoparticles were ground with ethanol, which can link hydroxyl bond on the surface of VO_2 nanoparticles. Secondly, the treated particles were mixed with water, there will be a thin water film on the surface for the hydrolysis in the next step. Finally, TEOS was added and it can be hydrolyzed to SiO_2 layer and few SiO_2 by-products (i.e.SiO_2 spheres) are formed in this process.

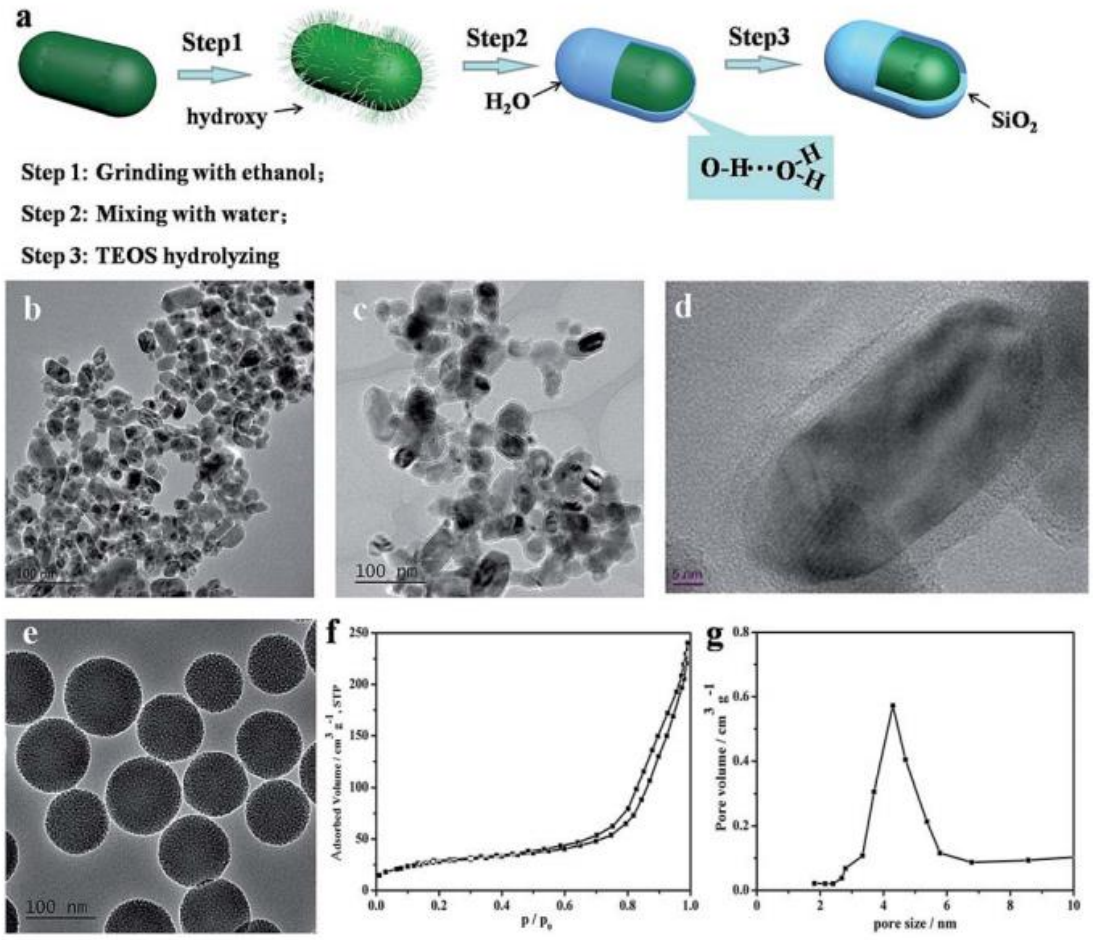

Figure 22 Schematic illustration of the route to synthesize VO_2@SiO_2 nanoparticles (a). TEM image of VO_2 (b) and VO_2@SiO_2 (c). HRTEM image of VO_2@SiO_2 (d). TEM image (e), N_2 adsorption-desorption curve (f) and pore distribution of MSNs (g).

Pure VO_2@SiO_2 core-shell nanoparticles can be synthesized successfully by this approach at room temperature. The silica shell was smooth and the thickness is uniform which is about 5 nm. The core-shell particles has a better inoxidizability, a higher reflectance, a higher visible transmittance and a larger solar modulation ability than VO_2 particles.

However, few research focus on the details of the protective performance of the VO_2 core-shell particles. Therefore, a VO_2@SiO_2 core-shell nanoparticles were synthesized in this chapter, and its performance such as oxidation resistance, acid resistance, and alkali resistance will be studied in detail.

Moreover, the optimal synthetic parameters were also studied for a high-quality nanoparticles in the smart window application, which should have uniform and small particles size and good dispersity.

2.4.3 VO_2@ZrO_2 core-shell structure

ZrO_2 is an interesting material which can be considered to synthesize the VO_2@ZrO_2 core-shell nanoparticles. The ZrO_2 relative papers are introduced here.

Many research about ZrO_2 [111-115]have been done in recent years, Firstly, it plays an important role in the catalyst application. Mondal et al. [111]have tried to synthesize the Ni/CeO_2-ZrO_2 catalyst. Ni/CeO_2-ZrO_2 and Rh-Ni/Ce catalysts can be used in catalytic steam which can reform bio-ethanol in presence of oxygen for hydrogen production. The catalysts were synthesized by an impregnation-co-precipitation method. The results show that the ZrO_2 can enhance the oxygen storage capacity of CeO_2 which is helpful to increase the catalytic activity.

Mortensen and coworkers [116]have invested Mo_2C/ZrO_2 as catalyst for hydrodeoxygenation of mixtures of phenol and 1-octanol. Molybdenum carbide was treated as a potential catalyst for bio-oil HDO,and Mo_2C/ZrO_2 can effectively convert

1-octanol to octane and octene at temperatures above 280 ˚C. Mo_2C/ZrO_2 is a selective catalyst for direct deoxygenation of phenol and 1-octanol.

Except the application in catalyst, the ZrO_2 was also an interesting material in the core-shell structure synthesis[117-121]. Menzies et al. have tried to prepare the nanostructured ZrO_2/TiO_2 core-shell electrodes for dye-sensitized solar cells[122]. After photo-excitation of the dye, the photo-injected electrons can be generated and go through the shell to the semiconductor core, and the semiconductor ZrO_2 layer can work as an energy barrier for charge recombination[123-124].For the synthesis of core-shell electrodes, zirconium isopropoxide was spin-coated over the titanium dioxide. Then the samples were sintered for half an hour between ZrO_2 shell depositions.

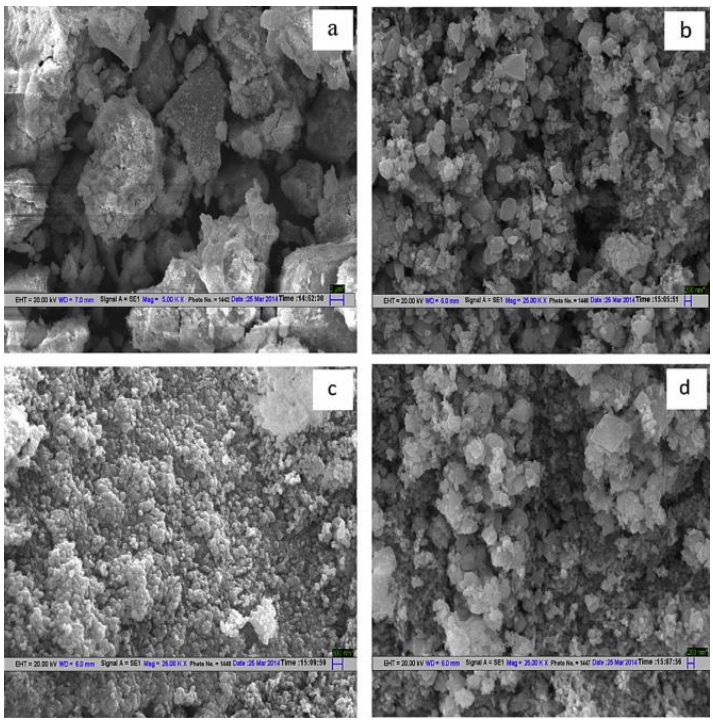

Figure 23 SEM images of prepared catalysts: (a) $CeO_2@ZrO_2$, (b) $30\%Ni/CeO_2@ZrO_2$, and (c & d) $1\%Rhe30\%Ni/CeO_2@ZrO_2$.

Ag-related core-shell nanoparticles were always attracted for researchers[125-129].$Ag@ZrO_2$ core-shell nanoparticles were prepared by Dhanalekshmi and his coworkers. The core-shell nanoparticles were synthesized by one-pot simultaneous

reduction of $AgNO_3$ and hydrolysis of zirconium (IV) isopropoxide. In that research, the antibacterial activity of $Ag@ZrO_2$ core-shell nanocomposites against *Escherichia coli* and *Staphylococcus aureus* and the antifungal performance against *Candida albicans*, *Candida glabrata*, *Aspergillis niger* and *Aspergillus flavus* were tested. Finally, the ZrO_2 supporters is helpful to prevent the aggregation of Ag nanoparticles and improve the antimicrobial activity and DNA intercalation than the Ag nanoparticles[130].

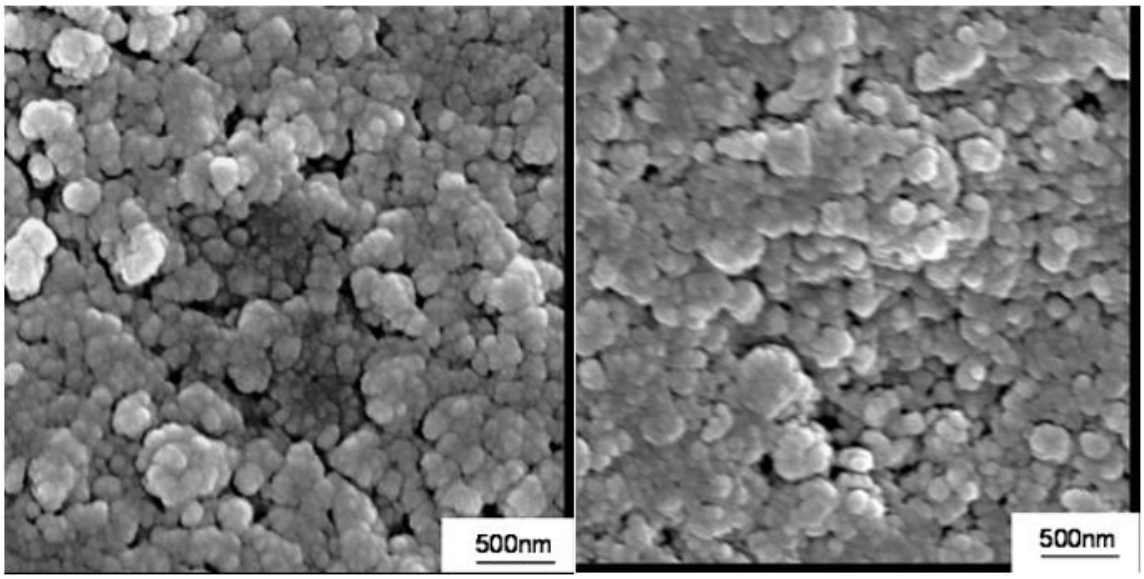

Figure 24 SEM of uncoated TiO_2 electrode (left) and ZrO_2 coated TiO_2 electrode.

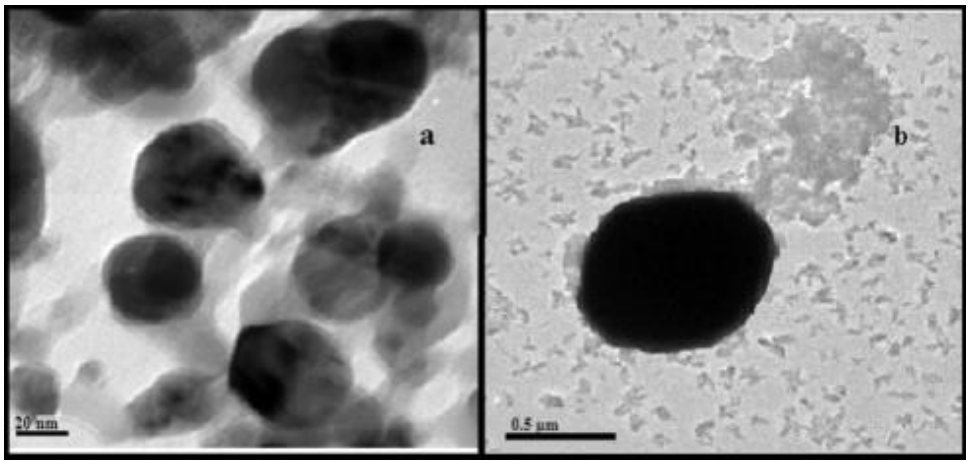

Figure 25 (a & b) HRTEM images of $Ag@ZrO_2$ core–shell NPs.

Chang et al. [131]also synthesized Ag@ZrO_2 core-shell structure through an atomic layer deposition method. Firstly, Ag nanowires were synthesized and cleaned. Then the Ag NWs were dispersed on a Si substrate. Lastly, the ZrO_2 shell were deposited using a commercial ALD system, Tetrakis (dimethylamino) zirconium ($Zr(NMe_2)_4$) was used as the precursor of Zirconia (Fig.26,27).

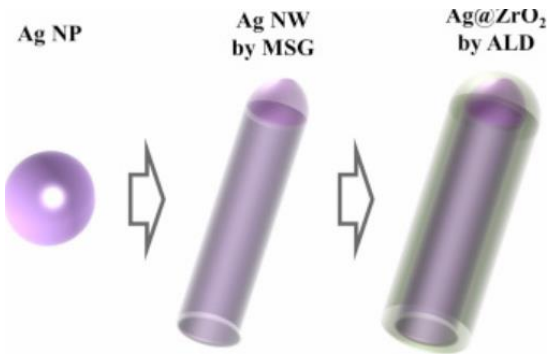

Figure 26 The process flow of ZrO_2-coated Ag NWs: Ag nanoparticle, Ag NW synthesis using SMG, and ZrO_2-coated Ag NW by ALD.

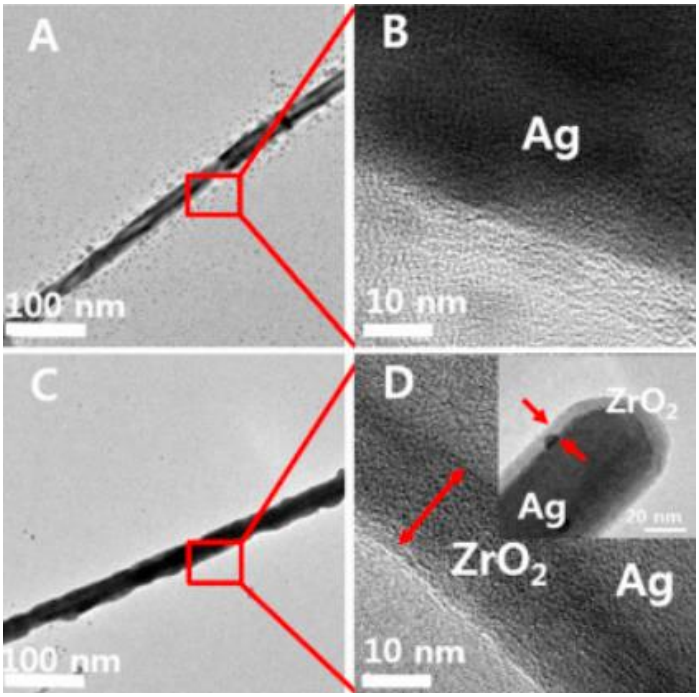

Figure 27 (A) Low-magnification and (B) high-magnification TEM images of a bare Ag NW; (C) low- magnification and (D) high-magnification TEM images of ZrO_2-coated Ag NWs.

And the results of the core-shell structure show that the ZrO_2 shell can improve the smooth of the Ag NW structure with a shell thickness of less than 1 nm. It is helpful to inhibit the agglomeration of the Ag NWs.

Fe_3O_4 core-shell nanostructure is another interesting area, as it is a significant magnetic material which can be used in diagnosis and therapy of cancer. Different Fe_3O_4 core-shell nanostructure have been synthesized in recent years[132-136].

Li et al. [137]prepared Fe_3O_4@ZrO_2 core-shell microspheres as affinity probes for selective enrichment and direct determination of phosphopeptides. In this research, the Fe_3O_4 microspheres were synthesized by a solvothermal reaction. Then the Fe_3O_4 microspheres were put into glucose solution, after the solvothermal reaction the Fe_3O_4 @ZrO_2 core-shell structure was prepared. The Fe_3O_4@C core-shell spheres were dispersed into zirconium isopropoxide solution. Then the final core-shell structure can be obtained (Fig 28)

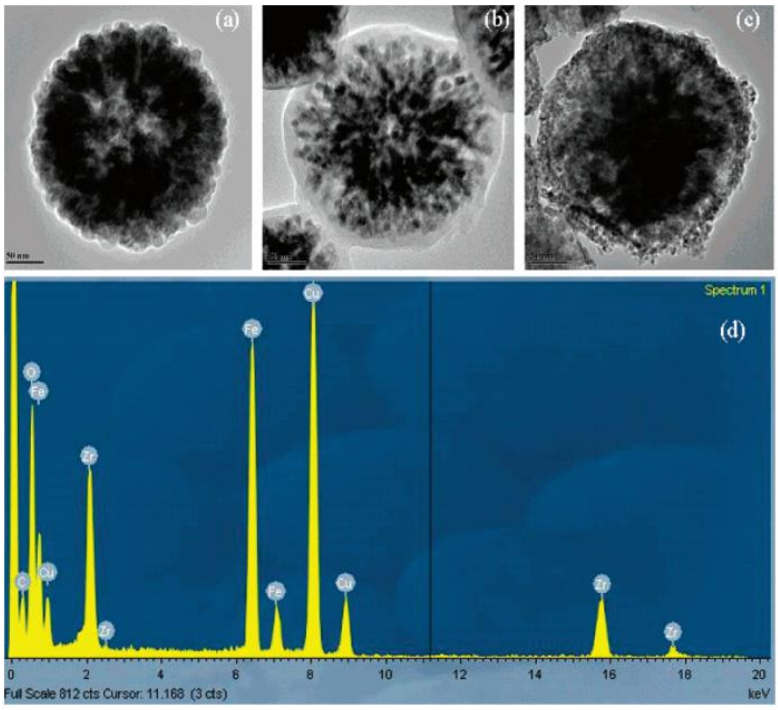

Figure 28 TEM images of (a) Fe_3O_4 microspheres, (b) Fe_3O_4@C microspheres, (c) Fe_3O_4@ZrO_2 core-shell microspheres. (d) The EDX spectrum data of the obtained Fe_3O_4@ZrO_2 core-shell microspheres.

In their research, a new method was used to prepare the Fe_3O_4@ZrO_2 microspheres, which has a nice core-shell structure. Moreover, the core-shell structure make a huge improvement in increasing the sensitivity and selectivity for the phosphorylated peptides, which is very helpful for the application in analysis of samples.

Wang and the coworkers [138]synthesized the Fe_3O_4@C@ZrO_2 multilayer structure to adsorb and remove phosphate. Firstly, the Fe_3O_4 microspheres and Fe_3O_4@C core-shell particles were synthesized by a hydrothermal method. Then the core-shell particles were dispersed into deionized water, and the $Zr(NO_3)_4$ solution was added. Finally, the particles were collected by a separation process. Washing and drying process was done to make sure the Fe_3O_4@C@ZrO_2 core-shell structure is clean (Fig 29).

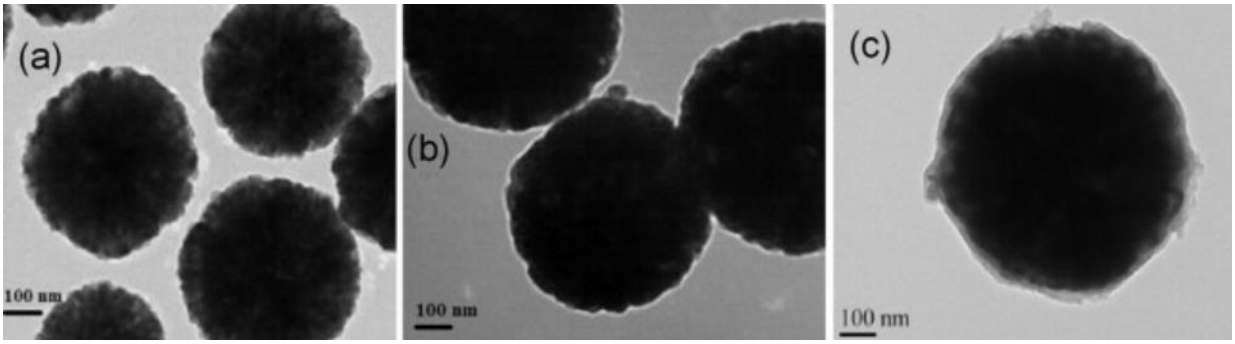

Figure 29 TEM images of (a) Fe_3O_4, (b) Fe_3O_4@C and (c) MFC@ZrO_2

The Fe_3O_4@C@ZrO_2 core-shell structure is consist of three components, the Fe_3O_4 core (500-700nm), the 10 nm carbonaceous shell, and 20 nm ZrO_2 shell. The Fe_3O_4@C has a low adsorption ability of the phosphate, however, the Fe_3O_4@C@ZrO_2 improve the phosphate adsorption enormously.

2.4.4 VO_2@TiO_2 core-shell structure

TiO_2 is a famous photocatalytic material, which can be used in self-cleaning application. The VO_2@TiO_2 core-shell nanoparticles can be multifunctional material. Therefore, some TiO_2 relative paper will be introduced in this section. Watanabe et al. [139] have tried to prepare the titanium dioxide coated glass by using the photoinduced hydrophilicity property of titanium dioxide. A sol-gel method[140-143] was used to synthesize the anatase polycrystalline samples and titanium alkoxide was the source of titanium. After that, the titanium alkoxide was coated on soda lime glass by a spin coating method, and a silicon dioxide layer was between them. Finally, the samples were annealed at 500 ˚C for 20 min in air. (Fig 30)

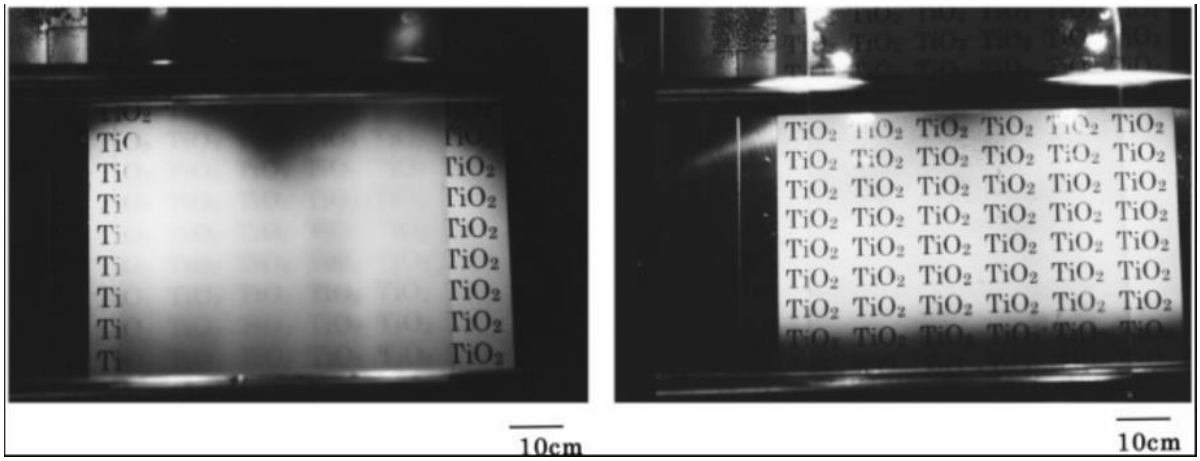

Figure 30 Photograph of steamed surfaces of usual glass (a) and TiO2 coated glass after enough UV illumination (b).

Fig 30 shows the antifogging effect of TiO_2 coated glass with the illumination of UV light. Yuranova and the coworkers have prepared self-cleaning cotton textiles which were treated with photoactive SiO_2/TiO_2 coating[144]. After mixing the titanium tetra-isopropoxide (TTIP) and acetic acid into tri-distilled water, the HNO_3 was also added. Then the mixture was heated to 80 ˚C for half an hour. After that, the cotton were immersed into the TiO_2 colloid and SiO_2 Ludox SM-30 to obtain the TiO_2-SiO_2 layers. The process can be schematically show in Fig.31.

A photo-induced discoloration of red wine stains experiment was conducted by the TiO_2-SiO_2 coated cotton textiles (Fig32). The TiO_2-SiO_2 coated cotton textiles were stained with wine, and after 0, 4, 8, 24 hours in a solar light simulator which is 90 mW/cm^2, the color change was different. With longer irradiation time, the discoloration was more obvious which means the TiO_2-SiO_2 coating is effective in removing the red wine stain.

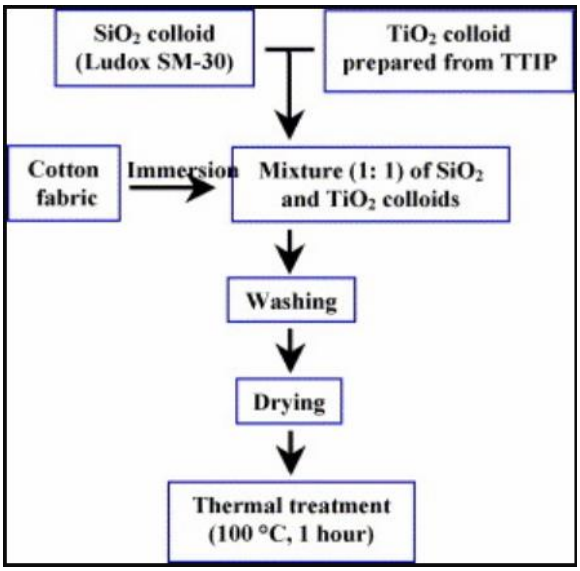

Figure 31 Scheme of the colloid preparation and cotton loading with TiO_2 and SiO_2 colloidal mixture.

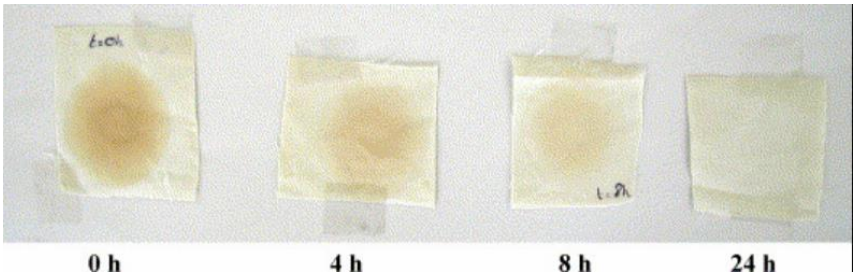

Figure 32 Discoloration of bleached cotton samples stained with wine on TiO_2–SiO_2-coated cotton textiles irradiated after 0, 4, 8 and 24 h in a solar light simulator with 90 mW/cm^2.

Different kinds of TiO_2 core-shell nanostructures have also been studied in recent years[145-149].Hirakawa et al. [145]synthesized a $Ag@TiO_2$ core-shell composite clusters to study the charge separation and catalytic activity of the core-shell structure. For the synthesis of $Ag@TiO_2$ shell cluster, the titanium-(triethanolaminato) isopropoxide $(N((CH_2)_2O)_3TiOCH(CH_3)_2)$ TTEAIP was prepared in 2-propanol. Then, $AgNO_3$ solution, DMF solution was added into TTEAIP-Ag solution. The amount of DMF and i-PrOH was significant in synthesizing the $Ag@TiO_2$ clusters. (Fig33)

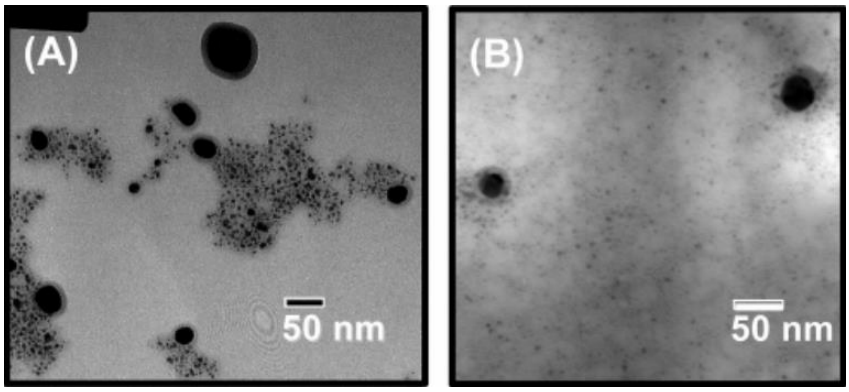

Figure 33 Transmission electron micrographs of $Ag@TiO_2$ colloids which were prepared using the composition of (A) 5 mM TiO_2 and 1 mM Ag and (B) 5 mM TiO_2 and 1 mM Ag. (C) Absorption spectra of colloidal (a) $Ag@TiO_2$ (b) $Ag@SiO_2$ and (c) TiO_2 suspension in ethanol.

For the core-shell structure, it has photoinduced charging and dark discharging of electrons. The composite clusters which have metal core-semiconductor shell are photocatalytically active and can be helpful to improve light induced electron-transfer reactions.

Liu et al. [150]synthesized one-dimensional $CdS@TiO_2$ core-shell nanocomposites used for photocatalyst for selective redox. The 1D $CdS@TiO_2$ core-shell nanoparticles were fabricated by template-free and facile two-step solvothermal method. Firstly, the CdS nanowires were grown in a modified approach. Then some cadmium diethyldithiocarbamate $(Cd(S_2CNEt_2)_2)$ was added to a Teflon-lined stainless steel autoclave to have a solvothermal reaction. After that, the core-shell

nanoparticles were prepared by a wet-chemistry method and tetrabutyl titanate (TBOT) was used as the titania source.

By this method, the CdS@TiO_2 core-shell nanocomposites (Fig 34) are prepared through a two-step solvothermal method. The TiO_2 shell is deposited on the surface

Figure 34 Schematic flowchart for two-step synthesis of 1D CdS@TiO_2 CSNs.

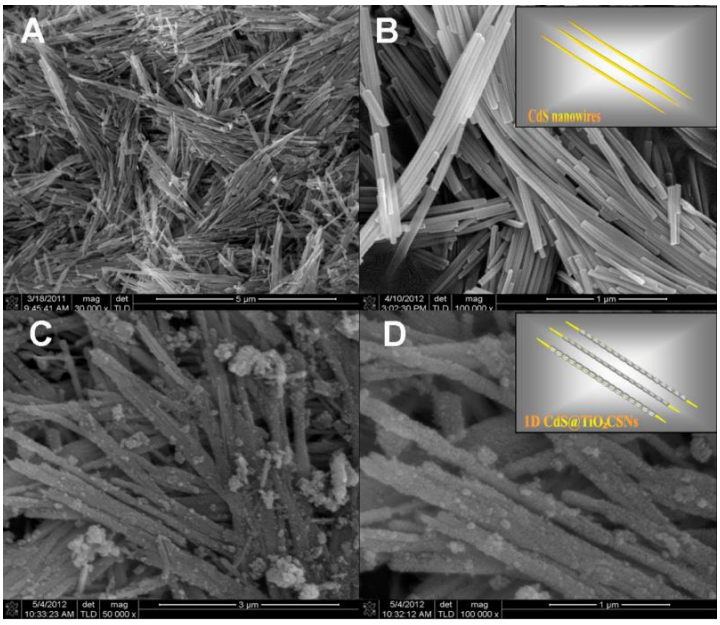

Figure 35 SEM images of the as-prepared samples of (A,B) CdS NWs and (C,D) 1D CdS@TiO_2 CSNs at different magnifications; in inserts of B and D are the corresponding schematic models/

of CdS core and this structure show much-improved photocatalytic activities due to the longer lifetime of photogenerated electron-hole pairs because of the 1D CdS@TiO_2 CSN.

Nano-sized TiO_2 photocatalytic has the water-splitting function, it is a potential material for the future hydrogen economy with many advantages, such as low-cost, environmentally friendly solar-hydrogen production[151]. However, few people studied the VO_2@TiO_2 core-shell nanostructures. And the combination of the VO_2 thermochromism and TiO_2 self-cleaning property should be meaningful in window coating area. Therefore, the VO_2@TiO_2 core-shell particles will be a multifunction material in building area. In this chapter, the synthesis of VO_2@TiO_2 core-shell particles and its performance will be talked.

2.5 Experimental techniques

Many experimental techniques were talked and used in this thesis for the preparation of the materials. Therefore, the corresponding knowledge of the experimental techniques will be introduced in this section.

In terms of the synthesis of vanadium oxide nanoparticles, the synthetic methods usually include hydrothermal method, sol-gel method, polymer-assisted deposition and some other methods. For the characterization of the prepared nanostructures, common methods such as scanning electron microscopy (SEM). Transmission electron microscopy (TEM), X-ray diffraction (XRD), and UV-Vis-NIR spectroscopic analysis were used. The details about these characterization techniques will be talked in this section.

2.5.1 X-ray diffraction

X-ray diffraction (XRD) [152-153]is a technique applied to study the crystal information of the materials. With changing the intensity of the X-ray beam diffracted from a particular incident angle, the test can give us some crystal information of this material. There are mainly three components of the X-ray diffractometer: X-ray tube, sample holder, and X-ray detector. At the first step, the samples need to be put on the sample holder to be measured. At the second step, X-ray beams will be generated from a cathode ray tube. The electrons in the cathode can be generated by a heated filament and accelerated by a high voltage. After that, the target materials will get the X-ray beams shoot and their inner shells electrons can be motivated. At the same time, a characteristic X-ray spectra (Kα and Kβ) will occur from the target material. Through the crystal monochromator filter, this X-ray spectra can gives out monochromatic X-rays. Some special material can be used as the target material, among them, copper is most commonly used for single-crystal diffraction, and the CuKα radiation is 1.5418Å. After the samples get the X-ray beam shoot, a rotary detector will work to test the diffracted X-rays from different angle.

For XRD, it have a number of merits. In the first place, this technique is mighty and fast at identifying unknown materials, particularly for the materials which have well-crystallized structure. Moreover, the XRD results are intuitionistic and shows an appropriate recognition of the material. Thirdly, the XRD technique has been used for decades, it has an extensively acceptability for its units. Lastly, the measurement of XRD only need a small amount of sample which is convenient for the researchers.

2.5.2 UV-Vis-NIR spectroscopic analysis

A spectrophotometer[154-155] is usually applied to test the reflection or absorbance characteristics of samples. For the need of the research, the wavelength of radiation

to be studied must in a limited range. Therefore, the radiation wavelength will be divided into ultra-violet (UV), visible (vis) and near infrared (NIR) radiation and they are defined as UV radiation (300 to 400nm), vis radiation (400 to 765 nm), NIR radiation (765 to 3200nm).

If the sample is illuminated with a radiation in particular wavelength, there might be an absorption of that radiation. However, it may not happen if the wavelength is different. This absorption phenomenon can be used to characterize materials. The absorption of radiation can happen in a reflection or transmission mode, and the graph of absorption versus wavelength is called a spectrum.

The spectrometers are commonly used equipment to analyze the materials' corresponding optical properties. The spectrometric analysis can be applied in a large range of applications, such as chemistry, physics, and engineering area. In this research, spectrometers are used in detecting the optical performance of smart window coatings and evaluating its thermochromic properties.
The range of UV-Vis-NIR light is usually from 250 to 3000nm, and the optical properties in that range can be detected by the UV-Vis-NIR spectrometer. The light source is made up of deuterium light and tungsten light. For the UV region, the light is provided by the deuterium lights and for the vis-NIR region, the light is offered by the tungsten lights. Meanwhile, the detector in the machine also include an UV-Vis detector and NIR detector. For the UV-Vis region, the detectors are played by the photomultiplier tubes and for the NIR detector, it is offered by the lead sulfide (PbS). Moreover, another detector, which is InGaAs detector is often used for the region in the wavelength of 800-1200 nm in order to avoid the crossover noise. And PhSe detectors can extend the NIR region to about 4 μm.

2.5.3 Scanning electron microscopy

With a focused beam of electrons, a scanning electron microscope (SEM)[156-157] is a kind of electron microscope that produces pictures of a sample through scanning the

surface of it. Atoms on the surface of the sample interact with electrons, producing different signals which have the information of the surface topography and composition of samples. The signal could be collected by detecting the secondary electrons emitted by atoms excited by the electron beam. The strength of the signal depends on the topography of the sample. An image shows the topography by collecting the secondary electrons.

In terms of the principles of the SEM, different signals can be collected in the SEM due to interactions of electron beam with different depths of samples. The signal emitted include: reflected or back-scattered electrons (BSE), secondary electrons (SE), light (cathodoluminescence) (CL), characteristic X-rays, absorbed current (specimen current) and transmitted electrons. Among them, secondary electrons are mainly employed to measure the surface topography.

Usually, in a typical SEM, an electron beam can be thermionically emitted from an electron gun fitted with a tungsten filament cathode. Tungsten has a property that it has a very high melting pointing and dramatic low vapor pressure of all metals, so it could be used in thermionic electron guns and can be electrically heated for electron emission. The low cost of this material is another advantage. Lanthanum hexaboride (LaB6) cathode is another cathode, it can be used in a standard tungsten filament SEM. Especially when the vacuum system is upgraded or field emission guns (FEG).

Usually, the energy of the electron beam is between 0.2 keV to 40 keV, and it will be condensed through one or two condenser lenses to a spot which is about 0.4 nm to 5 nm in diameter. Inside the electron column, the electron beam can go through pairs of deflector plates or pairs of scanning coils, and until the last lens, the beam can be deflected in the x and y-axes therefore the sample surface can be scanned in a raster fashion over a rectangular area.

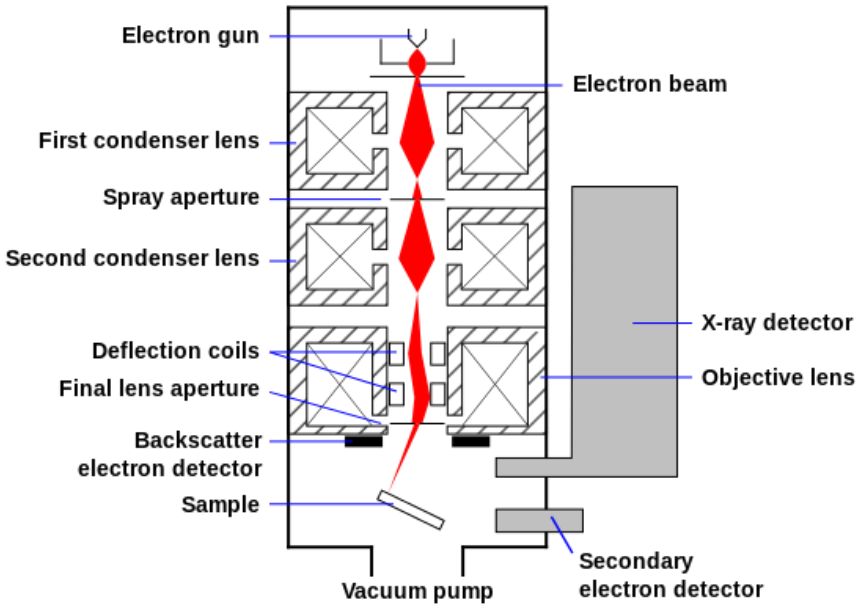

Figure 36 Schematic diagram of an SEM

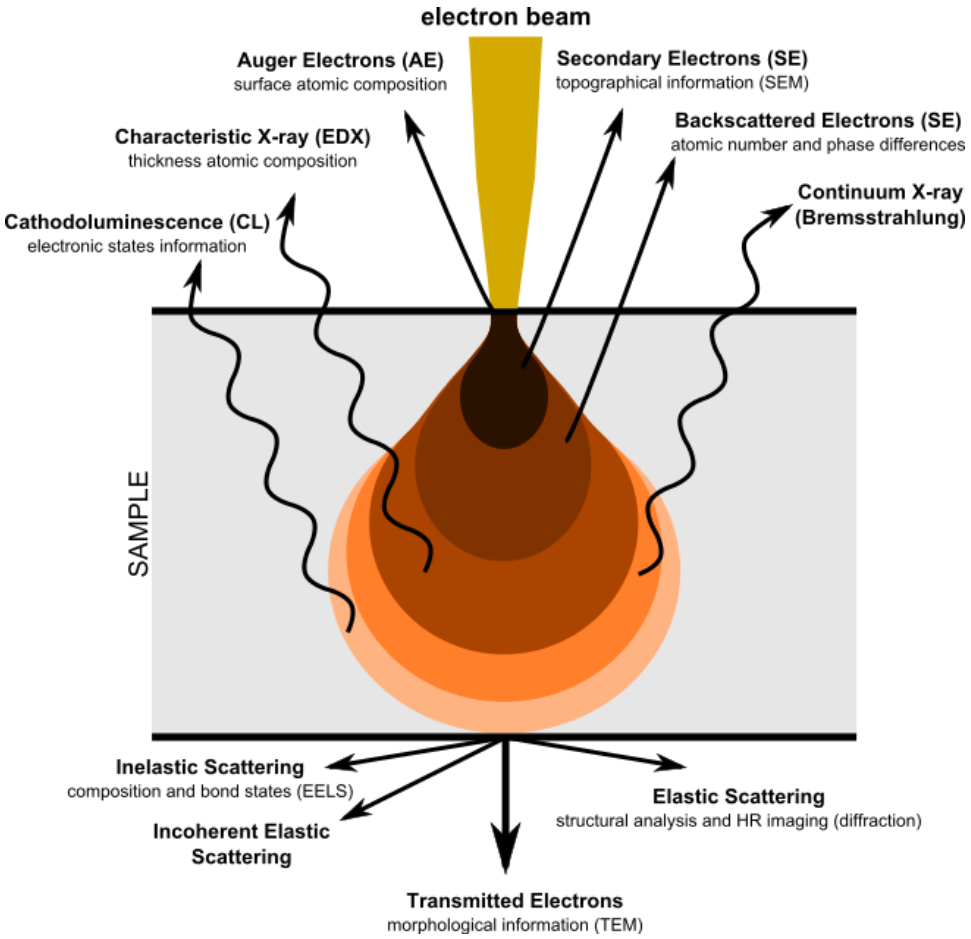

Figure 37 Signals emitted from different parts of the interaction volume (Source: Wikipedia)

The energy of the primary electron beam will be decreased when they interact with the repeated random scattering electrons, and absorption within a teardrop-shaped volume of the specimen can be known as the interaction volume. The interaction volume can increased from less than 100 nm to approximately 5 um on the surface. There are some factors which can affect the size of interaction volume, one of them is the electron's landing energy. Some other factors include the atomic number of the specimen and the specimen's density.

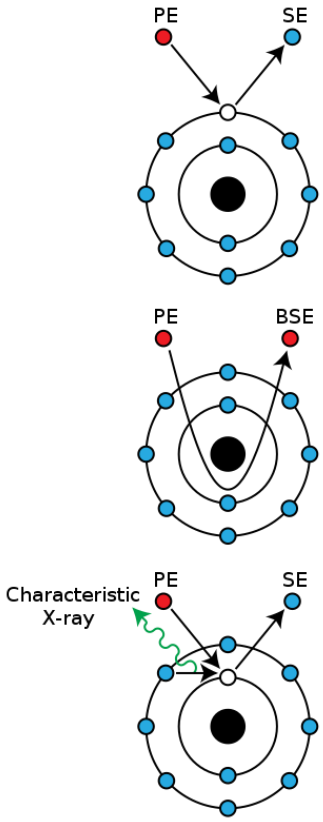

Figure 38. Schematic diagram of emission of secondary electrons, backscattered electrons, and characteristic X-rays from atoms of the sample (Source: Wikipedia)

The energy can be exchanged between the electron beam and specimen results in the reflection of high-energy electrons in different forms such as emission of secondary electrons by inelastic scattering, elastic scattering, and the emission of electromagnetic radiation. All of them can be tested by special detectors. Images of the distribution of specimen current can be created by the collected beam current absorbed by the specimen. Different kinds of electronic amplifiers can be used to

amplify the signals, and they can be shown as variations in brightness on a computer monitor.

2.5.4 Transmission electron microscopy

Transmission electron microscopy (TEM) [158-160] is a microscopy technique where a beam of electrons is transmitted through a specimen to form an image. The specimen can be an ultrathin section which is less than 100 nm thick or a solution dropped on a grid. With the beam transmitting through the specimen, the image can be formed from the interaction of the electrons with the samples. Then, the image can be magnified and focused onto an imaging device, such as a layer of photographic film, a fluorescent screen or a sensor such as a charge-coupled device.

Transmission electron microscopes has a significantly higher resolution than light microscopes, the reason is it has a smaller de Broglie wavelength of electrons. It can make the equipment collect good details, even if a single column of atoms, and it can be dramatically smaller than the light microscope. In physical, chemical and biological sciences, transmission electron microscopy is a major analytical approach. TEMs can be in various areas such as disease research, materials science, and virology, especially in pollution, semiconductor, and nanotechnology. At lower magnifications, as different materials have different composition and thickness, they have different absorption of electrons, and it can be reflected in the contrast of TEM images. At higher magnifications, intensity of images can be modulated by complex wave interactions, and show the images. Different modes of TEM can be applied in crystal orientation, chemical identity, sample induced electron phase shift, electronic structure as well as the regular absorption based spectrum.

The TEM is consist of specimen stage, vacuum system, electron lens, electron gun, and apertures. (Fig. 39). At the top of the equipment, there is an emission source, usually, it is a tungsten material needle or filament, or a single crystal source of lanthanum hexaboride (LaB_6). The voltage source inside the gun is very high (about

100-300 kV) and sufficient current can be given. Electrons can be emitted into the vacuum from the gun by thermionic or field electron emission. The electron source is traditionally mounted in a Wehnelt cylinder to give primary focus of the emitted electrons into a beam. A desired size and location of beam can then be focused from the upper lenses of the TEM.

Electron beam can be manipulated by two physical effects. Magnetic field can cause electrons to move due to the left-hand rule, therefore the electron beam can be manipulated. The usage of magnetic fields lead to the formation of magnetic lens of different focusing power, the shape of lens originating due to the magnetic flux in distribution.

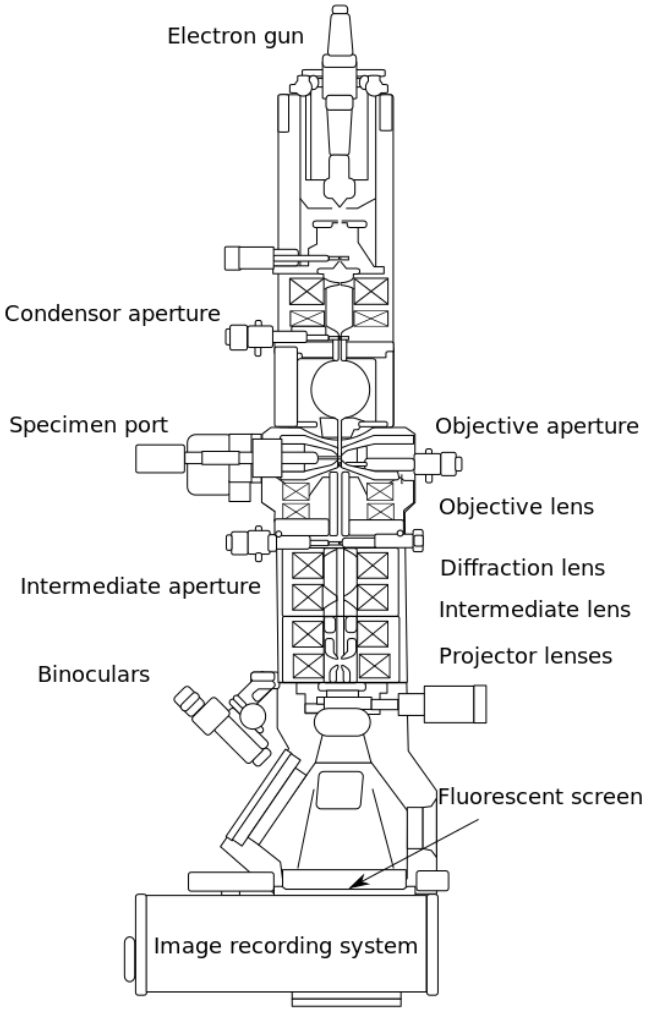

Figure 39 Schematic diagram of optical components in a basic TEM.(Source: Wikipedia)

The beam convergence could be obtained by the lenses in the TEM, as the angle of convergence with a different parameter, making the TEM the possible to change magnification just by changing the scale of current that flows in the coil. Usually, there are three proportions of lensing in the TEM system, the projector lenses, the condenser lenses, and the objective lenses. The condenser lenses lead to the formation of primary beam, the objective lenses can focus the beam to go through the sample. And the projector lenses can expand the beam onto the phosphor screen or other imaging equipment.

2.6 Problems and gaps

Although researchers are in the progress of addressing problems that may impede the commercialization in industry, there is still a lot of research work to do before the technology becomes fully mature in life.

- Modification of T_c. The current phase transition temperature T_c is still too high to be used in the smart window, it has become a necessary work to reduce the T_c effectively. The ideal T_c should between 25-30 ˚C, and this goal can be achieved by an elemental doping method. Among all the potential doping elements, metallic tungsten was treated as the most effective one. In recent decades, material scientists have tried to study the function of tungsten dopant in changing the transition temperature, by employing synchrotron radiation X-ray absorption spectroscopy. Moreover, the local structure and relationship between the tungsten atom and the VO_2 lattice was also studied by the first-principle calculation. The calculation work is beneficial to understand the mechanism of the transition and helping to look for other elements to decrease the T_c for VO_2.Except tungsten, many other elements were also used to the preparation of VO_2 films, for example, zinc, zirconium, and magnesium. Some of the elements can not only decreasing the T_c but also improving optical performances such as modifying T_{lum}, ΔT_{sol} and change the color of VO_2. At the same time, rare work has been done in the principle of

the changes. Much more work about the theoretical should completed to understand the relationship between doping elements and optical properties. For the smart window coating, co-doping is another potential method which has better effect than single elemental doping. The use of different kinds of doping elements will lead to a better properties of VO_2 films. However, more research need to be done to combine the doping element and performances of VO_2 films.

- Modification of low T_{lum} and ΔT_{sol}. Many methods can be employed to increase optical performances of VO_2 films, which includes elemental doping, constructing multilayers, combining with other substrates or using other nanostructure. From recent research results, by using appropriate methods, the optical properties can be 10 % in ΔT_{sol} and 40 % in $T_{lum.}$ Moreover, if a higher goal of optical properties want to be achieved, more strategies are needed to be combined, for instance, the employment of new nanostructure, new substrates, and addition of new dopants.
- Modification of color of VO_2 films. The color of VO_2 films is yellow, brown and dark blue. It has been another hinder for the application of smart window coating. The challenge has existed for a long time, even though some sorts of elemental doping (Titanium, Fluorine, Magnesium) can be helpful to deal with this problem. More work should be completed to control VO_2 itself in the next step. With the decrease of the film thickness, the color problem can also be improved. The optical transmittance of the VO_2 films can be improved when the film thickness is less than 150 nm or the porous structure was prepared.
- Chemical stability of VO_2 materials. VO_2 (M) is the functional phase for the application in smart window, however, it is not chemically stable in the moisture atmosphere. Even though some protective strategy have been tried, but the results are not good enough. In my research, different kinds of core-shell structures are synthesized and optimized to increase the chemical and thermal stablility for the VO_2 nanoparticles. The stability in acid, alkali and strong oxidizing environment are tested to prove the good performance of the core-shell nanostructures.

For all the mentioned problems, the stability problems were the most interesting part for the author. Therefore, different structures of VO_2 core-shell nanoparticles will be synthesized to deal with the chemical stability problems. Several core-shell structures are planned to be synthesized, such as VO_2@SiO_2, VO_2@TiO_2 and VO_2@ZrO_2 core-shell structures. And in this thesis, all the research will be focused on the synthesis of VO_2 nanoparticles, the synthesis of VO_2 core-shell nanoparticles and the test of their properties.

For the characterization and properties of the VO_2 nanoparticles, the research will be focused on the surface morphology, inner structure and crystal structure. SEM,TEM and XRD equipments will be used to test these properties. For the stability of the core-shell structure. The stability of the core-shell material will be tested in different environments, such as acid solution and alkali solution.

Chapter 3 Synthesis of VO_2 nanoparticles

3.1 Introduction

Vanadium dioxide VO_2 has got an increasing attention in these years as it has interesting properties and can be used in numerous applications such as catalysts, cathode materials for reversible lithium batteries, gas sensors, intelligent thermochromic windows, electrical and optical devices, laser shield and so on.[161] So a lot of work has been done on the synthesis of VO_2 nanoparticles.

Many methods have been used in the synthesis of VO_2 nanoparticles. Gas-based synthesis and solution-based deposition are two largest categories for the synthesis. Both of the methods have their advantages and disadvantages. For the gas-based method, it can give us the uniform and large-scale results easily. But it needs high-cost equipment which is difficult in some occasions. In terms of the solution-based approach, even though it has low cost in the process of preparation, it cannot get volume production in the industries.

Based on the experimental conditions of the lab and the future applications in the industry. Hydrothermal method was used in this research. The process of hydrothermal synthesis can be defined as an approach that the synthesis of single crystals that relies on the solubility of minerals in hot water and high-pressure conditions. The crystal growth is proceeded in an autoclave which is consisting of a steel pressure vessel. In the autoclave, the chemicals are supplied with water. Hydrothermal method is a commonly used method, as its simple route of synthesis, low cost, lower required temperature and environmentally friendly reaction conditions.

In this research, we worked on the synthesize of VO_2 (M) through a two-step hydrothermal method. A new method was used to synthesize smaller and purer VO_2 nanoparticles. Hydrazine solution was used as reduced agent in the hydrothermal process. All chemicals are analytical grade and used as received without purification.

The VO_2 nanoparticles were synthesized through a two-step hydrothermal process as follow steps:

- Vanadium pentoxide (V_2O_5) was dissolved in 50 mL deionized water.
- After stirring of 10 minutes using a magnetic stir bar, a proper amount of ammonia water was added into the solution and stirred for a short time.
- Then the accurate amount of hydrazine solution was added. The color of the solution was changed after a short period of time.
- The solution was furtherly diluted and transferred into the teflon liner of a stainless steel autoclave. The sealed steel autoclave was kept in an oven at 220˚C for 24 hours.
- After the reaction process, the autoclave was slowly cooled to room temperature.
- Moreover, ethanol was added to the cooled solution. The solution will stand overnight to make the particles sediment. The final solution was then washed by ethanol and water to remove unreacted chemical species and dried in air at 60 ˚C for three hours.
- A post-annealing process was used to get the monoclinic phase VO_2 nanoparticles. The as-prepared powder was ground and transfer into the tube furnace, which was calcined at high temperature for one hour. Besides, the morphology and composition of vanadium oxide can be varied by adjusting the hydrothermal conditions.

3.1.1 Experimental mechanism

Firstly, a cheap and common vanadium source, vanadium pentoxide (V_2O_5), was put into aqueous solution which contains ammonia water. And the solid V_2O_5 will be reacted into NH_4VO_3 solution.

$$V_2O_5+2NH_3.H_2O=2NH_4VO_3+H_2O$$

Secondly, the reducing agent hydrazine (N_2H_4) solution was added to the mixed solution.

And hydrous vanadyl hydroxide microparticles of $VO(OH)x(OH_2)n$ were formed. The oxidation state of $VO(OH)x(OH_2)n$ is based on the amount of N_2H_4, and it was between III and IV. After that, the suspension which contains $VO(OH)_x(OH_2)_n$ microspheres were transferred into an autoclave. Through the hydrothermal reaction, the microspheres were dehydrated and furtherly crystallized to $VO(OH)_x$ nanocrystals. Then, the VO(OH)x nanocrystals were heated in air for the conversion to obtain VO_2 nanocrystals. At this stage, the VO_2 nanocrystals were in metastable or mineral phase. Finally, the VO_2 nanocrystals were annealed in an inert atmosphere to obtain monoclinic VO_2 (M/R) nanocrystals, which exhibits unique thermochromic properties.

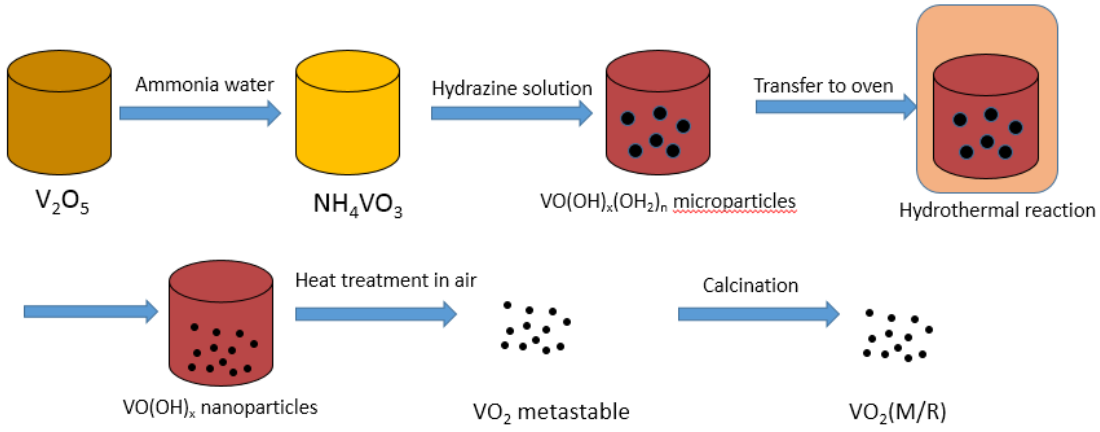

Figure 40 Schematic image of the method used for the synthesis

Compared with the conventional hydrothermal method for fabrication of pure VO_2 (M) nanoparticles, our approach has several major merits. On one hand, this method is more energy consumption effective as it reduced the hydrothermal temperature from 260 °C to less than 220 °C. Consequently, the reaction pressure can be reduced by more than 50% to the original level. On the other hand, the VO_2 nanoparticles prefer to grow on the wall of the containers in the reaction, and it may affect the large-scale fabrication. In this method, the nucleation of particles occurred in ambient conditions,

which stops the particle adhesion to the reactors. Finally, the conventional reaction has a low reaction kinetics for the formation of VO_2 (M), however, this method has a relatively higher reaction and yield.

3.2 Effect of hydrazine concentration

3.2.1 Materials and chemicals

Vanadium (V) oxide (V_2O_5), ammonia water (wt.28%), hydrazine hydrate solution (78-82%), ethanol (absolute) were purchased from Sigma-Aldrich Co. Australia and stored at room temperature. Deionized (DI) pure water was acquired from the local purest water company. All reagents were used directly without any treatment.

3.2.2 Experimental process

Many factors can affect the final obtained monoclinic phase VO_2 nanoparticles. Firstly, how the concentration of hydrazine solution can affect the synthesis was studied.[162] Zhou etc have synthesized the VO_2 nanorods with the hydrazine as a reducing agent, however, in their experiment, the annealing time is too long. In my research, ammonia water was used to control the pH environment. And the annealing time is two hours which is much shorter. The experimental process is as follow:

- 1.1 g of V_2O_5 powder was used as vanadium source.
- Different amount of hydrazine hydrate solution was used to make the molar ratio of V_2O_5 to N_2H_4 as 0.12, 0.24, 0.36, 0.48, 0.60 and 0.72 respectively.
- The other parameters are just follow the methods which have been described below (Table.2).

As we can see from Fig.41, before the hydrothermal reaction, the color of the solution has been different. With the increase of the hydrazine amount, the color is

darker. It indicates that the concentration of vanadium ions is different in these samples/

	V_2O_5 (g)	N_2H_4 (µL)	Hydrothermal Temperature (°C)	Annealing Temperature (°C)	N_2H_4: V_2O_5 (Molar radio)
A	1.1	300	220	700	0.72
B	1.1	250	220	700	0.60
C	1.1	200	220	700	0.48
D	1.1	150	220	700	0.36
E	1.1	100	220	700	0.24
F	1.1	50	220	700	0.12

Table 3. Experimental parameters of the VO_2 nanoparticle synthesis

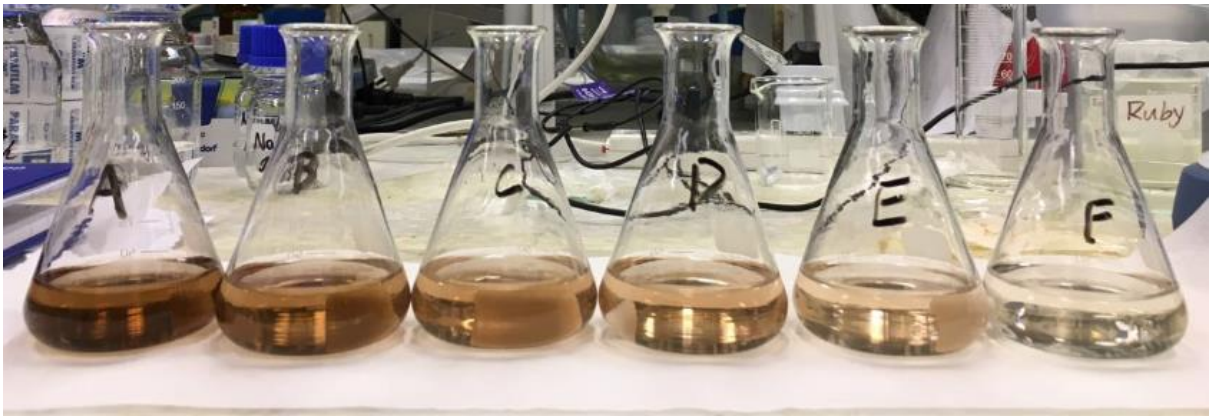

Figure 41 Hydrothermal solution before the hydrothermal reaction

3.2.3 Characterization

After the hydrothermal reaction, the particles were centrifuged, and washed for several times. Then the clean particles were dried at 60 °C for 3 hours. After that, X-ray diffraction (XRD) analyses were conducted on a Rigaku Miniflex 600 Diffractometer (Japan) with Cu Kα radiation (λ¼1.5418 Å) using a voltage and current of 40 kV and 15 mA, respectively. The sample was measured at a scanning

rate of 4°/min. XRD spectra was measured to check the composition of the results. As we can see from Fig.42, there is not clear crystal structure of VO_2 or relative materials. Therefore, a further annealing treatment was necessary to get the VO_2 (M) nanoparticles.

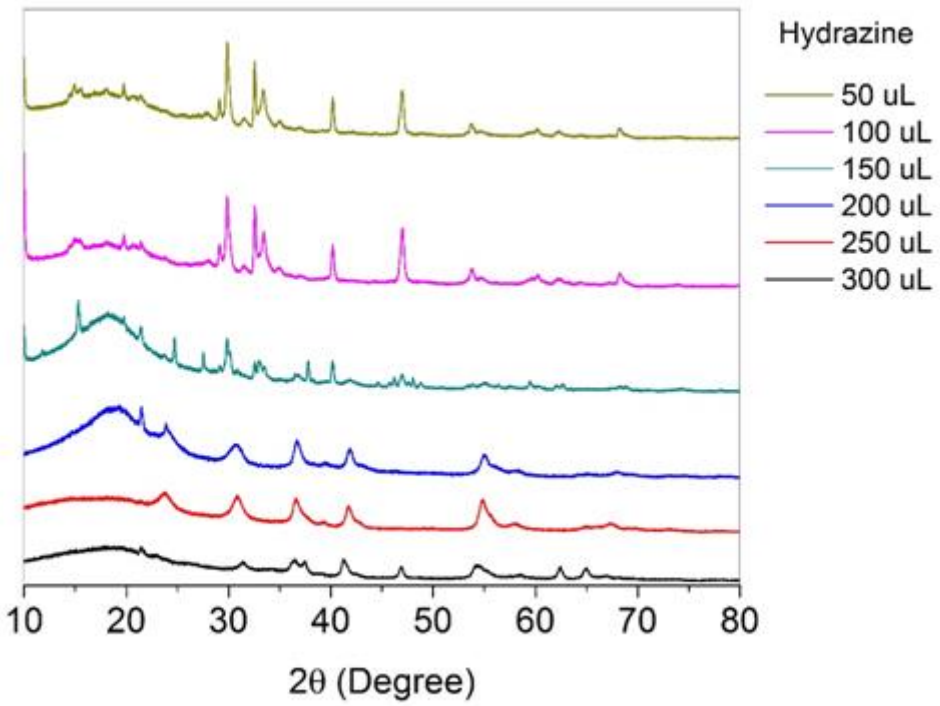

Figure 42 XRD spectra of the particles after hydrothermal reaction

Therefore, a pre-heat treatment and annealing process were conducted. The particles were heated in an oven with 180 °C in order to treat the surface to remove the hydroxyl ion, which is important to increase the dispersity of the particles. The XRD was also conducted to check the composition of the particles.

As we can see from Fig.43, there is still not a clear monoclinic phase VO_2 in this step. The peaks are mainly from some vanadium precursors. Preissa et al.[163] have published a paper about the synthesis of vanadium from solution-derived precursors,

it shows the XRD information of the precursor which has a similar pattern with my results.

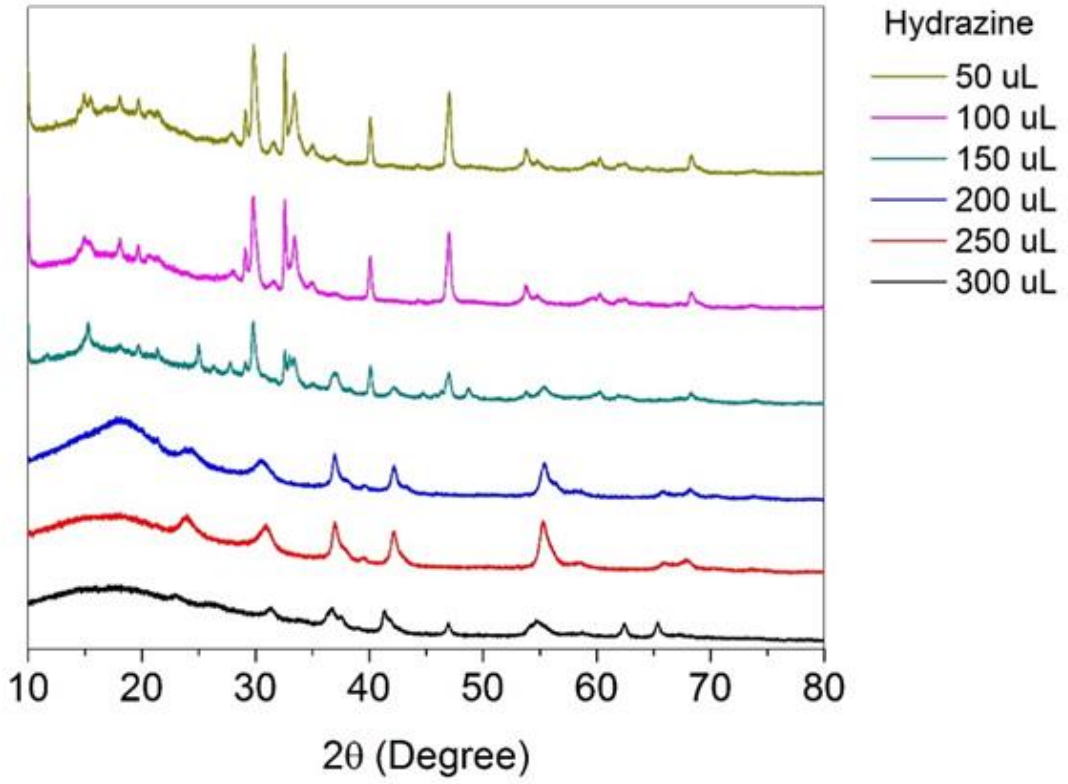

Figure 43 XRD spectra of 180 °C pre-annealed particles.

Moreover, a post-annealing process was done in the next step. For the purpose of getting monoclinic crystal structure of the nanoparticles, a pre-annealed particles were highly needed. The process was completed with the following steps:

- The pre-heat treated sample was put into the tube furnace.
- N_2 gas was flowed into the tube for half an hour to make sure all the oxygen inside was removed.
- With the protection of N_2 gas, the annealing process was conducted with 700 ˚C temperature for two hours. The heating rate was 10 ˚C/min.

The composition information was measured by an X-ray diffraction meter. As we can see from Fig.44, after a post-annealing process, a clear monoclinic VO_2 crystal structure can be got. It means that the post annealing process is necessary and meaningful to get the VO_2 (M) material.

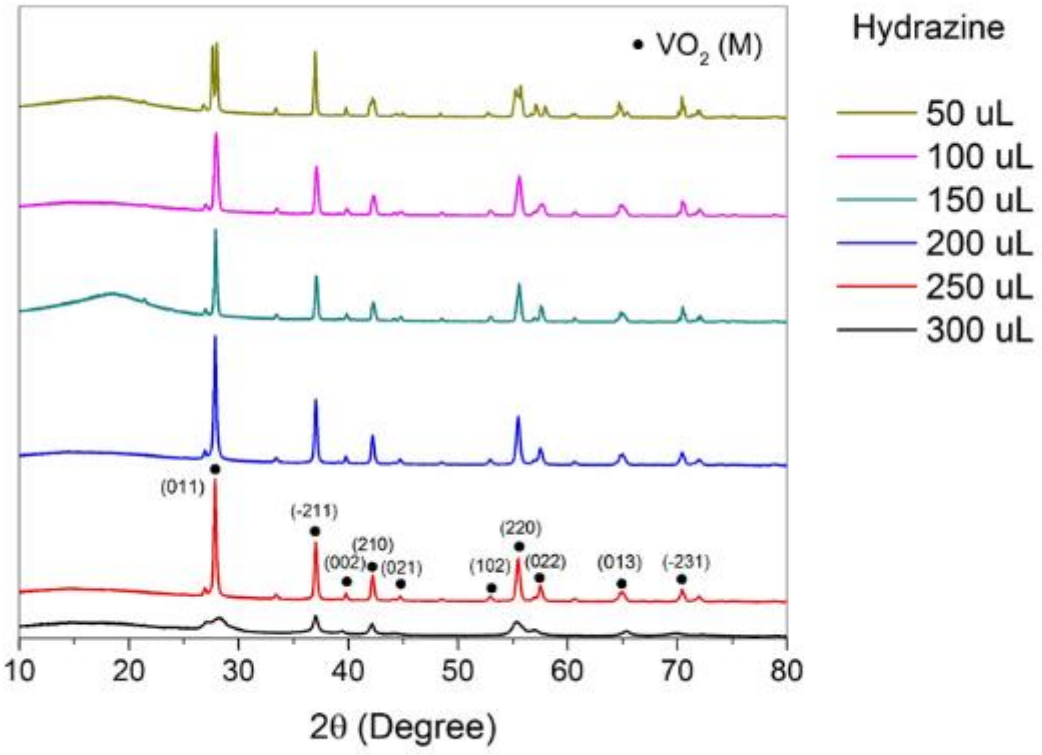

Figure 44 XRD spectra after post annealing process

The results were similar to Gao's work [164] which approves that the monoclinic VO_2 nanoparticles were synthesized. The XRD pattern of VO_2 is matched to PDF-44-0252 VO_2 (M) (*P*21/*c*), which is shown in Fig. 44. The lattice constants are a=5.75 Å, b= 4.52 Å, c=5.38Å. The planes such as (0 1 1), (-2 1 1), and (2 1 0) can be seen in the graph. There is no impurity detected in the sample. He also indicated that the increasing synthesis temperature can improve the crystallinity of the nanoparticles. Meanwhile, the amount of hydrazine solution also affects the composition of the final VO_2 nanoparticles. When the amount of V_2O_5 is 1.1g, VO_2 (M) nanoparticles can be obtained with a wide range amount of hydrazine solution. Particularly, when the

molar ratio of V_2O_5 to hydrazine is between 0.24 and 0.60, the composition is all monoclinic nanoparticle.

Besides the composition information of the samples, the morphology was also a significant factor for the samples. In order to check the morphology of the obtained VO_2 (M) nanoparticles, the SEM images were taken by a FEI Magellen 400 FEG SEM equipment.

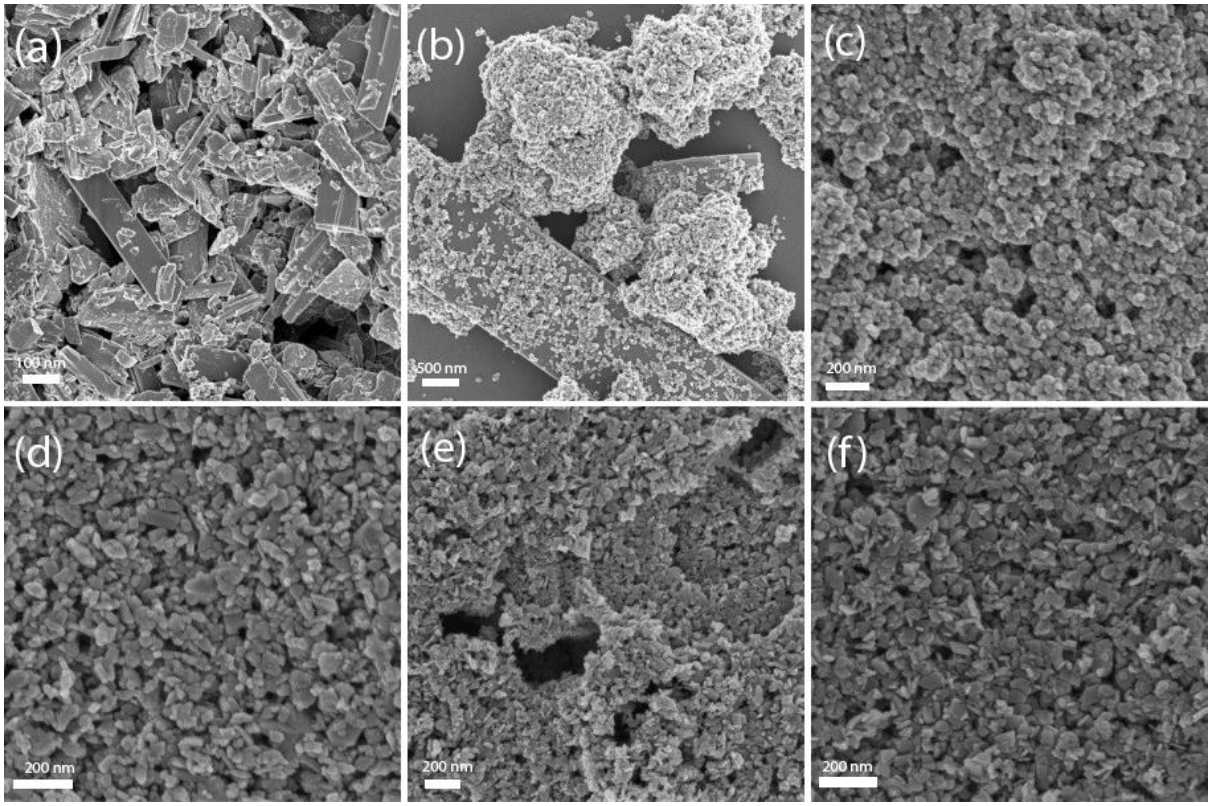

Figure 45 SEM of the VO_2 nanoparticles by using different amount of N_2H_4 solution, (a) 300 µL, (b) 250 µL (c) 200 µL, (d) 150 µL, (e) 100 µL, (f) 50 µL.

As we can see from Fig.45, when the amount of hydrazine hydrate solution was 300 µL, the morphology was large bar shape particles. The length of the particle was larger than 300 nm and the diameter was 30 nm. When the concentration was decreased to 250 µL, there was a mixture of big bar particles and small particles.

The small particles were on the surface of the large particles. It seems that the big particles started to split at this concentration. After that, when the hydrazine solution was decreased into 200 and 150 µL, most of the particles were small particles. The size was about 50 nm. Moreover, when the hydrazine solution was reduced to 100, 50 µL, all the particles were small particles with 40 nm size. And the morphology was little diamond shape.

Gao et al [164] have also tried to synthesize the VO_2 nanoparticles, and faced shot rod-like nanoparticles were prepared. My results were quite similar to that results when the hydrazine solution concentration was in a correct range.

Moreover, the particles size reduced with the decrease of the hydrazine amount. When the amount of hydrazine solution was reduced from 250 to 50 µL, there always be a relatively clear M phase structure, however, the morphology was different. Only when the hydrazine amount was smaller than 200 µL, it had a good particles shape and size.

In conclusion, the best molar ratio between V_2O_5 and hydrazine is 0.24~0.48. And the size is much smaller than Gao's results[102].

3.2.4 Results analysis

In this section, the effect of the concentration of hydrazine solution in the hydrothermal process was studied. As we can see from the SEM images, the amount of hydrazine solution can affect the morphology of the VO_2 nanoparticles dramatically. In fact, many factors can affect the size and morphology of the nanoparticles in the hydrothermal reaction, which include reaction temperature, reaction time, agitation speed, solvent and concentration of precursors.

Sometime, the particles will be larger due to its consuming smaller particles, it is also known as "Ostwald ripening" [165]. The hydrazine hydrate may affect the Ostwald ripening process, which can affect the size of particle finally, as the hydrazine can affect the pH of the solution.

In this experiment, the concentration of N_2H_4 can influence the formation of $VO(OH)_x(OH_2)_n$, which is important in the process of hydrothermal reaction. Therefore, it can make a huge impact on the size and morphology of the final VO_2 nanoparticles.

With higher concentration of hydrazine solution, larger size of $VO(OH)_x(OH_2)_n$ microparticles will be formed, and the final VO_2 nanoparticles will be in larger size. However, when the concentration of hydrazine solution is decreased, the size of $VO(OH)_x(OH_2)_n$ microparticles will be relatively small, which will lead to smaller VO_2 nanoparticles.

When the molar ratio between hydrazine solutions to V_2O_5 is 0.12~0.72, the monoclinic phase of VO_2 can all be synthesized successfully. However, only when the molar ratio is 0.24~0.60, can the particles have a small and uniform morphology. The nanoparticles have several features such as large specific surface area, large amount of surface atoms, and high surface energy, which makes it different with other materials. So the reduced agent (hydrazine hydrate solution) plays an important role in the synthesis results. In this experiment, the amount of hydrazine solution affects the morphology of the VO_2 nanoparticles significantly. For instance, the size of the particles was reduced with the decrease of the reduced agent amount. Even though the composition can mainly maintain its monoclinic phase.

3.3 Effect of post-annealing process

Temperature is another factor which can affect the morphology of nanoparticles in the hydrothermal process. Some researchers have found that temperature is an essential factor in preparing the TiO_2 nanotube. The yield of TiO_2 nanotube can be 80%~90% when the hydrothermal temperature is 100~150 °C, and the TiO_2 nanotube can get a higher specific surface area when the temperature achieve

150 °C. It shows that the temperature can influence the yield and morphology of nanomaterials in hydrothermal reaction.

Moreover, the high-temperature annealing can always lead to an aggregation of the particles. Theoretically, many reasons can be found to lead to an aggregation of nanoparticles:

- (a) Many positive and negative charges on the surface of nanoparticles can lead to the aggregation of them.
- (b) Nanoparticles have large specific surface area and surface energy, which makes them unstable in energy.
- (c) The short distance between nanoparticles can lead to a large Van der Waals' force which can cause the aggregation of nanoparticles.
- (d) The hydrogen bond and other chemical bonds also lead to the strong aggregation between the nanoparticles.

Calcination temperature plays an important role in the aggregation of nanoparticles, Guo et al. indicated that the higher carnation temperature can lead to a heavier aggregation. However, the calcination can also affect the composition and application of VO_2 smart coating material. High temperature is also a waste of energy in the synthetic process. Therefore, another experiment has been tried to study this post annealing process.

Several methods can be helpful in dealing with the aggregation problem, such as adding dispersing agent, adding surface coating, using mechanical force method, and using ultrasonication etc. For rear of impact of dispersing agent in the application, a mechanical force method was used by grinding the particles to disperse the particles. Ultrasonic process was used after the calcination process to tackle the aggregation.

3.3.1 Materials and chemicals

Vanadium (V) oxide (V_2O_5), ammonia water (wt.28%), hydrazine hydrate solution (78-82%), ethanol (absolute) were purchased from Sigma-Aldrich Co. Australia and

stored at room temperature. Deionized (DI) pure water was acquired from the local purest water company. All reagents were used directly without any treatment.

3.3.2 Experimental process

All the synthesis was conducted with the previous hydrothermal method. After the annealing process, the obtained particles were treated with grind and ultrasonic process. The prepared VO_2 nanoparticles were annealed at 700 °C and 750 °C respectively. A grinding and ultrasonic treatment was used to reduce the aggregation of the particles. The research detailed can be seen in table 3.

Annealing temperature (˚C)	**700**	**750**
Grind	a	d
Ultrasonication for10 minutes	b	e
Ultrasonication for 30 minutes	c	f

Table 4 Annealing of VO_2 nanoparticles with assistance of grind and ultrasonic treatment, a. 700 ˚C with grinding, b,700 ˚C with 10 mins ultrasonication, c. 700 ˚C with 30 mins ultrasonication, d.750 ˚C with grinding, e. 750 ˚C with10 mints ultrasonication, f. 750 ˚C 30 mins ultrasonication.

3.3.3 Characterizations

Then the morphology of the particles were checked through the SEM images.

As we can see from the SEM images (Fig.46), the annealing process can lead to an aggregation. However, the grind and ultrasonic process can improve the dispersity of the particles. With extending the ultrasonic time, the dispersity can get a dramatic improvement.

Particularly, the VO_2 particle size (c and f) which were synthesized in different temperature (700 ˚C and 750 ˚C) were also measured. As we can see from Fig.46 (a) and (d), only with grinding, the aggregation phenomenon is severe, even though the particles size is not too big.

And it happens in both 700 ˚C and 750 ˚C annealing conditions. With the assistance of short time ultrasonication process (10 minutes), both the samples synthesized in 700 ˚C and 750 ˚C get a big improvement of the particles aggregation. It is much easier to see the particles one by one rather than a big bulk size particles. Finally, with a longer time ultrasonication treatment (30 minutes), the aggregation problem was solved better. The particles were almost dispersed broadly and uniformly.

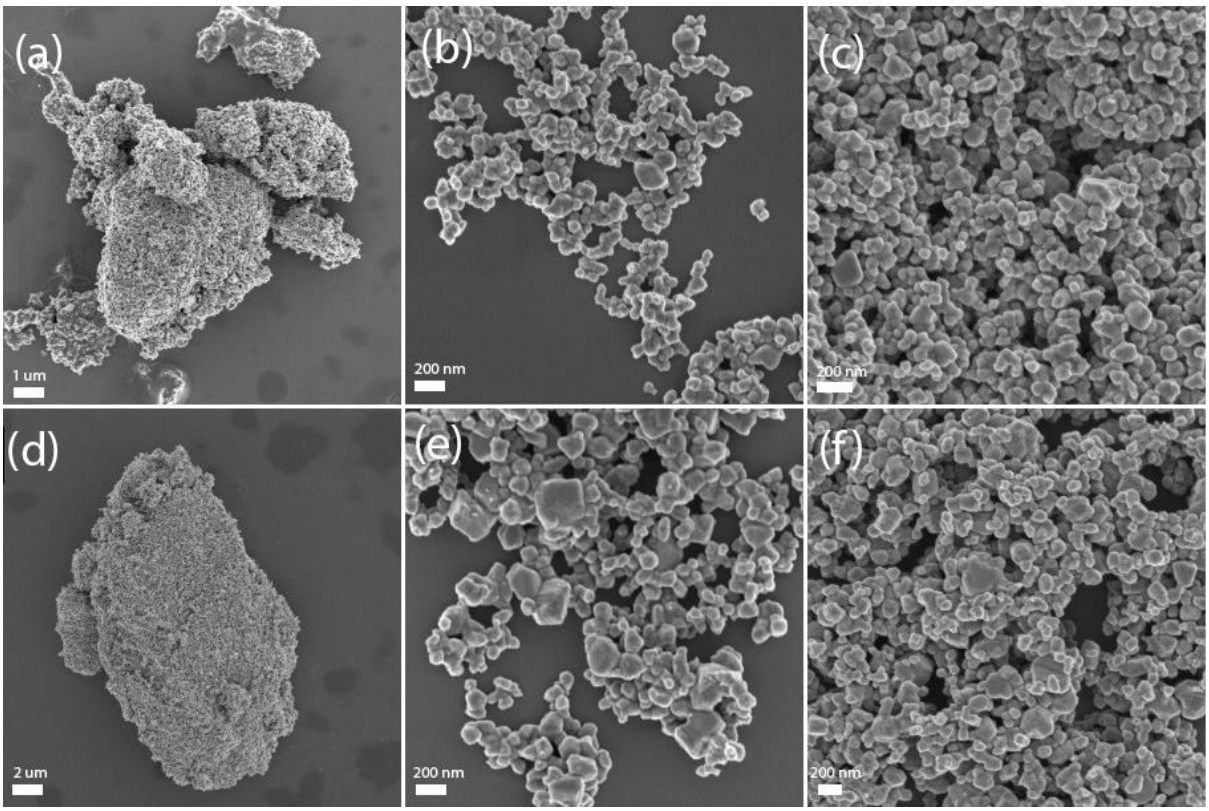

Figure 46 SEM images of the VO_2 particles got in different annealing temperature, after grinding and ultrasonic process; (a) 700 ˚C & grind, (b) 700 ˚C & 10 min ultrasonic treatment , (c) 700 ˚C & 30 min ultrasonic treatment, (d) 750 ˚C & grind, (e) 750 ˚C & 10 min ultrasonic treatment, (f) 750 ˚C, 30 min ultrasonic treatment.

3.3.4 Results analysis

In this session, the aggregation problem of the VO_2 nanoparticles by hydrothermal method was studied. As we all know, after the high-temperature annealing progress, the particles will tend to aggregate together, which will affect the morphology of the particles and influent the final application.

Therefore, in this experiment, mechanical force method and ultrasonic method were used to deal with the aggregation problem in the synthesis of VO_2 nanoparticles. The samples were synthesized in two different temperatures: 700 ˚C and 750 ˚C. In both conditions, the particles will be synthesized by the previous hydrothermal method. From the experimental results, we can see that:

- The grinding method is not strong enough to disperse the VO_2 nanoparticles. Big particle cluster can also be seen from the SEM image even after grinding treatment.
- With short time (10 minutes) ultrasonic treatment, the VO_2 nanoparticles can get a big improvement in the dispersity. The particles can be uniformly spread in the SEM image.
- With a longer time (30 minutes) ultrasonic treatment, the dispersity of the VO_2 nanoparticles have better results. There is almost no big particles in the view and all the space is filled with uniform VO_2 small particles.

It means that the treatment of grind and ultrasonic are all useful in dispersing the nanoparticles.

3.4 Optimal annealing temperature for the synthesis of VO_2 (M) nanoparticles

As we have talked, the post-annealing progress is very important in preparing the monoclinic VO_2 nanoparticles which has the thermochromic property. However, the high-temperature annealing process can lead to a waste of energy and aggregation of particles, therefore, an optimal annealing temperature was studied in this section. With the optimal annealing temperature, the prepared VO_2 nanoparticles can show a better dispensability in a good composition.

VO_2 is a representative binary compound, it has a variety of polymorphs, including VO_2(M), VO_2(R), VO_2(B),VO_2(A),VO_2(C), VO_2(D),etc. Only VO_2(M/R) shows a fully reversible first-order metal-to-insulator transition (MIT) due to a crystallographic transition between a low-temperature monoclinic phase (M) and a high-temperature tetragonal phase (R).Therefore, the annealing process is necessary to guarantee the pure composition of VO_2 nanoparticles.

In this section, the annealing temperature was adjusted from 650 ˚C to 700 ˚C to check the composition of the samples. Firstly, the effect of high annealing temperature was studied by comparing the particle size of particles with annealing, particles with 700˚C annealing and particles with 750 ˚C annealing.

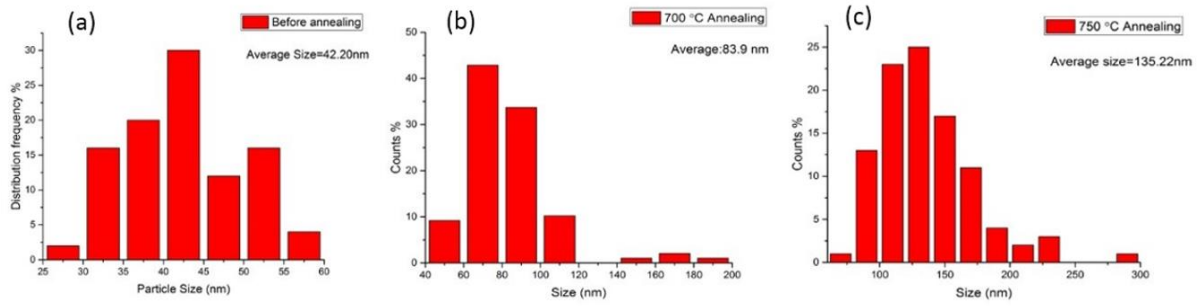

Figure 47 Size distribution of VO_2 nanoparticles before and after annealing process (a) before annealing process (b) annealing at 700 ˚C (c) annealing at 750 ˚C

As we can see from the above image, the average particle size before annealing is 42.2nm. When the particles were annealed at 700 ˚C, the average particle size was increased to 83.9nm. Moreover, the average particle size will be up to 136.2 nm when the annealing temperature was increased to 750 ˚C.

Therefore, the high annealing temperature plays an important role in increasing the final VO_2 nanoparticle size. For the purpose of studying the optimal annealing temperature, the following experiment was conducted.

3.4.1 Materials and chemicals

Vanadium (V) oxide (V_2O_5), ammonia water (wt.28%), hydrazine hydrate solution (78-82%), ethanol (absolute) were purchased from Sigma-Aldrich Co. Australia and stored at room temperature. Deionized (DI) pure water was acquired from the local purest water company. All reagents were used directly without any treatment.

3.4.2 Experimental process

As we have discussed above, M phase VO_2 nanoparticles are difficult to synthesize just through hydrothermal reaction. In this study, a post-annealing process was conducted to get the M phase VO_2. And a serious of temperatures (650 °C to 750 °C) were used to test the optimal temperature for the post-annealing process.

Firstly, the air in the tube furnace was removed by inflating the tube with N_2 gas for half an hour. Then, the annealing temperature was set from 650 °C to 750 °C with one hour reaction time and 10˚C/min heating rate. After that, the temperature was cooled to room temperature, the final black particles were collected and used to do the characterization.

3.4.3 Characterization

The XRD measurement was done to check the composition of VO_2 nanoparticles synthesized in different annealing temperature. As we can see from the image (Fig. 48), the M phase VO_2 appears at 650 ˚C and becomes stable at 660 ˚C. After that, until 700 ˚C, the crystal structure of VO_2 keeps M phase. As the low temperature can not only saves a lot of energy consumption but only helps to increase the dispersity of particles, the 660 ˚C will be the best temperature in this research.

The XRD spectra further verified the phase purity of monoclinic phase VO_2. Since 660 °C, all of the peals in the spectra can be indexed to monoclinic phase VO_2 (JCPDS card no. 72-0514, *P*21/*c, a*=0.5743 nm*, b*= 0.4517 nm*, c*=0.5375 nm*, and β* =122.61°).It indicates that the monoclinic phase VO_2 can be obtained when the annealing temperature is higher than 660 °C[166]

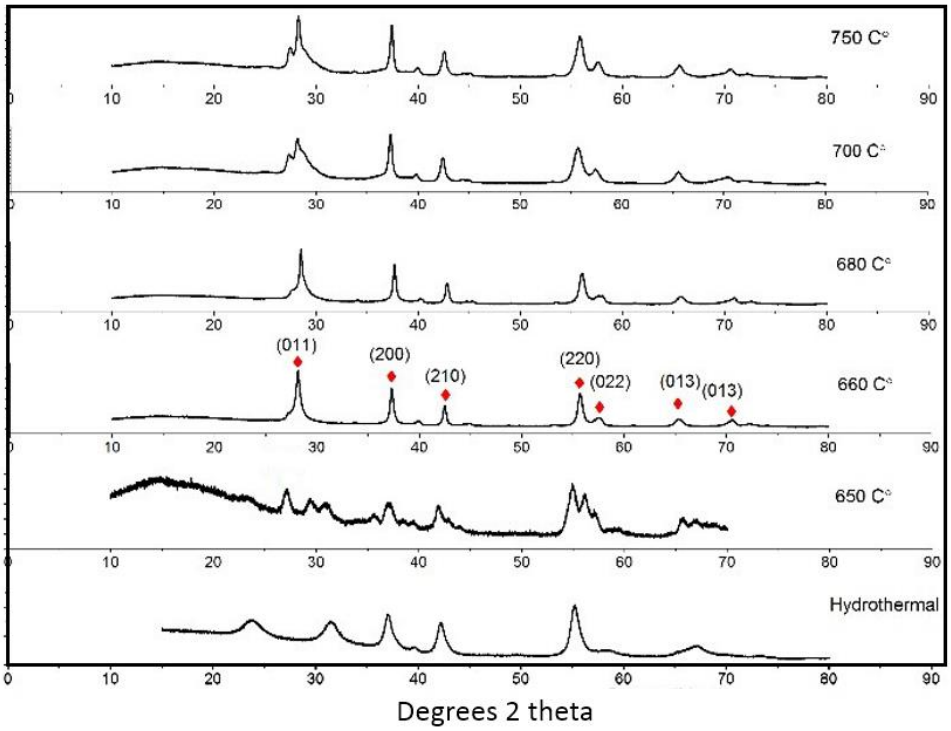

Figure 48 XRD spectra of VO_2 nanoparticles with different annealing temperature from 650 ˚C to 700 ˚C.

3.4.4 Results analysis

Annealing temperature is essential in the synthesis of monoclinic VO_2 nanoparticles as VO_2 has a lot of polymorphs. For the purpose of smart window application and saving energy consumption, the optimal annealing temperature was studied in this section.

As we can see from the XRD spectra, the samples annealed in 650 ˚C, 660 ˚C, 680 ˚C, 700 ˚C and 750 ˚C were compared in the image. When the annealing temperature is 650 ˚C, there is some VO_2 monoclinic peaks, but the XRD peak is not so clear. Moreover, when the annealing temperature is 660˚C, a clear monoclinic phase VO_2 can be seen at the first time. Therefore, 660˚C is the optimal annealing temperature in this experiment. For the reason of the size enlargement of the particles, there are mainly two reasons, the Ostwald ripening, and oriented attachment. In terms of Ostwald ripening, the larger particles occur based on the dissolution of the smaller one. For the oriented attachment, the larger particles appear due to the merging of smaller ones. Both of them depend on the temperature. As bigger particles are more energetically stable, the smaller ones tend to aggregate together. And oriented attachment occurs because the aggregation decreases the interphase boundary and surface energy of the system.

Based on the reason, the annealing tempter should maintain as low as possible to reduce the aggregation phenomenon. As the monoclinic phase is essential and the annealing process is necessary, the optimal annealing temperature is around 660 ˚C

3.5 Thermochromic property

90% of the solar energy is distributed between 250 nm and 1500 nm in the solar irradiance. VO_2 has a solar modulation ability by changing from insulator phase to metal phase, which has different transmittance, especially in near-IR region. Through

the phase transfer, VO_2 exhibits a large variance in NIR transmittance, while keeping the visible transmittance stable. Therefore, the optical properties of VO2 films were tested to check its thermochromic properties.

As we can see from Fig. 49, the transmittance spectra is similar in high temperature (90 °C) and low temperature (20 °C). Theoretically, the transmittance in high temperature should be much lower than the transmittance in low temperature, especially in NIR region. There are some reasons for the weak thermochromic property of the VO_2 films. Firstly, the thickness of the VO_2 film can affect the thermochromic property. The VO_2 films cannot exhibit an outstanding optical property if the VO_2 film is too thick. Secondly, the size distribution of VO_2 nanoparticles can also influent the optical properties dramatically. The VO_2 films can show a good optical property only with a uniform film. The preparation of VO_2 film may affect the final optical property, which seems that there is not good thermochromic property. More work should be performed to increase the film quality.

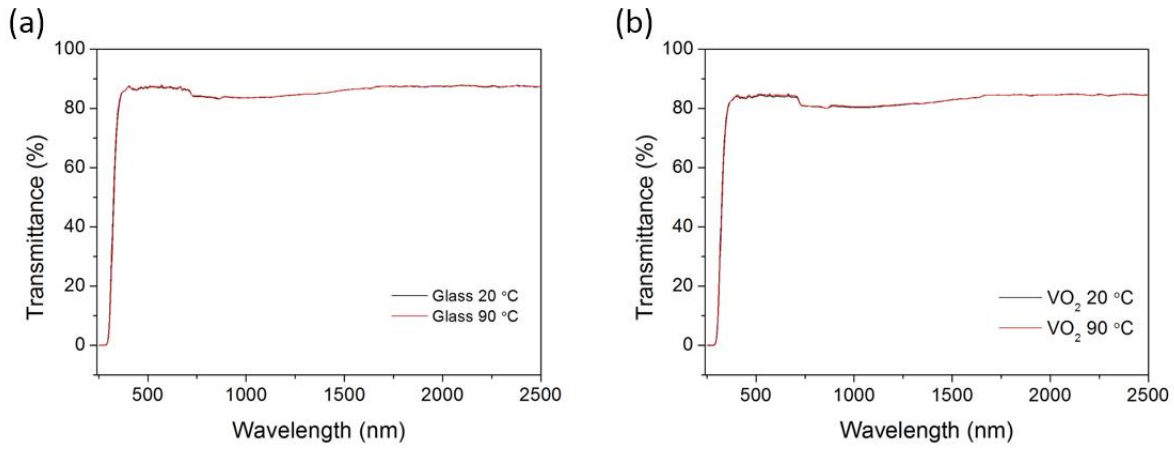

Figure 49 Transmittance spectra of (a) glass and (b) VO_2 nanoparticles coated glass, the samples are measured at 20 °C and 90 °C respectively.

3.6 Summary

In this chapter, the importance and synthesis of VO_2 (M) nanoparticles were talked. As we all know, VO_2 (M) is a thermochromic material which can be used in smart window application, therefore the synthesis and application problem should be modified and solved to improve the performance of smart window coating. As we can see from the above results, VO_2 (M) nanoparticles were synthesized successfully through a post-annealing hydrothermal method. Through the XRD, it is pure monoclinic phase VO_2 which is functional in smart window application.

- In this hydrothermal synthesis, the hydrazine solution plays an important role. Even though the monoclinic phase VO_2 can be synthesized by a wide range of concentration of hydrazine solution. A good morphology can only be got when the molar ratio of N_2H_4 to V_2O_5 is between 0.24 and 0.60. And SEM images were tested to keep the particles in a rod shape which has the potential to be a smart window film coating. The reason is that the concentration of N_2H_4 can influence the formation of $VO(OH)_x(OH_2)_n$, which is significant in the process of hydrothermal reaction. Larger size of $VO(OH)_x(OH_2)_n$ microparticles will be formed with higher concentration of hydrazine solution and the final VO_2 nanoparticles will be in larger size.
- Moreover, the aggregation problem of the VO_2 nanoparticles by hydrothermal method was studied. With high-temperature annealing process, the VO_2 nanoparticles are easily to be aggregated. Therefore, a grinding method and ultrasonic treatment was used to separate the nanoparticles. Based on the experimental results, the grinding method not strong enough to disperse the VO_2 nanoparticles. Big particle cluster can also be seen from the SEM image even after grinding treatment. The ultrasonic treatment is much useful to make the VO_2 samples have a better dispersity.
- Besides, an aggregation can occur during the annealing process. So the optimal annealing temperature was studied to save the energy and decrease the aggregation phenomenon. By changing the annealing temperature from

650 ˚C to 750 ˚C, the XRD information was studied to get the best annealing temperature. Based on the experimental results, the characteristic peaks of monoclinic VO_2 appears at 660 ˚C, therefore, 660℃ was found to be the best annealing temperature in the synthesis.

Chapter 4 Preparation of VO_2@SiO_2 core-shell nanoparticles

Even though the VO_2 (M) has been synthesized successfully, it is always a problem to keep VO_2 in stable performance under environment with high oxygen partial pressures for a long time[167].Therefore, the stability study was performed later. Core-shell structure is a good method to deal with this problem.

Silicon dioxide, also known as silica. It is a kind of oxide of silicon and the chemical formula is SiO_2. SiO_2 coating[168-172] is a common coating material as it has excellent biocompatibility, stability, nontoxicity, and easily furthered conjugation with various functional groups. The stöber synthesis[173-177] and reverse microemulsion methods[178-182] are two commonly used methods for silica coating. The difference between these two methods is that the first method can only be applied for the particles soluble in the polar media. The inert silica shells can dramatically protect core nanoparticles from corrosion from surrounding media[183].

Therefore, in this chapter, the VO_2@SiO_2 was tried to synthesis, and the relative characteristic properties were tested, including its morphology, acid resistance ability, alkali resistance ability, oxidation agent resistance ability and UV light resistance ability.

4.1 Synthesis of VO_2@SiO_2 core-shell nanostructure by stöber method

4.1.1 Materials and chemicals

Tetraethyl orthosilicate (TEOS, 98%), ammonia water (28%), ethanol (absolute) were purchased from Sigma-Aldrich Co. Australia and stored at room temperature. VO_2 (M) nanoparticles are synthesized by the previous experiment. Deionized (DI) pure water was acquired from the local purest water company. All reagents were used directly without any treatment.

4.1.2 Experimental mechanism

The stöber method is a commonly used chemical process which is usually used to fabricate silica (SiO_2) particles, and the particles can be in controllable and uniform size. This method was firstly reported by Werner stöber and his team in 1968. It is still an important way to synthesize silica nanoparticles today. It is an example of a sol-gel process where a molecular precursor (typically tetraethylorthosilicate, TEOS) is firstly reacted with water in an alcoholic solution, the resulting molecules then join together to build larger structures.

The Stöber method is a sol-gel approach to synthesize monodisperse (uniform) spherical silica (SiO_2) materials. Silica precursor tetraethyl orthosilicate (TEOS) can be hydrolyzed in alcohol (usually methanol or ethanol) with the presence of ammonia, which is the catalyst.

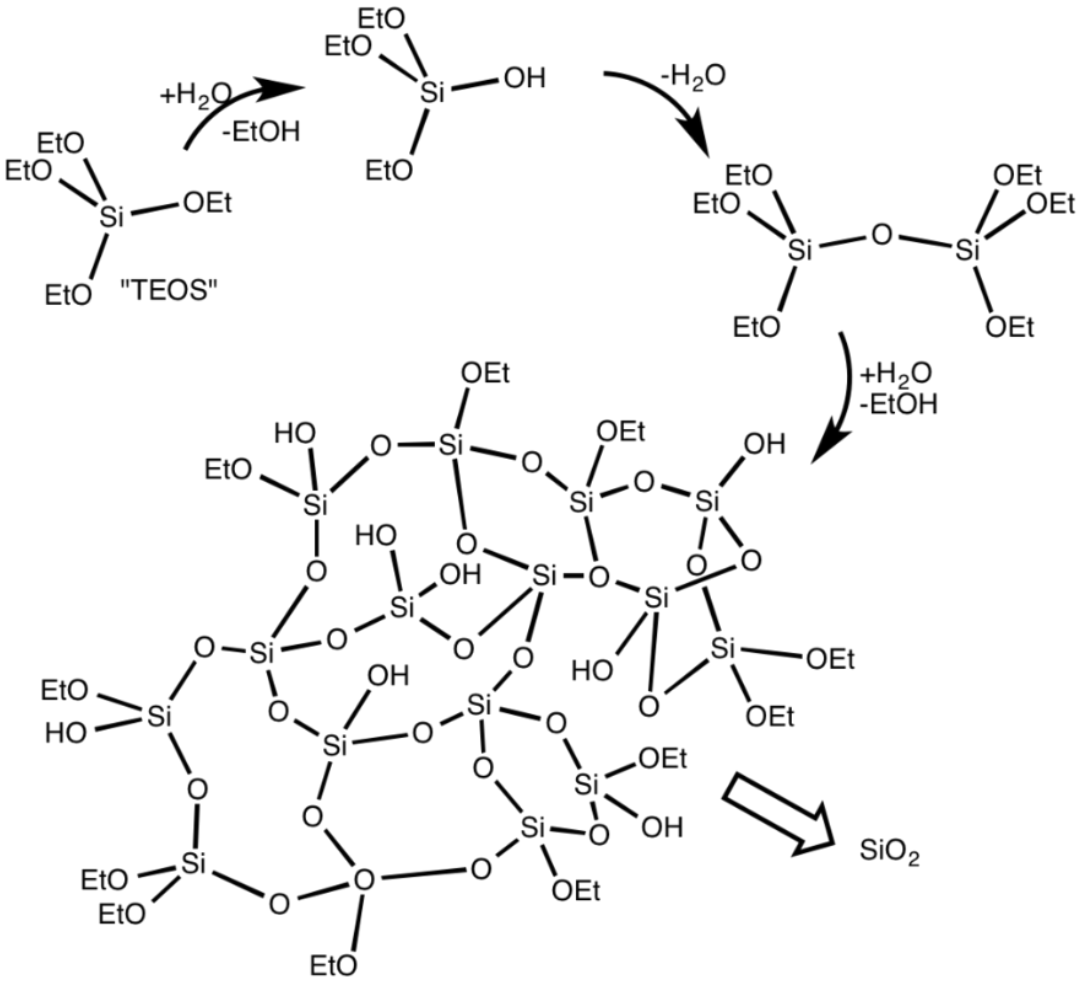

Figure 50 Simplified representation of the hydrolysis and condensation of TEOS in the Stöber process

$$Si(OEt)_4 + H_2O \rightarrow Si(OEt)_3OH + EtOH$$

$$Si(OEt)_4 + 2H_2O \rightarrow Si(OEt)_2(OH)_2 + 2\ EtOH$$

A serious of mixture of ethoxysilanols (such as $Si(OEt)_3(OH)$, $Si(OEt)_2(OH)_2$), and even $Si(OH)_4$, which can then condense with either TEOS or another silanol with loss of alcohol or water.

$$2\ Si(OEt)_3OH \rightarrow (EtO)_3Si\text{-}O\text{-}Si(OEt)_3 + H_2O$$

$$Si(OEt)_3OH + Si(OEt)_4 \rightarrow (EtO)_3Si\text{-}O\text{-}Si(OEt)_3 + EtOH$$

$$Si(OEt)_3OH + Si(OEt)_2(OH)_2 \rightarrow (EtO)_3Si\text{-}O\text{-}Si(OEt)_2OH + H_2O$$

More hydrolysis of the ethoxy groups and following condensation generates crosslinking.

4.1.3 Experiments process

In this study, the stöber method was used to synthesize the VO_2@SiO_2 core-shell structure.

Firstly, as-prepared VO_2 particles were dispersed into ethanol solution, stirring for ten minutes. After that, it was added into a mixed solution which contains ethanol, DI water and ammonia water. They were mixed and stirred for 30 minutes. Then TEOS solution was added into the solution drop by drop in ten minutes. The reaction time was about two to four hours. Finally, an ultrasonic process was conducted to increase the dispersity of the solution. After the reaction, it was washed and dried in 60 ˚C for two hours.

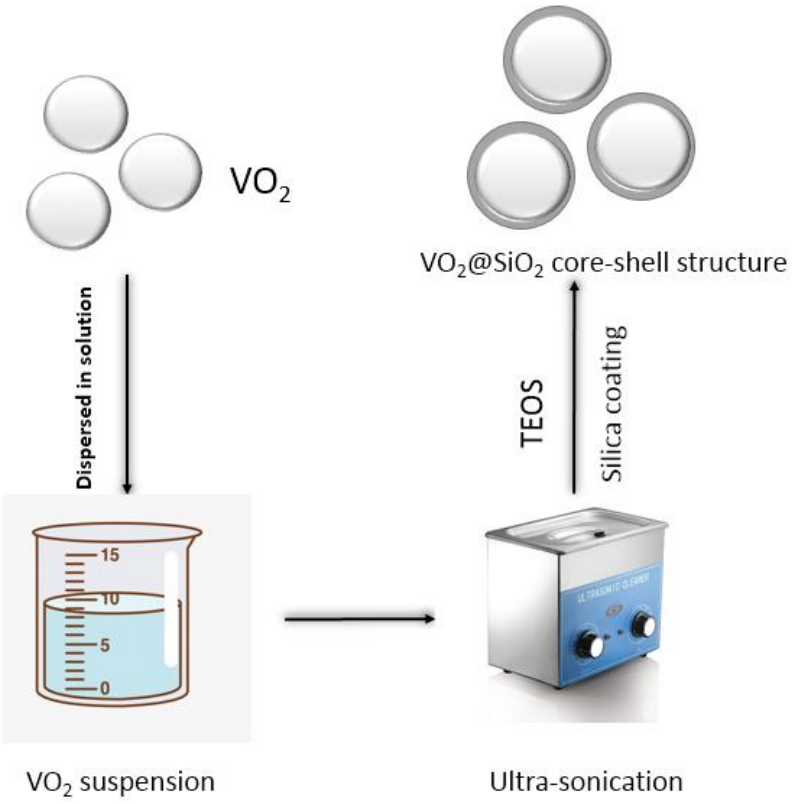

Figure 51 Formation process of VO_2@SiO_2 core-shell nanoparticles

4.1.4 Characterizations of the VO_2@SiO_2 core-shell nanostructure

Firstly, optical properties were tested to characterize the core-shell nanostructure. The UV-Visible spectrum was got to characterize the VO_2 and VO_2@SiO_2 nanoparticles. Usually, few people test the UV-Vis spectrum of the VO_2 nanoparticles. In this research, the UV-Vis spectrum was tested.

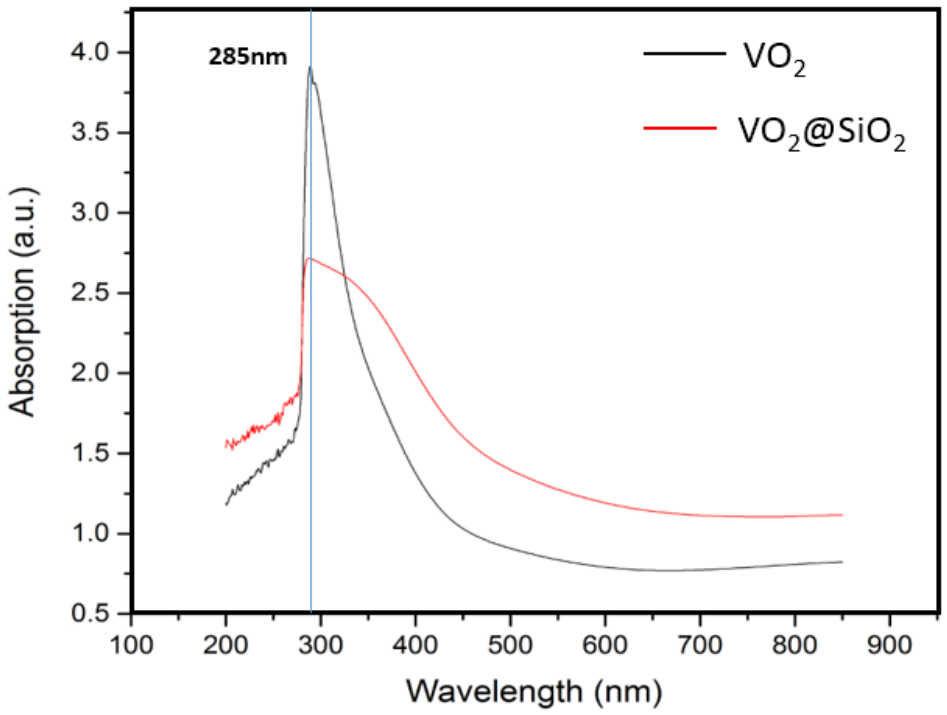

Figure 52 UV-Vis spectrum of VO_2 (black line) nanoparticles and VO_2@SiO_2 (red line) core-shell nanoparticles

As we can see, the VO_2 nanoparticles have a UV absorption at 285 nm, and VO_2@SiO_2 particles have UV absorption at around 280 nm. Yu et al tried to prepare the VO_2 thin films, and the thermally aged $VO(acac)_2$ precursor show a similar UV-Vis absorption spectra, which has an absorption peak at about 300 nm.Yonghong[184] et al, have tried to synthesize SiO_2/Ag core-shell nanoparticles, which has a similar blue shift phenomenon with thicker SiO_2 shell structure in the UV-Vis spectrum.

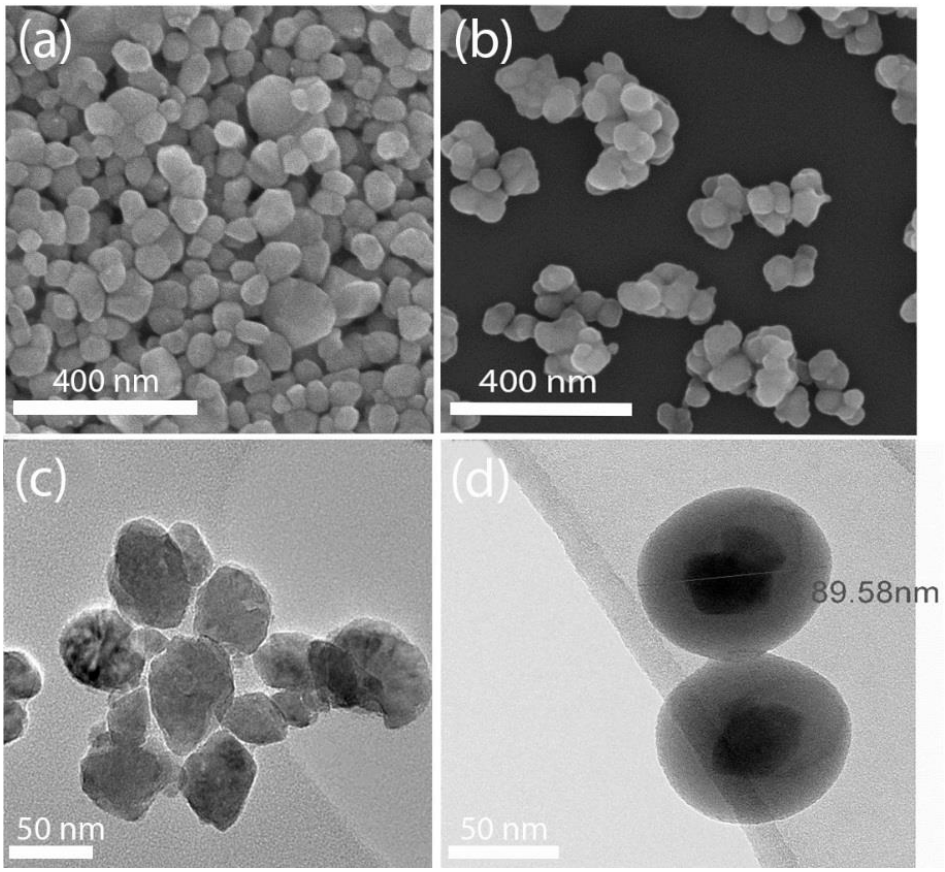

Figure 53 An overall comparison of VO_2 and VO_2@SiO_2 nanoparticles, (a) SEM image of VO_2 nanoparticles; (b) SEM image of VO_2@SiO_2 core-shell nanoparticles; (c) TEM image of VO_2 nanoparticles; (d) TEM image of VO_2@SiO_2 core-shell nanoparticles.

Secondly, the microstructure was observed with a transmission electron microscope (FEI Tecnai G2 T20) and a scanning electron microscope (FEI Magellan 400 FEG SEM). As we can see from the TEM image (Fig.53), the VO_2 particles were coated by the SiO_2 successfully. And the diameter of the particle is about 90 nm, with a 30nm core and a 30nm shell. The morphology and dispersity of the nanoparticles were dramatically good.

Therefore, the VO_2@SiO_2 core-shell nanoparticles were synthesized successfully. In the next step, the optical synthetic parameters were studied in the next sections.

4.2 Effect of TEOS concentration

For the purpose of synthesizing particular size VO_2@SiO_2 core-shell particles, different TEOS amount was used in the process. For purpose of getting the optimal amount of TEOS, other variables were maintain stable.

The research parameters were listed by the following table.

	Ethanol (mL)	**Amount of water (mL)**	**Reaction time (h)**	**$NH_3.H_2O$ (mL)**	**VO_2 (g)**	**TEOS (μL)**
L0	50	10	1	1	0.02	0
L1	50	10	1	1	0.02	50
L2	50	10	1	1	0.02	100
L3	50	10	1	1	0.02	150
L4	50	10	1	1	0.02	200
L5	50	10	1	1	0.02	250

Table 5 The experimental parameters of the VO_2@SiO_2 core-shell nanoparticles by using different amount TEOS

0.02g VO_2 nanoparticles were all dispersed into 50 mL ethanol. The amount of water is all 10 mL. The amount of TEOS was increase from 0 to 250 μL.

4.2.1 UV spectrum of the VO_2@SiO_2 core-shell nanoparticles

Optical properties were tested for the samples (L0-L5) by the UV-Vis spectrum. As we can see from Fig.54, with the increase of TEOS amount, the peak position of UV spectrum also increases. The absorbance peak position is increased from 395nm to 435 nm with the increase of TEOS from 50 μL to 250 μL

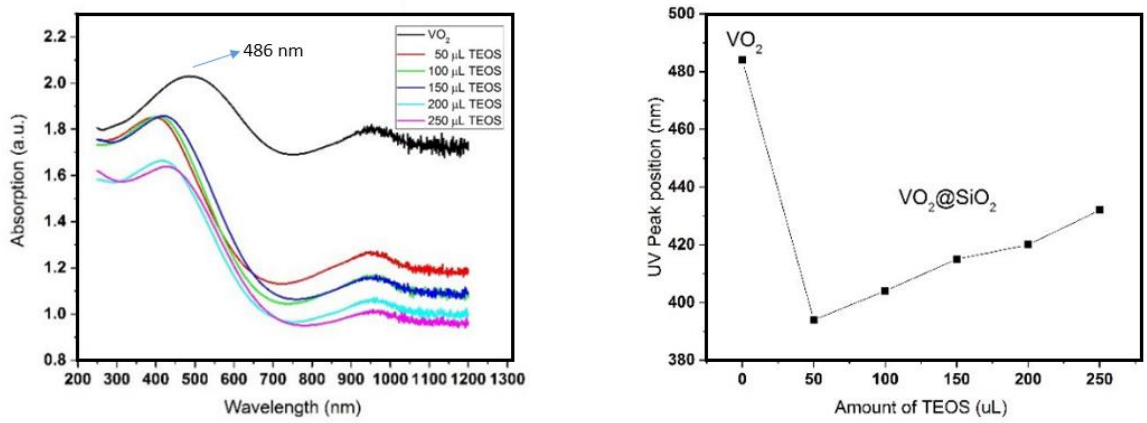

Figure 54 UV-Vis absorption of VO_2@SiO_2 core-shell nanoparticles, and its maximum absorption position.

Similar results have been seen in the gold-coated Fe_2O_3 nanoparticles[185]. Dani et al. have tried to synthesize the Au@Fe_2O_3 core-shell nanoparticles and the UV absorbance position was changed with different gold shell thickness. The UV absorbance position can be increased from 532 nm to 606nm by thicker gold shell Quantum dots also have a similar phenomenon, Dabbousi et al. have tried to synthesize (CdSe) ZnS core-shell quantum dots[186]. With different diameters (23 Å to 55 Å) the absorption are broader and have a red-shift.

Therefore, the VO_2@SiO_2 may have a similar phenomenon with these core-shell structures. It means the VO_2@SiO_2 core-shell nanoparticles are synthesized successfully.

4.2.2 SEM images of the VO_2@SiO_2 core-shell particles

Besides the optical property, the dispersity and morphology were also tested by the scanning electron microscope (SEM). The SEM images of VO_2 and VO_2@SiO_2 particles are measured in different magnification as follow. (Fig.55-Fig.60)

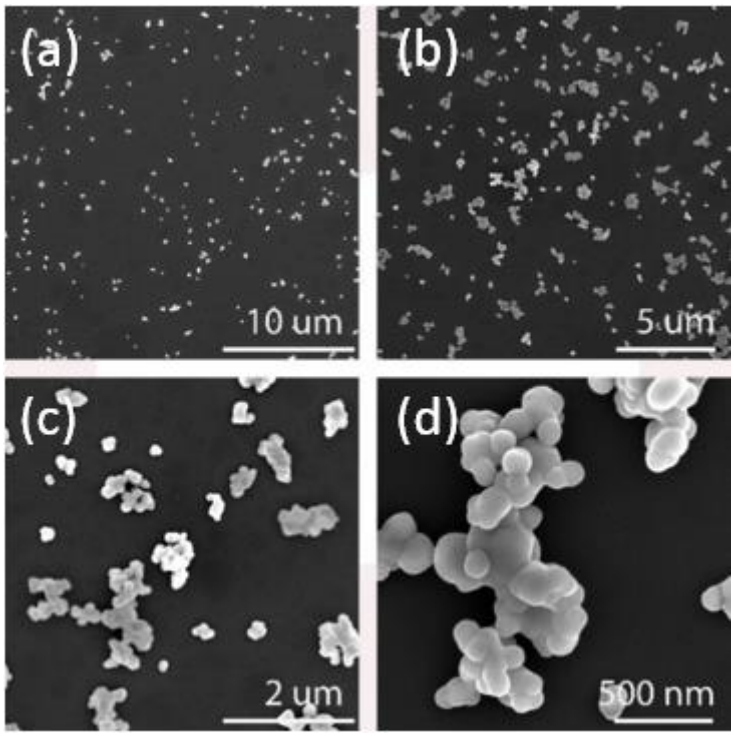

Figure 55 Different magnification SEM images of VO_2 nanoparticles

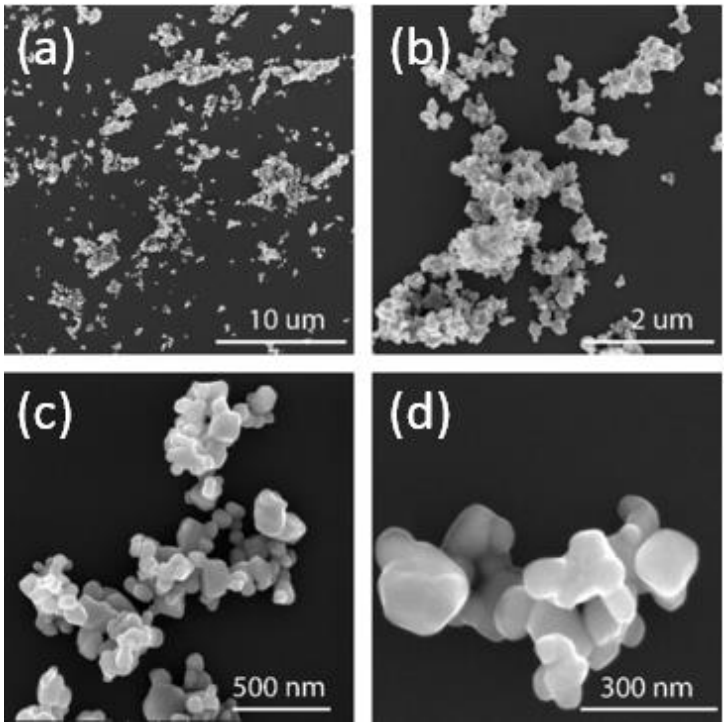

Figure 56 Different magnification SEM images of VO_2@SiO_2 core-shell nanoparticles synthesized with 50 µL TEOS

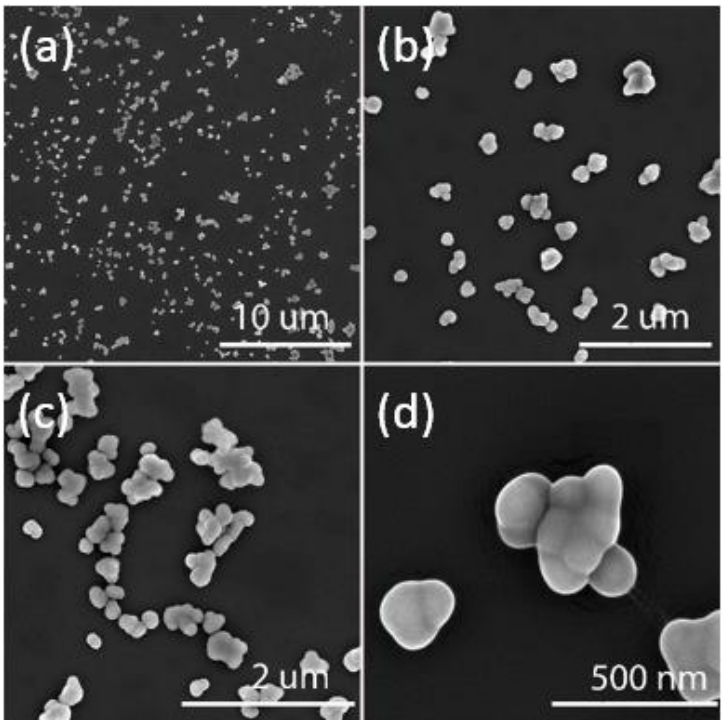

Figure 57 Different magnification SEM images of VO_2@SiO_2 core-shell nanoparticles synthesized with 100 µL TEOS

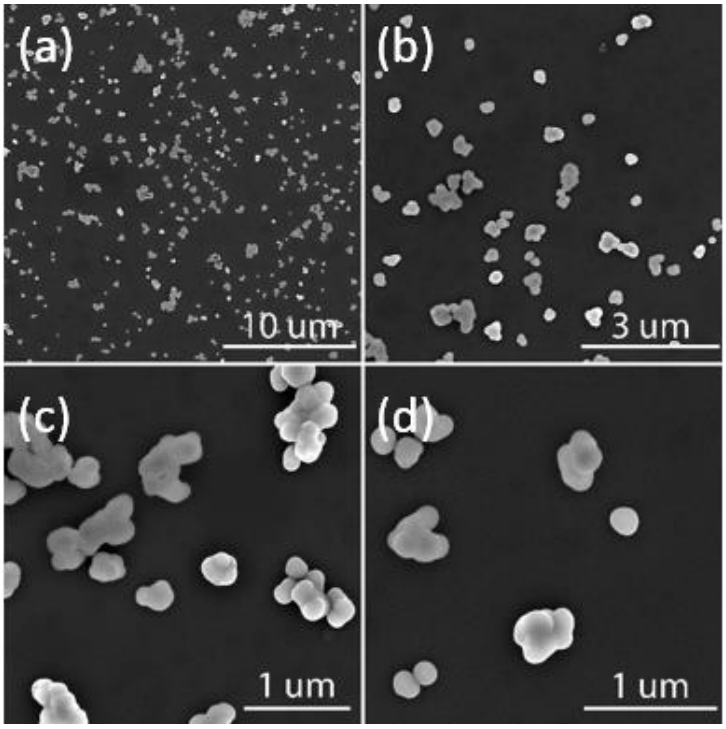

Figure 58 Different magnification SEM images of VO_2@SiO_2 core-shell nanoparticles synthesized with 150 µL TEOS

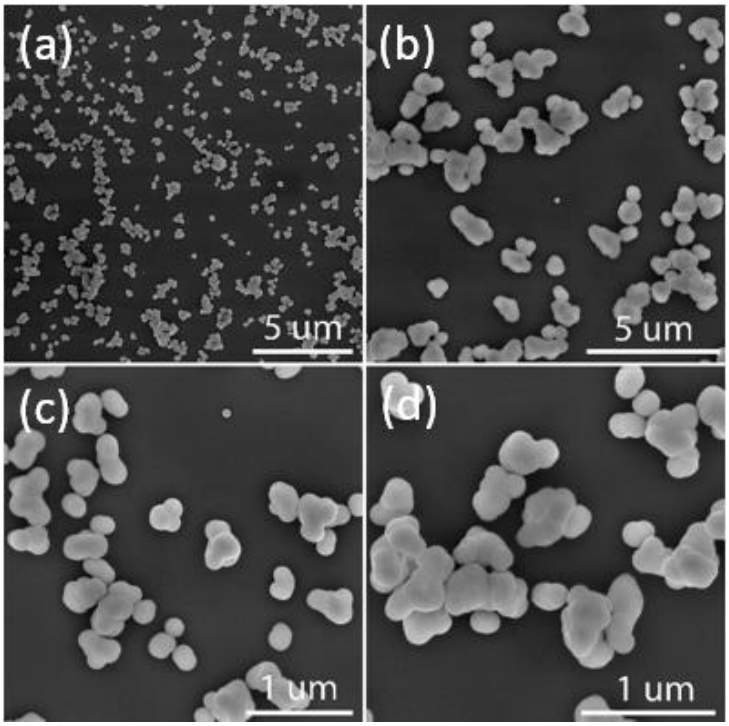

Figure 59 Different magnification SEM images of VO_2@SiO_2 core-shell nanoparticles synthesized with 200 µL TEOS

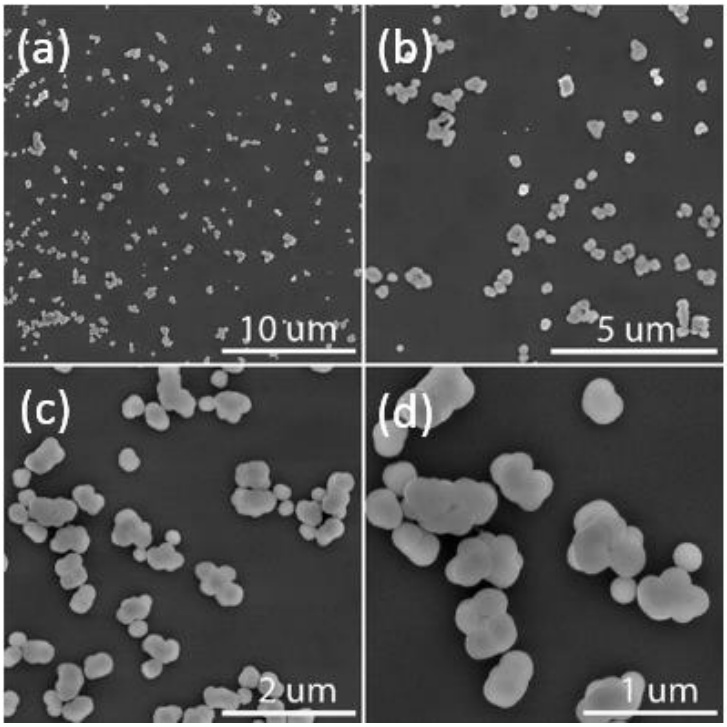

Figure 60 Different magnification SEM images of VO_2@SiO_2 core-shell nanoparticles synthesized with 250 µL TEOS

As we can see from the above SEM images, the dispersity of the VO_2 and VO_2@SiO_2 core-shell nanoparticles were all uniform. With different amount of TEOS, the morphology of the VO_2@SiO_2 core-shell nanoparticles was a little bit different. When the amount of TEOS was 50 µL, the morphology was better than the pure VO_2 nanoparticles. Moreover, with the increase of the TEOS amount, the appearance of the core-shell nanoparticles was smoother, and the dispersity of the particles is better. And the size of the particles was also increased with the addition of TEOS solution. The average diameter was increased from 50 nm to 200 nm.

Wang[110] et al also tried to synthesize a similar structure of the core-shell particles. However, their surface morphology was not as good as our results. For their results, most of the particles were column-like, sharp and smaller than 100 nm. For our results, the particles also have a smooth surface and uniform size distribution.

4.2.3 TEM images of the VO_2@SiO_2 core-shell particles and shell thickness distribution

Except the SEM, a transmission electron microscope (TEM) was used to test the core-shell structure. The nanoparticles were also measured in different amplification to check the overall and local morphology The TEM images of pure VO_2 nanoparticles and VO_2@SiO_2 synthesized by different amount of TEOS were shown in the following images.

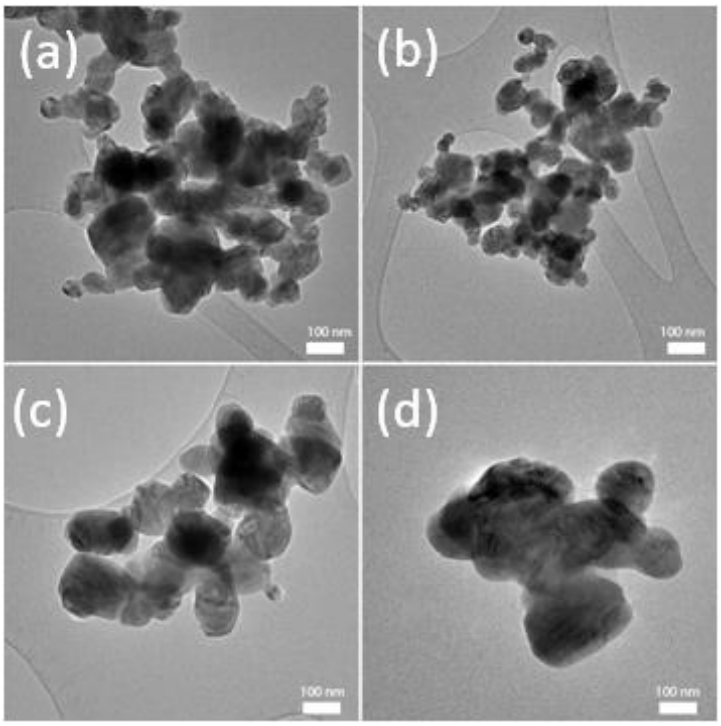

Figure 61 Different magnification TEM images of VO_2 nanoparticles

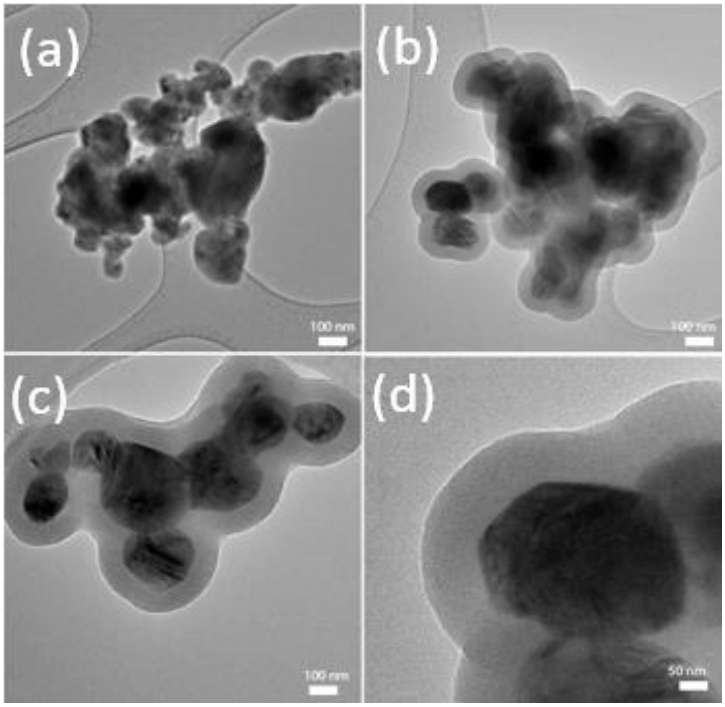

Figure 62 Different magnification TEM images of VO_2@SiO_2 core-shell nanoparticles synthesized with 50 µL TEOS

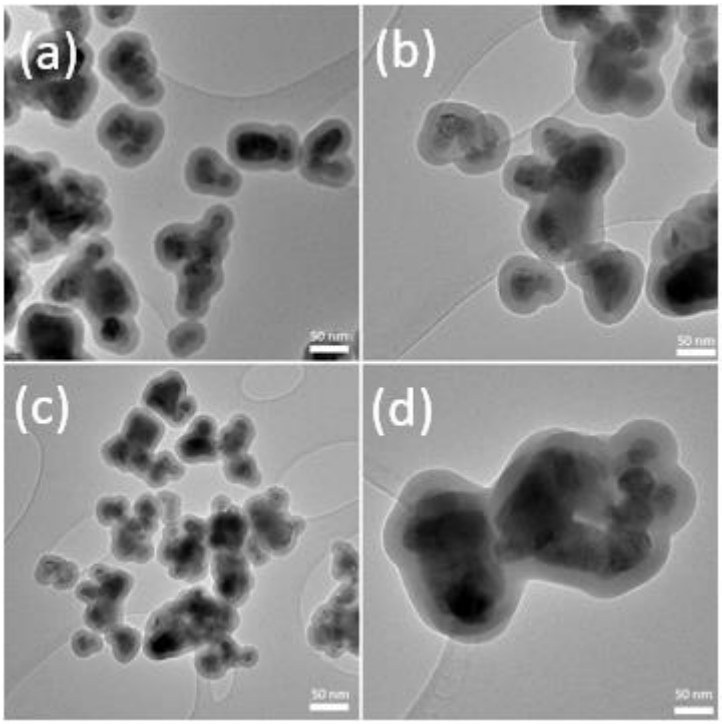

Figure 63 Different magnification TEM images of VO_2@SiO_2 core-shell nanoparticles synthesized with 100 µL TEOS

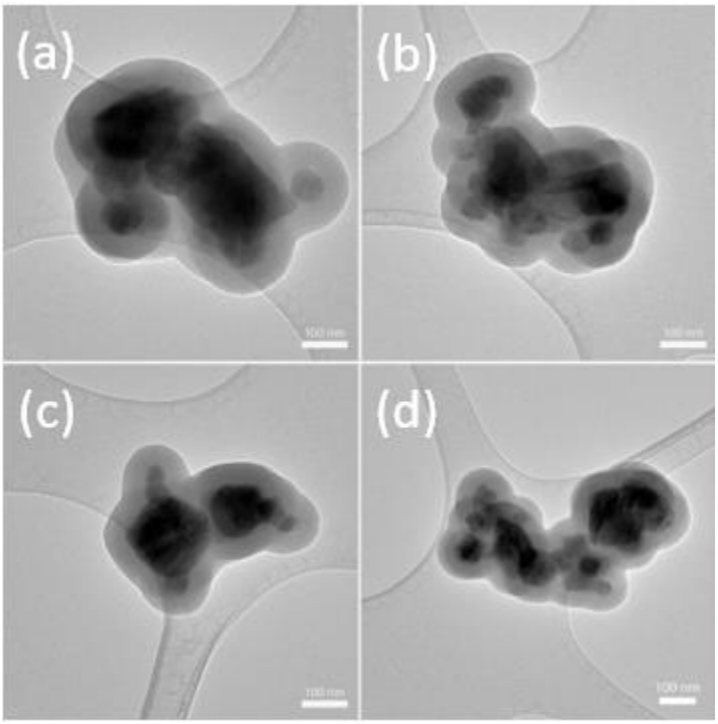

Figure 64 Different magnification TEM images of VO_2@SiO_2 core-shell nanoparticles synthesized with 150 µL TEOS

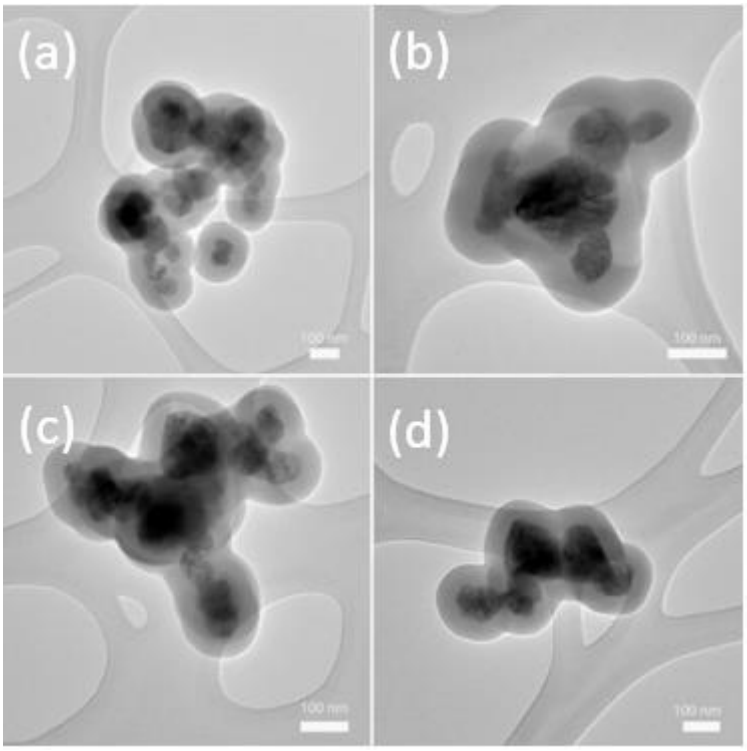

Figure 65 Different magnification TEM images of VO_2@SiO_2 core-shell nanoparticles synthesized with 200 µL TEOS

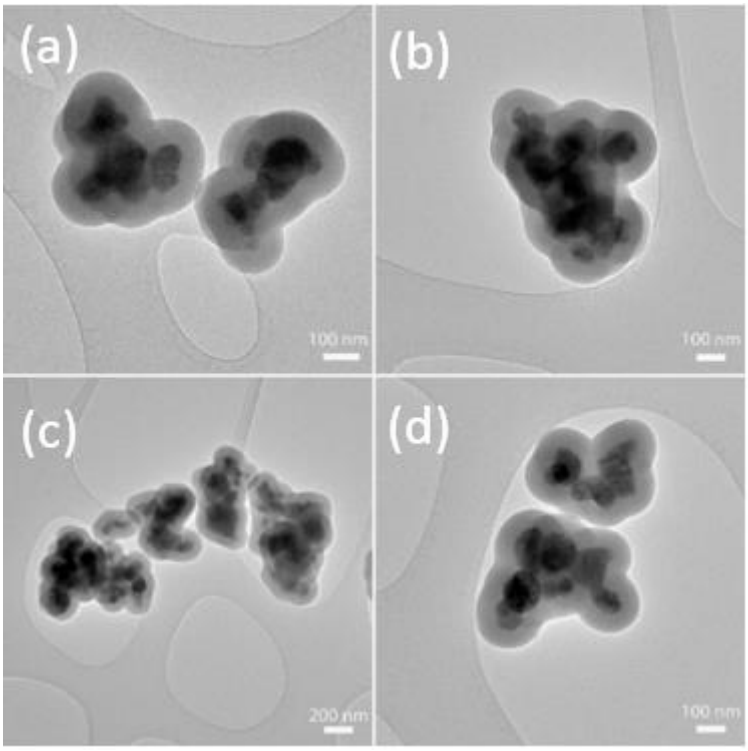

Figure 66 Different magnification TEM images of VO_2@SiO_2 core-shell nanoparticles synthesized with 250 µL TEOS

As the above images shown, a clear core-shell structure can be seen when TEOS was applied to form the core-shell structure. From Fig.60 to Fig.65, the shell structures are all well formed with the increase amount of TEOS (50 µL to 250 µL). The thickness of the shell structure was also measured and calculated to explore the relationship between the usage of TEOS and the thickness of the SiO_2 shell.

Lu et al.[187] have synthesized VO_2@SiO_2@Au core-shell nanoparticles. They also indicated that the SiO_2 layer can significantly improve the anti-oxidation ability. In their case, the VO_2@SiO_2 particles tend to become rod-like particles with average size of about 187.6nm. However, in our case, the size can be smaller than 100 nm by adjusting the amount of TEOS. Moreover, the thickness silica shell is between 10-30 nm, which is also similar and good enough. And in our case, the silica shell be thinner than 10 nm with a small amount of TEOS.

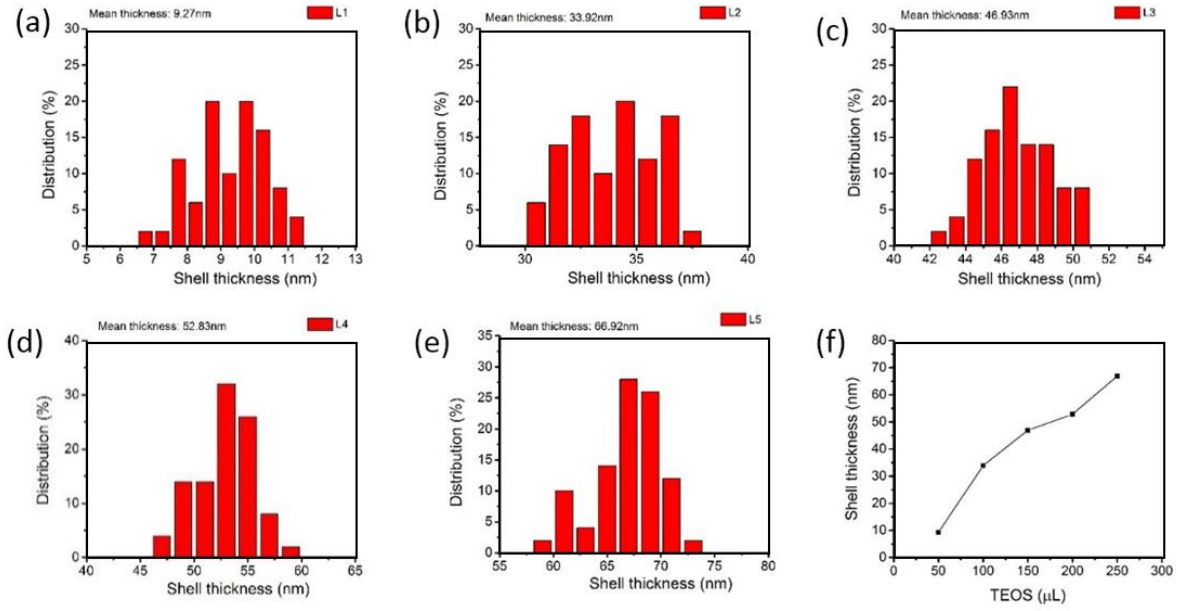

Figure 67 Shell thickness distribution of VO_2@SiO_2 nanoparticles with different amount of TEOS, (a) 50 µL TEOS (b) 100 µL TEOS, (c) 150 µL TEOS, (d) 200 µL TEOS, (e) 250 µL TEOS and (f) increase trend of the shell thickness.

Fig 67 shows the SiO_2 shell thickness of the core-shell nanoparticles. The thickness are 9.3 nm, 33.9 nm, 46.9 nm, 52.8nm ,66.9nm when the amount of TEOS were increased from 50 µL to 250 µL. Therefore, the thickness of the SiO_2 can be adjusted through applying different amount of TEOS. That is a meaningful result for the application in the industry. With the increase of the TEOS, the average shell

thickness was also increased. With the thicker SiO_2 shell, the VO_2 nanoparticles may get a better thermochromic or resistance performance.

4.2.4 Results analysis

In this section, the VO_2@SiO_2 core-shell nanoparticles were synthesized through stöber method. And this experiment mainly focuses on the effect of TEOS concentration in the synthetic process. The amount of VO_2 was kept as 0.02g in the core-shell particles synthesis. And the relative experimental materials were also kept stable. The experiment was performed by only changing the amount of TEOS from 0 to 250 µL.

Gao et al. have synthesized plate-like VO_2(M)@SiO_2 core-shell nanoparticles for smart window application[188].In that research, the oxalic acid was used as a reduced agent, and a hydrothermal method was also used to synthesize the VO_2 (B) nanoparticles. Then the VO_2 (B) was coated with SiO_2 shell and the core-shell structure was heated to get the final VO_2 (M) @SiO_2 core-shell nanoparticles.

However, in my research, hydrazine solution was used as a reduced agent, therefore the morphology of the VO_2 nanoparticles' shape was round rather than plate-like. Moreover, more uniform VO_2@SiO_2 core-shell nanoparticles can be obtained.

Based on the SEM images, the morphology of the VO_2 and VO_2@SiO_2 core-shell nanoparticles were all well-dispersed and near round. According to the TEM images, clear core-shell structure can be seen in the images, and with the increase of the TEOS amount, the shell thickness can be increased. By measure and calculation of the shell thickness, it is increased from 9 nm to 67 nm. Therefore, the amount of TEOS plays an important role in synthesizing the SiO_2 shell for the VO_2@SiO_2 core-shell nanoparticles.

4.3 Effect of reaction time

In the last session, it was found that the amount of TEOS can affect the SiO_2 shell thickness in the synthesis process. Except the amount of TEOS, other variables were also checked. The reaction time is one of them. After the TEOS was added, the hydrolysis reaction will happen and the hydrolysis reaction time should be very dramatic for the thickness of the VO_2@SiO_2 core-shell nanoparticles. The synthesis was performed using same method, however, the reaction time was altered from zero minute to two hours (Table 5).

	Ethanol (mL)	**Water (mL)**	**$NH_3.H_2O$ (mL)**	**VO_2 (g)**	**TEOS (μL)**	**Reaction Time (min)**
T1	50	10	1	0.02	100	0
T2	50	10	1	0.02	100	10
T3	50	10	1	0.02	100	20
T4	50	10	1	0.02	100	30
T5	50	10	1	0.02	100	60
T6	50	10	1	0.02	100	120

Table 5 Experimental parameters for VO_2@SiO_2 core-shell nanoparticles with different reaction time from 0 minutes to two hours.

4.3.1 SEM images of VO_2@SiO_2 core-shell nanoparticles with different reaction time

Similar with the previous study, the morphology of the samples (T1-T6) was measured by the scanning electron microscope (SEM). They also show a good morphology and dispersity (Fig.68-Fig.73).

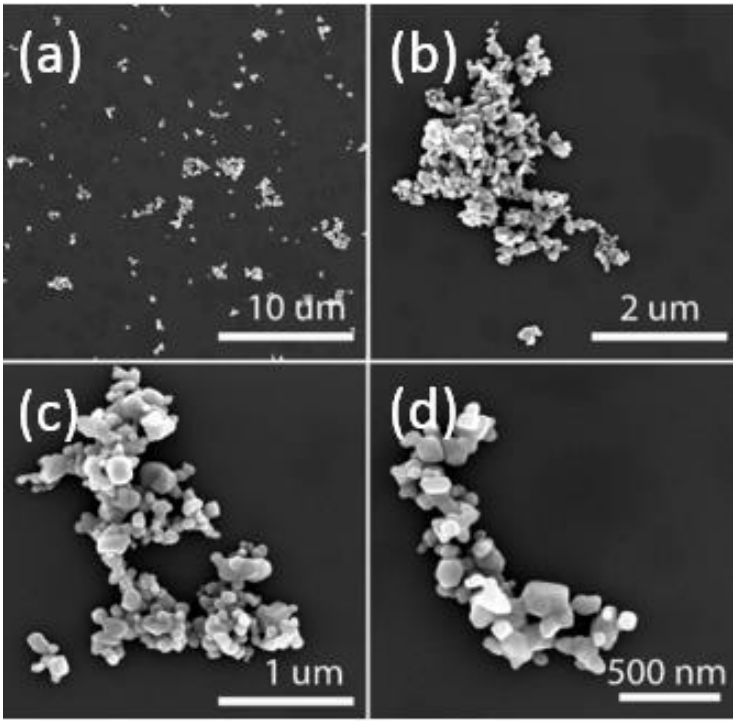

Figure 68 Different magnification SEM images of VO_2@SiO_2 core-shell nanoparticles with 0 minute reaction time

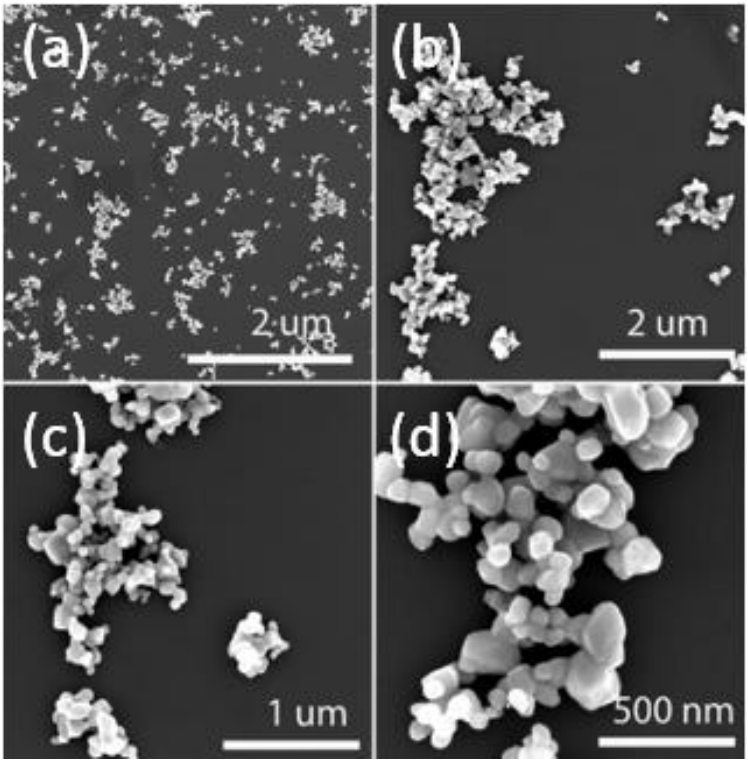

Figure 69 Different magnification SEM images of VO_2@SiO_2 core shell nanoparticles with 10 minute reaction time

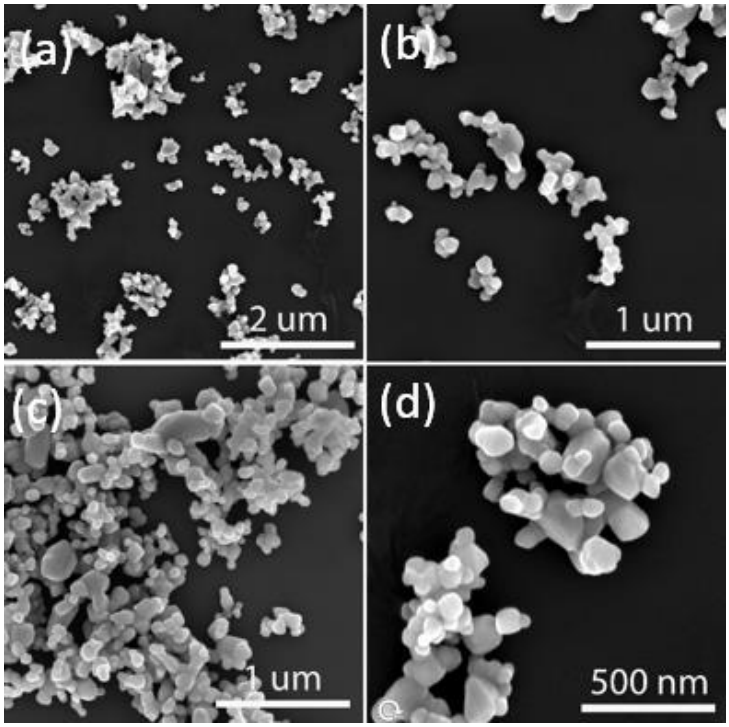

Figure 70 Different magnification SEM images of VO_2@SiO_2 core shell nanoparticles with 20 minute reaction time

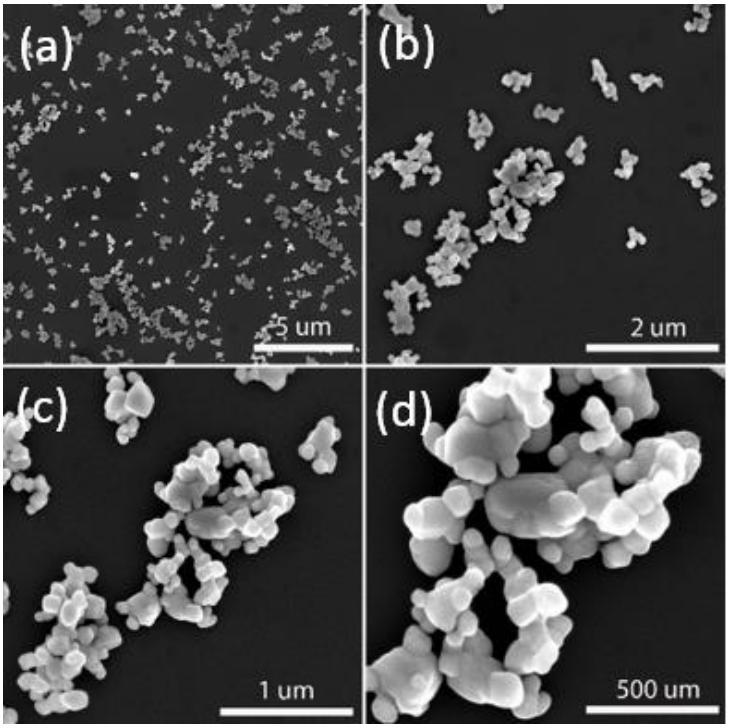

Figure 71 Different magnification SEM images of VO_2@SiO_2 core shell nanoparticles with 30 minute reaction time

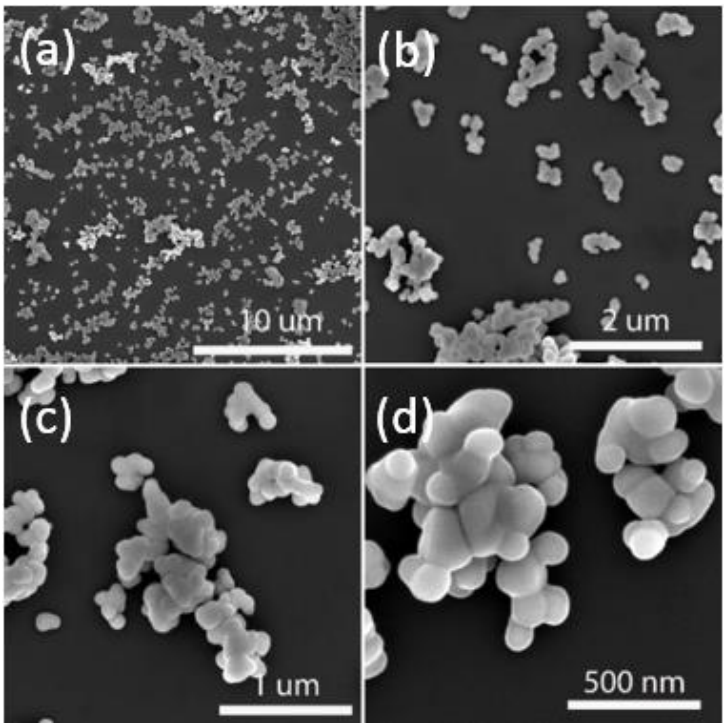

Figure 72 Different magnification SEM images of VO_2@SiO_2 core shell nanoparticles with one hour reaction time

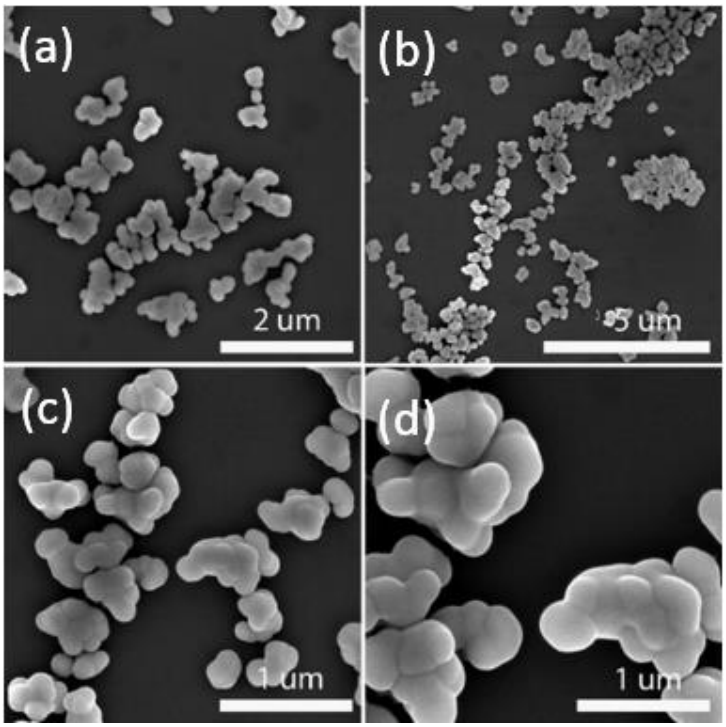

Figure 73 Different magnification SEM images of VO_2@SiO_2 core shell nanoparticles with two hours reaction time

For the SEM images of VO_2@SiO_2 core-shell nanoparticles synthesized with different reaction time, much difference about the dispersity of VO_2 and VO_2@SiO_2 core-shell nanoparticles can be seen. By increasing the amount of reaction time, the surface of the core-shell nanoparticles was smoother, and the dispersity of the particles is better. And the size of the particles was also increased with the extension of reaction time. The average diameter was increased from 50 nm to 300 nm.

4.3.2 TEM images and shell thickness distribution

A transmission electron microscope (TEM) was used to test the core-shell structure. The nanoparticles were also measured in different amplification to check the overall and local morphology

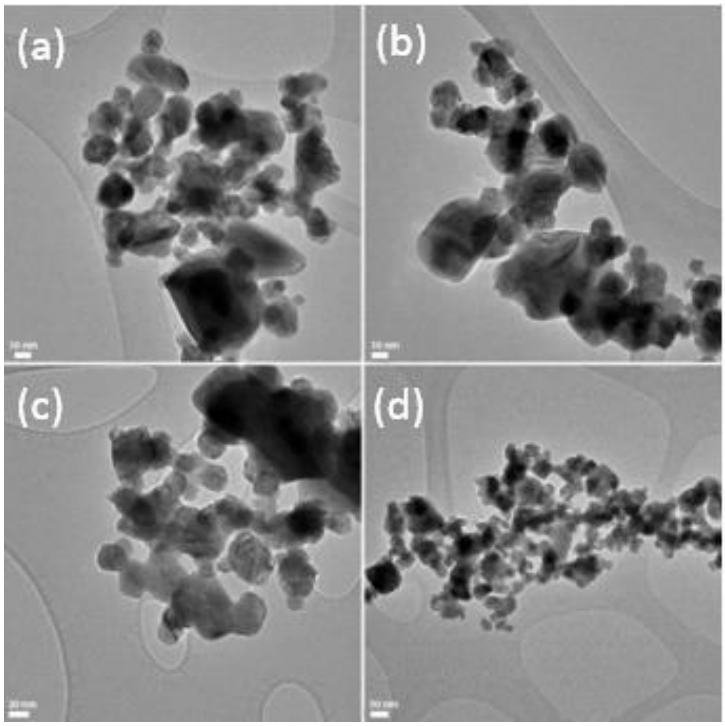

Figure 74 Different magnification TEM images of VO_2@SiO_2 core shell nanoparticles with 0 min reaction time

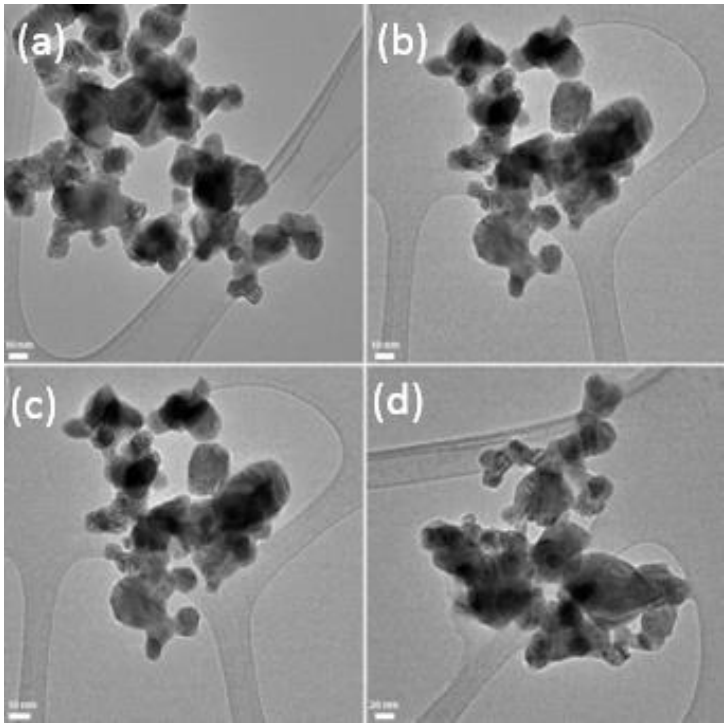

Figure 75 Different magnification TEM images of VO_2@SiO_2 core-shell nanoparticles with 10 mins reaction time

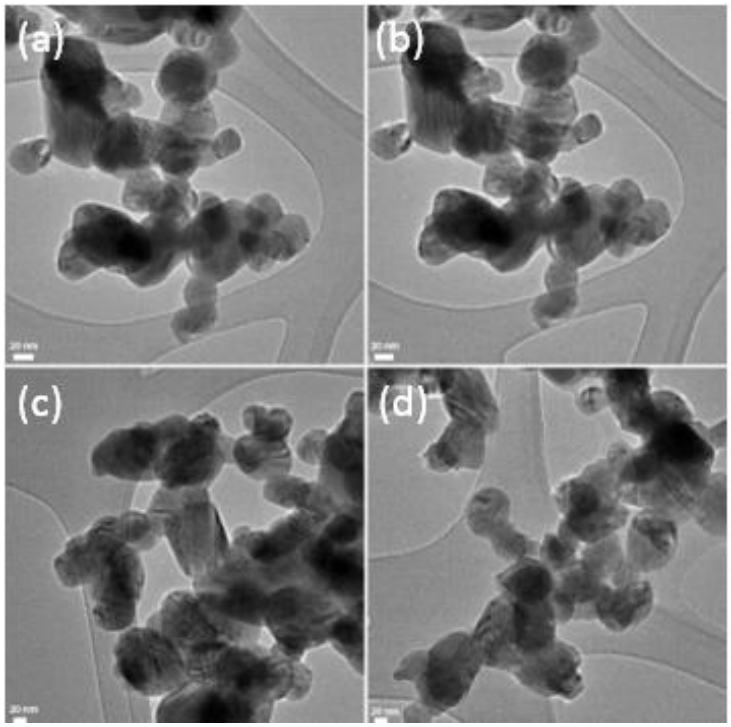

Figure 76 Different magnification TEM images of VO_2@SiO_2 core-shell nanoparticles with 20 mins reaction time

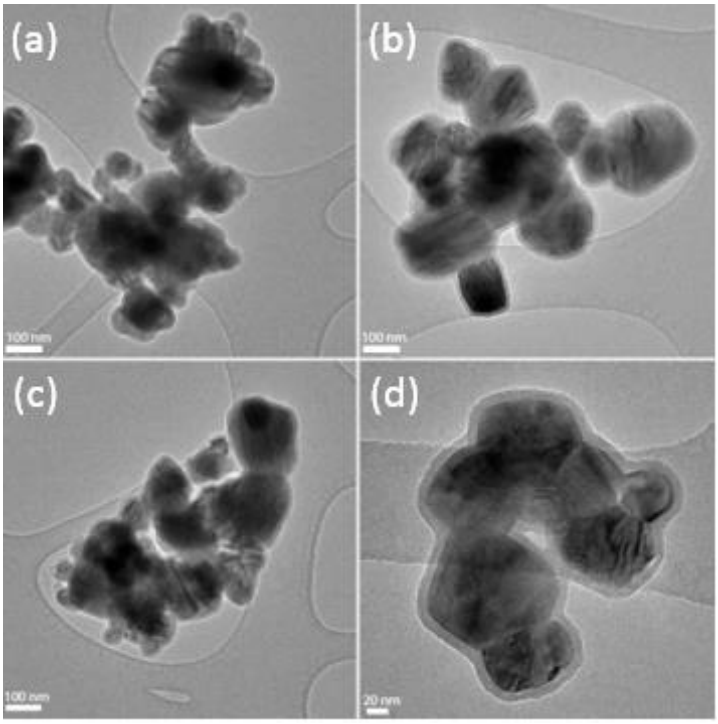

Figure 77 Different magnification TEM images of VO_2@SiO_2 core-shell nanoparticles with 30 mins reaction time

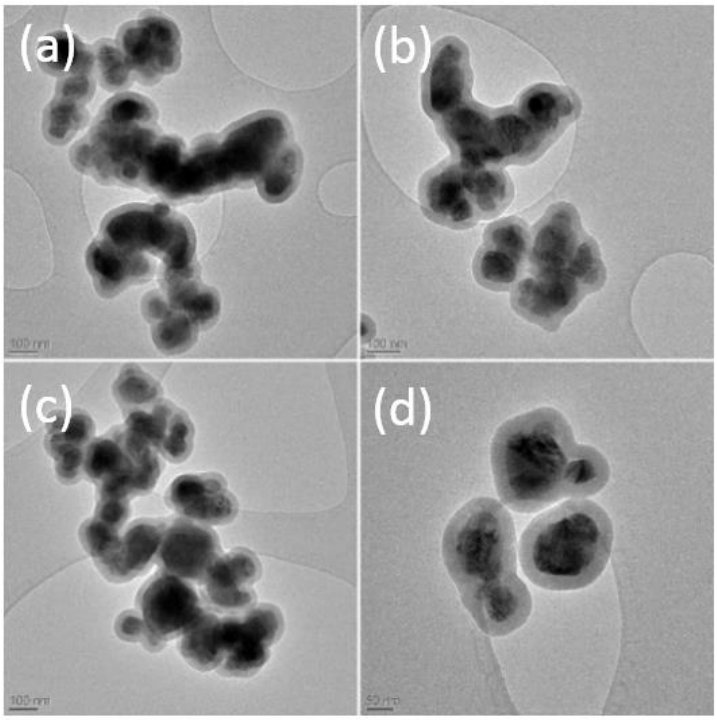

Figure 78 Different magnification TEM images of VO_2@SiO_2 core shell nanoparticles with 1 hour reaction time

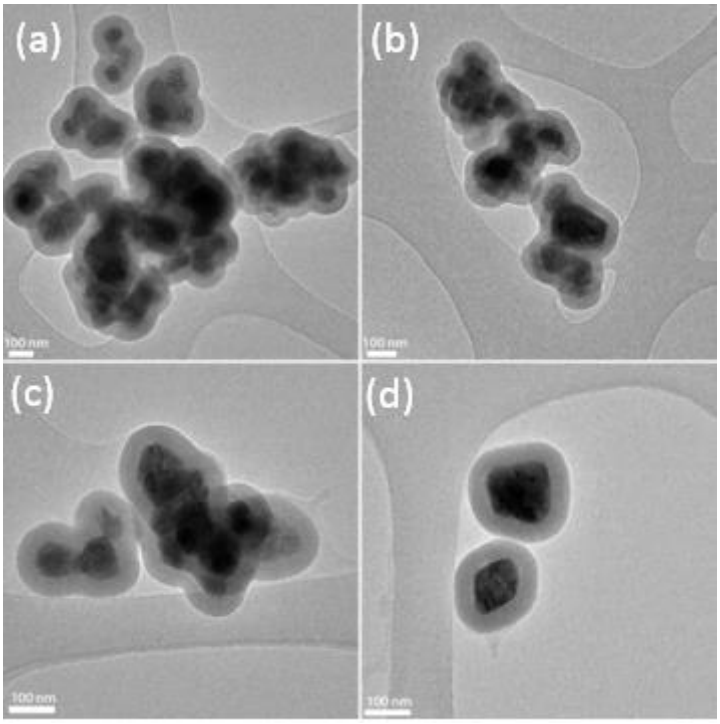

Figure 79 Different magnification TEM images of VO_2@SiO_2 core shell nanoparticles with 2 hours reaction time

Similar to the amount of TEOS, the reaction time can also regulate and control the SiO_2 shell thickness. In order to explore the relationship between the thickness of SiO_2 shell and reaction time, the shell thickness was measured and calculated. Because T1 and T2's shell is so thin that it is difficult to measure the thickness. Only T3-T6 were measured as following (Fig 80):

From Fig.73 to Fig.75, the shell structure is not so clear. It means that clear core-shell structure cannot be synthesized if the reaction time is less than 30 minutes. With the increase of reaction time, the shell thickness of the VO_2@SiO_2 was increased from 3.2nm to 42.8nm. They are 3.2nm, 8.7nm, 24.9nm and 42.8 nm when the reaction time was increased from 20 minutes to two hours.

Therefore, SiO_2 coating reaction time can also increase the thickness of the SiO_2 shell.

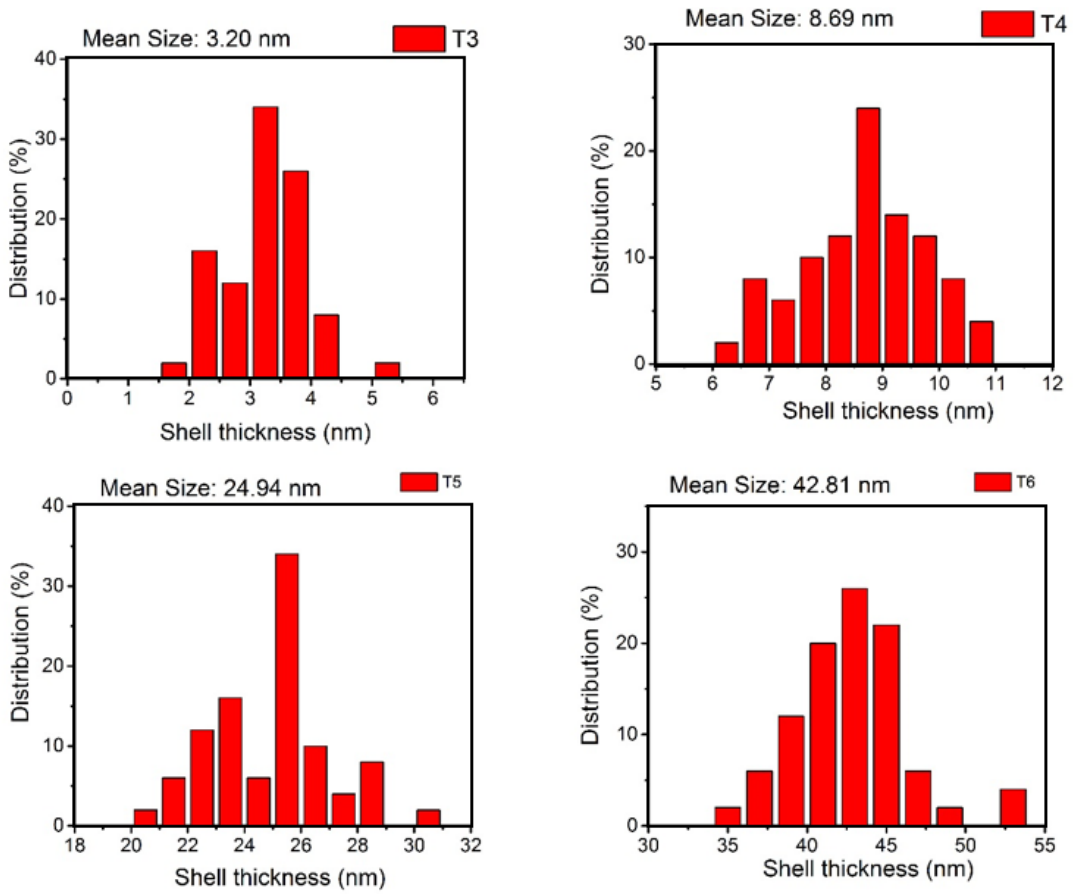

Figure 80 Shell thickness statistical distribution, (T3) 20 mins, (T4) 30 mins, (T5)1 h and (T6)2 h reaction time.

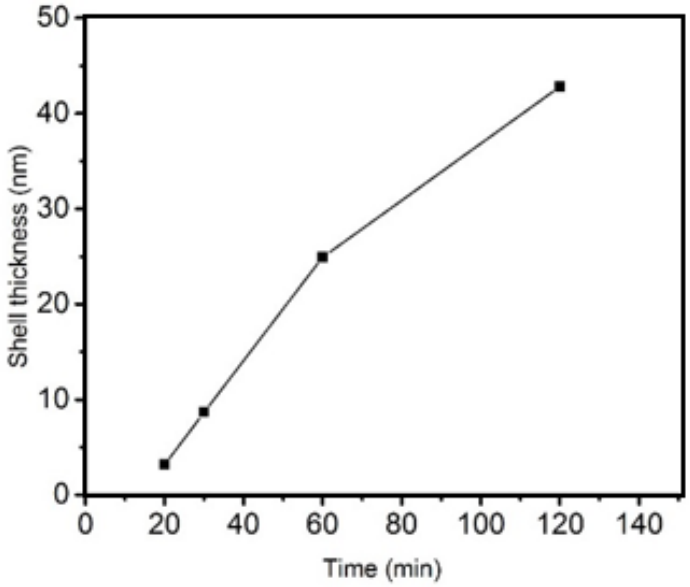

Figure 81 Shell thickness of VO_2@SiO_2 with different reaction time.

4.3.3 Results analysis

Except the amount of TEOS, the reaction time in the SiO_2 coating was also studied in this section.

From the SEM images, the morphology of the core-shell particles were in good condition with the change of the SiO_2 coating time. Based on the TEM images, the SiO_2 shell thickness can be increased up to around 43 nm when the hydrolysis reaction time was extended to 2 hours. However, the thickness will only be 3 nm when the reaction time was 20 minutes with same other experimental parameters. And it was also found that, if the hydrolysis was too short (less than 20 minutes), no shell structure can be seen in the TEM images, which means that the reaction needs some time to form a solid SiO_2 shell.

4.4 Stability performance

As we all know, VO_2 is not stable in moisture air atmosphere. It can be oxidized to other vanadium oxide. VO_2@SiO_2 core-shell particles can be a good method to protect the VO_2. In the following research, how the VO_2@SiO_2 structure can protect the VO_2 were tested.

4.4.1 Stability performance in acid/alkali environment

Firstly, with the development of the society, the acid rain problem has been a significant problem as the increase of the emission of greenhouse gas. It can inevitably affect the building window, therefore, the acid assistance of the VO_2@SiO_2 core-shell nanoparticles were tested. Various concentration of hydrochloric acid (HCl) solution and sodium hydroxide (NaOH) solution were used as the corrosion solution to accelerate the corrosion process. The details of the experiment can be seen in the following table.

	Ethanol (mL)	Water (mL)	$NH_3.H_2O$ (mL)	VO_2 (g)	TEOS (uL)	SiO_2 shell thickness (nm)
L0	50	10	1	0.02	0	0
L1	50	10	1	0.02	50	9.3
L2	50	10	1	0.02	100	33.9
L3	50	10	1	0.02	150	46.9
L4	50	10	1	0.02	200	52.8
L5	50	10	1	0.02	250	66.9

Table 6 Different pH value of HCl and NaOH solution used to corrode the VO_2@SiO_2 nanoparticles synthesized by different concentration of TEOS.

In this experiment, the VO_2@SiO_2 core-shell nanoparticles with different thickness of SiO_2 shell were used to test the function of SiO_2 shell in protecting the particles against acid and alkali corrosion.

The VO_2 and VO_2@SiO_2 core-shell nanoparticles were dispersed into the acid or alkali solution. Then the solution was used to check the UV-Vis absorbance every one hour. If the material is stable in the solution, its UV-Vis spectrum will be similar. If it can be affected by the acid or alkali solution, the UV-Vis light absorbance will be changed.

As we can see from Fig. 82, when the pH is less than 5, all the samples (VO_2 and VO_2@SiO_2 nanoparticles) can be affected by the acid solution. Their UV absorption will be decreased with longer treatment time. Both the VO_2 nanoparticles and VO_2@SiO_2 core-shell nanoparticles have a decrease of UV light absorption with the strong acid treatment.

When the pH is between 9 and 11, the UV absorption performance is not affected dramatically, which means the VO_2 and VO_2@SiO_2 core-shell nanoparticles are relatively stable in the alkali environment.

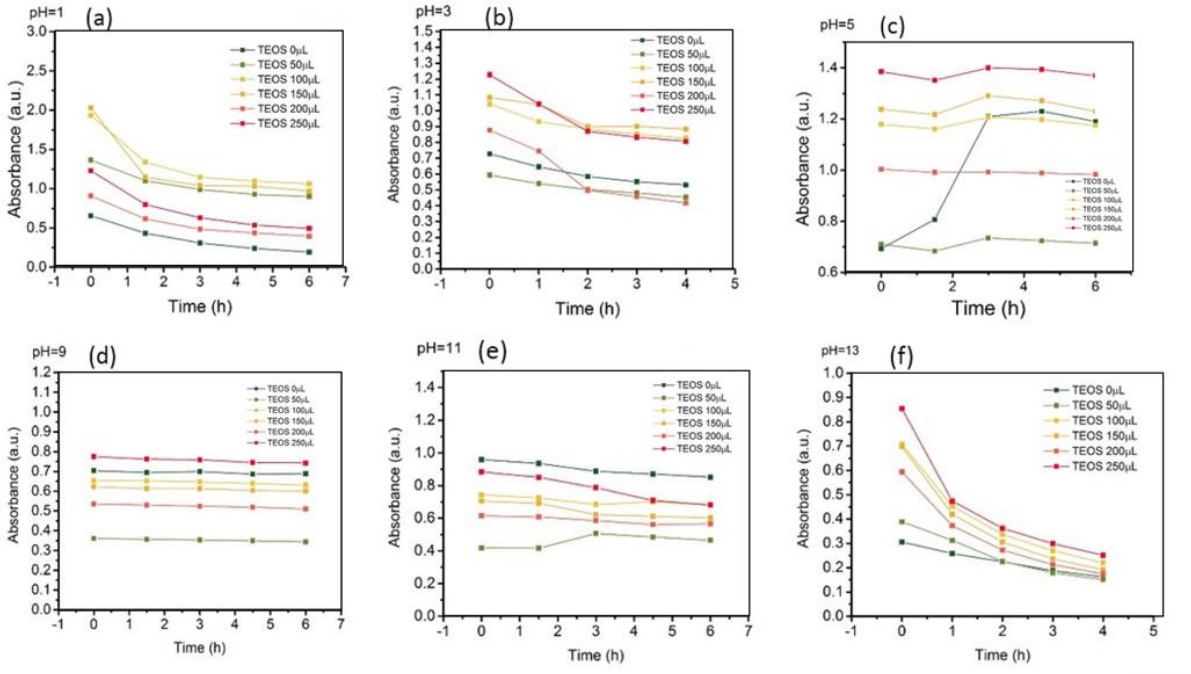

Figure 82 UV absorbance of the VO_2@SiO_2 core-shell nanoparticles after mixing with different pH value solutions. (a) pH=1 (b) pH=3, (c) pH=5, (d) pH=9, (e) pH=11, (f) pH=13

As we all know, the pH of acid rain is around 5.2, therefore the performance of VO_2@SiO_2 core-shell particles at pH 5 is more valuable. As we can see, when pH=5, the UV absorption of VO_2 nanoparticles was affected dramatically, while the core-shell structure was stable, which means the core-shell nanoparticles can protect the VO_2. Therefore, the core-shell nanoparticles are very meaningful for the commercial use.

4.4.2 Stability performance in oxidation environment

Besides the corrosion of acid and alkali solution. The resistance to oxidation property is also tested in this research. H_2O_2 was used to evaluate the resistance to oxidation property of the VO_2@SiO_2 core-shell nanoparticles. VO_2@SiO_2 core-shell nanoparticles with different thickness of SiO_2 shell (L0, L1 and L5) were used to

study this. The solution contains nanoparticles was mixed with some H_2O_2 solution (Table 6), and the UV absorbance of the mixed solution was tested every ten minutes.

VO_2@SiO_2 core-shell nanoparticles	**SiO_2 thickness (nm)**
L0 (VO_2)	0
L1 (VO_2@SiO_2)	9.3
L5 (VO_2@SiO_2)	66.9

Table 7 Experimental details of VO_2@SiO_2 core-shell nanoparticles with oxidation assistance.

The principle of the reaction is similar with the acid or alkali resistance. If the nanoparticles are stable in the solution, as we can see from Fig 82, the UV absorbance of L0 is decreased immediately

When the H_2O_2 was added into it. The UV absorption spectrum was changed immediately. It means the strong oxidation agent can affect the UV absorption of VO_2 nanoparticles. VO_2 can be oxidized into high valance of vanadium oxide. However, the L1 and L5 have a better resistance to the oxidation of the H_2O_2 solution. It shows that the SiO_2 shell is helpful to protect the VO_2 nanoparticles from oxidizing. And the thicker SiO_2 shell has a better protecting performance.

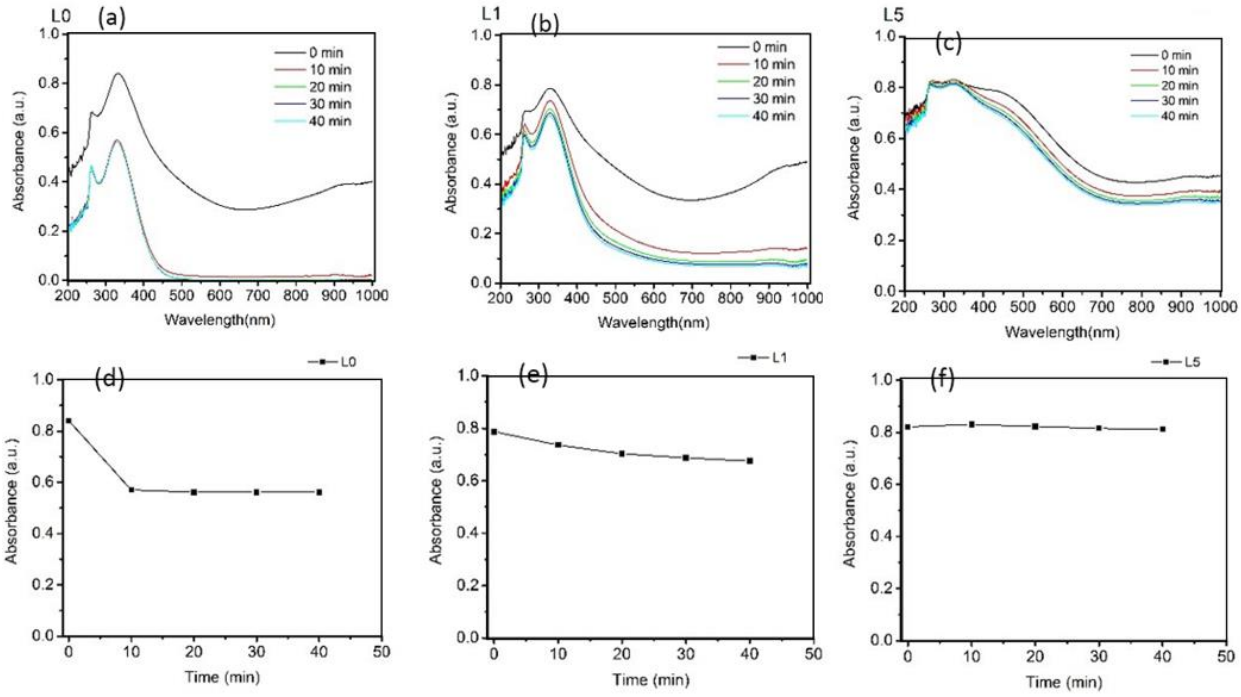

Figure 83 UV absorbance of VO_2@SiO_2 core-shell nanoparticles after oxidation reaction with H_2O_2. (a) VO_2 nanoparticles after oxidation and test the UV absorbance, (b) VO_2@SiO_2 core-shell nanoparticles with 9.27 nm shell thickness after oxidation and test

4.4.3 Stability performance in UV irritation

Moreover, UV light may also lead to the VO_2 to be oxidized to a higher oxidation state. Therefore, the resistance to UV property was also tested.

Sample L0 (VO_2) and L1 (VO_2@SiO_2) were used in this research. An appropriate amount of nanoparticles were exposed to the UV irradiation, then they were made into a dispersed solution and the UV absorbance was tested. The UV absorbance was recorded with the time going to check if the samples can bear long time UV light irritation.

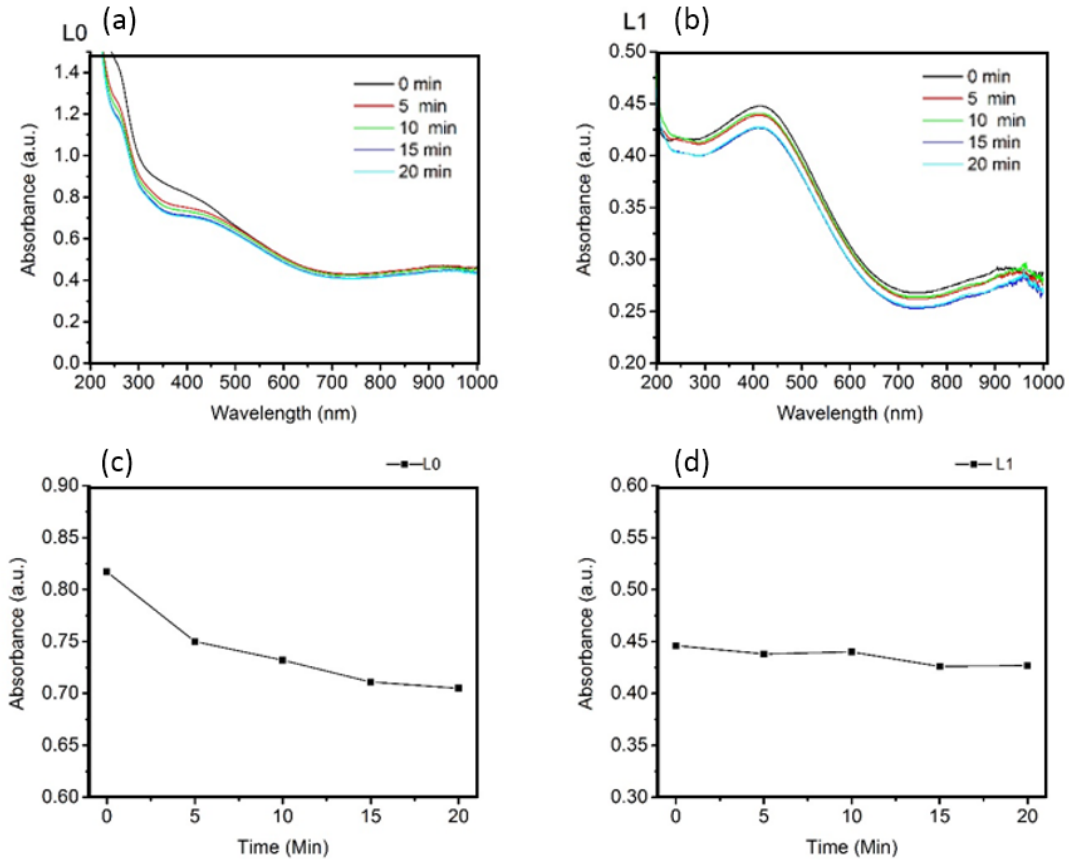

Figure 84 UV absorbance spectrum for the samples under the irradiation of UV light. (a). UV-Vis absorptions of VO2 nanoparticles with different time, (b). UV-Vis absorptions of VO_2@SiO_2 nanoparticles with different time, (c). UV absorption value of (a) at 400 nm. (d) UV absorption value of (b) at 400 nm.

As we can see from Fig.84, the UV absorbance of VO_2 (L0) was decreased quickly with the irritation to the UV light. However, for the VO_2@SiO_2 core-shell nanoparticles, the absorbance decrease speed is less than the VO_2.It remains stable with the long time UV irradiation. Therefore, the VO_2@SiO_2 structure was valid for the protection from the UV light.

4.5 Thermochromic property

Similar with the VO_2 nanoparticles, the optical property of VO_2@SiO_2 core-shell nanoparticles is also tested to check if the SiO_2 can improve the thermochromic property of the samples. As we can see from Fig. 85, the transmittance spectra of the samples is similar to each other in high and low temperature. Moreover, there is not significant difference even though the TEOS is increased from 10 µL to 200 µL.

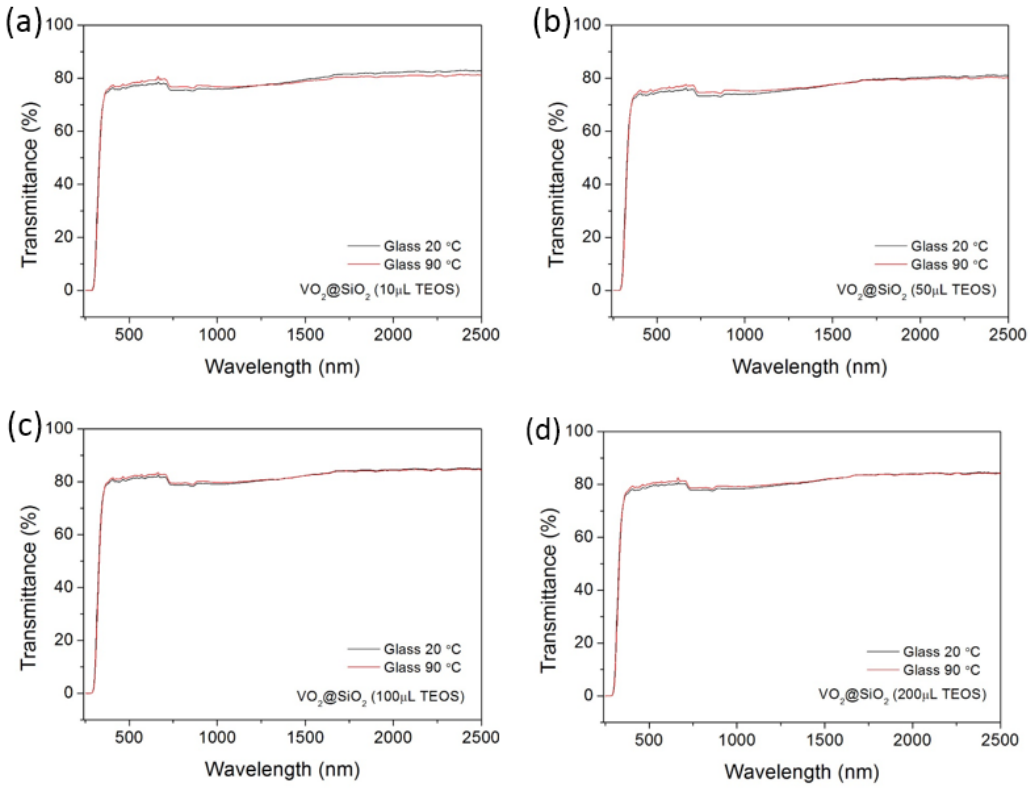

Figure 85 Transmittance spectra of VO_2@SiO_2 core-shell nanoparticles with different amount of TEOS in 20 °C and 90 °C respectively. (a)10µL TEOS, (b) 50 µL TEOS, (c) 100 µL TEOS and (d) 200 µL TEOS

Theoretically, the transmittance in high temperature should be much lower than the transmittance in low temperature, especially in NIR region. There are many reasons for the weak thermochromic property of the VO_2 films. Firstly, the thickness of the VO_2 film can affect the thermochromic property. The VO_2 films cannot exhibit an

outstanding optical property if the VO_2 film is too thick. Secondly, the size distribution can also influent the optical properties dramatically. The VO_2 films can show a good optical property only with a uniform film. The preparation of VO_2 film may affect the final optical property, which seems that there is not good thermochromic property. More work should be done to increase the film quality.

4.6 Summary

In this chapter, the VO_2@SiO_2 core-shell nanoparticles were synthesized through a stöber method. From the TEM images, a transparent SiO_2 shell structure was successfully grown on the surface of the inner VO_2 core.

Then, some experimental parameters was studied to check their effects. The amount of TEOS is firstly checked. The VO_2 nanoparticles were maintain the same amount and the TEOS was increased from 50 µL to 250 µL. SEM and TEM images were taken to test the morphology and the SiO_2 shell structure of the core-shell nanoparticles. By adjusting the amount of TEOS, the core-shell nanoparticles have a more uniform morphology and better dispersity. Through measuring the thickness of the SiO_2 shell, it is increased from 9 nm to 67 nm.

Besides, the TEOS, the reaction is found another factor which can affect the final core-shell structure. The reaction time of the synthesis was increased from 10 minutes to 2 hours. Similar with the adjustment of TEOS amount, the increasing reaction time can also modify the particle morphology and enhance the dispersity. By the measurement of TEM images, the SiO_2 shell can be changed from several nanometers to about 43 nanometers with the increase of reaction time.

After the successful synthesis of VO_2@SiO_2 core-shell nanoparticles, the protection ability of the SiO_2 shell was studied. Based on the UV-Vis spectrum, with the protection of the SiO_2 shell structure, the VO_2 particles have a better stability to acid, alkali and oxidation environment. It also has a better stability for the UV light. And

with the thicker SiO_2 shell structure, the particle has a better chemically stable performance.

Aibin et al [189] have tried to synthesize the VO_2@SiO_2 core-shell structure. However, in their research the morphology is long nanobar structure. And they did not give so much preparation details for the synthesis. In my study, it is found that the amount of TEOS and reaction time can affect the final core-shell structure dramatically.

Chapter 5 Fabrication of VO_2@ZrO_2 nanostructures

5.1 Introduction

Zirconium dioxide (ZrO_2), also known as zirconia, is a white crystalline oxide of zirconium. The melting point and boiling point of it are 2715 ˚C and 4300 ˚C respectively. So it is a kind of thermally stable material. It is chemically stable and has high melting point, high conductive resistance, high refractive index and low thermal expansiveness. It is often used as a protective coating on other particles. Zirconia nanoparticles (ZrO_2 NPs) have attracted much attention in bio-analytical application due to their chemical inertness, lack of toxicity and affinity for the groups containing oxygen[190-191].

As ZrO_2 has a lot of brilliant properties. In this chapter, the VO_2@ZrO_2 core-shell structure was fabricated to check that if the VO_2@ZrO_2 core-shell has a better performance.

5.1.1 Materials and chemicals

Tetraethyl Orthosilicate (TEOS), Zirconium (IV) butoxide solution, ammonia water (wt.28%), ethanol (absolute) were purchased from Sigma-Aldrich Co. Australia and stored at room temperature. VO_2 (M) nanoparticles are synthesized by the previous experiment. Deionized (DI) pure water was acquired from the local purest water company. All reagents were used directly without any treatment.

5.1.2 Experimental mechanism

A sol-gel process was happened in the core-shell structure synthesis.

For the science of materials, the sol-gel method is defined as a method for producing solid materials from small molecules. Basically, this method is used for preparation of metal oxides, such as the SiO_2 and TiO_2. The process includes transfer of monomers into a colloidal solution (sol) which is the precursor for an integrated network (or gel) of either separated particles or network polymers. Usually, metal alkoxides, $M(OR)_4$ are very reactive and can react with water vigorously. It includes the hydrolysis and condensation process.

$$\text{Hydrolysis: } M(OR)n + nH_2O \rightarrow M(OH)_n + nROH$$

$$\text{Condensation: } M(OH)_n + M(OH)_n \rightarrow (OH)_{n-1}M\text{-}O\text{-}M\text{-}(OH)_{n-1} + H_2O$$

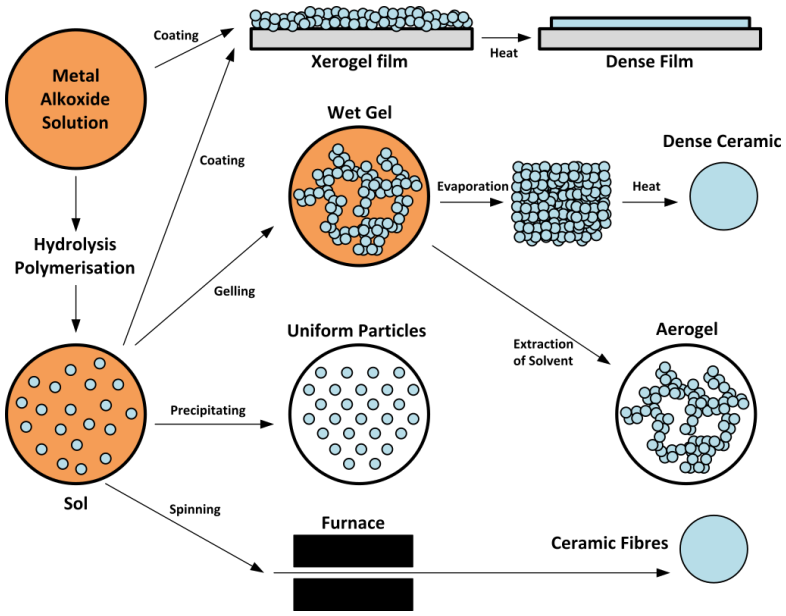

Figure 86 Schematic representation of the different stages and routes of the sol-gel technology, from Wikipedia

For the synthesis of VO_2@ZrO_2 core-shell structure, the Zirconium butoxide has been used to be the precursor for the sol-gel process. Then the ZrO_2 can be grown on the surface of VO_2 nanoparticles.

5.2 Fabrication of VO_2@ZrO_2 core-shell nanoparticles

Firstly, a relatively similar method as the synthesis of VO_2@SiO_2 was used to try to get the VO_2@ZrO_2 core-shell structure. The synthesis process is as follow:

- VO_2 nanoparticles were dispersed into ethanol.
- Then the mixture solution was ultrasonicated to get a better dispersion.
- At the same time, 50 µL Zr (IV) butoxide solution was dispersed into 10 mL ethanol to get the solution A.
- Different amount of solution A was added into the previous VO_2 solution. Polymer-surfactant hydroxypropyl cellulose (HPC) was also added to improve the results.
- DI water was added to conduct the hydrolysis reaction.
- Reaction time is about one hour.
- Then the obtained the core-shell particles were washed three times and dried in a 60 ˚C oven.
- The obtained VO_2@ZrO_2 nanoparticles were annealed at 500 ˚C to get a crystal structure.

In this study, the function of HPC and the effect of the amount of Zr was studied in this experiment. The experimental details can be seen in the following table:

	VO_2 (mg)	**HPC (mg)**	**Ethanol (mL)**	**H_2O (uL)**	**Solution A (mL)**
A	10	5	20	100	1
B	10	5	20	100	2
C	10	5	20	100	5
D	10	N/A	20	100	1
E	10	N/A	20	100	2
F	10	N/A	20	100	5

Table 8 Experimental parameters of synthesizing VO_2@ZrO_2 core-shell nanoparticles

5.2.1 UV absorption spectrum of VO_2@ZrO_2 core-shell nanoparticles

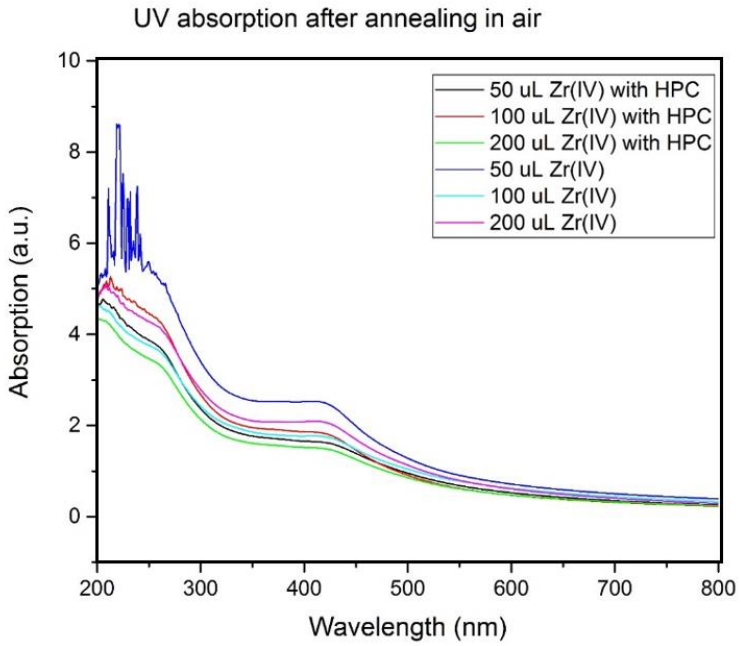

Figure 87 UV spectrum of VO_2@ZrO_2 core-shell nanoparticles with and without HPC

Firstly, the optical property of the samples were tested by the UV-Vis spectrum. As we can see from Fig.85, all of the samples have an absorption at around 430nm. And the amount of Zr (IV) butoxide solution and HPC cannot affect the absorption peak position. Meijun et al.[192] have tried to synthesize zirconia, including monoclinic ZrO_2 and tetragonal ZrO_2, they have a UV absorption at 230 nm and 210 nm respectively. However, in our case, the ZrO_2 absorption was not quite clear. The reason might be the amount of ZrO_2 was too less to have an obvious UV absorption in the UV-Vis spectrum.

5.2.2 SEM images of the VO_2@ZrO_2 core-shell nanoparticles

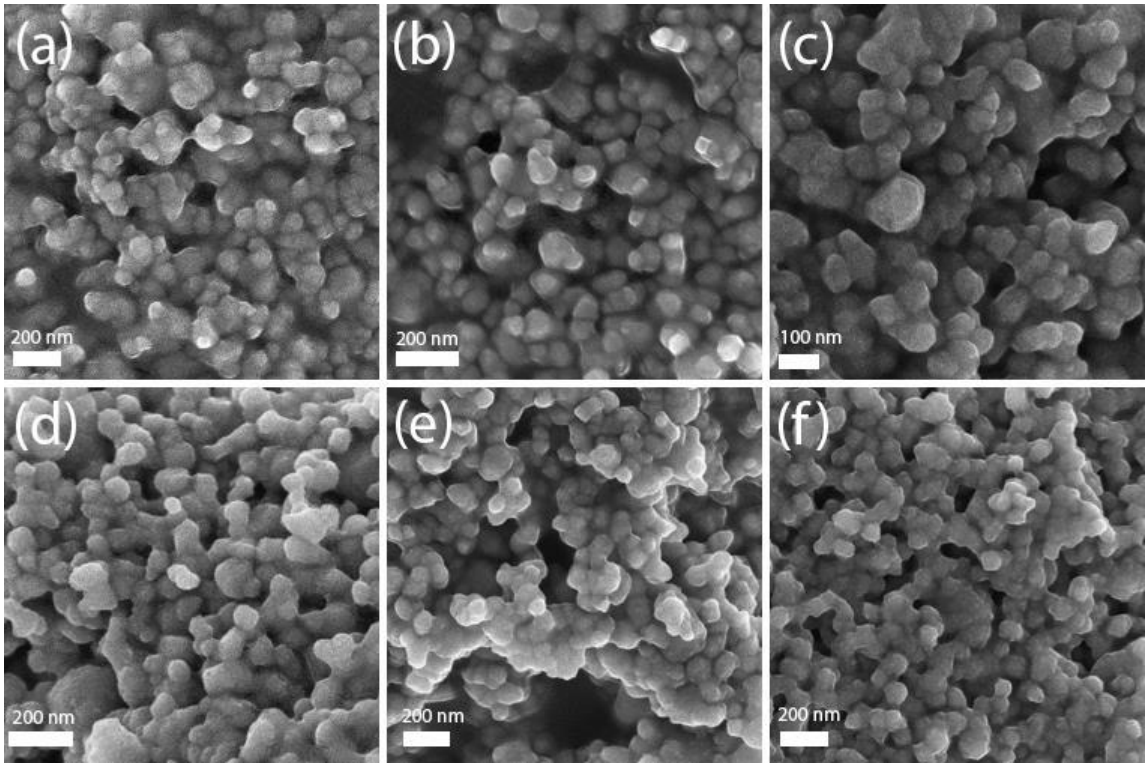

Figure 88 SEM image of VO_2@ZrO_2 core-shell nanoparticles, (a) 5uL Zr (IV) butoxide with HPC, (b) 10 uL Zr (IV) Zr (IV) butoxide with HPC, (c) 25 uL Zr (IV) Zr (IV) butoxide with HPC,(d) 5uL Zr (IV) butoxide, (e) 10 uL Zr (IV) Zr (IV) butoxide and (f) 25 uL Zr (IV) Zr (IV) butoxide.

Beside the optical properties, the morphology of the VO_2@ZrO_2 core-shell nanoparticles was tested by the SEM. As we can see from the SEM images, the morphology was almost similar with the VO_2 particles. And the size was also similar among different groups. The size of the particles was all stable and about 100nm.

5.2.3 TEM images of VO_2@ZrO_2 core-shell nanoparticles

For the study of core-shell structure, the TEM images were taken. As we can see from the TEM image, the core-shell structure is not clear. No matter with or without HPC, it seems that the ZrO_2 layer is not well synthesized on the surface of the VO_2 particles.

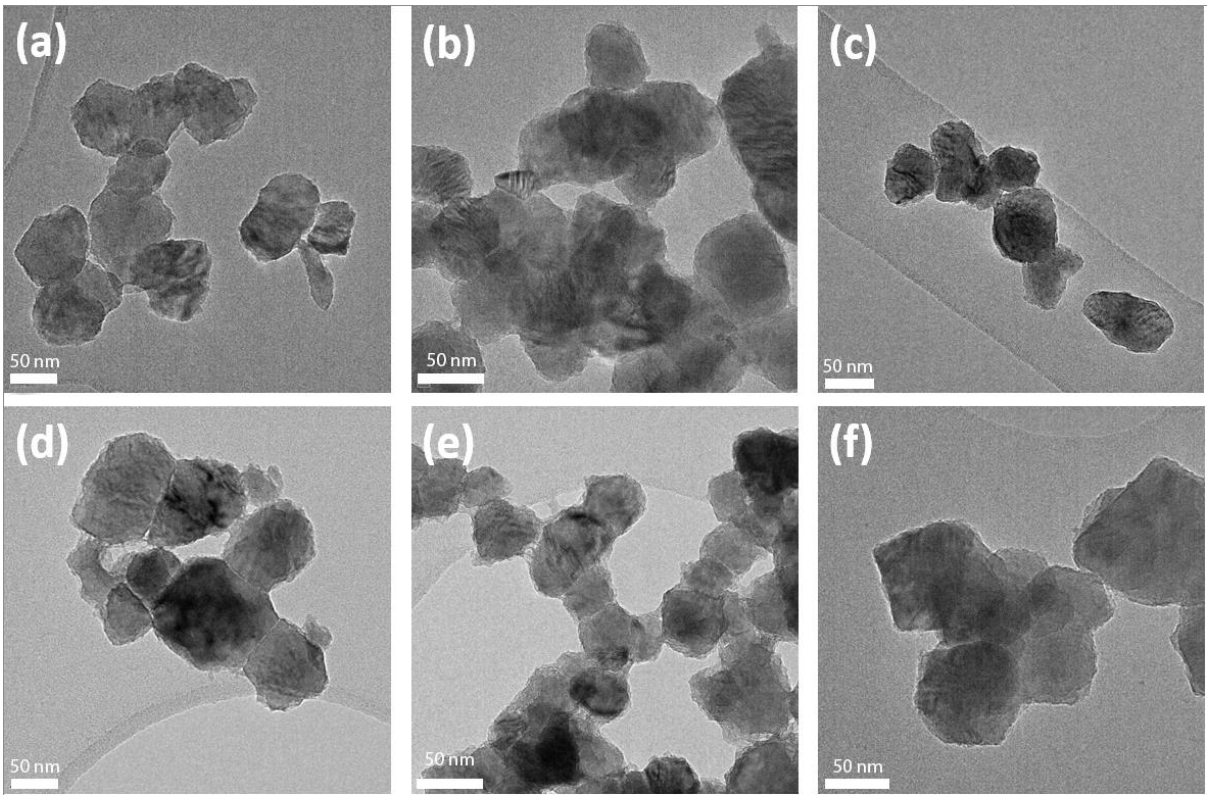

Figure 89 TEM image of VO_2@ZrO_2 core-shell nanoparticles, (a) 5uL Zr (IV) butoxide with HPC, (b) 10 uL Zr (IV) Zr (IV) butoxide with HPC, (c) 25 uL Zr (IV) Zr (IV) butoxide with HPC,(d) 5uL Zr (IV) butoxide, (e) 10 uL Zr (IV) Zr (IV) butoxide and (f) 25 uL Zr (IV) Zr (IV) butoxide.

Therefore, VO_2@ZrO_2 core-shell structure cannot be synthesized easily by the VO_2@SiO_2 coating method. A new method is needed to complete the coating process.

5.2.4 Analysis

In this section, an attempt to synthesize the VO_2@ZrO_2 core-shell structure was performed. Different amount of Zr(IV) butoxide solution was used to synthesize the core-shell structure. With the increase of the Zr(IV) butoxide solution, which was increased from 1 ml to 5 ml. Based on the SEM images, the morphology of the results were similar with the pure VO_2 nanoparticles. Moreover, from the TEM

images, the ZrO_2 shell structure was not clear, which means the ZrO_2 shell structure cannot be synthesized easily by changing the amount of Zr (IV) butoxide, The surfactant HPC was also used to try to synthesize the core-shell structure. However, there is still no clear core-shell structure even with the help of HPC. Therefore, a new method was needed to be put forward to deal with the problem.

5.3 Fabrication of VO_2@SiO_2@ZrO_2 core-shell structures with different SiO_2 shell

It is difficult to get a good VO_2@ZrO_2 core-shell nanoparticles. The synthesis of VO_2@SiO_2@ZrO_2 multi-layered core-shell nanoparticles is used to deal with the difficult synthesis of VO_2@ZrO_2 core-shell nanoparticles. The synthesis procedures are as follows:

Firstly, VO_2@SiO_2 was synthesized as previous method. Then the multi-shell nanostructures are synthesized as the following steps:

- The synthesized VO_2@SiO_2 particles were dispersed in 50 mL ethanol, then they were sonicated to get uniform mixed solution.
- 200uL Zr (IV) butoxide was added into 10 mL ethanol (Solution A).
- Different amount of solution A was added into the previous mixed solution.
- A small amount of water was added to complete the hydrolysis reaction, and the reaction time is 2 hours.
- The obtained particles were washed by ethanol for 3 times and dried in a 60 ˚C oven.
- Finally, the particles were annealed in a N_2 gas protected tube furnace in 500 ˚C for 2 hours.

5.3.1 Fabrication of VO_2@SiO_2@ZrO_2 multi-layered core-shell particles with different amount of TEOS

How the TEOS amount can affect the results of the multi-layered core-shell particles were tested in this section.

The experiment was conducted with different amount of TEOS when synthesizing the VO_2@SiO_2 core-shell particles, the details can been see in the following table:

	TEOS (uL)	Reaction time (h)	Solution A (mL)	Amount of water (uL)
A	0	1	1	100
B	50	1	1	100
C	100	1	1	100
D	200	1	1	100

Table 9 Experimental parameters for synthesizing the VO_2@SiO_2@ZrO_2 multi-layered core-shell structure.

5.3.2 SEM images of VO_2@SiO_2@ZrO_2 multi-layered core-shell particles with different amount of TEOS

The morphology of the VO_2@SiO_2@ZrO_2 were tested through the SEM images. As we can see from Fig.88, the morphology of VO_2@SiO_2@ZrO_2 multi-layered structure was similar with the VO_2 nanoparticles. The size is around 100 nm with a relatively good dispersity. Even with different amount of TEOS, there is not huge difference for the size of the particles.

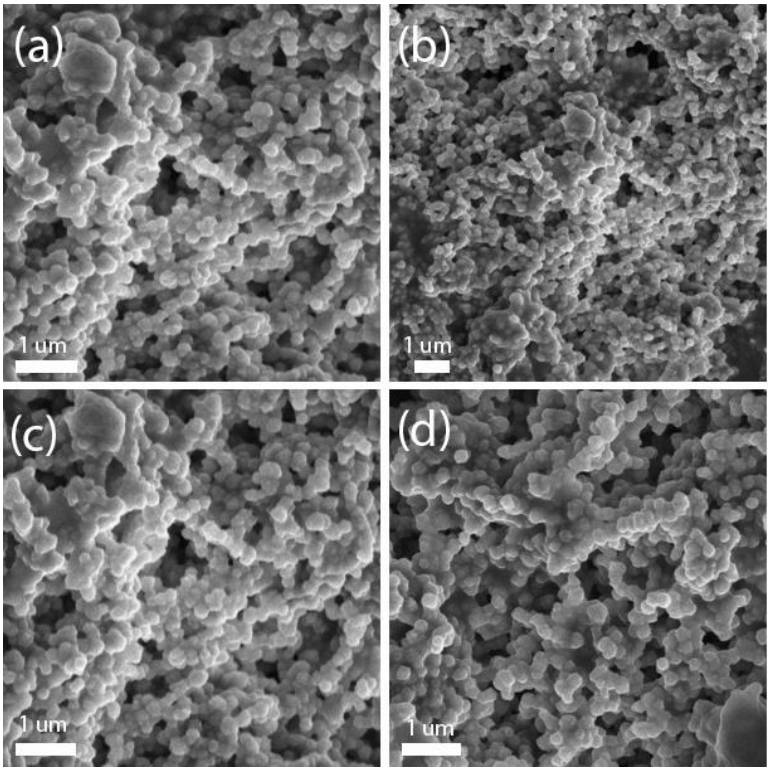

Figure 90 SEM images of VO_2@SiO_2@ZrO_2 multi-layered core-shell nanoparticles with different amount of TEOS, (a) No TEOS, (b) 50 µL TEOS, (c) 100 µL TEOS and (d) 200 uL TEOS

5.3.3 TEM images of VO_2@SiO_2@ZrO_2 multi-layered core-shell particles with different amount of TEOS

For the study of the core-shell structure, as we can see from Fig. 89 (a), the morphology of particles is irregular without the assistance of SiO_2. However, with the assistance of SiO_2, the morphology is much more round and the core-shell layers structure is clearer. It is obvious that there is a transparent SiO_2 coating layer between the VO_2 particle and thin ZrO_2 layer. And with different amount of TEOS, the structure is all clear. And the protective shell is increased with the increase of TEOS.

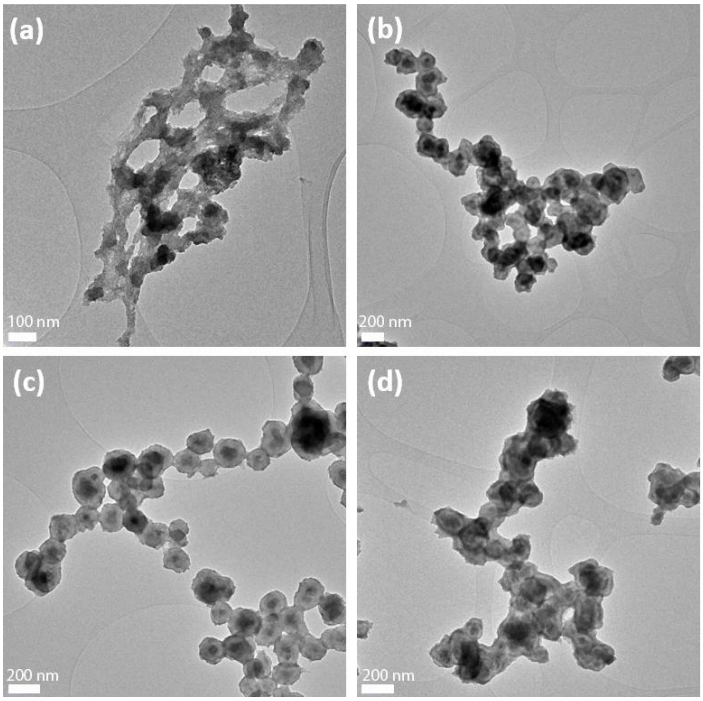

Figure 91 TEM images of VO_2@SiO_2@ZrO_2 multi-layered core-shell nanoparticles with different amount of TEOS, (a) No TEOS, (b) 50 µL TEOS, (c) 100 µL TEOS and (d) 200 uL TEOS

5.3.4 XRD and EDS images

X-ray diffraction (XRD) analyses were performed to check the composition of the VO_2@SiO_2@ZrO_2 multi-layered nanoparticles.

X-ray diffraction (XRD) analyses were conducted on a Rigaku Miniflex 600 diffractometer (Japan) with Cu Kα radiation (λ¼1.5418 Å) using a voltage and current of 40 kV and 15 mA, respectively. The sample was measured at a scanning rate of 4°/min. As we can see from the XRD images, the VO_2 (M) information can be seen easily from the image. The lattice constants are a=5.75 Å, b= 4.52 Å, c=5.38Å. The planes such as (0 1 1), (-2 1 1), and (2 1 0) can be seen in the graph. There is no impurity detected in the sample. Even though we can see the ZrO_2 layer in the TEM image, but there is not clear ZrO_2 crystal information in this XRD image. The reason might be the amount of ZrO_2 is too small to get a clear ZrO_2 peak.

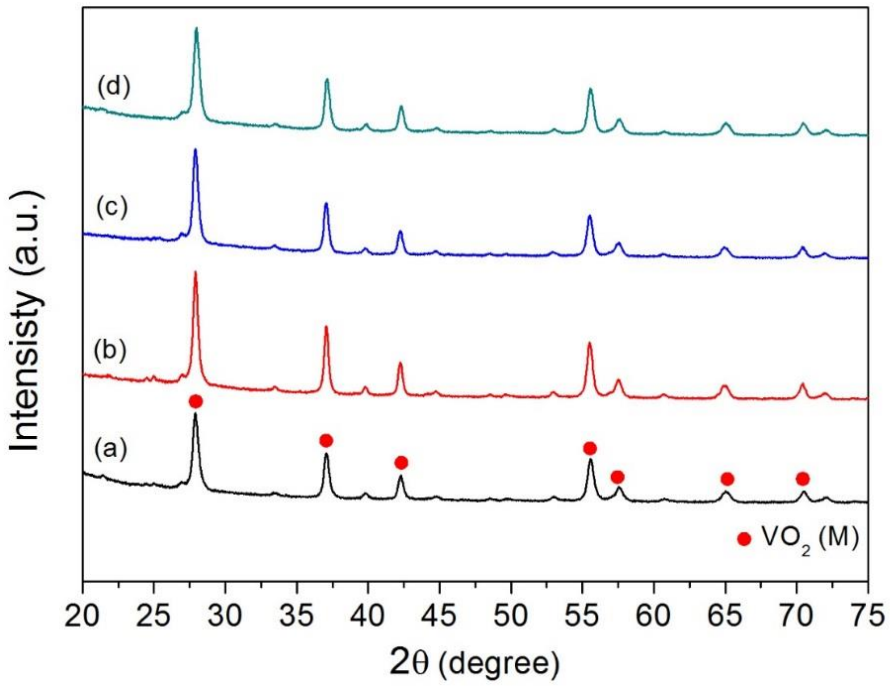

Figure 92 XRD images of VO_2@SiO_2@ZrO_2 multi-layered core-shell nanoparticles with different amount of TEOS, (a) No TEOS, (b) 50 µL TEOS, (c) 100 µL TEOS and (d) 200 uL TEOS

Besides the XRD measurement, an energy-dispersive X-ray spectroscopy (EDX) was used to prove the composition of the samples. Through an EDX measurement, Fig. 91 and Fig.92 show us the element distribution of the samples. As we can see, Si and Zr can be seen from spectrum, which means the VO_2 was coated by SiO_2 and ZrO_2 successfully. The content of silicon and zirconium is 18.5% and 6.2%, which proves the existence of thick SiO_2 layer and thin ZrO_2 layer.

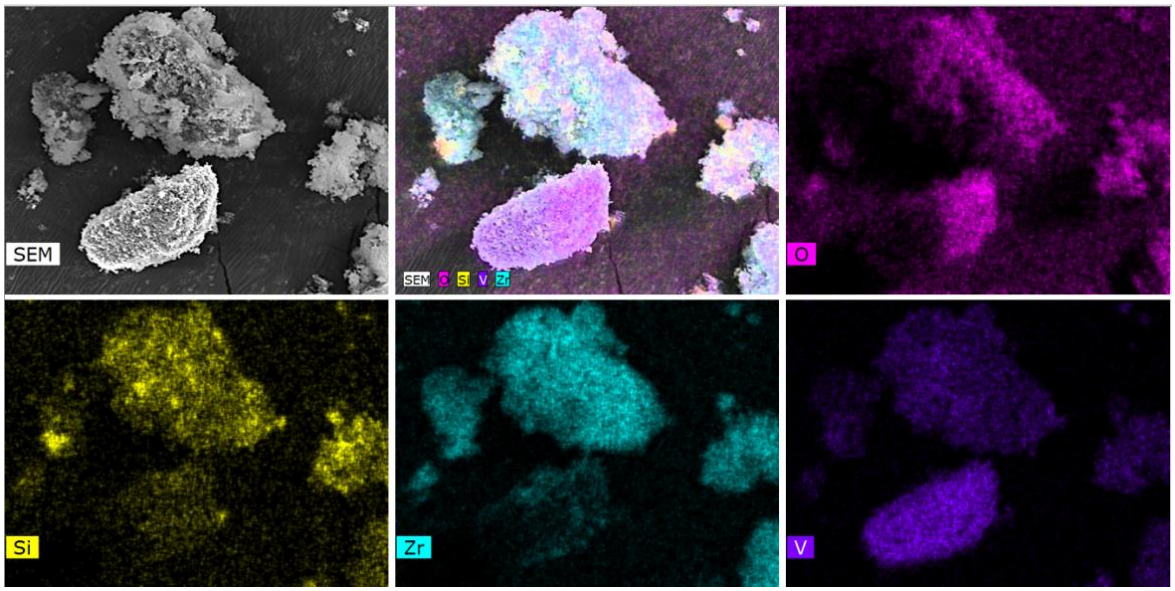

Figure 93 EDX images of VO_2@SiO_2@ZrO_2 multi-layered core-shell nanoparticles.

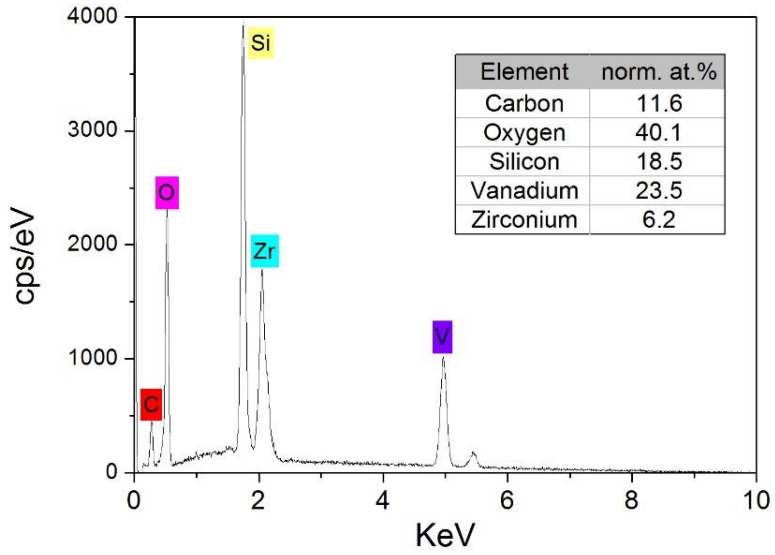

Figure 94 Element distribution from EDX

After the synthesis of VO_2@SiO_2@ZrO_2 core-shell structure, the stability performance of the particles were test in the next step.

5.3.5 Stability performance of the multi-layered core-shell nanoparticles

As we can see from the above results, the middle SiO_2 layer is helpful to deposit the ZrO_2 on the surface of VO_2. A triple layered structure is synthesized. Moreover, the stability performance of the structure will be tested, including the acid resistance, alkali resistance, and oxidation resistance.

5.3.5.1 Acid resistance performance

The VO_2@SiO_2@ZrO_2 multi-layered particles were dispersed into hydrochloric acid solution (pH=5), the UV-Vis absorption was tested every one hour to check the stability in acid solution. Different amount of TEOS was used to synthesize the particles to check if TEOS can affect the performance of acid resistance in such a structure.

As we can see from Fig. 93 (a), there is no TEOS used in this sample, which means, it is pure VO_2 nanoparticles. The UV-Vis spectrum was measured every one hour, and all the absorption information was displayed in one spectrum. For the gaps of the lines, it indicated the stability of the samples. The large gaps mean that the UV absorption was changed a lot with the long time acid treatment. Therefore, for the pure VO_2 nanoparticles, it can be affected dramatically with the acid treatment.

From Fig 93 (b) to (d), the TEOS was used in the synthesis, and the amount of TEOS was increased from 50 µL to 200 µL. As we can see from the images, the gaps between the lines were decreasing with the increase amount of TEOS. Which means that larger amount of TEOS leads to a better stability in acid solution.

Similar with the VO_2@SiO_2 core-shell nanoparticles, the thicker SiO_2 has a better acid resistance in such a structure.

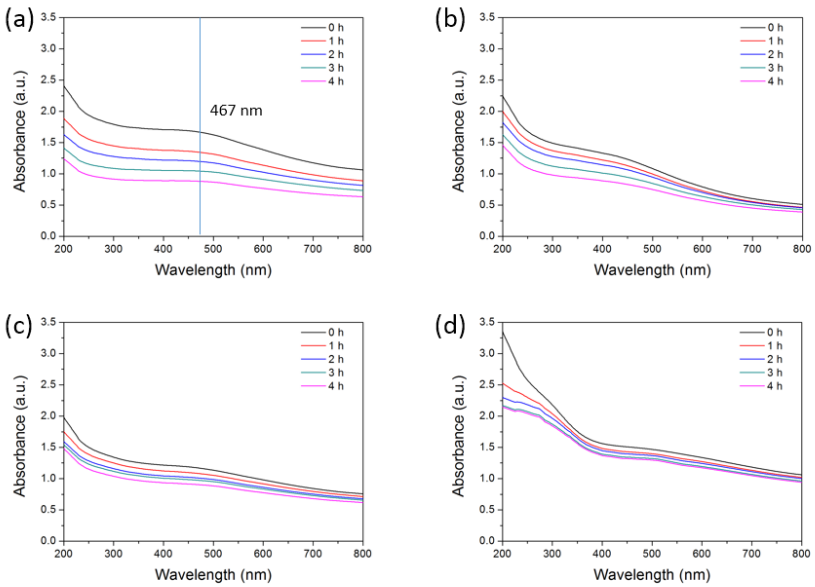

Figure 95 Acid resistance performance of VO_2@SiO_2@ZrO_2 multi-layered core-shell nanoparticles with (a) No TEOS, (b) 50 µL TEOS, (c) 100 µL TEOS and (d) 200 µL TEOS.

5.3.5.2 Alkali resistance performance

Similar method was used to measure the alkali resistance of the VO_2@SiO_2@ZrO_2 core-shell structure. The alkali solution was prepared by dissolving the sodium hydroxide into the DI water to make the pH to 9. Then the multilayered particles were dispersed into the alkali solution (pH=9), and the UV-Visible light absorption spectrum were used to achieve the purpose.

As Fig. 94 shows, the pure VO_2 also has a large difference of UV-Vis spectrum when the alkali solution treatment time was different. Moreover, when the TEOS was used to synthesize the core shell structure, the gaps between the UV-Vis spectrums were decreased with the increase of TEOS from 50 µL to 200 µL.

The results in alkali resistance testing were similar with the acid resistance testing. As we can see, from Fig.94 (a) to (d), the space between lines was decreasing, which means that the stability was increasing. More TEOS can lead to a higher alkali resistance in the VO_2@SiO_2@ZrO_2 multi-layered core-shell nanoparticles.

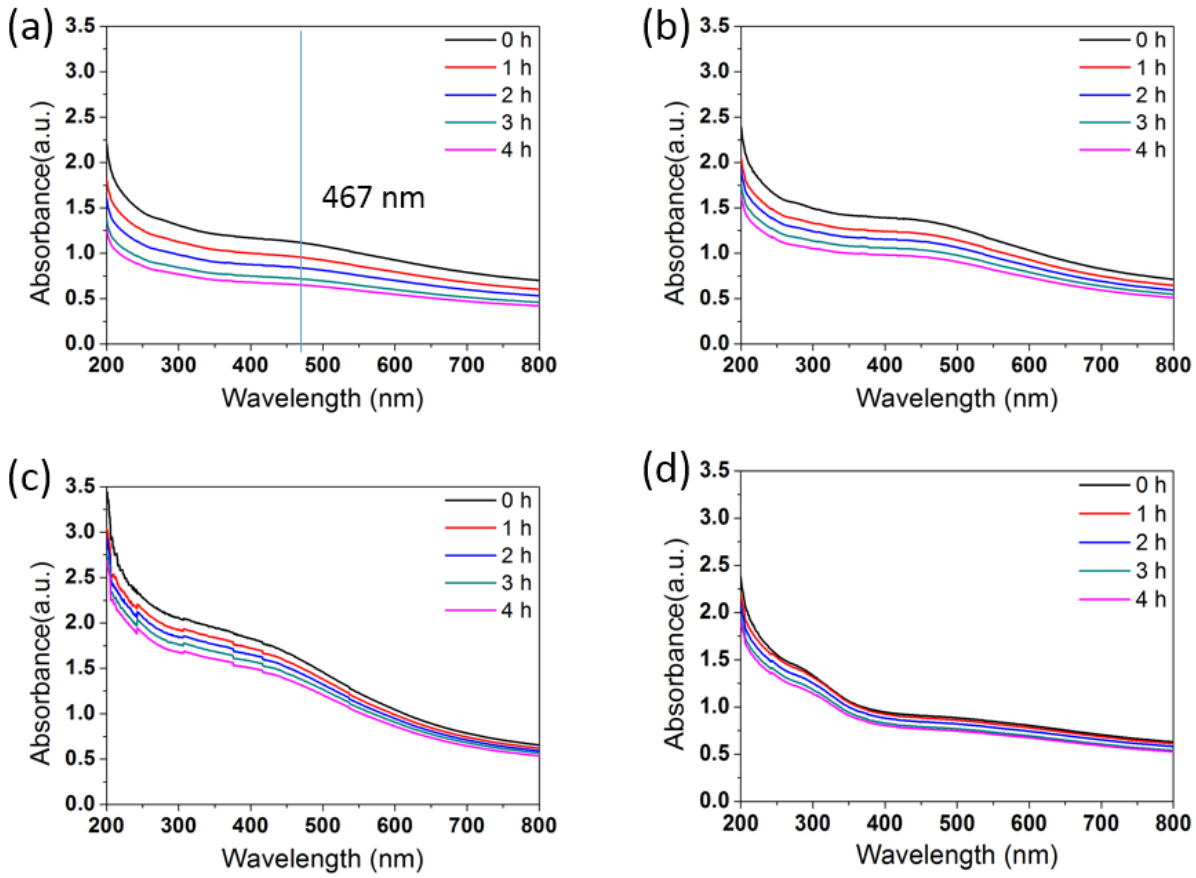

Figure 96 Alkali resistance performance of VO_2@SiO_2@ZrO_2 multi-layered core-shell nanoparticles, (a) No TEOS, (b) 50 µL TEOS, (c) 100 µL TEOS and (d) 200 µL TEOS.

5.3.5.3 Oxidation resistance performance

Hydrogen peroxide (H_2O_2) is a commonly used oxidation agent. In this experiment, H_2O_2 was used to check the anti-oxidation ability of the multi-layered structure.

The H_2O_2 was prepared to an appropriate concentration which was 0.1 M. Then the nanoparticles were dispersed into the solution and the UV-Vis spectrum was measured.

From Fig 95 (a), the pure VO_2 nanoparticles have a very weak stability against H_2O_2 solution. The UV-Vis absorption has an immediate decrease in the first hour oxidizing agent treatment. However, with the addition of TEOS, the core shell structure has a better stability in the UV-Vis absorption. As we can see, from Fig.95

(a) to (d), the space between lines is decreasing, which means that the stability is also increasing.

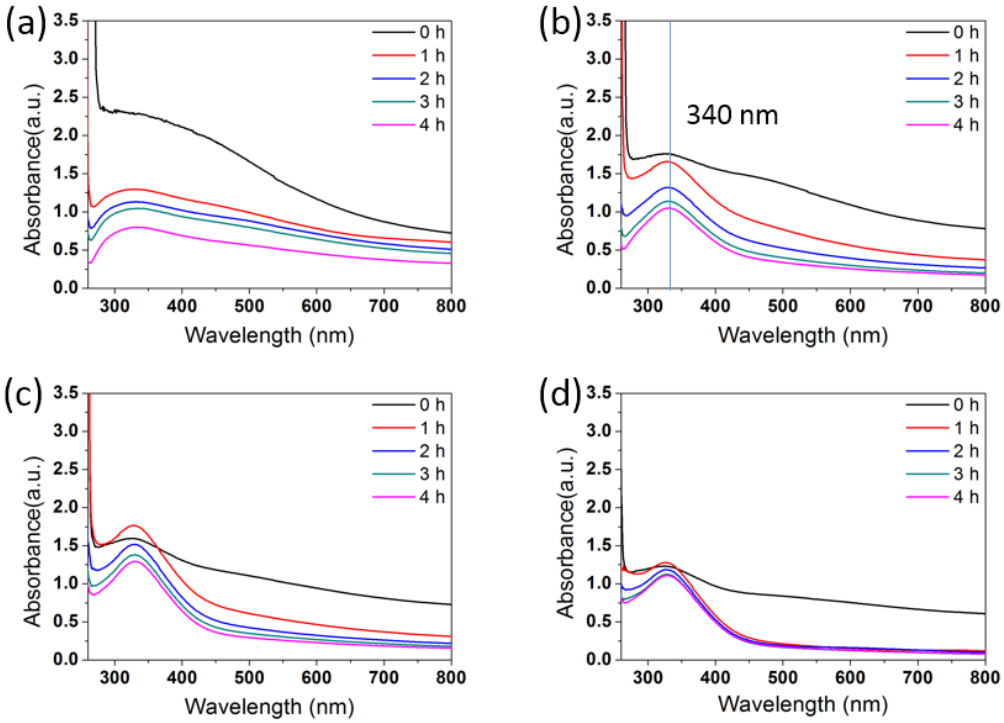

Figure 97 Oxidation resistance performance of VO_2@SiO_2@ZrO_2 multi-layered core-shell nanoparticles (a) No TEOS, (b) 50 µL TEOS, (c) 100 µL TEOS and (d) 200 µL TEOS.

In this experiment, VO_2@SiO_2@ZrO_2 was synthesized successfully. Moreover, the morphology was much better than the VO_2@ZrO_2 core-shell nanoparticles. It can also give a dramatically good performance of acid resistance, alkali resistance and oxidation resistance performance.

5.3.6 Results analysis

As the VO_2@ZrO_2 core shell nanoparticles were difficult to synthesize. In this section, the VO_2@SiO_2@ZrO_2 multi-layered core-shell structures were prepared successfully. The SiO_2 middle layer plays an important role in combining the VO_2 and ZrO_2 material. As the SiO_2@ZrO_2 core-shell nanoparticles were easier to be prepared[193]. And the VO_2@SiO_2 core-shell has been synthesized successfully in the previous study.

After the obtaining of the VO_2@SiO_2@ZrO_2 multi-layered core-shell structures, the characterization work was done in the following step. Based on the SEM and TEM results, the size of the core-shell nanoparticles was uniform with a good dispersity and the core-shell structure was clear. Moreover, the core-shell particles were synthesized with different SiO_2 middle layer.

After that, the stability performance were checked, which includes the stability in acid, alkali and oxidizing environment. And the stability performance of the nanoparticles were measured. From the resistance test of acid, alkali and oxidation agent, it shows that the core-shell particles exhibits a better resistance ability with a thicker SiO_2 middle layer, which is similar to the VO_2@SiO_2 core-shell structure. For the VO_2 nanoparticles, the UV-Vis spectrum changed a lot with the time going. However, by adding the TEOS, the core-shell structure has a better performance to maintain a better stability.

5.4 ZrO_2 coating reaction time and VO_2@SiO_2@ZrO_2 core-shell nanoparticles

As we have synthesized the VO_2@SiO_2@ZrO_2 core-shell nanoparticles successfully. The optimized experimental parameters need to be studied. In this section, the hydrolysis reaction time in the ZrO_2 coating process was studied.

5.4.1 Experimental details for the synthesis process

The synthesis process was almost same with the previous results. Different reaction time was processed for the ZrO_2 coating reaction. And the TEOS maintains at 50 µL. The reaction details can be seen as the follow table:

	TEOS (µL)	Reaction time (min)	Solution A (mL)	DI water (µL)
A	50	10	1	100
B	50	30	1	100
C	50	60	1	100
D	50	120	1	100

Table 10 Experimental parameters for synthesizing the VO_2@SiO_2@ZrO_2 multi-layered core-shell structure with different ZrO_2 coating time.

Firstly, the VO_2@SiO_2 core-shell nanoparticles were synthesized as previous study. Secondly, different VO_2@SiO_2@ZrO_2 core-shell nanoparticles were prepared by changing the ZrO_2 coating time. Finally, the characterization was done to check the properties of the samples.

5.4.2 SEM images of VO_2@SiO_2@ZrO_2 multi-layered core-shell particles with different ZrO_2 coating time

The morphology of the VO_2@SiO_2@ZrO_2 nanoparticles were characterized by the SEM images. The samples with different coating time (10 minutes to 2 hours) were measured.

As we can see from the SEM images (Fig. 96), the morphology is similar with the VO_2 nanoparticles. With the increase of the ZrO_2 coating time, it seems that the

particles aggregation is a little bit heavier. But the particles still remain a good dispersity. The morphology remains stable in the multi-layered structure. When the coating time is longer than one hour, the aggregation problem occurs. However, the diameter of the nanoparticles was stable at around 100 nm. It means that, the longer coating time may lead to some ZrO_2 accumulation between the core shell structures.

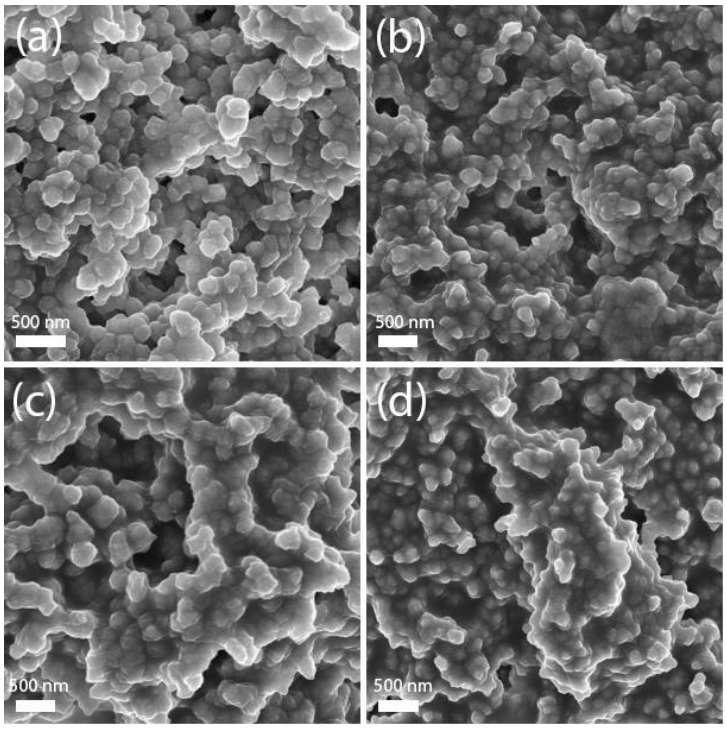

Figure 98 SEM images of VO_2@SiO_2@ZrO_2 multi-layered nanoparticles with different coating time, (a) 10 min, (b) 30 min, (c) 1h and (d) 2h.

5.4.3 TEM images of VO_2@SiO_2@ZrO_2 multi-layered core-shell particles with different ZrO_2 coating time

After the morphology measurement, the core-shell structure of the VO_2@SiO_2@ZrO_2 core-shell structure was measured through the TEM images. Generally, the samples synthesized by different ZrO_2 coating time show a good core-shell structure.

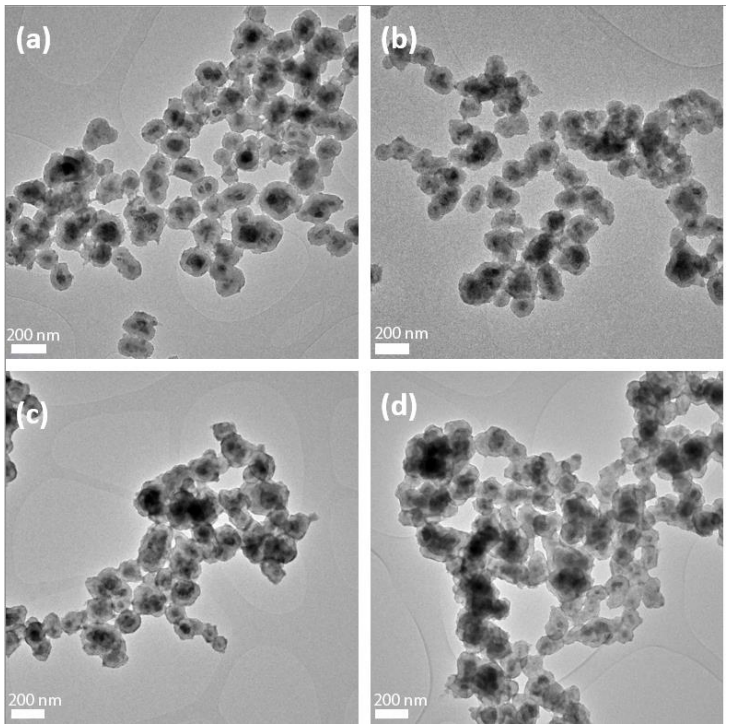

Figure 99 TEM images of VO_2@SiO_2@ZrO_2 multi-layered nanoparticles with different coating time, (a) 10 min, (b) 30 min, (c) 1h and (d) 2h.

As we can see from Fig.97, the core-shell structure is clear in the TEM image. And with the longer reaction time, the shell structure is clearer. It shows that the core-shell nanostructure can be obtained successfully with different reaction time (10 min to 2h).From the image, a black VO_2 core structure can be seen, and the transparent SiO_2 shell structure was grown on the VO_2 core. After that, the thin and black ZrO_2 shell can also be seen on the surface of the SiO_2.

5.4.4 XRD images VO_2@SiO_2@ZrO_2 multi-layered core-shell particles with different ZrO_2 coating time

From the SEM and TEM images, it has been known that the morphology and structure of the VO_2@SiO_2@TiO_2 is good. Furtherly, the composition statement was measured by the X-ray diffraction analysis (XRD).

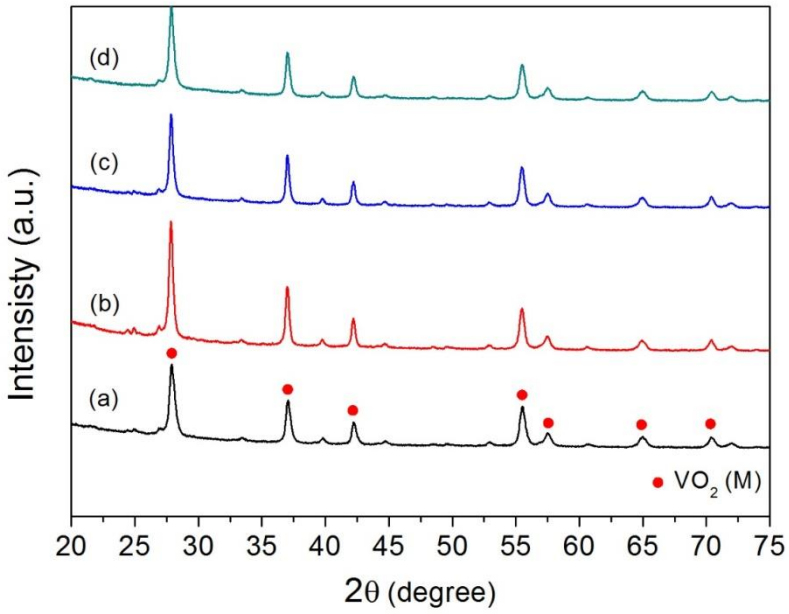

Figure 100 XRD images of VO_2@SiO_2@ZrO_2 multi-layered nanoparticles with different coating time, (a) 10 min, (b) 30 min, (c) 1h and (d) 2h.

X-ray diffraction (XRD) analyses were conducted on a Rigaku Miniflex 600 diffractometer (Japan) with Cu Kα radiation (λ¼1.5418 Å) using a voltage and current of 40 kV and 15 mA, respectively. The samples were measured at a scanning rate of 4°/min.

As we can see from the XRD images, the VO_2 (M) information can be seen easily from the image. The lattice constants are a=5.75 Å, b= 4.52 Å, c=5.38Å. The planes such as (0 1 1), (-2 1 1), and (2 1 0) can be seen in the graph. There is no impurity detected in the sample. In this case, there is also not clear ZrO_2 crystal information in

this XRD image. The reason might be the amount of ZrO_2 is too small to get a clear ZrO_2 peak. However, the previous EDS spectrum can prove the existence of the ZrO_2 layer.

5.4.5 Stability performance of the multi-layered nanoparticles synthesize by different coating time

As the VO_2@SiO_2@ZrO_2 core-shell nanoparticles have been synthesized with different ZrO_2 coating time. The relationship between the chemical stability and different ZrO_2 coating time should be studied in the next step. For the measurement of the stability performance, the core-shell nanoparticles were dispersed into the solution which contains acid, alkali and oxidation agent. The UV-Vis light absorption spectrum was measured every hour to check the change of the sample. If the core-shell nanoparticles were stable in the solution, the UV-Vis light spectrum will remain stable, however, if the core-shell nanoparticles were affected by the solution, the UV-Vis light absorption is changed. Therefore, we can judge the stability of the samples by measuring the gaps between the UV-Vis spectrum lines.

5.4.5.1 Acid resistance performance

Firstly, the acid resistance were tested. Different VO_2@SiO_2@ZrO_2 core-shell nanoparticles were dispersed into hydrochloric acid solution (pH=5). The UV-Vis absorption spectrum was measured every one hour. From Fig 99 (a) to (d), it can be seen that, the gaps between the lines were smaller, which means the VO_2@SiO_2@ZrO_2 core-shell nanoparticles have a better stability when the ZrO_2 coating time is longer.

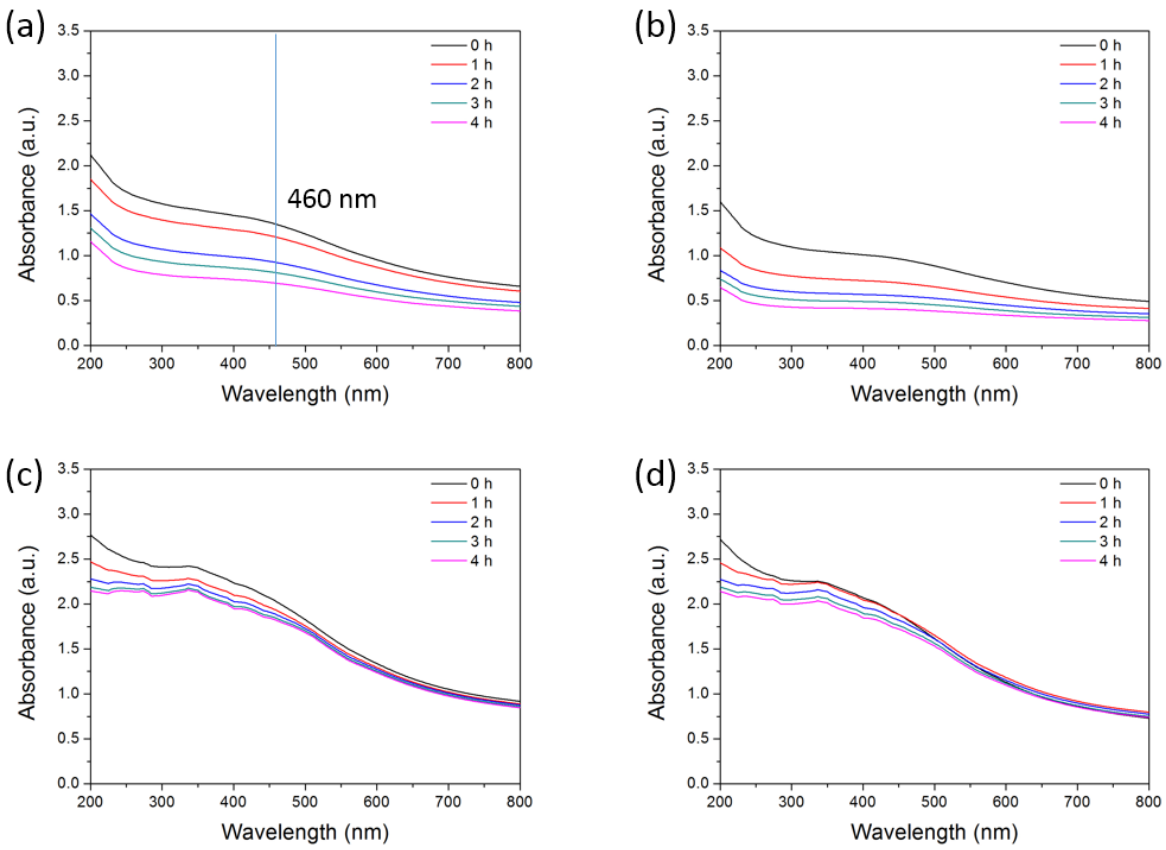

Figure 101 UV-Vis light absorption spectrum of VO_2@SiO_2@ZrO_2 multi-layered nanoparticles with different coating time in acid solution, (a) 10 min, (b) 30 min, (c) 1h and (d) 2h.

5.4.5.2 Alkali resistance performance

After the acid resistance test, the alkali resistance was also tested. Different VO_2@SiO_2@ZrO_2 core-shell nanoparticles were dispersed into sodium hydroxide solution (pH=9). Then the UV-Vis absorption spectrums were measured. From Fig. 100 (a), it shows that the shorting ZrO_2 coating time (10 minutes) leads to a large gap between the UV-Vis spectrums, which means the thin ZrO_2 layer cannot bear the alkali corrosion. However, the longer ZrO_2 coating time gives better results. It exhibits that the thicker ZrO_2 shell gives a better alkali resistance.

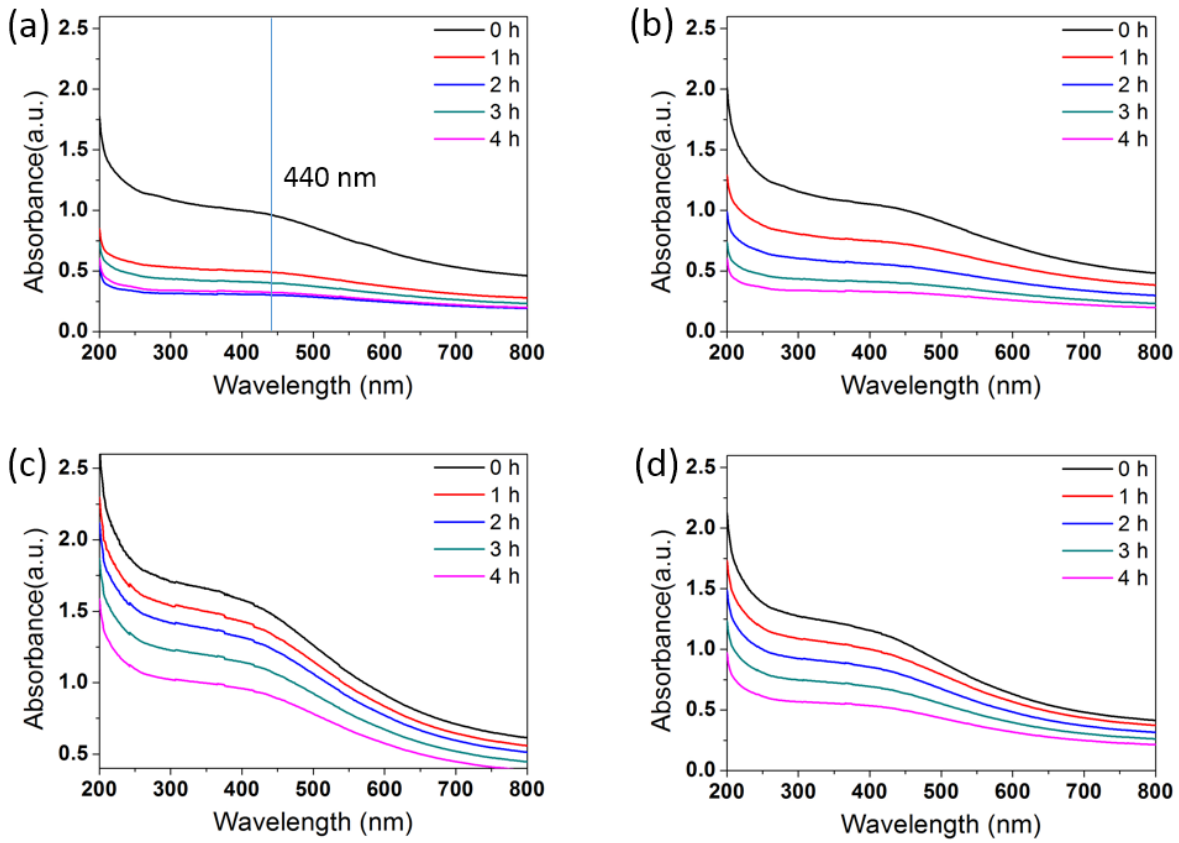

Figure 102 UV-Vis light absorption spectrum of VO_2@SiO_2@ZrO_2 multi-layered nanoparticles with different coating time in alkali solution, (a) 10 min, (b) 30 min, (c) 1h and (d) 2h.

5.4.5.3 Oxidation resistance performance

Finally, the oxidation resistance performance was tested. The VO_2@SiO_2@ZrO_2 core-shell nanoparticles were dispersed into H_2O_2 solution (0.1M). And the UV-Vis absorption spectrum was tested to observe the stability of the nanoparticles. If the samples are not stable, the UV-Vis light absorption will be decreased with the time going on. Fig 101 (a) shows that the short time coating cannot provide a good stability against H_2O_2 solution. With the increase of the reaction time (up to 2 hours), the gaps of the spectrum have a better performance, which means the thicker ZrO_2 shell can also provide a better oxidation assistance property.

Based on the above UV-Vis spectrum, the samples have a better resistance to acid, alkali and oxidation solution. Therefore, the ZrO_2 coating layer is very helpful to improve the stability of the VO_2 nanoparticles.

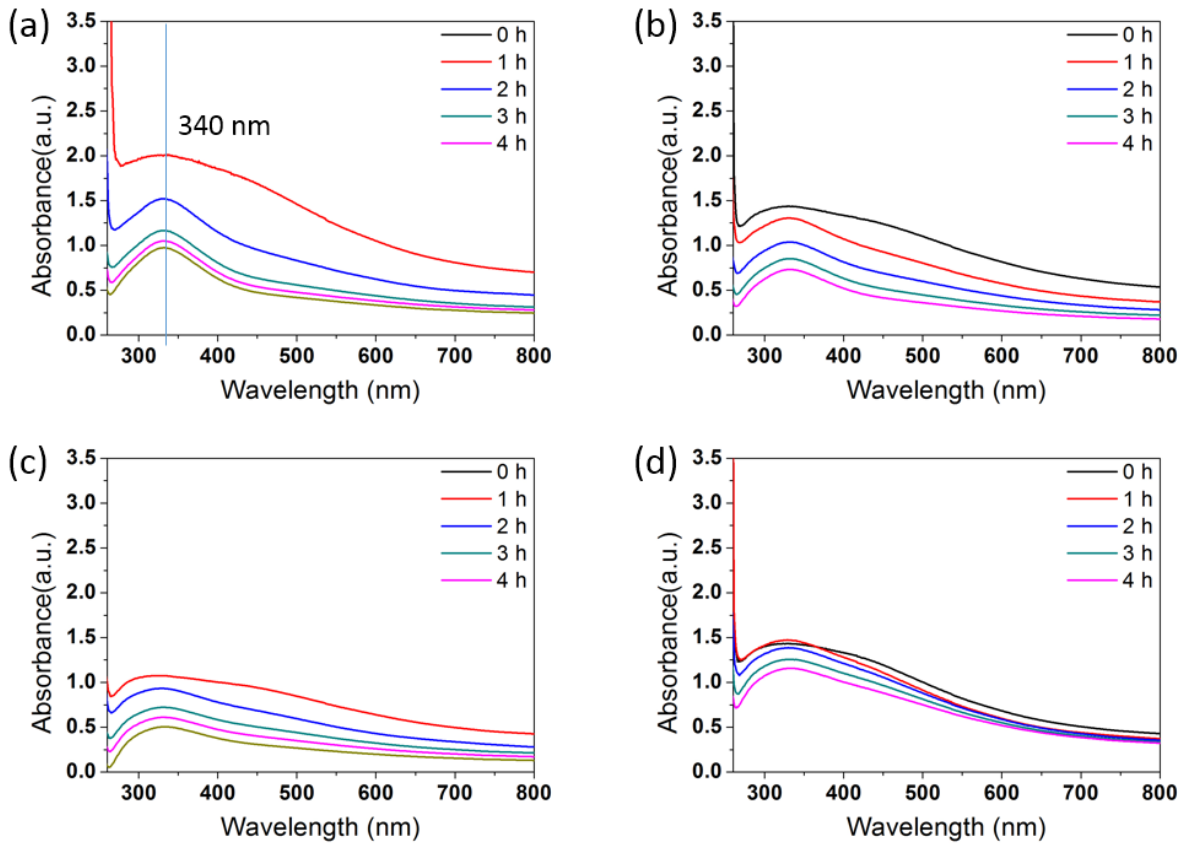

Figure 103 UV-Vis light absorption spectrum of VO_2@SiO_2@ZrO_2 multi-layered nanoparticles with different coating time in H_2O_2 solution, (a) 10 min, (b) 30 min, (c) 1h and (d) 2h.

5.5.6 Results analysis

After the successful synthesis of VO_2@SiO_2@ZrO_2 core-shell nanoparticles, the ZrO_2 coating time was studied in this section. The coating time was increased from 10 minutes to 2 hours.

After that, the SEM images were used to test the morphology of the nanoparticles. It shows that the VO_2@SiO_2@ZrO_2 core-shell nanoparticles also have a good

dispersity and size distribution with different ZrO_2 coating time. TEM images were used to measure the core-shell structure of the samples. It exhibits that a three-layer structure can be seen easily. Even though only monoclinic VO_2 can be found in the XRD images, less ZrO_2 information can be seen as the small amount, however, the ZrO_2 information can be detected from EDX analysis.

Moreover, the stability of the $VO_2@SiO_2@ZrO_2$ core-shell nanoparticles were tested in the next step. In this section, the influence of ZrO_2 coating reaction time was studied for the preparation of $VO_2@SiO_2@ZrO_2$ core-shell nanoparticles. With the longer of the coating time, it shows that the ZrO_2 layer is much clearer and thicker.

Moreover, the stability of the core-shell structure was tested by dispersing the nanoparticles into acid, alkali and oxidation solution. Based on the UV-Vis light spectrum, the thicker ZrO_2 layer can help the core-shell structure has a better stability. It means the core-shell structure is meaningful for improving the stability of VO_2 nanoparticles.

5.5 Zr(IV) butoxide solution and $VO_2@SiO_2@ZrO_2$ core-shell nanoparticles

Except the ZrO_2 coating time, other experimental parameters may also affect the synthesis process. Therefore, in this section, the amount of Zr (IV) butoxide solution was studies in the core-shell formation process.

5.5.1 Experimental details for the synthesis process

The synthetic process is similar with the previous experiments. However, the addition of Zr(IV) butoxide is different. The experimental condition can be seen in the following table. (Tab 10)

	TEOS (µL)	Reaction time (H)	Zr (IV) butoxide (µL)	Amount of water (µL)
A	50	1	10	100
B	50	1	20	100
C	50	1	50	100
D	50	1	100	100

Table 11 Experimental parameters with different amount of Zr (IV) butoxide solution.

Firstly, the VO_2@SiO_2 were synthesized as previous study. Then the VO_2@SiO_2@ZrO_2 core-shell nanoparticles were prepared with different amount of Zr (IV) butoxide solution from 10 µL to 100 µL.

5.5.2 SEM images of VO_2@SiO_2@ZrO_2 multi-layered nanoparticles with different amount of ZrO_2 coating

Firstly, the morphology of the VO_2@SiO_2@ZrO_2 core-shell nanoparticles were characterized by the SEM images. The samples with different amount of Zr (IV) butoxide solution (10 µL to 100 µL) were measured.

As we can see from the SEM images (Fig. 102), the morphology is almost same with the VO_2 nanoparticles. With the increase of the Zr (IV) butoxide solution, it seems that the particles aggregation is a little bit heavier. But the dispersity of the particles was still good. The morphology remains stable in the multi-layered structure. More Zr (IV) butoxide solution can lead to an accumulation problem. But the diameter of the nanoparticles was stable at around 100 nm.

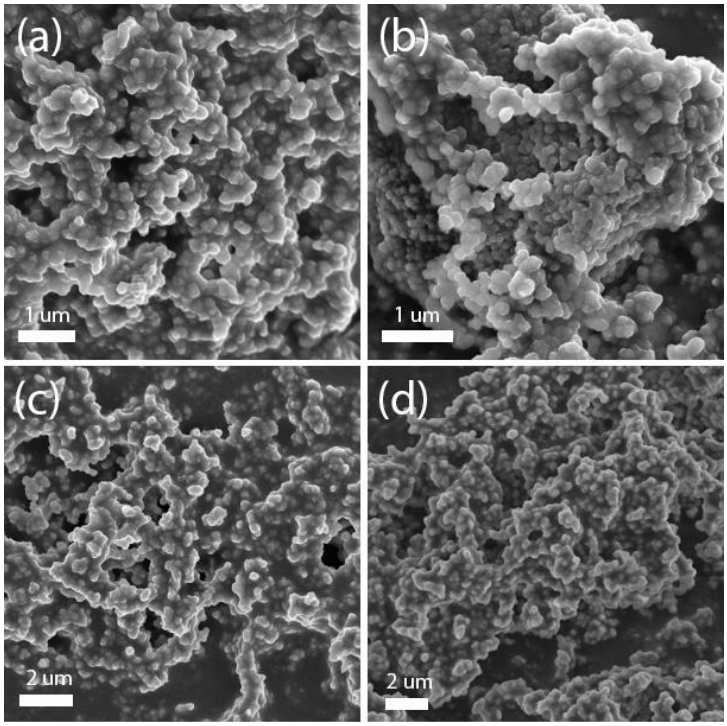

Figure 104 SEM images of VO_2@SiO_2@ZrO_2 multi-layered nanoparticles with different amount of Zr (IV) butoxide solution, (a) 10 uL, (b) 20 uL, (c) 50 µL and (d) 100 uL Zr (IV) butoxide solution

According to the SEM results, with the increase of the Zr(IV) butoxide solution, the dispersity of the particles was decreased, however, the morphology of the particles was still stable in the results. The aggregation of the particles can be attributed to the high level hydrolysis of the Zr(IV) precursors.

5.5.3 TEM images of VO_2@SiO_2@ZrO_2 multi-layered core-shell particles with different amount of ZrO_2 coating

Besides the SEM image, the TEM images were also obtained to check the core-shell structure. As we can see from Fig 105, a dark layer can be seen on the surface of the particles.

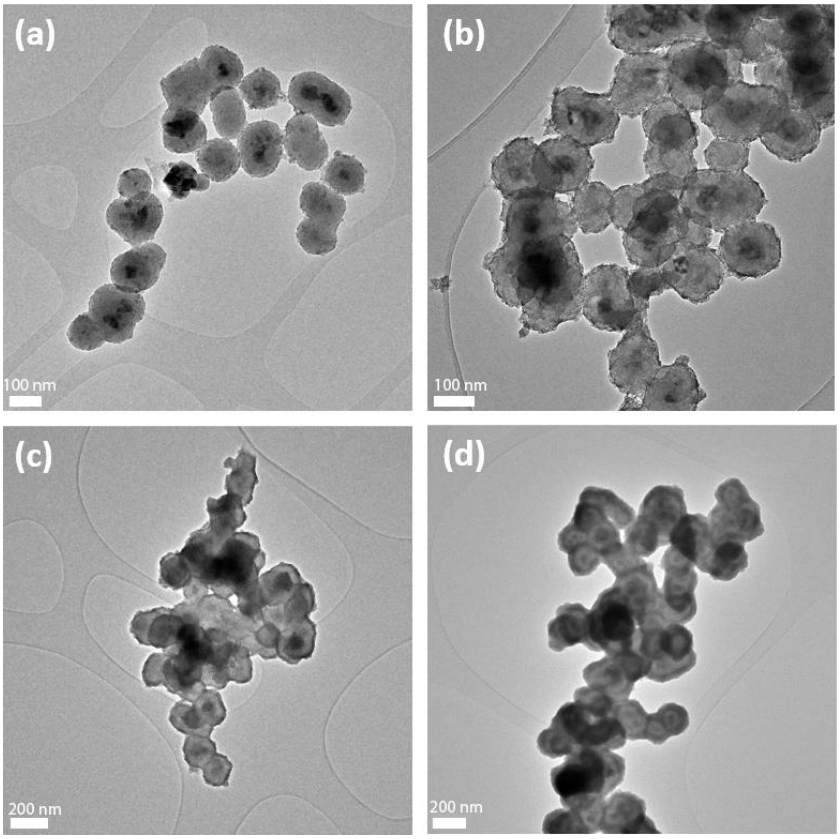

Figure 105 TEM images of VO_2@SiO_2@ZrO_2 multi-layered core-shell nanoparticles with different amount of Zr (IV) solution, (a) 10 uL (b) 20 uL, (c) 50 uL and (d) 100 uL Zr (IV) butoxide solution

Same as the previous synthesis of VO_2@SiO_2@ZrO_2, the black VO_2 core is surrounded with transparent SiO_2 layer and dark ZrO_2 layer. With the higher level of Zr(IV) butoxide solution, the ZrO_2 was thicker and darker. For Fig.105 (a), when the Zr (IV) butoxide solution was little, the ZrO_2 layer was not clear, however, when the amount was increased (Fig 103 (b)-(d)), the ZrO_2 layer was much darker and clearer. However, the size and diameter of the particles were in a good range within 100 µL Zr (IV) butoxide solution.

5.5.4 XRD images VO_2@SiO_2@ZrO_2 multi-layered core-shell particles with different amount of ZrO_2 coating

The composition information was also tested by the XRD equipment. X-ray diffraction (XRD) analyses were conducted on a Rigaku Miniflex 600 diffractometer (Japan) with Cu Kα radiation (λ¼1.5418 Å) using a voltage and current of 40 kV and 15 mA, respectively. The samples were measured at a scanning rate of 4°/min.

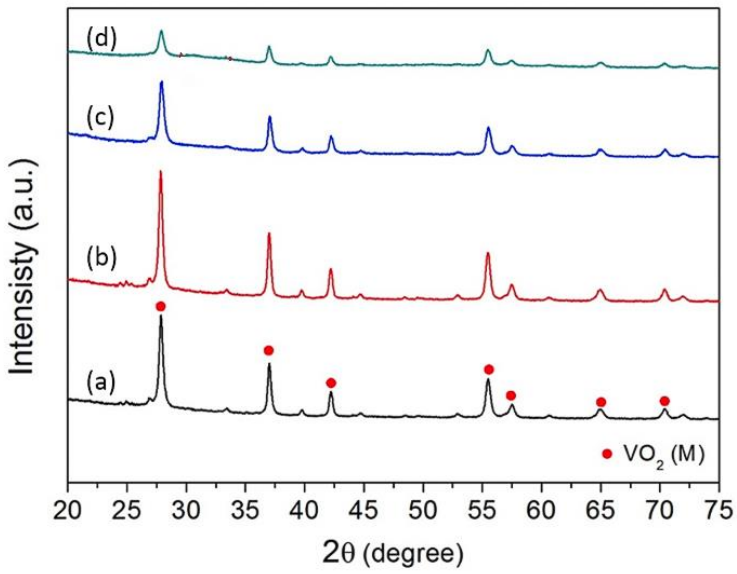

Figure 106 XRD images of VO_2@SiO_2@ZrO_2 multi-layered core-shell nanoparticles with different amount of Zr (IV) solution, (a) 10 uL, (b) 20 uL, (c) 50 uL and (d) 100 uL Zr (IV) butoxide solution

From the XRD image, VO_2 (M) was clearly shown in the spectrum, however, there is still no information of ZrO_2 cannot be seen. Similar with previous data, the lattice constants are a=5.75 Å, b= 4.52 Å, c=5.38Å. The planes such as (0 1 1), (-2 1 1), and (2 1 0) can be seen in the graph. There is no impurity detected in the sample. The reason may also be the amount of ZrO_2 is too small to be detected. When the Zr(IV) butoxide solution was 50 µL, there is a small peak about ZrO_2 can be detected. And the previous EDS spectrum can prove the existence of the ZrO_2 layer.

5.5.5 Stability performance of the multi-layered core-shell nanoparticles

5.5.5.1 Acid resistance performance

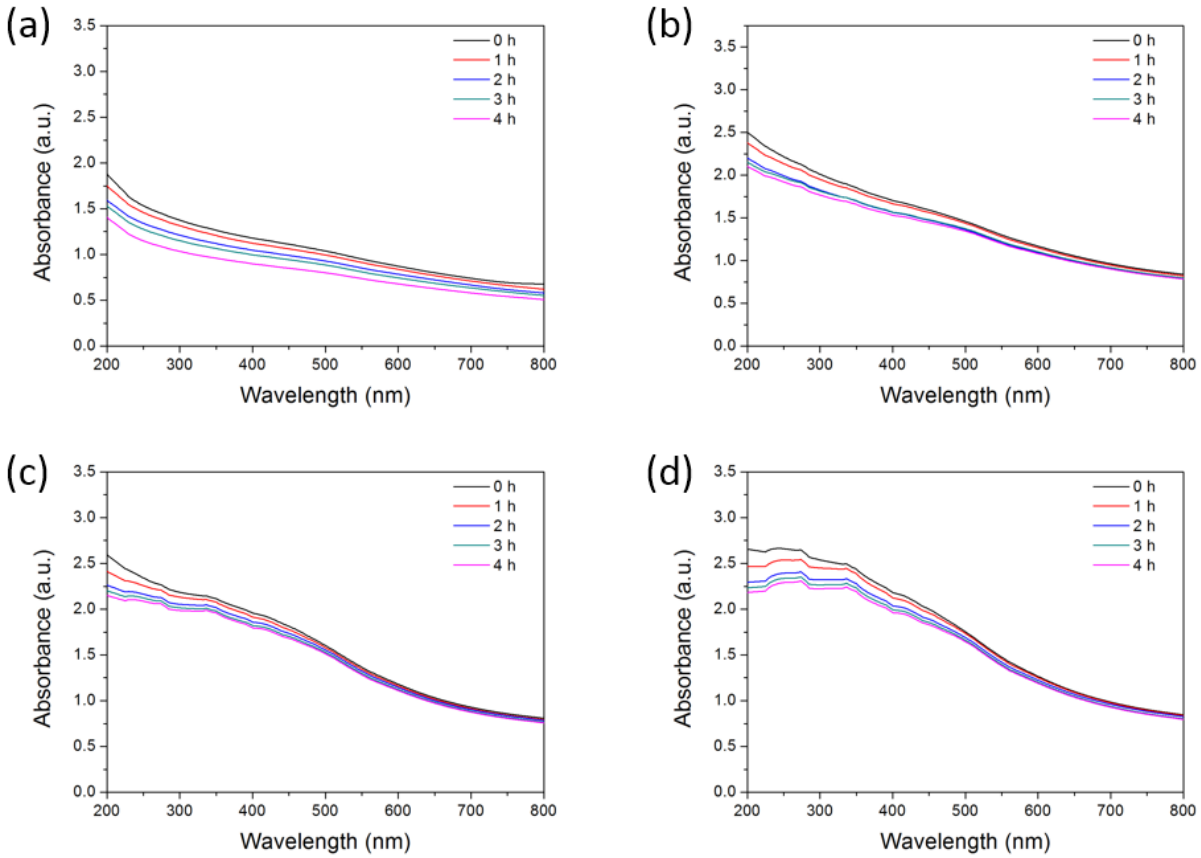

Figure 107 UV-Vis light absorption spectrum of VO_2@SiO_2@ZrO_2 multi-layered nanoparticles with different amount of Zr (IV) solution coating in acid solution (pH=5), (a) 10 uL, (b) 20 uL, (c) 50 uL and (d) 100 uL Zr (IV) butoxide solution.

After the synthesis of the core-shell structure successfully, the chemical stability performance was also tested to check if the ZrO_2 coating amount can affect the stability.

Firstly, the acid resistance were tested. Different VO_2@SiO_2@ZrO_2 core-shell nanoparticles were dispersed into hydrochloric acid solution (pH=5). The UV-Vis absorption spectrums were measured every one hour. From Fig 107 (a) to (d), it can

be seen that, the gaps between the lines were smaller, which means the VO_2@SiO_2@ZrO_2 core-shell nanoparticles have a better stability when there is a larger amount of Zr(IV) butoxide solution. However, the different was not as significant as the ZrO_2 coating time.

5.5.5.2 Alkali resistance performance

After the acid resistance study, the alkali resistance study was done. the VO_2@SiO_2@ZrO_2 samples with different Zr (IV) butoxide amount were dispersed into sodium hydroxide solution (pH=9). And the UV-Vis spectrum were tested every one hour to check the change of the spectrum.

From Fig. 108 (a), it shows that the small amount of Zr (IV) butoxide solution used in the synthesis of VO_2@SiO_2@ZrO_2 core-shell nanoparticles lead to a large gap between the UV-Vis spectrums, which means the thin ZrO_2 layer cannot bear the alkali corrosion. However, with a larger amount of Zr (IV) butoxide in synthesis (Fig.108 (b)-(d)), the gaps of the spectrum were smaller, which shows that thicker ZrO_2 shell gives a better alkali resistance.

5.5.5.3 Oxidation resistance performance

Finally, the oxidation resistance performance was measured. The VO_2@SiO_2@ZrO_2 core-shell nanoparticles were dispersed into H_2O_2 solution (0.1M). And the UV-Vis absorption spectrum was tested to check the stability properties of the nanoparticles. If the samples are easily to be affected by the oxidizing agent, the UV-Vis light absorption will be decreased with the time going on. Fig 109 (a) shows that the small amount of ZrO_2 coating amount cannot provide a good stability against H_2O_2 solution. With the increase of the ZrO_2 coating, the gaps of the spectrum has a better

performance, which means the thicker ZrO_2 shell can also provide a better oxidation assistance property.

As we can see from the optical results, with different amount of ZrO_2 coating, the ZrO_2 layer thickness may increase with the increase amount of Zr (IV) butoxide solution. ZrO_2 can form a thin layer on the surface of the SiO_2. And it gives a good acid resistance, alkali resistance and oxidation resistance property.

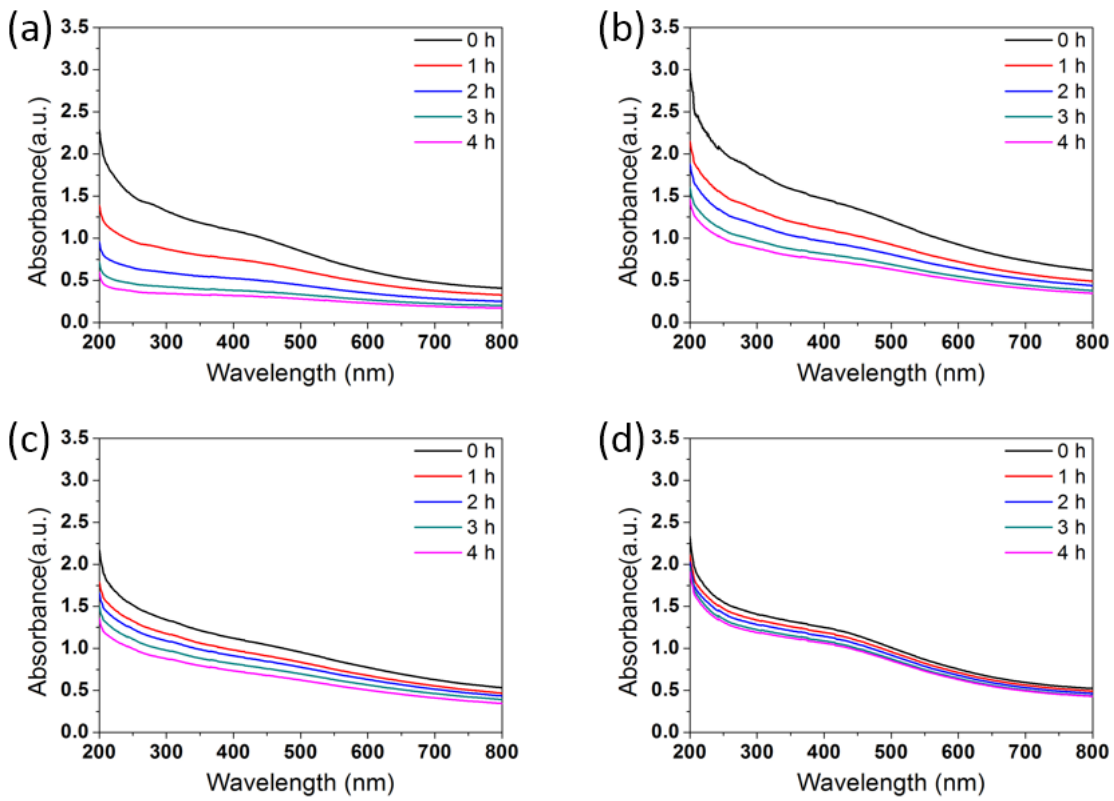

Figure 108 UV-Vis light absorption spectrum of VO_2@SiO_2@ZrO_2 multi-layered nanoparticles with different amount of Zr (IV) solution coating in alkali solution (pH=9), (a) 10 uL, (b) 20 uL, (c) 50 uL and (d) 100 uL Zr (IV) butoxide solution.

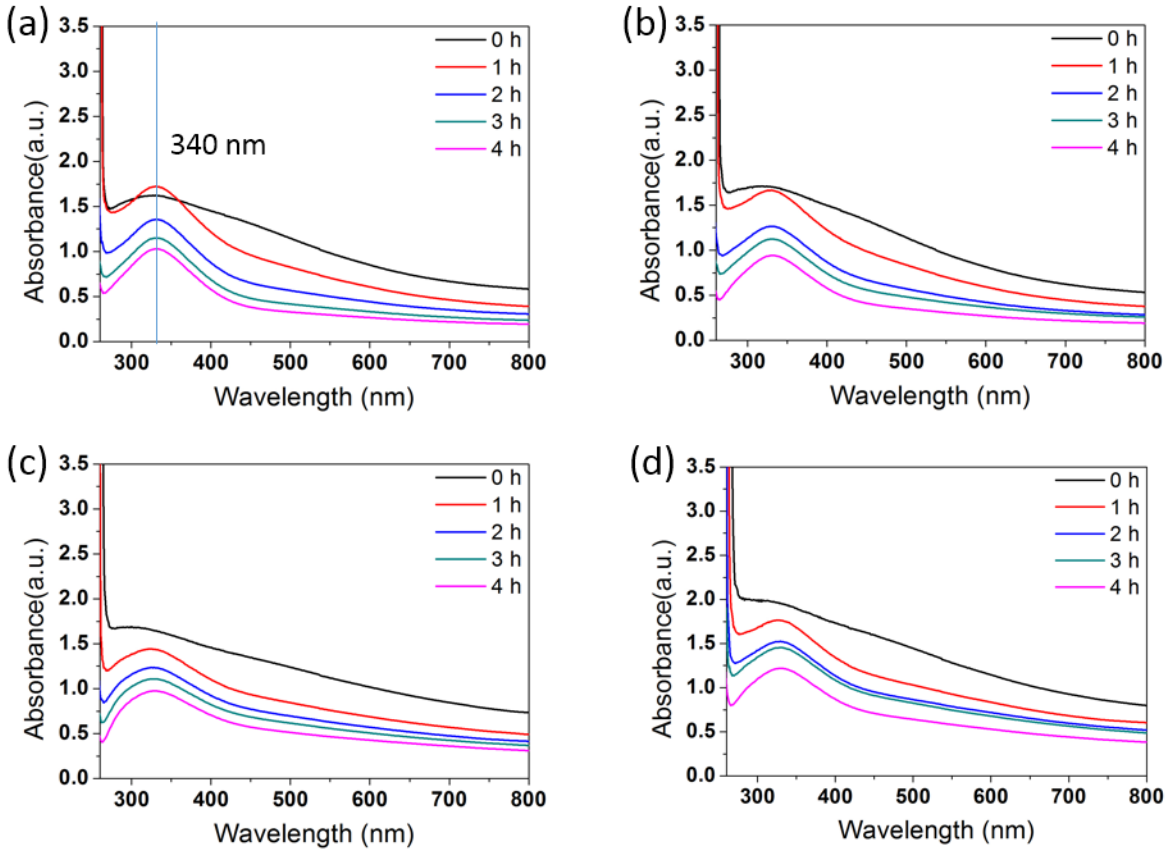

Figure 109 UV-Vis light absorption spectrum of VO_2@SiO_2@ZrO_2 multi-layered nanoparticles with different amount of Zr (IV) solution coating in H_2O_2 solution, (a) 10 uL Zr (IV) solution, (b) 20 uL Zr (IV) solution, (c) 50 uL Zr (IV) solution and (d) 100 uL Zr (IV) solution.

5.5.6 Results analysis

In last section, the ZrO_2 coating time was proven to be significant in the synthesis process. In this section, the amount of Zr (IV) butoxide solution was studied in the synthesis of VO_2@SiO_2@ZrO_2 core-shell nanoparticles.

Firstly, the SEM and TEM images were taken to characterize the morphology and core-shell structure. From the SEM images, the size distribution and dispersity are good even when the nanoparticles were synthesized with different amount of Zr (IV) butoxide solution. Based on the TEM images, the VO_2@SiO_2@ZrO_2 three-layer structure was clear. And with the increase of the Zr (IV) butoxide solution, the ZrO_2 layer is thicker. After the characterization of the nanoparticles. The chemical stability was studied. Based on the UV-Vis absorption spectrum, the increased Zr (IV)

butoxide solution can lead to a better stability, including acid resistance, alkali resistance and oxidation resistance.

It means the core-shell structure is useful for improving the stability of the VO_2 nanoparticles. And the increase of ZrO_2 coating amount can provide a better stability performance.

5.6 Thermochromic property

Similar with the VO_2 nanoparticles, the optical property of $VO_2@SiO_2@ZrO_2$ core-shell nanoparticles is also tested to check if the dual-layer structure can improve the thermochromic property of the samples. As we can see from Fig. 110, the transmittance spectra of the samples is similar to each other in high and low temperature. Furtherly, there is not significant difference even though the amount of Zr (IV) butoxide is increased from 10 µL to 100 µL.

In fact, the transmittance in high temperature should be much lower than the transmittance in low temperature, especially in NIR region. There are some reasons for the weak thermochromic property of the VO_2 films. Firstly, the thickness of the VO_2 film can affect the thermochromic property. The VO_2 films cannot exhibit an outstanding optical property if the VO_2 film is too thick. Secondly, the size distribution can also influent the optical properties dramatically. The VO_2 films can show a good optical property only with a uniform film. The preparation of VO_2 film may affect the final optical property, which seems that there is not good thermochromic property. More work should be performed to increase the film quality.

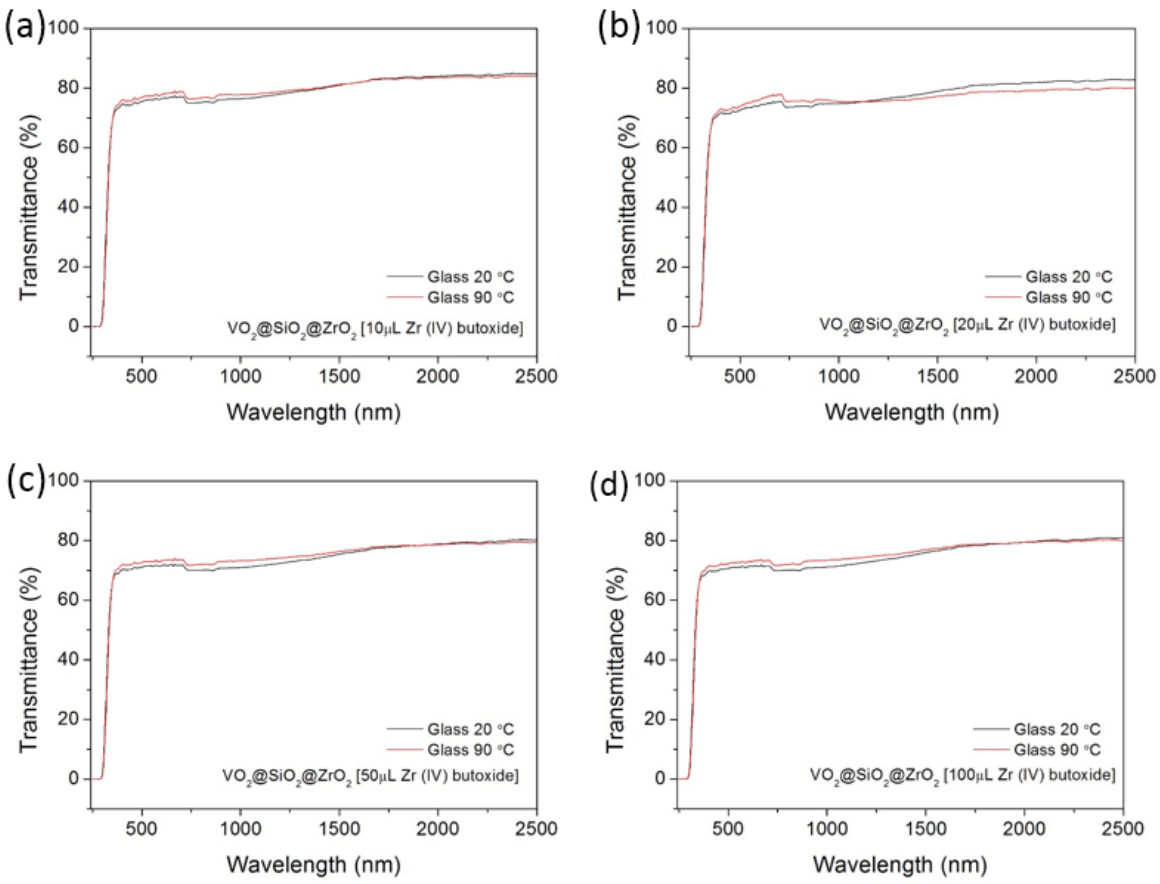

Figure 110 Transmittance spectra of VO_2@SiO_2@ZrO_2 core-shell nanoparticles with different amount of Zr (IV) butoxide solution in 20 °C and 90 °C respectively, (a) 10 µL (b) 20 µL, (c) 50 µL and (d) 100 µL Zr (IV) butoxide.

5.7 Summary

In this chapter, the VO_2@ZrO_2 core-shell nanostructure were tried to synthesize. However, the VO_2@ZrO_2 core-shell structure was difficult to be obtained even with different amount of Zr (IV) butoxide solution. And the application of surfactant (HPC) was not helpful to deal with the problem

Therefore, the VO_2@SiO_2@ZrO_2 multi-layered structure was attempt to synthesize. After the synthesis of VO_2@SiO_2 core-shell nanoparticles, the ZrO_2 layer was tried to synthesis on the surface of the SiO_2. And it was fabricated successfully. Moreover, the effect of the amount of TEOS, the coating reaction time and coating ZrO_2 amount was studied to get the optimized experimental parameters.

Firstly, the amount of TEOS was studied in the synthesis of VO_2@SiO_2@ZrO_2 core-shell structure. From the SEM and TEM characterization results, the morphology is good with the increase of the TEOS. Moreover, the stability of the core-shell structure was enhanced with thicker SiO_2 middle layer.

Secondly, the ZrO_2 coating reaction time was studied in the fabrication of VO_2@SiO_2@ZrO_2 core-shell structure. In terms of the ZrO_2 layer coating time, when the coating time is increased from ten minutes to two hours, a clear multilayer structure can be obtained.

Finally, the amount of Zr(IV) precursor amount was studied in the synthetic process. For the increase of the Zr(IV) precursor amount, a much thicker layer of ZrO_2 can be got. Besides the synthesis, the stability performance was also checked by using acid, alkali and oxidation solution. For all the VO_2@SiO_2@ZrO_2 multi-layered nanostructure, they have a better stability performance than the pure VO_2 nanoparticles. They maintain a better chemical stability when they meet acid solution (pH=5), alkali solution (pH=9) and H_2O_2 solution, which means that the ZrO_2 layer makes a crucial role in protecting the VO_2 core material.

Chapter 6 VO_2@TiO_2 nanocomposites synthesis

6.1 Introduction

Titanium dioxide, also known as titanium (IV) oxide or titania, is a very interesting material. It has numerous and diverse applications[194-198]. It can be used as sunscreens[199], photovoltaic cells[200], and different kinds of environmental and biomedical applications[201-202], such as photocatalytic degradation of pollutants[203-205], water purification[206-208], biosensing[209-211], and drug delivery[212].

As it exhibits photocatalytic activity under ultraviolet (UV) irradiation, it can be used as outdoor building materials. It can substantially reduce concentrations of airborne pollutants such as nitrogen oxides and volatile organic compounds. So it can be used in the development of self-cleaning glass and anti-fogging coating.

In this chapter, the synthesis of VO_2@TiO_2 was studied. Different amount of TiO_2 precursor and coating time were used to check if the VO_2@TiO_2 can be synthesized successfully. If the VO_2@TiO_2 core-shell nanoparticles can be synthesized, a new smart window coating with multifunction can be obtained. That will be a new start for the future window application which has thermochromic, anti-fogging, self-clean properties.

6.1.1 Materials and chemicals

Tetraethyl orthosilicate (TEOS), Titanium (IV) butoxide solution, ammonia water (wt.28%), ethanol (absolute) were purchased from Sigma-Aldrich Co. Australia and

stored at room temperature. VO_2 (M) nanoparticles are synthesized by the previous experiment. Deionized (DI) pure water was acquired from the local purest water company. All reagents were used directly without any treatment.

6.1.2 Experimental mechanism

The method used to synthesize TiO_2 shell is similar with the VO_2@ZrO_2 method.

Usually, metal alkoxides, M $(OR)_4$ are very reactive and can react with water vigorously. The high reactivity of metal alkoxides towards water leads to complex hydrolysis and polymerization chemistry. In the hydrolysis process, the alkoxo ($^-$OR) groups can be replaced by hydroxo (OH^-) or oxo (O^{2-}) ligands.

Dealcoholation and dehydration are two basic reaction for the hydroxyl-metal alkoxides (A) tend to react [213].

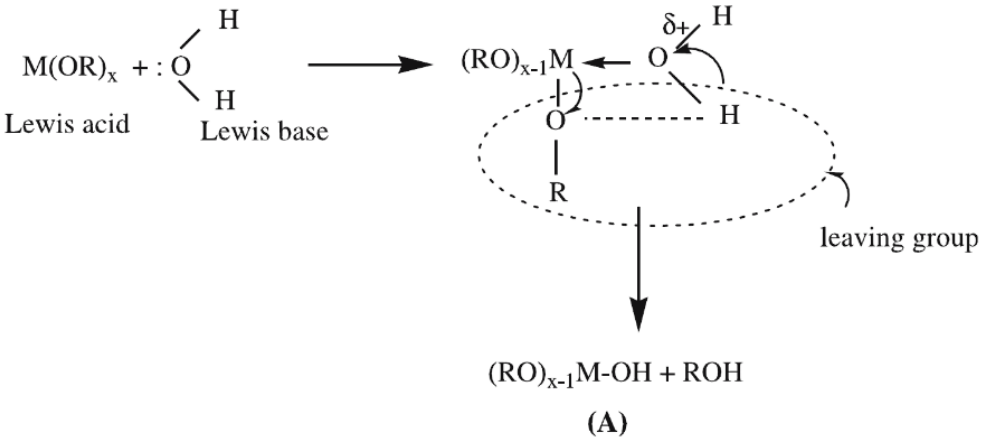

Figure 111 schematic diagram of the hydrolysis reaction

Dealcoholation:

$(RO)_{x-1}MOH + ROM(OR)_{x-1} \rightarrow (RO)_{x-1}MOM(OR)_{x-1}+ROH$

Dehydration:

$(RO)_{x-1}MOH + HOM(OR)_{x-1} \rightarrow (RO)_{x-1}MOM(OR)_{x-1} + H_2O$

Similar with the previous VO_2@ZrO_2 core-shell structure, the sol-gel method was used to synthesize the VO_2@TiO_2 core-shell sturcutre.

6.2 Synthesis of VO_2@TiO_2 core-shell nanoparticles

6.2.1 Synthesis process of VO_2@TiO_2 core-shell nanoparticles

Firstly, 0.01g VO_2 was dispersed in 25ml ethanol for 15 minutes. Then the titanium solution was prepared by dissolving 50ul, 60uL, 70uL, 80ul, 100ul, 500ul titanium (IV) butoxide (TBT) into 25ml ethanol solution for stirring 10 minutes.

After that, the titanium solution was added to the VO_2 suspension by 3 steps:

- 20 ml of TBT solution was added, then the mixture was sonicated for 10 minutes
- 20 ml of TBT solution was added , then the mixture was sonicated for 5 minutes
- 10ml of TBT solution was added , then the mixture was sonicated for 5 minutes

After that, the reaction time was continued for two hours. Finally, the particles were washed by DI water, dried at 60 °C and annealed at 500 °C.

	VO_2 (mg)	**Ethanol (mL)**	**TBT (μL)**	**Reaction time (h)**
A	10	50	50	2
B	10	50	60	2
C	10	50	70	2
D	10	50	80	2
E	10	50	100	2
F	10	50	500	2

Table 12 Experimental details of VO_2@TiO_2 core-shell nanoparticles with different amount of TBT.

6.2.2 TEM images of the VO_2@TiO_2 core-shell nanoparticles

TEM images were taken to check the VO_2@TiO_2 core shell structure with different amount of TBT. As we can see from Fig.112, there is no clear TiO_2 layer shell structure from (a) to (d). When the TBT amount increased from 80 to 100 µL, the thick TiO_2 layer appears suddenly. Therefore, it is difficult to get a clear and stable VO_2@TiO_2 core-shell nanoparticles. As a result, another method is needed to deal with this problem.

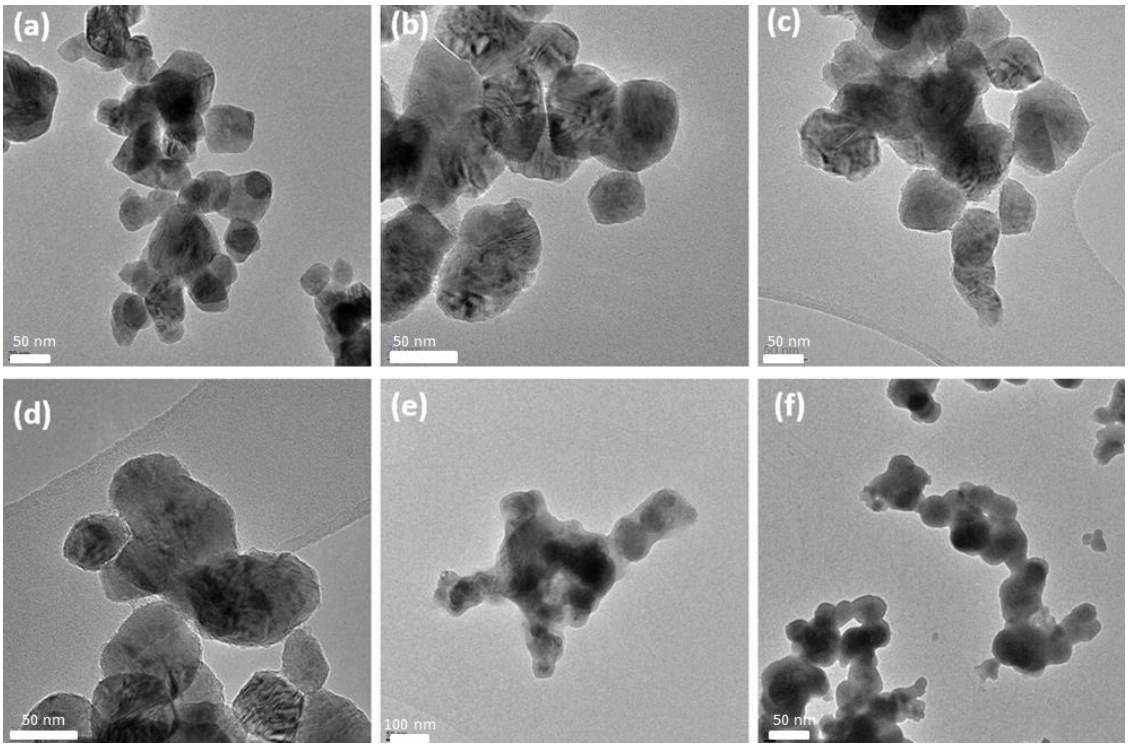

Figure 112 TEM images of VO_2@TiO_2 core-shell nanoparticles with different amount of TBT.(a) 50 µL TBT, (b) 60 µL TBT, (c) 70 µL TBT, (d) 80 µL TBT, (e) 100 µL TBT and (f) 500 µL TBT

6.3 Synthesis of VO_2@TiO_2 with assistance of surfactant

As the synthesis of VO_2@TiO_2 is difficult, a surfactant assisted method was tried to synthesize the core-shell nanoparticles. Two common used sufanctant polyvinylpyrrolidone (PVP) and poly dimethyl diallyl ammonium chloride (PDDA) were used to modify the synthesis.

Firstly, the VO_2 nanoparticles were dispersed into ethanol solution. Then some surfactant (PVP/PDDA) was added to the mixture to modify the surface of the VO_2 nanoparticles. After that, the surfactant was washed off by ethanol and only a little surfactant can be left on the surface of the VO_2 nanoparticles.

Then, the modified VO_2 nanoparticles were used as core material and the VO_2@TiO_2 core-shell structure was synthesized by a wet-chemistry method. The pretreated VO_2 particles were dispersed into ethanol solution. Then the titanium (IV) butoxide (TBT) solution was added to the solution. The mixture will be stirred until a uniform solution was formed. Then a little amount of water was added to start the hydrolysis reaction. After the hydrolysis reaction, the particles were washed by DI water and ethanol, then the particles were dried in 60 ˚C for 2 hours.

6.3.1 UV-Visible light absorption spectrum

After the synthesis of the VO_2@TiO_2 core-shell nanoparticles, the samples were dispersed into ethanol and the UV-Vis light spectrums were tested.

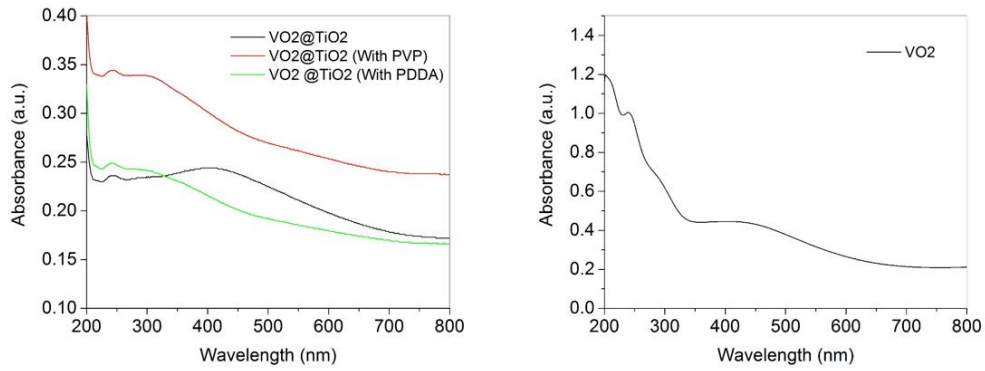

Figure 113 UV-Visible light absorption spectrum of VO_2 and VO_2@TiO_2 with PVP and PDDA.

As we can see from the image, the spectrum of VO_2@TiO_2 (no surfactant) and VO_2 were very similar. Both of them have an absorption peak at around 440 nm. However, the spectrum VO_2@TiO_2 (PVP/PDDA) were different from them. VO_2@TiO_2 (PVP) and VO_2@TiO_2 (PDDA) have an absorption peak at 310 nm rather than 440nm which means the VO_2@TiO_2 core-shell structure may be established with the help of PVP and PDDA.

Except the UV-Vis absorption spectrum, other analysis is necessary to prove the successful synthesis of VO_2@TiO_2 core-shell structure. TEM images will be taken in the next steps.

6.3.2 TEM images of VO_2@TiO_2 with surfactant

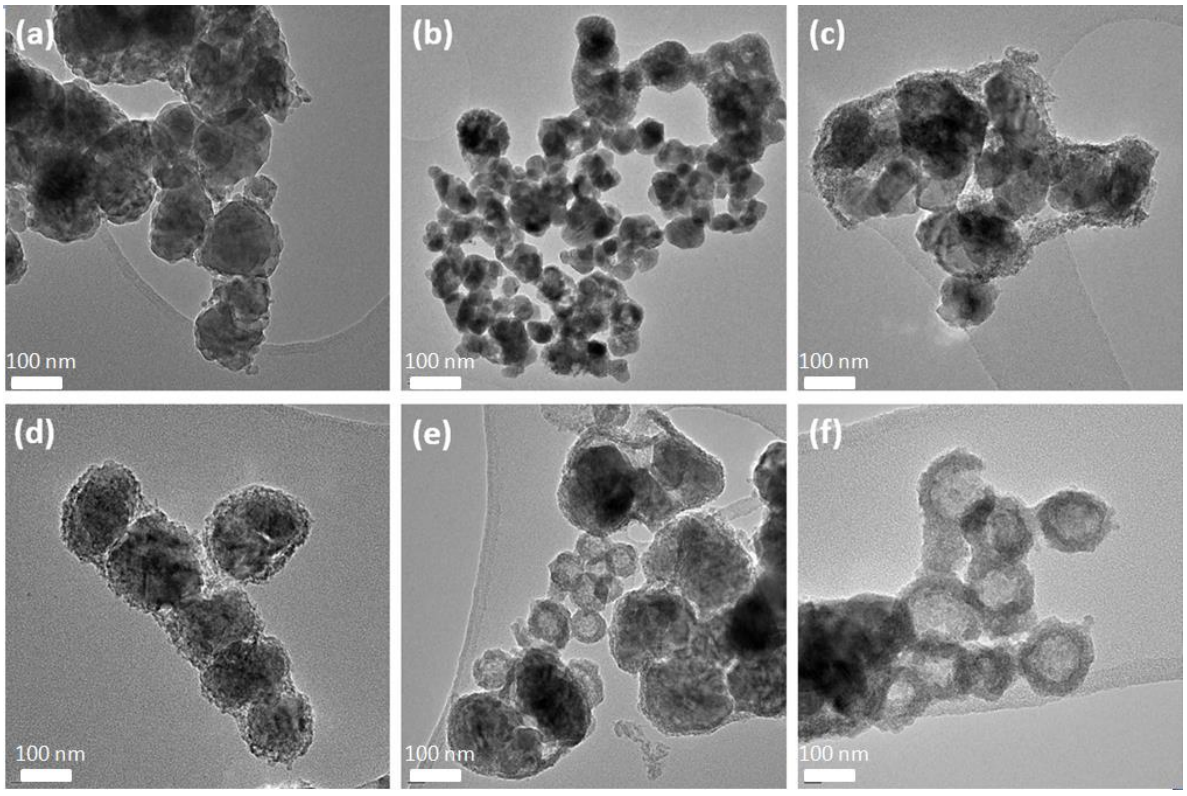

Figure 114 TEM images of VO_2@TiO_2 core-shell nanoparticles, (a,b)VO_2@TiO_2 core-shell nanoparticles, (c,d) VO_2@TiO_2 with PVP, (e,f) VO_2@TiO_2 with PDDA

TEM images of the VO_2@TiO_2 core-shell nanoparticles with and without the assistance of surfactant were shown in the above images As we can see from Fig.114, without the assistance of surfactant the core-shell structure is not clear (a,b). However, when the PVP and PDDA were added, a clear core-shell structure can be seen. For the PVP group, a thin TiO_2 layer can be seen on the surface of VO_2 nanoparticles. And the particle size is around 100 nm. For the PDDA group, the TiO_2 can be found on the surface of VO_2, however, there are some empty TiO_2 balls in the around area. The reason for the formation of TiO_2 empty balls is the existence of PDDA. With a special PDDA concentration, there will be a reverse micelle system which helps the synthesis of TiO_2 balls by a reverse microemulsion method. Moreover, for all the nanoparticles, the dispersity is a big problem, and the surfactant may lead to the accumulation of the nanoparticles.

6.3.3 Stability performances

As we have synthesized the VO_2@TiO_2 core-shell nanoparticles successfully, the resistance to environmental stimulate was also studied. The core-shell particles were dispersed into ethanol solution and the UV-Vis absorption spectrum were tested every 30 minutes against HCl solution (pH=5) and NaOH solution (pH=9). The spectrum comparisons of VO_2 nanoparticles, the VO_2@TiO_2 core-shell nanoparticles (no surfactant), the VO_2@TiO_2 core-shell nanoparticles (PVP) and VO_2@TiO_2 core-shell nanoparticles (PDDA) were shown in the following figures.

6.3.3.1 Acid resistance property of VO_2@TiO_2 core-shell nanoparticles

Firstly, for the acid resistance, all the VO_2@TiO_2 core-shell nanoparticles were dispersed into hydrochloric acid solution (pH=5), and the UV-Vis light absorption spectrum were tested in the above images.

For the UV-Vis light absorption spectrum, the absorption of VO_2, VO_2@TiO_2 has a huge difference with the time going on. For the pure VO_2 nanoparticles, VO_2@TiO_2 core-shell nanoparticles without surfactant, VO_2@TiO_2 core-shell nanoparticles with PVP, they all have a bad acid resistance. However, for the group of PDDA assisted synthesized nanoparticles, the change in UV-Vis absorption spectrum is smaller than other groups, which means that the core-shell structure has a better acid resistance than other nanoparticles.

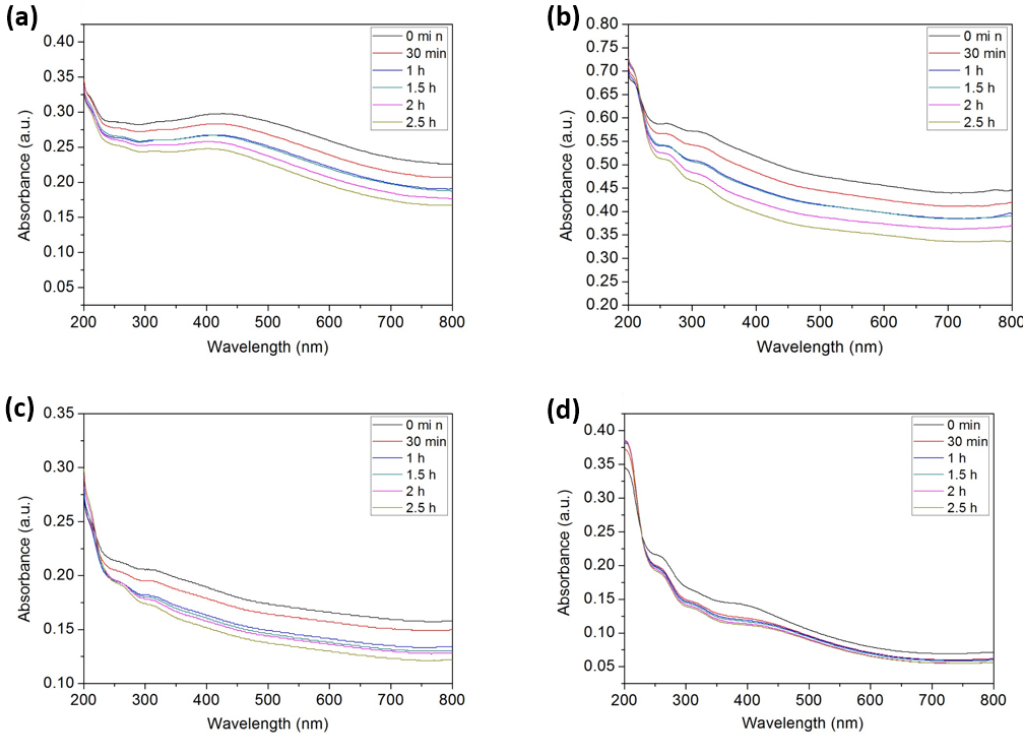

Figure 115 UV spectrum of different particles in acid solution (pH=5), (a) VO_2 nanoparticles, (b) VO_2@TiO_2 core-shell nanoparticles (c) VO_2@TiO_2 core-shell nanoparticles with PVP and (d) VO_2@TiO_2 core-shell nanoparticles with PDDA

6.3.3.2 Alkali resistance property of VO_2@TiO_2 core-shell nanoparticles

Secondly, for the alkali resistance, all the VO_2@TiO_2 core-shell nanoparticles were dispersed into NaOH solution (pH=9), and the UV-Vis light absorption spectrums were tested in the above image.

In terms of the UV-Vis light absorption spectrum, the absorption of VO_2, VO_2@TiO_2 have a big change with the time going on. For the pure VO_2 nanomaterial, VO_2@TiO_2 core-shell nanoparticles without surfactant, VO_2@TiO_2 core-shell nanoparticles with PVP, they changed dramatically in the UV-Vis absorption spectrum. However, for the group of PDDA assisted synthesized nanoparticles, the difference in UV-Vis absorption spectrum is smaller than other groups, which means that this core-shell structure has a better alkali resistance than other nanoparticles.

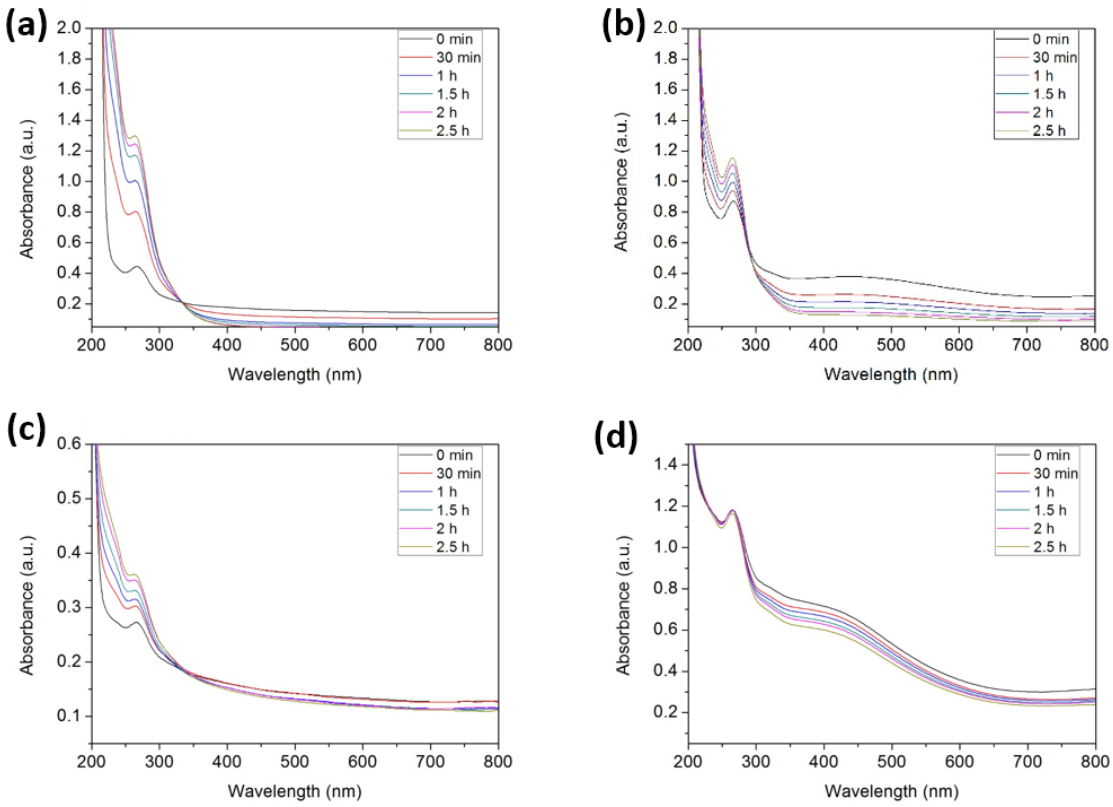

Figure 116 UV spectrum of different VO_2@TiO_2 core-shell nanoparticles in alkali solution (pH=9), (a) VO_2 nanoparticles, (b) VO_2@TiO_2 core-shell nanoparticles,(c) VO_2@TiO_2 core-shell nanoparticles with PVP and (d) VO_2@TiO_2 core-shell nanoparticles with PDDA.

6.3.4 Results Analysis

As the synthesis of VO_2@TiO_2 core-shell nanoparticles cannot give us a clear core-shell structure, a surfactant assisted method was used in this section.

In this section, the VO_2@TiO_2 were synthesized successfully by the assistance of PVP and PDDA. With the help of surfactant PVP and PDDA, a clear TiO_2 layer was grown on the surface of VO_2 nanoparticles through the TEM images.

After the synthesis of the core-shell particles, the stability performances were also measured by testing the UV-Vis absorption spectrum in acid and alkali conditions. Based on the change of the UV-Vis light spectrum, the results show that all the pure VO_2 nanoparticles, VO_2@TiO_2 core-shell nanoparticles without surfactant and with PVP did not have a good acid and alkali resistance. However, the VO_2@TiO_2 core-shell structure synthesized by the assistance of PDDA have a better resistance to acid and alkali atmosphere.

6.4 TiO_2 coating amount and VO_2@SiO_2@TiO_2 core-shell nanoparticle

In the previous chapter, a VO_2@SiO_2@ZrO_2 core-shell nanoparticles gives a better chemical stability. Therefore, besides the VO_2@TiO_2 core-shell nanoparticles, the VO_2@SiO_2@TiO_2 core-shell nanoparticles was also tried to synthesize to check if the multilayered structure has a better morphology and property.

6.4.1 Synthesis of VO_2@SiO_2@TiO_2 multilayered structure with different TiO_2 coating amount

Firstly, the VO_2@SiO_2 particles were synthesized as previous process, then the VO_2@SiO_2 particles were dispersed into 50 mL ethanol, and sonicated to get a uniform mixed solution. Then a Ti sourse solution is prepared by adding 1 mL Ti(IV) butoxide into 10mL ethanol (solution A). Then different amount of solutions were added to the previous mixed solutuion. After 30 minutes agitation, 500 µL water was added to start the hydrolysis reaction. And it reacted for 2 hours. Finally, the particles

were washed by ethanol 3 times and dried in the oven in 60 ˚C for 5 hours. Then the particles were annealed in 500℃ for 2 hours. The reaction details can be seen in the following table12.

	VO_2 (mg)	TEOS (μL)	Ti (IV) butoxide (μL)	Reaction time (h)
A	10	100	10	2
B	10	100	20	2
C	10	100	50	2
D	10	100	100	2

Table 13 Synthesis details of the VO_2@SiO_2@TiO_2 particles with different Ti (IV) butoxide, (a) 10 μL Ti (IV) butoxide，(b) 20 μL Ti (IV) butoxide, (c) 50 μL Ti (IV) butoxide and (d) 100 μL Ti (IV) butoxide.

6.4.2 SEM images VO_2@SiO_2@TiO_2 multilayered structure with different TiO_2 coating amount

SEM images of the VO_2@SiO_2@TiO_2 multilayered structure were measured to check the morphology of the particles with different TiO_2 coating amount.

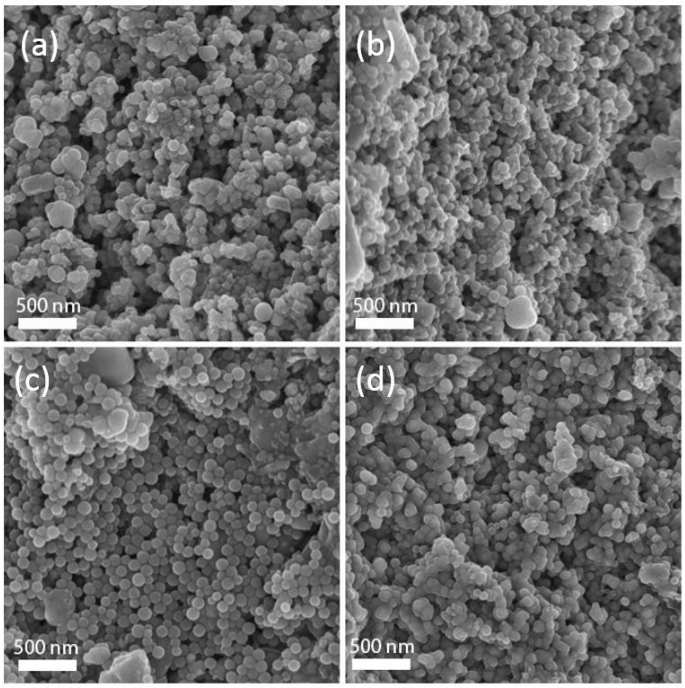

Figure 117 SEM images of VO_2@SiO_2@TiO_2 multi-layered nanostructure,(a) 10 µL Ti(IV) butoxide,(b) 20 µL Ti(IV) butoxide,(c) 50 µL Ti(IV) butoxide, (d) 100 µL Ti(IV) butoxide

6.4.3 TEM images VO_2@SiO_2@TiO_2 multilayered structure with different TiO_2 coating amount

After that, TEM images were measured to check the core-shell structure of the VO_2@SiO_2@TiO_2 multilayered particles.

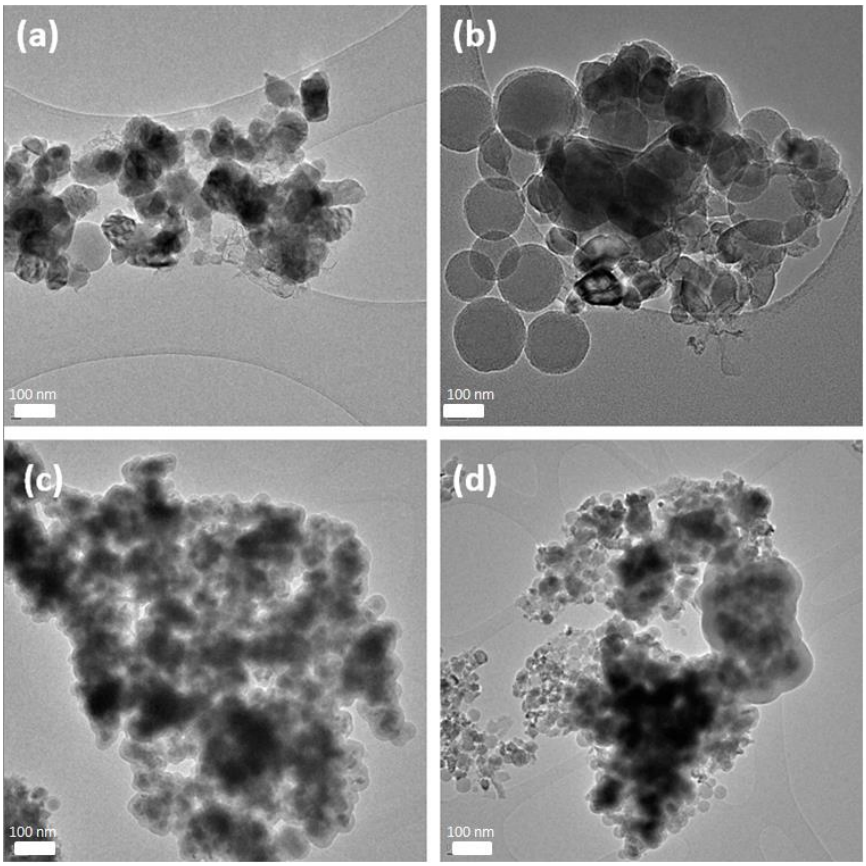

Figure 118 TEM images of VO_2@SiO_2@TiO_2 multi-layered nanostructure,(a) 10 µL Ti(IV) butoxide,(b) 20 µL Ti(IV) butoxide,(c) 50 µL Ti(IV) butoxide, (d) 100 µL Ti(IV) butoxide

As we can see from the TEM images, the TiO_2 can be coated on the surface of VO_2 in Fig 118 (c) (d), but when the amount of Ti (IV) butoxide increased, it prefers to become the TiO_2 balls by itself. After the increase of the Ti (IV) butoxide, many core-shell particles can be seen, but there are still some TiO_2 balls in the samples. The morphology of nanoparticles are not uniform and dispersed. More research need to do to increase the morphology.

6.4.4 XRD and EDS images of VO_2@SiO_2@TiO_2 multilayered structure with different TiO_2 coating amount

The composition information was tested by XRD equipment. X-ray diffraction (XRD) analyses were conducted on a Rigaku Miniflex 600 diffractometer (Japan) with Cu Kα radiation (λ¼1.5418 Å) using a voltage and current of 40 kV and 15 mA, respectively. The sample was measured at a scanning rate of 4°/min.

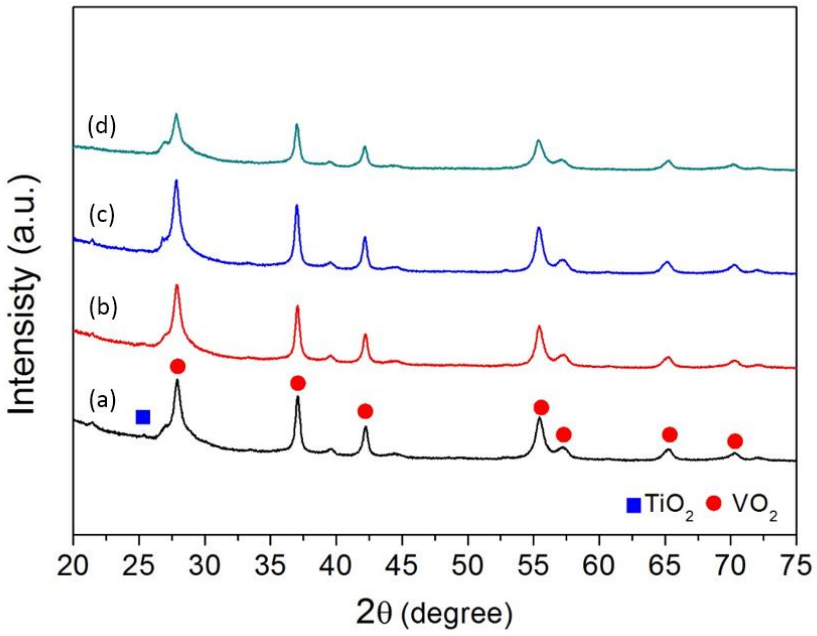

Figure 119 XRD spectra of VO_2@SiO_2@TiO_2 multi-layered nanostructure,(a) 10 µL Ti(IV) butoxide,(b) 20 µL Ti(IV) butoxide,(c) 50 µL Ti(IV) butoxide, (d) 100 µL Ti(IV) butoxide

VO_2 (M) information can be seen in the spectrum, and some TiO_2 can also been seen in the spectrum. However, the signal of TiO_2 is not strong because of the small coating amount. The lattice constants are a=5.75 Å, b= 4.52 Å, c=5.38Å. The planes such as (0 1 1), (-2 1 1), and (2 1 0) can be seen in the graph. There is no impurity detected in the sample. The EDS measurement was done to study the composition of the samples.

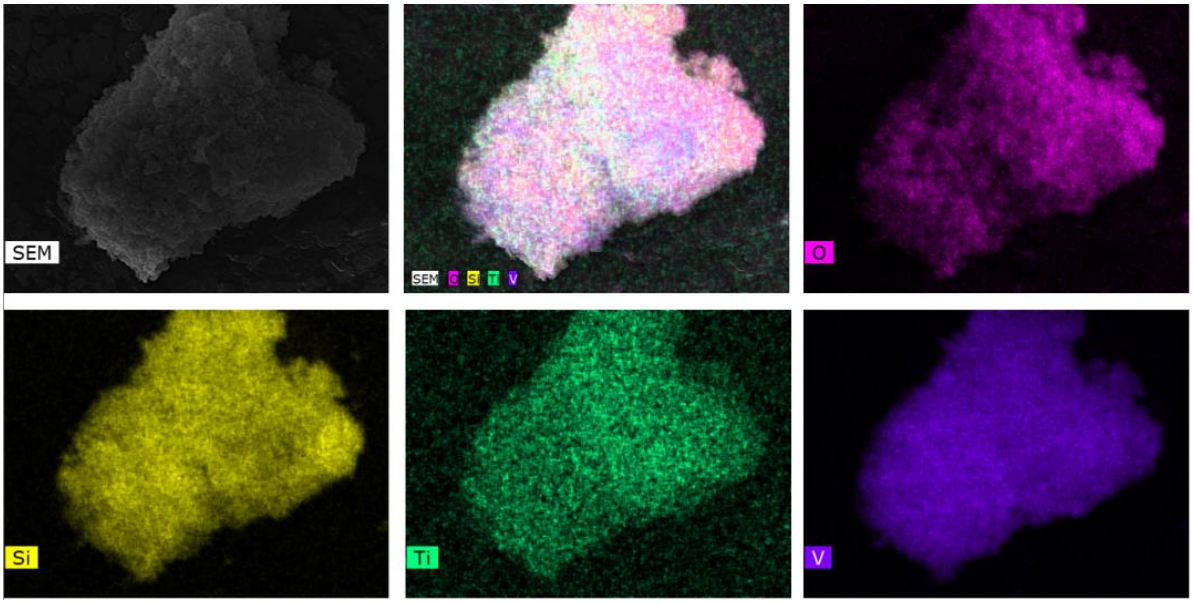

Figure 120 EDS mapping spectrum of the VO_2@SiO_2@TiO_2 multilayered particles.

From the EDS mapping spectrum, the existence of Ti element and Si element were obvious. And the shape of the elements shows that the Ti and Si were deposited on the surface of the VO_2 nanoparticles.

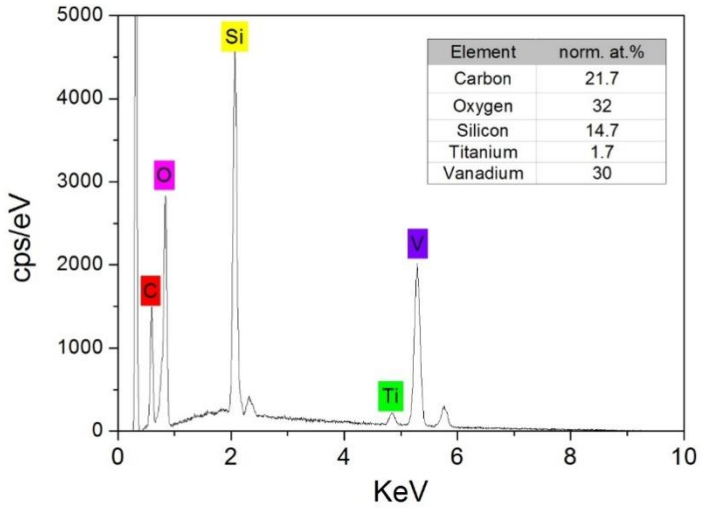

Figure 121 Element composition of the VO_2@SiO_2@TiO_2 multilayered particles.

The element composition image show that there is 1.7% Ti and 14.7% Si in the samples, which proves the existence of Ti and Si element. And it means the VO_2@SiO_2@TiO_2 multilayered structure has been synthesized successfully.

6.4.5 Acid resistance property

Except the morphology and composition of the VO_2@SiO_2@TiO_2 multilayered structure, the acid resistance property was also measured. The particles were dispersed in HCl (pH=5) solution and the UV-Vis light spectrums were tested.

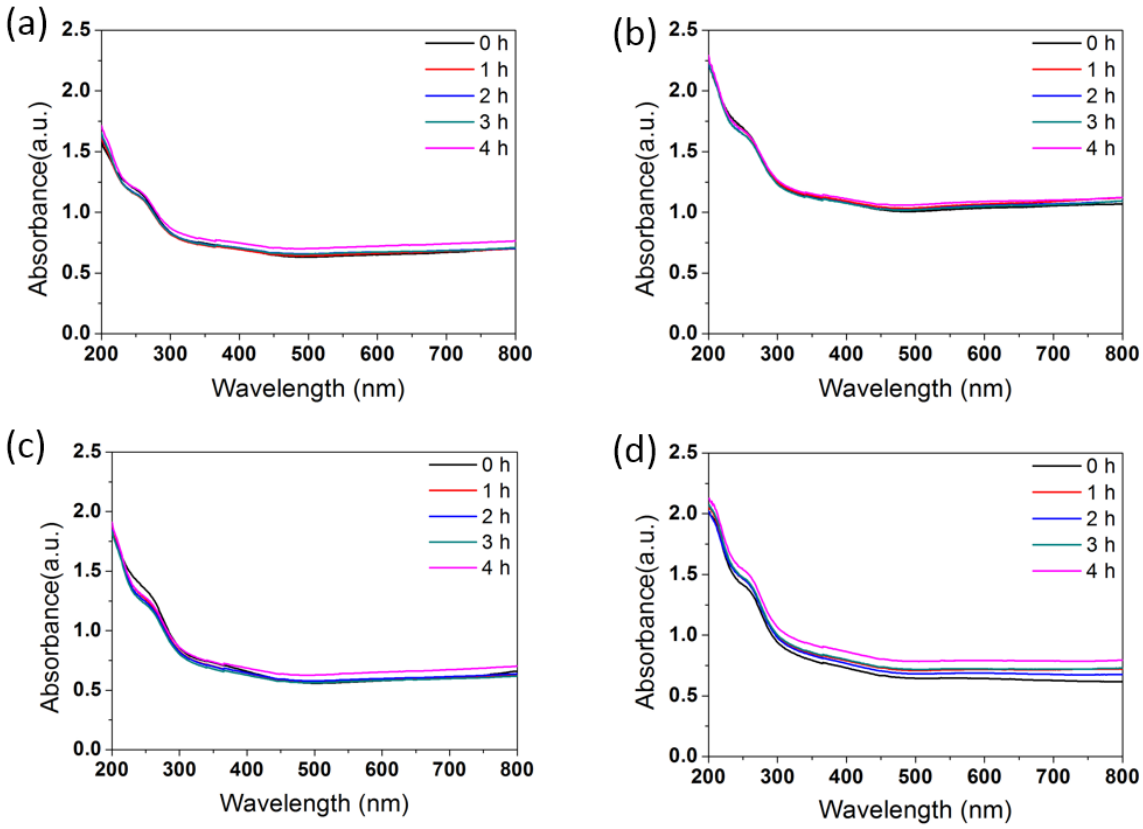

Figure 122 UV-Vis light absorption of VO_2@SiO_2@TiO_2 nanoparticles in acid solution (pH=5)with different amount of Ti(IV) butoxide,(a) 10 µL Ti(IV) butoxide,(b) 20 µL Ti(IV) butoxide,(c) 50 µL Ti(IV) butoxide, (d) 100 µL Ti(IV) butoxide

With different amount of Ti (IV) butoxide, the gaps between the lines were similar and small which means the core-shell structure was stable in the acid solution.

6.4.6 Results analysis

In this section, the VO_2@SiO_2@TiO_2 multilayered particles were synthesized. And the particles were synthesized with an increase of the Ti(IV) butoxide amount. The particles show good morphology. However, there are some TiO_2 balls in the samples, especially when the amount of Ti (IV) butoxide is increased. From the XRD images, the monoclinic VO_2 can be seen clearly, but the signal of TiO_2 was not clear because of the small coating amount. The EDX mapping shows the existence of TiO_2 and SiO_2 on the surface of VO_2 nanoparticles.

The core-shell structure has a good stability against the HCl (pH=5) solution. As the gaps between spectrum lines are small and stable.

6.5 TiO_2 coating reaction time and VO_2@SiO_2@TiO_2 core-shell nanoparticles

6.5.1 Synthesis process VO_2@SiO_2@TiO_2 multilayered structure with different TiO_2 coating reaction time

Except the TiO_2 coating amount, the TiO_2 coating reaction time was tested in this section. The synthesis process is similar with previous experiment, only the TiO_2 coating time is different. The experimental details can be seen in the following table.

	VO_2 (mg)	**TEOS (μL)**	**Ti (IV) butoxide (μL)**	**Reaction time (mins)**
A	10	100	50	10
B	10	100	50	30
C	10	100	50	60
D	10	100	50	120

Table 14 Synthesis details of the VO_2@SiO_2@TiO_2 particles with different reaction time.

6.5.2 SEM images VO_2@SiO_2@TiO_2 multilayered structure

Firstly, the morphology of the VO_2@SiO_2@TiO_2 core-shell nanoparticles were measured by SEM images. With different TiO_2 coating time, the difference can be seen from the images.

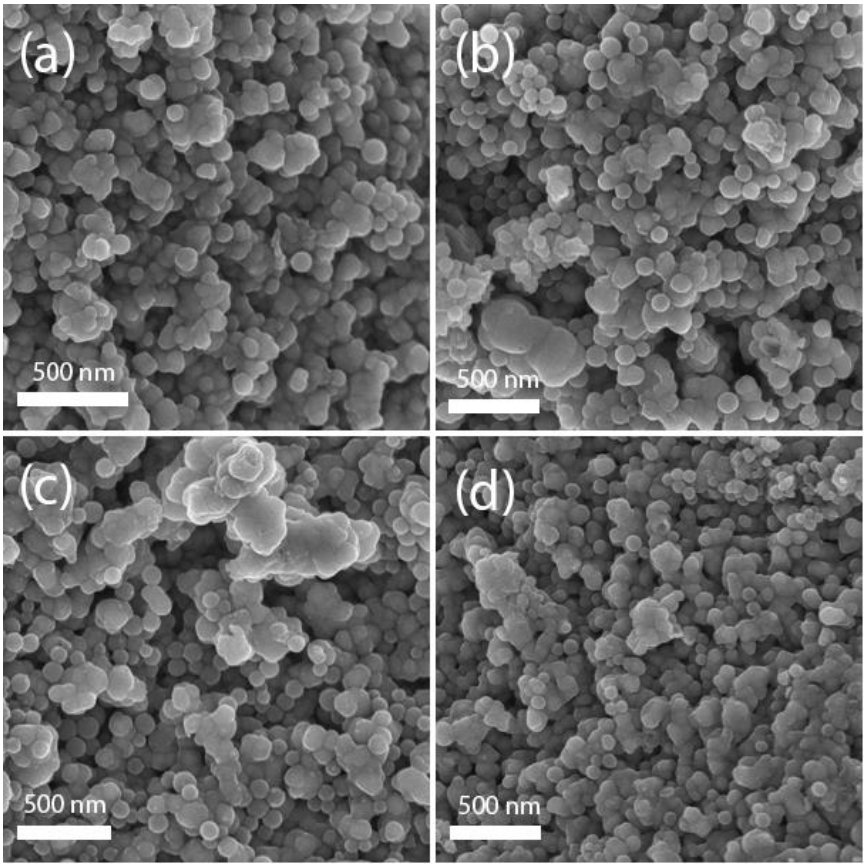

Figure 123 SEM images of VO_2@SiO_2@TiO_2 multi-layered nanostructure with different coating time, (a) 10 minutes, (b) 30 minutes, (c) 1 hour, (d) 2 hours

According to the images, the particles were dispersed well and the morphology was similar with the VO_2 (M) nanoparticles. And the size of the particles was around 100 nm. But we can also see some TiO_2 particles among the results, which means TiO_2 nanoaparticles are easy to form with different reaction time.

6.5.3 TEM images VO_2@SiO_2@TiO_2 multilayered structure

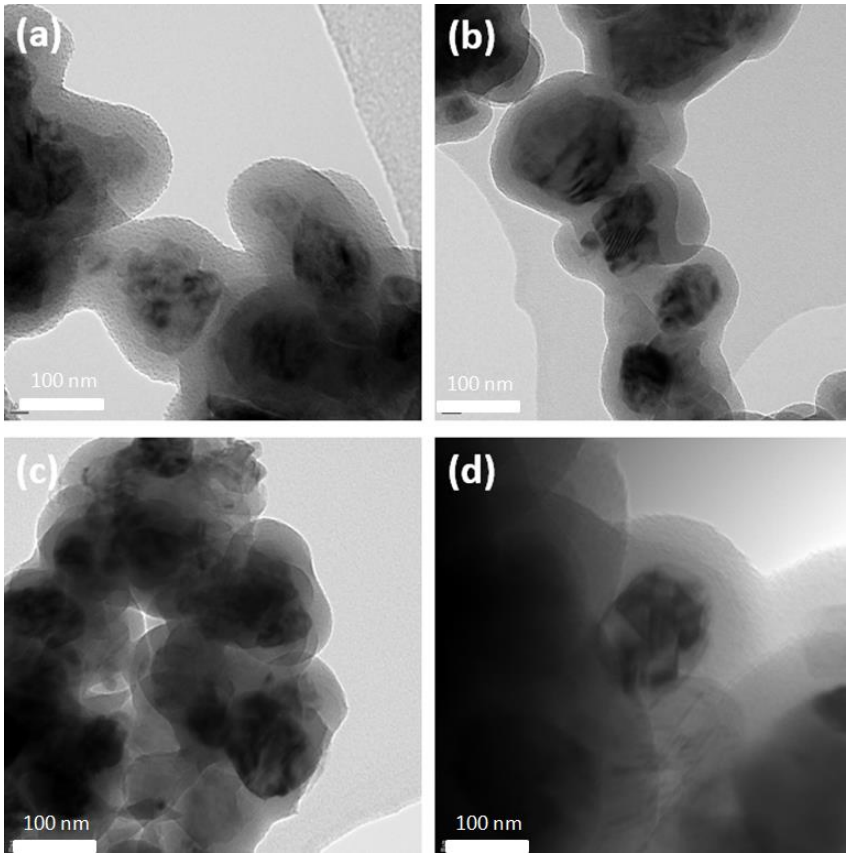

Figure 124 TEM images of VO_2@SiO_2@TiO_2 multi-layered nanostructure with different coating time,(a) 10 minutes ,(b) 30 minutes,(c) 1 hour, (d) 2 hours

TEM images were taken to check the core-shell structure of the VO_2@SiO_2@TiO_2 multilayered nanoparticles. In this image, the shell structure was clear and with the increase of the reaction time, the TiO_2 shell was thicker. But the shell might be SiO_2 shell rather than TiO_2 shell. The TiO_2 shell may be a very thin layer on the surface of SiO_2 layer.

With different magnification, the shell structure is transparent layer which is coated on the surface of VO_2 nanoparticles.

6.5.4 XRD spectra VO_2@SiO_2@TiO_2 multilayered structure

The compositional information was measured by the XRD equipment, X-ray diffraction (XRD) analyses were conducted on a Rigaku Miniflex 600 diffractometer (Japan) with Cu Kα radiation (λ¼1.5418 Å) using a voltage and current of 40 kV and 15 mA, respectively. The samples were measured at a scanning rate of 4°/min.

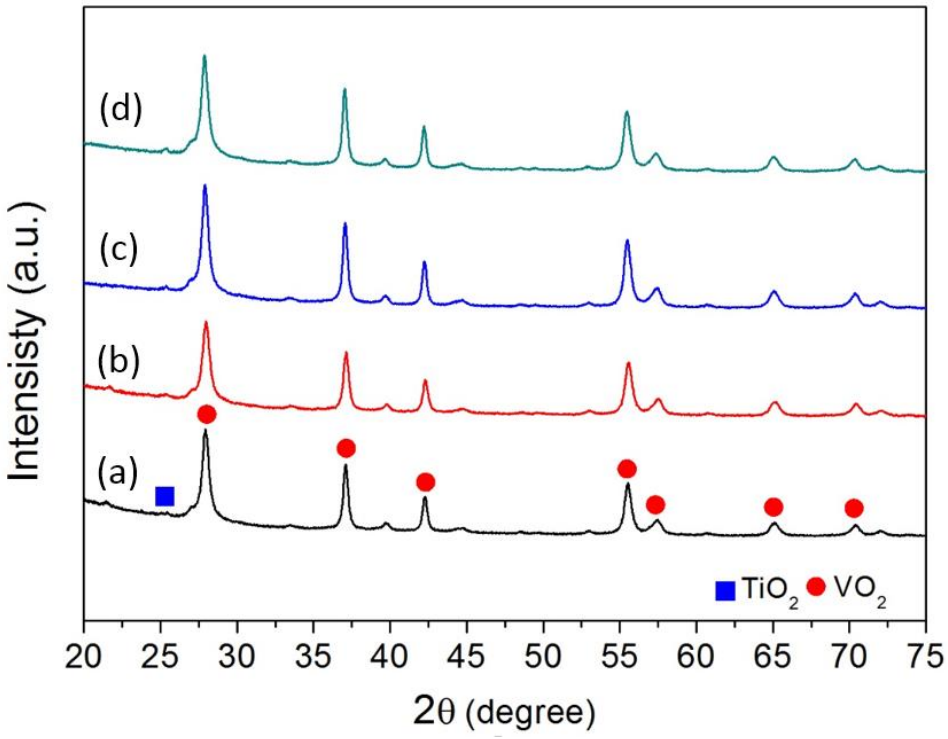

Figure 125 XRD spectra of VO_2@SiO_2@TiO_2 multi-layered nanostructure with different coating time,(a) 10 minutes ,(b) 30 minutes,(c) 1 hour, (d) 2 hours

Similar with the previous study, VO_2 (M) information can be seen in the spectrum, and some TiO_2 can also been seen in the spectrum However, the signal of TiO_2 is not strong because of the small coating amount. The lattice constants are a=5.75 Å, b= 4.52 Å, c=5.38Å. The planes such as (0 1 1), (-2 1 1), and (2 1 0) can be seen in the graph. There is no impurity detected in the sample.

6.5.5 Acid resistance property

Except the morphology and composition of the VO_2@SiO_2@TiO_2 multilayered structure, the acid resistance property were also measured. The particles were dispersed in HCl (pH=5) solution and the UV-Vis light spectrums were tested.

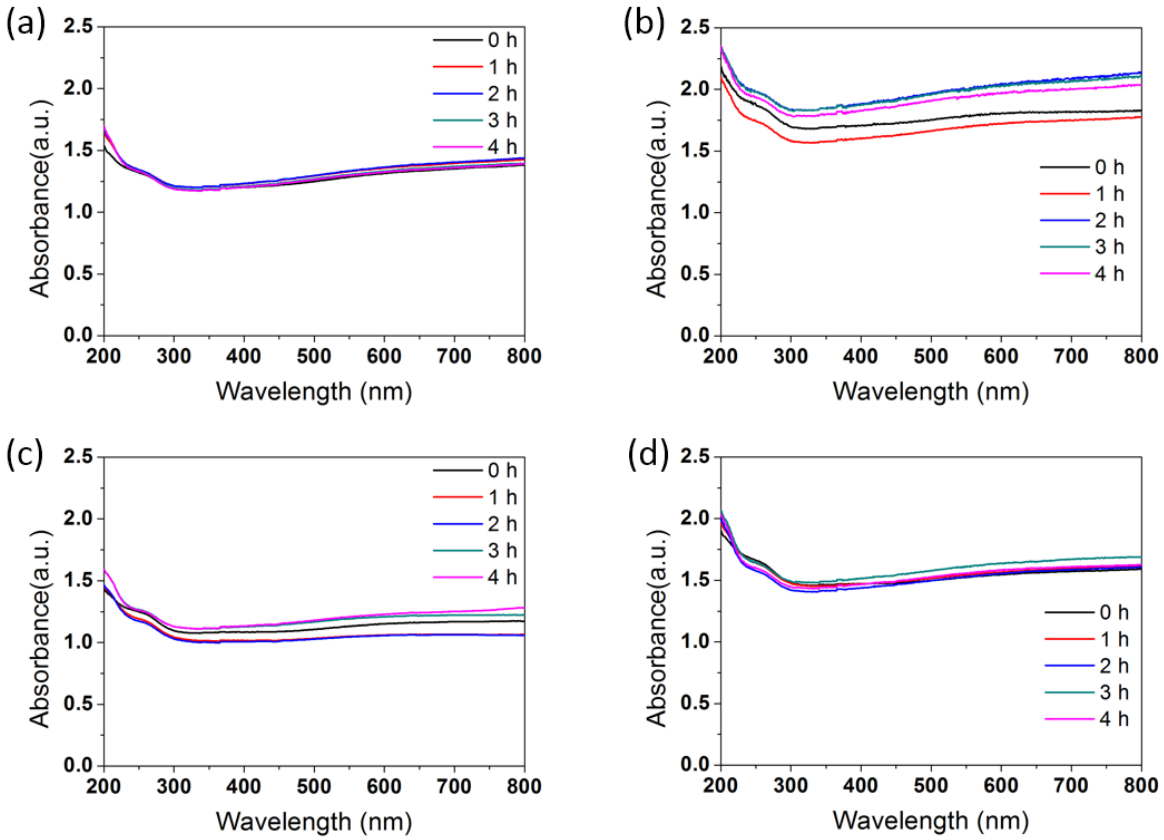

Figure 126 UV-Vis light absorption of VO_2@SiO_2@TiO_2 nanoparticles in acid solution (pH=5)with coating time,(a) 10 minutes ,(b) 30 minutes,(c) 1 hour, (d) 2 hours

The spectrum lines were also stable which means the synthesized structures have good stability even though the reaction time was increased from 10 minutes to 2 hours. The gaps between the UV-Vis absorption spectrum were small. However, there is not obvious trend of the acid resistance with different TiO_2 coating time.

6.5.6 Results analysis

In this section, the VO_2@SiO_2@TiO_2 multilayered particles were synthesized with different TiO_2 coating time from 10 minutes to 2 hours. The particles showed good morphology. But the core-shell structure was not clear. The TiO_2 layer was a thin layer on the surface of SiO_2 layer. And the TiO_2 tended to form nanoparticles by itself. From the XRD image, the monoclinic VO_2 can be seen easily. And only a small TiO_2 can be seen because of the small coating amount.

Moreover, the core-shell structure has a good stability against the HCl (pH=5) solution. As the gaps between spectrum lines were small and stable.

6.6 Amount of water and VO_2@SiO_2@TiO_2 core-shell nanoparticles

6.6.1 Synthesis process VO_2@SiO_2@TiO_2 multilayered structure with different amount of water

When the Ti (IV) butoxide was added into the TiO_2 coating reaction, some water was added to start the hydrolysis reaction. Therefore, the amount of water was studied in this section. The experimental process is similar with previous process, only the amount of water is different.

	VO_2 (mg)	**TEOS (μL)**	**Ti (IV) butoxide (μL)**	**Reaction time (min)**	**Amount of water (μL)**
A	10	100	10	60	100
B	10	100	20	60	200
C	10	100	50	60	500
D	10	100	100	60	1000

Table 15 Synthesis details of the VO_2@SiO_2@TiO_2 particles with different amount of water, (a) 100 µL water, (b) 200 µL water, (c) 500 µL water and (d) 1 mL water

6.6.2 SEM images VO_2@SiO_2@TiO_2 multilayered structure with different amount of water

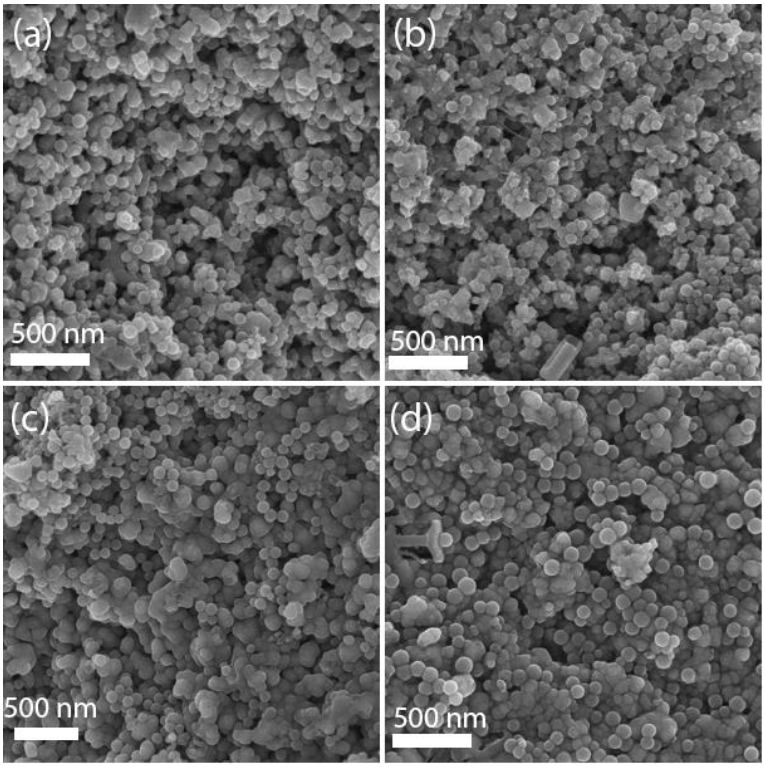

Figure 127 SEM images of VO_2@SiO_2@TiO_2 multi-layered nanostructure with different amount of water,(a) 100 µL,(b) 200 µL,(c) 500 µL, (d) 1 mL

The morphology of the VO_2@SiO_2@TiO_2 with different water in reaction was measured by the SEM images. According to the images, the particles were dispersed well and the morphology was similar to the VO_2 (M) nanoparticles. But similar with previous results, there are many TiO_2 balls among the final nanoparticles. The size of the particles is all among 100-150 nm.

6.6.3 TEM images VO_2@SiO_2@TiO_2 multilayered structure with different amount of water

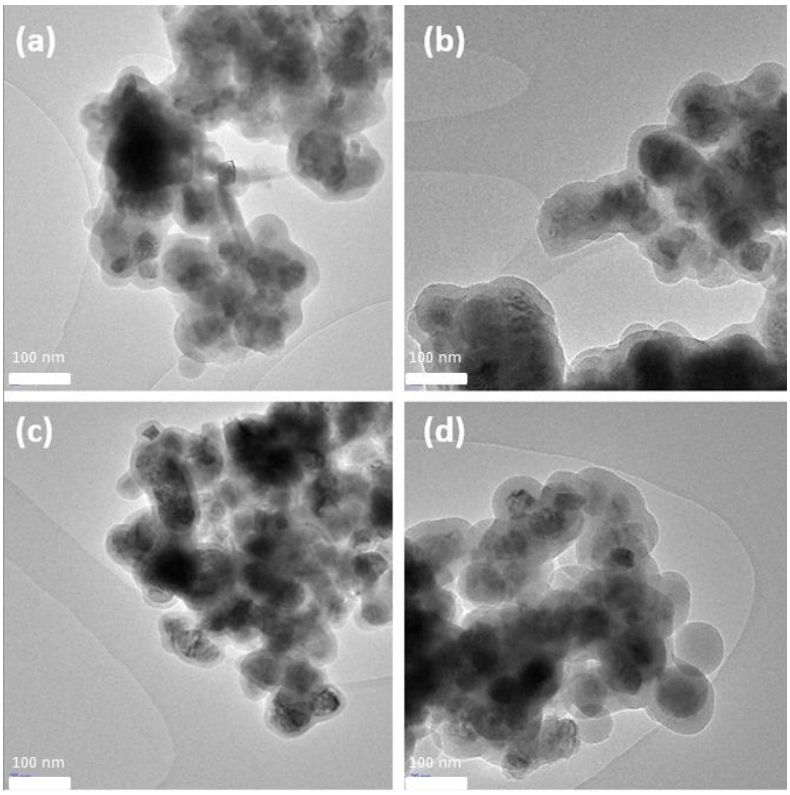

Figure 128 TEM images of VO_2@SiO_2@TiO_2 multi-layered nanostructure with different amount of water,(a) 100 µL,(b) 200 µL,(c) 500 µL, (d) 1 mL

TEM images were taken to check the core-shell structure of the VO_2@SiO_2@TiO_2 multilayered structure. From Fig.128 (a) to (d), the SiO_2 shell can be seen on the surface of VO_2 nanoparticles, but the TiO_2 was a very thin layer on the surface, which is not obvious. There were also some TiO_2 balls among the final results.

The reason is that TiO_2 balls were synthesized by a sol-gel method. The shell structure is thicker with the increase of water.

6.6.4 XRD spectra VO_2@SiO_2@TiO_2 multilayered structure with different amount of water

The compositional information was measured by the XRD equipment, X-ray diffraction (XRD) analyses were conducted on a Rigaku Miniflex 600 diffractometer (Japan) with Cu Kα radiation (λ¼1.5418 Å) using a voltage and current of 40 kV and 15 mA, respectively. The sample was measured at a scanning rate of 4°/min.

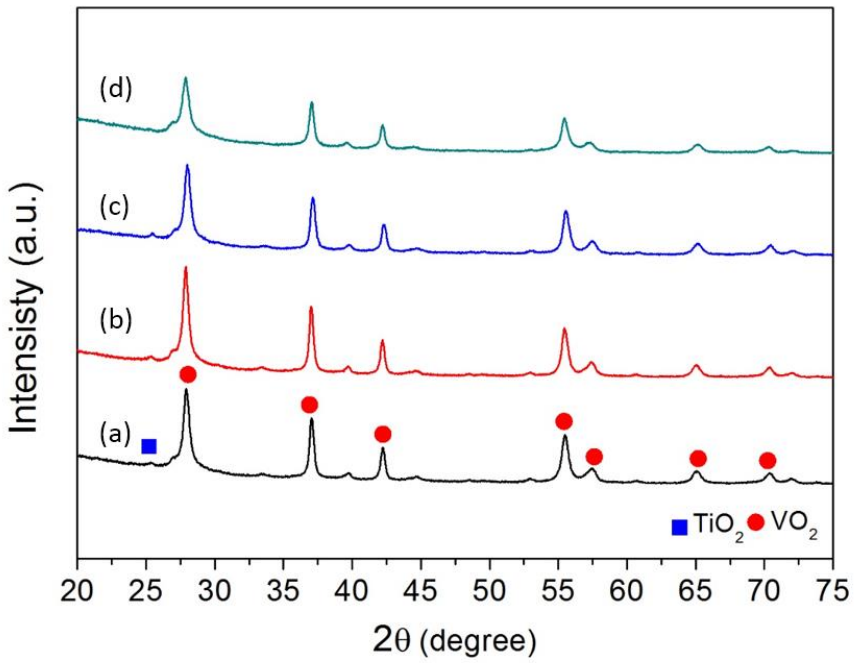

Figure 129 XRD spectra of VO_2@SiO_2@TiO_2 multi-layered nanostructure with different amount of water,(a) 100 µL,(b) 200 µL,(c) 500 µL, (d) 1 mL

Similar with the previous study, VO_2 (M) information can be seen in the spectrum, and some TiO_2 can also been seen in the spectrum. However, the signal of TiO_2 is still not strong because the small coating amount. The lattice constants are a=5.75 Å, b= 4.52 Å, c=5.38Å. The planes such as (0 1 1), (-2 1 1), and (2 1 0) can be seen in the graph. There is no impurity detected in the sample.

6.6.5 Acid resistance property

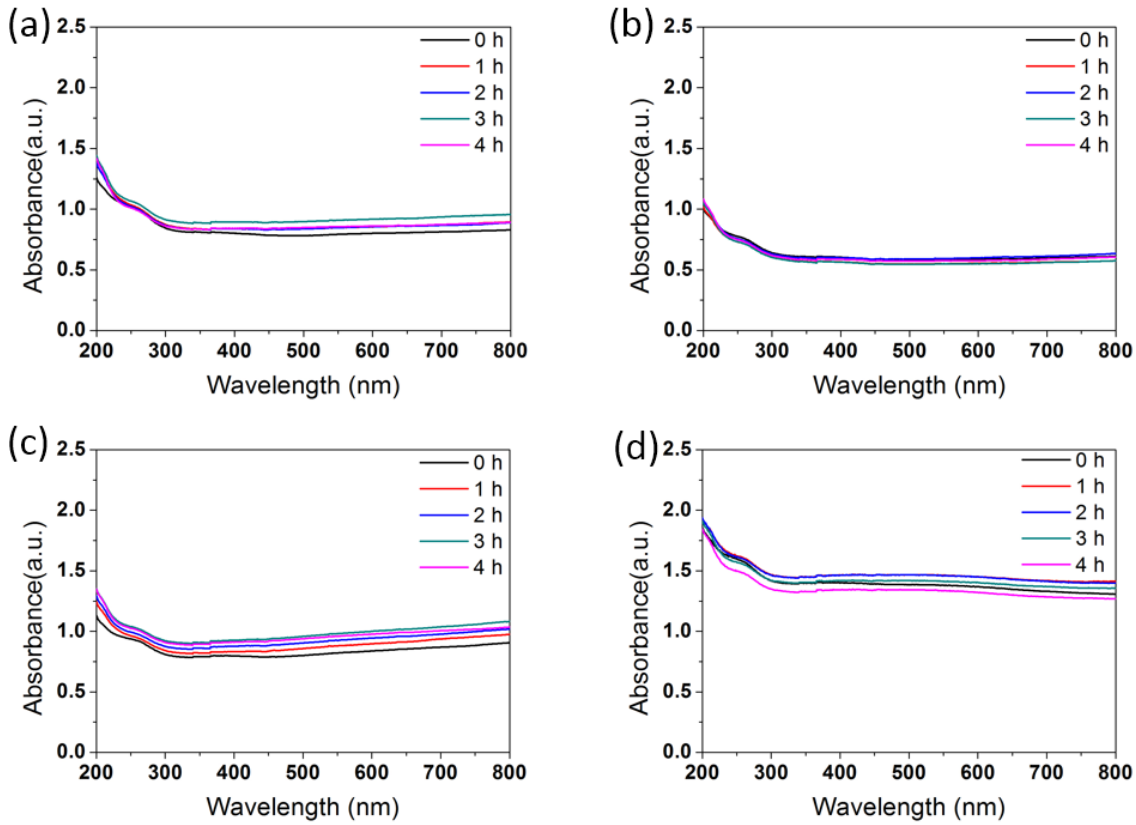

Figure 130 UV-Vis light absorption of VO_2@SiO_2@TiO_2 nanoparticles in acid solution (pH=5)with different amount of water,(a) 100 µL,(b) 200 µL,(c) 500 µL, (d) 1 mL.

Except the morphology and composition of the VO_2@SiO_2@TiO_2 multilayered structure, the acid resistance property was also measured. The particles were dispersed in HCl (pH=5) solution and the UV-Vis light spectrums were tested.

The spectrum lines were also stable which means the synthesized structure has a good stability even though the amount of water was increased from 100 µL to 1 mL. Overrally, the performance was not as good as the VO_2@SiO_2 core shell nanostructure. Therefore, more work need to be done to increase the performance of the VO_2@SiO_2@TiO_2 nanoparticles.

6.6.6 Results analysis.

In this section, the VO_2@SiO_2@TiO_2 multilayered particles were synthesized with different amount of water in the hydrolysis reaction. From the SEM images, the particles show good morphology. And the size of the nanoparticles is among 100-150 nm. From the TEM images, an obvious SiO_2 layer can be seen on the surface of VO_2 nanoparticles, but the TiO_2 is only a thin layer on the surface.

Moreover, the core-shell structure has a good stability against the HCl (pH=5) solution. As the gaps between spectrum lines are small and stable even with different amount of water in synthetic reaction.

6.7 Thermochromic property

Similar with the VO_2 nanoparticles, the optical property of VO_2@SiO_2@TiO_2 core-shell nanoparticles is also tested to check if the dual-layer structure can improve the thermochromic property of the samples. As we can see from Fig. 131, the transmittance spectra of the samples is similar to each other in high and low temperature. Moreover, there is not significant difference even though the amount of Ti (IV) butoxide is increased from 10 µL to 100 µL. The reason can be that the size distribution and the thickness of the film are not good enough.

Usually, the transmittance in high temperature should be much lower than the transmittance in low temperature, especially in NIR region. There are some reasons for the weak thermochromic property of the VO_2 films. Firstly, the thickness of the VO_2 film can affect the thermochromic property. The VO_2 films cannot exhibit an outstanding optical property if the VO_2 film is too thick. Secondly, the size distribution can also influent the optical properties dramatically. The VO_2 films can show a good optical property only with a uniform film. The preparation of VO_2 film may affect the

final optical property, which seems that there is not good thermochromic property. More work should be performed to increase the film quality.

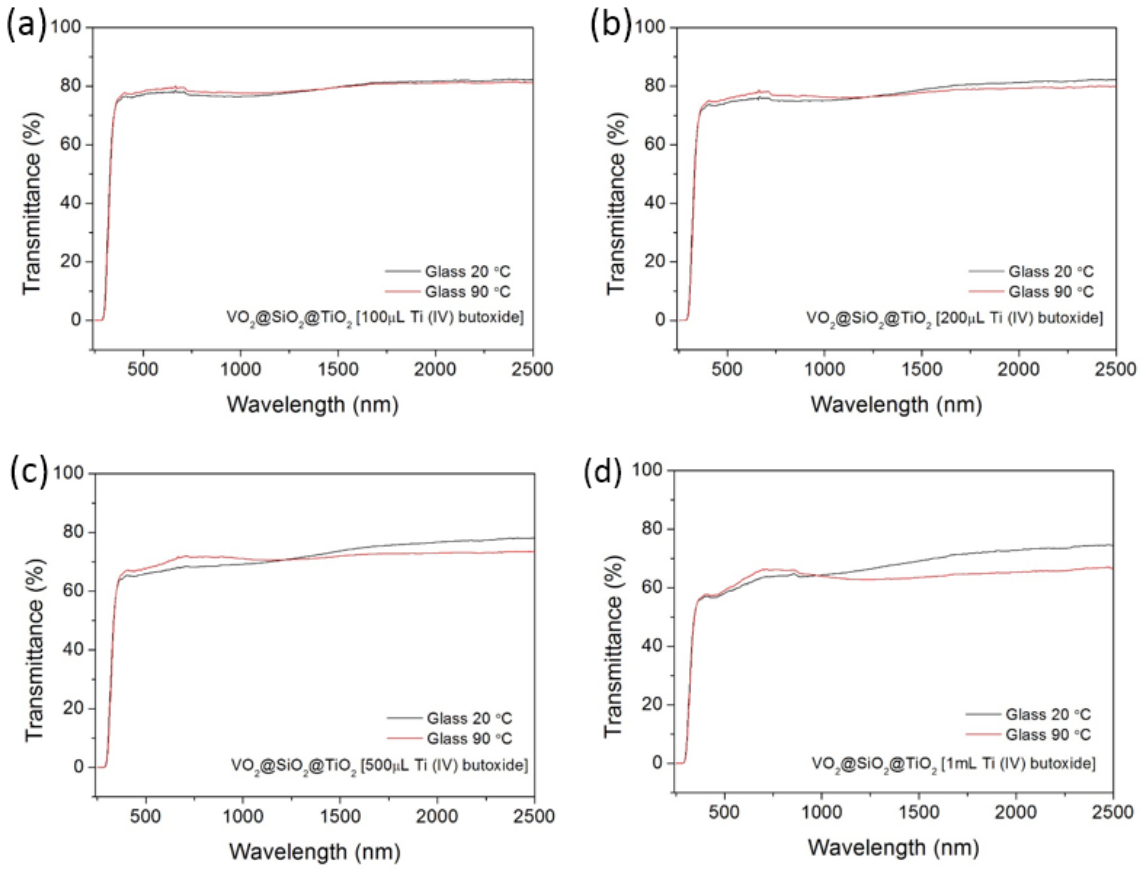

Figure 131 Transmittance spectra of VO_2@SiO_2@TiO_2 core-shell nanoparticles with different amount of Ti (IV) butoxide solution in 20 °C and 90 °C respectively, (a) 100 μL (b) 200 μL, (c) 500 μL and (d) 1 mL Ti(IV) butoxide.

6.8 Summary

In this chapter, the VO_2@TiO_2 was synthesized to protect the VO_2 nanoparticles. However, it is not like VO_2@SiO_2 core-shell structure, TiO_2 is difficult to grow on the surface of VO_2. Through the SEM images, it is difficult to control the TiO_2 layer on the surface of VO_2 nanoparticles.

Therefore, some surfactants (PVP and PDDA) were used to improve the results. By using the surfactants, a much clearer core-shell structure was got. A thin TiO_2 layer can be seen by the TEM images. And it shows a good acid and alkali resistance performance.

Besides, the VO_2@SiO_2@TiO_2 multi-layered structures were also tried to synthesis. Different experimental parameters were studied in the synthesis of VO_2@SiO_2@TiO_2 core–shell nanoparticles, including the TiO_2 coating time, TiO_2 coating amount and water used in the synthesis. From the SEM images, the morphology of the core-shell nanoparticles is uniform. However, there are many TiO_2 balls in the solution. The TiO_2 tends to form large particles by itself. Finally, the acid resistance of the multi-layered structure was tested in HCl solution (pH=5), and the results show that this structure is helpful in enhancing the stability of the VO_2 (M) nanoparticles. But it is not as strong as the SiO_2 shell structure and ZrO_2 shell structure.

Chapter 7 Conclusions and future work

7.1 Research conclusions

In this research, the VO_2 nanoparticles and relative core-shell nanoparticles were synthesized successfully. The characterizations and properties were measured after the successful synthesis.

For the synthesis of VO_2 nanoparticles. It was fabricated by a hydrothermal method. And the optimal method of the synthesis was studied. It is found that the nanoparticle size and morphology can be affected by changing hydrazine amount in the hydrothermal process. Besides the amount of hydrazine amount, some other studies were also done. In terms of the post-annealing progress, it is essential to get a monoclinic phase VO_2 through a high temperature annealing process. However, a heavy particle aggregation will occur at the same time, the grinding method and ultrasonic treatment were found useful to increase the dispersity of the samples. Moreover, the optimal annealing temperature was studied to minimize the aggregation problem and reduce the energy cost of the synthesis. By studying the composition information of the samples annealed at different temperature, the best annealing temperature will be 660 ˚C.

After that, the research was focused on the protection of the VO_2 nanoparticles.

Firstly, $VO_2@SiO_2$ core-shell nanoparticles were synthesized successfully. A very clear core-shell structure can be seen in the TEM images. Many experimental parameters were studied in the synthesis process. From the results, the concentration of TEOS and reaction time can affect the shell thickness of the core-shell particles. After that, the resistance properties of the core-shell nanoparticles were measured. By comparing the pure VO_2 nanoparticles and $VO_2@SiO_2$ core-shell nanoparticles, the core-shell nanoparticles have a better resistance to acid/alkali

corrosion, resistance to oxidation and UV light. It proves that the VO_2@SiO_2 core-shell structure can really protect the VO_2 material.

Secondly, except the VO_2@SiO_2 core-shell nanostructure, the VO_2@ZrO_2 core-shell structure was also used to protect the VO_2 particles. However, it is found that VO_2@ZrO_2 cannot be synthesied easily. The reason might be that the ZrO_2 is difficult to grow on the surface of VO_2 because of the same electrical potential. Therefore, a VO_2@SiO_2@ZrO_2 multi-layered structure was used to deal with this problem. In this research, optical experimental parameters were studied including the ZrO_2 coating time and ZrO_2 coating amount. A clear multilayer structure was successfully synthesized. Moreover, the resistance properties against acid, alkali and oxidation solution were also tested. The results show that it also has acceptable chemical stability performance.

Finally, the VO_2@TiO_2 was furtherly studied to protect the VO_2. In this research, the VO_2@TiO_2 was used to synthesis with or without the assistance of surfactant (PVP, PDDA). And it shows that the surfactant is beneficial to get a better core-shell structure. On the other hand, the VO_2@SiO_2@TiO_2 was also tried to be synthsized. The core-shell structure can be seen by the TEM images but there are many TiO_2 balls in the solution. In the same way, the resistance agianst the acid solution was tested. Even though the TiO_2 layer is unclear, the VO_2@TiO_2 still has a good resistance ability.

In summary, in my research, VO_2 nanoarpticles and VO_2 core-shell structrues, such as VO_2@SiO_2, VO_2@SiO_2@ZrO_2, VO_2@TiO_2 and VO_2@SiO_2@TiO_2 are successfully synthesized. Among them, VO_2@SiO_2, VO_2@SiO_2@ZrO_2 core-shell particles have good resistance against acid, alkali and oxidation solutions.

7.2 Future work

In the future, there are still many work to be compeleted.

Firstly, the VO_2@TiO_2 core-shell structure needs a futher study to improve its composition. It is important to avoid the existance of TiO_2 particles as it is a potential material for multifunctional windows application. It will combine the thermochromic ability of VO_2 and photocatalytic ability of TiO_2.

Secondly, the VO_2 nanoparticles and VO_2 core-shell nanocomposites need to be made into film by depositing on the surface of glass. For the stability of the film, a similar test need to be finished to measure the stability performance of the films.

Lastly, the size distribution of VO_2 nanocomposites should be modified to make a more uniform VO_2 film. In terms of the thermochormic property of all the VO_2 nanocomposites, the thickness of the film should be controlled to improve the optical performance.

References

1. Mott, N. F.; Friedman, L., Metal-insulator transitions in VO2, Ti2O3 and Ti2-x V x O3. *Philosophical Magazine* **1974,** *30* (2), 389-402.
2. Withers, P. C., Measurement of VO2, VCO2, and evaporative water loss with a flow-through mask. *Journal of Applied Physiology* **1977,** *42* (1), 120-123.
3. Goodenough, J. B., The two components of the crystallographic transition in VO2. *Journal of Solid State Chemistry* **1971,** *3* (4), 490-500.
4. Mendialdua, J.; Casanova, R.; Barbaux, Y., XPS studies of V2O5, V6O13, VO2 and V2O3. *Journal of Electron Spectroscopy and Related Phenomena* **1995,** *71* (3), 249-261.
5. Stefanovich, G.; Pergament, A.; Stefanovich, D., Electrical switching and Mott transition in VO2. *Journal of Physics: Condensed Matter* **2000,** *12* (41), 8837.
6. Eyert, V., The metal-insulator transitions of VO2: A band theoretical approach. *arXiv preprint cond-mat/0210558* **2002**.
7. Morin, F. J., Oxides Which Show a Metal-to-Insulator Transition at the Neel Temperature. *Physical Review Letters* **1959,** *3* (1), 34-36.
8. Jensen, K. F., Chemical vapor deposition. ACS Publications: 1989.
9. Park, J.-H.; Sudarshan, T., *Chemical vapor deposition*. ASM international: 2001; Vol. 2.
10. Reina, A.; Jia, X.; Ho, J.; Nezich, D.; Son, H.; Bulovic, V.; Dresselhaus, M. S.; Kong, J., Large area, few-layer graphene films on arbitrary substrates by chemical vapor deposition. *Nano letters* **2008,** *9* (1), 30-35.
11. Wu, J. J.; Liu, S. C., Low‐temperature growth of well‐aligned ZnO nanorods by chemical vapor deposition. *Adv Mater* **2002,** *14* (3), 215-218.
12. Koide, S.; Takei, H., Epitaxial growth of VO2 single crystals and their anisotropic properties in electrical resistivities. *Journal of the Physical Society of Japan* **1967,** *22* (3), 946-947.
13. Vernardou, D.; Louloudakis, D.; Spanakis, E.; Katsarakis, N.; Koudoumas, E., Thermochromic amorphous VO 2 coatings grown by APCVD using a single-precursor. *Solar Energy Materials and Solar Cells* **2014,** *128*, 36-40.
14. Wilkinson, M.; Kafizas, A.; Bawaked, S. M.; Obaid, A. Y.; Al-Thabaiti, S. A.; Basahel, S. N.; Carmalt, C. J.; Parkin, I. P., Combinatorial atmospheric pressure chemical vapor deposition of graded TiO2–VO2 mixed-phase composites and their dual functional property as self-cleaning and photochromic window coatings. *ACS combinatorial science* **2013,** *15* (6), 309-319.
15. Crane, J.; Warwick, M.; Smith, R.; Furlan, N.; Binions, R., The application of electric fields to aerosol assisted chemical vapor deposition reactions. *Journal of The Electrochemical Society* **2011,** *158* (2), D62-D67.
16. Warwick, M. E.; Ridley, I.; Binions, R., Thermochromic vanadium dioxide thin films from electric field assisted aerosol assisted chemical vapour deposition. *Surface and Coatings Technology* **2013,** *230*, 163-167.
17. Westwood, W., Physical vapor deposition. In *Microelectronic Materials and Processes*, Springer: 1989; pp 133-201.
18. Kong, Y.; Yu, D.; Zhang, B.; Fang, W.; Feng, S., Ultraviolet-emitting ZnO nanowires synthesized by a physical vapor deposition approach. *Applied Physics Letters* **2001,** *78* (4), 407-409.
19. Narayan, J.; Tiwari, P.; Chen, X.; Singh, J.; Chowdhury, R.; Zheleva, T., Epitaxial growth of TiN films on (100) silicon substrates by laser physical vapor deposition. *Applied physics letters* **1992,** *61* (11), 1290-1292.
20. Jeong, J.; Lee, J.; Lee, C. J.; An, S.; Yi, G.-C., Synthesis and characterization of high-quality In2O3 nanobelts via catalyst-free growth using a simple physical vapor deposition at low temperature. *Chemical Physics Letters* **2004,** *384* (4-6), 246-250.
21. Moutinho, H.; Hasoon, F.; Abulfotuh, F.; Kazmerski, L., Investigation of polycrystalline CdTe thin films deposited by physical vapor deposition, close‐spaced sublimation, and sputtering. *Journal of Vacuum Science & Technology A: Vacuum, Surfaces, and Films* **1995,** *13* (6), 2877-2883.
22. Grave, D. A.; Schmitt, M. P.; Robinson, J. A.; Wolfe, D. E., Stress induced phase transition in Gd 2 O 3 films by ion beam assisted reactive electron beam-physical vapor deposition (EB-PVD). *Surface and Coatings Technology* **2014,** *242*, 68-73.
23. Djouadi, M.; Vasin, A.; Nouveau, C.; Angleraud, B.; Tessier, P., Deposition of boron nitride films by PVD methods: transition from h-BN to c-BN. *Surface and Coatings Technology* **2004,** *180*, 174-177.
24. Rymarczyk, J.; Czerwosz, E.; Kozłowski, M.; Dłużewski, P.; Kowalski, W., The influence of technological PVD process parameters on the topography, crystal and molecular structure of nanocomposite films containing palladium nanograins. *Polish Journal of Chemical Technology* **2014,** *16* (3), 18-24.
25. Livage, J., Vanadium pentoxide gels. *Chemistry of Materials* **1991,** *3* (4), 578-593.
26. Liu, S.-J.; Fang, H.-W.; Su, Y.-T.; Hsieh, J.-H., Metal–insulator transition characteristics of Mo-and Mn-doped VO2 films fabricated by magnetron cosputtering technique. *Japanese Journal of Applied Physics* **2014,** *53* (6), 063201.

27. Fuls, E.; Hensler, D.; Ross, A., Reactively sputtered vanadium dioxide thin films. *Applied Physics Letters* **1967,** *10* (7), 199-201.
28. Batista, C.; Teixeira, V., VO2-Based Thermochromic Thin Films for Energy Efficient Windows.
29. Jiang, M.; Li, Y.; Li, S.; Zhou, H.; Cao, X.; Bao, S.; Gao, Y.; Luo, H.; Jin, P., Room temperature optical constants and band gap evolution of phase pure M 1-VO 2 thin films deposited at different oxygen partial pressures by reactive magnetron sputtering. *Journal of Nanomaterials* **2014,** *2014*, 28.
30. Chen, X.; Li, J.; Lv, Q., Thermoelectrical and optical characteristics research on novel nanostructured VO 2 thin film. *Optik-International Journal for Light and Electron Optics* **2013,** *124* (15), 2041-2044.
31. Ba, C. O.; Bah, S. T.; D'Auteuil, M.; Fortin, V.; Ashrit, P.; Vallée, R., VO 2 thin films based active and passive thermochromic devices for energy management applications. *Current Applied Physics* **2014,** *14* (11), 1531-1537.
32. Guo, Y.; Liu, Y.; Zou, C.; Qi, Z.; Wang, Y.; Xu, Y.; Wang, X.; Zhang, F.; Zhou, R., Oxygen pressure induced structure, morphology and phase-transition for VO2/c-sapphire films by PLD. *Applied Physics A* **2014,** *115* (4), 1245-1250.
33. Leroy, J.; Bessaudou, A.; Cosset, F.; Crunteanu, A., Structural, electrical and optical properties of thermochromic VO 2 thin films obtained by reactive electron beam evaporation. *Thin Solid Films* **2012,** *520* (14), 4823-4825.
34. Antonelli, D. M.; Ying, J. Y., Synthesis of hexagonally packed mesoporous TiO2 by a modified sol–gel method. *Angewandte Chemie International Edition* **1995,** *34* (18), 2014-2017.
35. Lee, J.-H.; Ko, K.-H.; Park, B.-O., Electrical and optical properties of ZnO transparent conducting films by the sol–gel method. *Journal of Crystal Growth* **2003,** *247* (1-2), 119-125.
36. Jeon, H.-J.; Yi, S.-C.; Oh, S.-G., Preparation and antibacterial effects of Ag–SiO2 thin films by sol–gel method. *Biomaterials* **2003,** *24* (27), 4921-4928.
37. Yu, J.; Zhao, X.; Zhao, Q., Effect of surface structure on photocatalytic activity of TiO2 thin films prepared by sol-gel method. *Thin solid films* **2000,** *379* (1-2), 7-14.
38. Tadanaga, K.; Katata, N.; Minami, T., Formation Process of Super‐Water‐Repellent Al2O3 Coating Films with High Transparency by the Sol‐Gel Method. *Journal of the American Ceramic Society* **1997,** *80* (12), 3213-3216.
39. Velichko, A.; Pergament, A.; Putrolaynen, V.; Berezina, O.; Stefanovich, G., Effect of memory electrical switching in metal/vanadium oxide/silicon structures with VO 2 films obtained by the sol–gel method. *Materials Science in Semiconductor Processing* **2015,** *29*, 315-320.
40. Greenberg, C. B., Undoped and doped VO2 films grown from VO (OC3H7) 3. *Thin solid films* **1983,** *110* (1), 73-82.
41. Jiazhen, Y.; Yue, Z.; Wanxia, H.; Mingjin, T., Effect of Mo-W Co-doping on semiconductor-metal phase transition temperature of vanadium dioxide film. *Thin Solid Films* **2008,** *516* (23), 8554-8558.
42. Song, L.; Huang, W.; Zhang, Y.; Li, D.; Shi, Q.; Zheng, S.; Li, N.; Xu, Y., Characteristics of CeOx–VO2 composite thin films synthesized by sol–gel process. *Journal of Materials Science: Materials in Electronics* **2013,** *24* (9), 3496-3503.
43. Cho, J.-H.; Byun, Y.-J.; Kim, J.-H.; Lee, Y.-J.; Jeong, Y.-H.; Chun, M.-P.; Paik, J.-H.; Sung, T. H., Thermochromic characteristics of WO 3-doped vanadium dioxide thin films prepared by sol–gel method. *Ceramics International* **2012,** *38*, S589-S593.
44. Wu, J.; Huang, W.; Shi, Q.; Cai, J.; Zhao, D.; Zhang, Y.; Yan, J., Effect of annealing temperature on thermochromic properties of vanadium dioxide thin films deposited by organic sol–gel method. *Applied Surface Science* **2013,** *268*, 556-560.
45. Liu, B.; Zeng, H. C., Hydrothermal synthesis of ZnO nanorods in the diameter regime of 50 nm. *Journal of the American Chemical Society* **2003,** *125* (15), 4430-4431.
46. Yang, S.; Zavalij, P. Y.; Whittingham, M. S., Hydrothermal synthesis of lithium iron phosphate cathodes. *Electrochemistry Communications* **2001,** *3* (9), 505-508.
47. Cundy, C. S.; Cox, P. A., The hydrothermal synthesis of zeolites: history and development from the earliest days to the present time. *Chemical Reviews* **2003,** *103* (3), 663-702.
48. Subramanian, V.; Zhu, H.; Vajtai, R.; Ajayan, P.; Wei, B., Hydrothermal synthesis and pseudocapacitance properties of MnO2 nanostructures. *The Journal of Physical Chemistry B* **2005,** *109* (43), 20207-20214.
49. Chen, J.; Whittingham, M. S., Hydrothermal synthesis of lithium iron phosphate. *Electrochemistry Communications* **2006,** *8* (5), 855-858.
50. Monfort, O.; Roch, T.; Satrapinskyy, L.; Gregor, M.; Plecenik, T.; Plecenik, A.; Plesch, G., Reduction of V 2 O 5 thin films deposited by aqueous sol–gel method to VO 2 (B) and investigation of its photocatalytic activity. *Applied Surface Science* **2014,** *322*, 21-27.
51. Wang, N.; Magdassi, S.; Mandler, D.; Long, Y., Simple sol–gel process and one-step annealing of vanadium dioxide thin films: synthesis and thermochromic properties. *Thin Solid Films* **2013,** *534*, 594-598.
52. Guo, Y.; Zou, C.; Liu, Y.; Xu, Y.; Wang, X.; Yu, J.; Yang, Z.; Zhang, F.; Zhou, R., Facile preparation of vanadium oxide thin films on sapphire (0001) by sol–gel method. *J Sol-Gel Sci Technol* **2014,** *70* (1), 40-46.
53. Guo, Y.; Xu, H.; Zou, C.; Yang, Z.; Tong, B.; Yu, J.; Zhang, Y.; Zhao, L.; Wang, Y., Evolution of structure and electrical properties with annealing time in solution-based VO 2 thin films. *Journal of Alloys and Compounds* **2015,** *622*, 913-917.
54. Ban, C.; Whittingham, M. S., Nanoscale single-crystal vanadium oxides with layered structure by electrospinning and hydrothermal methods. *Solid State Ionics* **2008,** *179* (27), 1721-1724.
55. Liu, J.; Li, Q.; Wang, T.; Yu, D.; Li, Y., Metastable vanadium dioxide nanobelts: hydrothermal synthesis, electrical transport, and magnetic properties. *Angewandte Chemie* **2004,** *116* (38), 5158-5162.

56. Kang, L.; Gao, Y.; Luo, H.; Chen, Z.; Du, J.; Zhang, Z., Nanoporous thermochromic VO2 films with low optical constants, enhanced luminous transmittance and thermochromic properties. *ACS applied materials & interfaces* **2011,** *3* (2), 135-138.
57. Du, J.; Gao, Y.; Luo, H.; Kang, L.; Zhang, Z.; Chen, Z.; Cao, C., Significant changes in phase-transition hysteresis for Ti-doped VO 2 films prepared by polymer-assisted deposition. *Solar Energy Materials and Solar Cells* **2011,** *95* (2), 469-475.
58. Zhang, Z.; Gao, Y.; Kang, L.; Du, J.; Luo, H., Effects of a TiO2 buffer layer on solution-deposited VO2 films: enhanced oxidization durability. *The Journal of Physical Chemistry C* **2010,** *114* (50), 22214-22220.
59. Saeli, M.; Piccirillo, C.; Parkin, I. P.; Binions, R.; Ridley, I., Energy modelling studies of thermochromic glazing. *Energy and Buildings* **2010,** *42* (10), 1666-1673.
60. Burkhardt, W.; Christmann, T.; Franke, S.; Kriegseis, W.; Meister, D.; Meyer, B.; Niessner, W.; Schalch, D.; Scharmann, A., Tungsten and fluorine co-doping of VO2 films. *Thin Solid Films* **2002,** *402* (1-2), 226-231.
61. Nethravathi, C.; Rajamathi, C. R.; Rajamathi, M.; Gautam, U. K.; Wang, X.; Golberg, D.; Bando, Y., N-doped graphene–VO2 (B) nanosheet-built 3D flower hybrid for lithium ion battery. *ACS applied materials & interfaces* **2013,** *5* (7), 2708-2714.
62. Cavanna, E.; Segaud, J.; Livage, J., Optical switching of Au-doped VO2 sol-gel films. *Materials Research Bulletin* **1999,** *34* (2), 167-177.
63. Romanyuk, A.; Steiner, R.; Marot, L.; Oelhafen, P., Temperature-induced metal–semiconductor transition in W-doped VO2 films studied by photoelectron spectroscopy. *Solar Energy Materials and Solar Cells* **2007,** *91* (19), 1831-1835.
64. Mai, L.; Hu, B.; Hu, T.; Chen, W.; Gu, E., Electrical Property of Mo-Doped VO2 Nanowire Array Film by Melting− Quenching Sol− Gel Method. *The Journal of Physical Chemistry B* **2006,** *110* (39), 19083-19086.
65. Beteille, F.; Morineau, R.; Livage, J.; Nagano, M., Switching properties of V1− xTixO2 thin films deposited from alkoxides. *Materials research bulletin* **1997,** *32* (8), 1109-1117.
66. Li, S.; Li, Y.; Jiang, M.; Ji, S.; Luo, H.; Gao, Y.; Jin, P., Preparation and characterization of self-supporting thermochromic films composed of VO2 (M)@ SiO2 nanofibers. *ACS applied materials & interfaces* **2013,** *5* (14), 6453-6457.
67. Futaki, H.; Aoki, M., Effects of various doping elements on the transition temperature of vanadium oxide semiconductors. *Japanese journal of applied physics* **1969,** *8* (8), 1008.
68. Tan, X.; Yao, T.; Long, R.; Sun, Z.; Feng, Y.; Cheng, H.; Yuan, X.; Zhang, W.; Liu, Q.; Wu, C., Unraveling metal-insulator transition mechanism of VO2 triggered by tungsten doping. *Scientific reports* **2012,** *2*.
69. Zhang, Y.; Tan, X.; Huang, C.; Meng, C., Hydrothermal treatment with VO2 (B) nanobelts for synthesis of VO2 (A) and W doped VO2 (M) nanobelts. *Materials Research Innovations* **2015,** *19* (4), 295-302.
70. Mlyuka, N.; Niklasson, G.; Granqvist, C.-G., Thermochromic multilayer films of VO 2 and TiO 2 with enhanced transmittance. *Solar Energy Materials and Solar Cells* **2009,** *93* (9), 1685-1687.
71. Manning, T. D.; Parkin, I. P.; Pemble, M. E.; Sheel, D.; Vernardou, D., Intelligent window coatings: atmospheric pressure chemical vapor deposition of tungsten-doped vanadium dioxide. *Chemistry of Materials* **2004,** *16* (4), 744-749.
72. Burkhardt, W.; Christmann, T.; Franke, S.; Kriegseis, W.; Meister, D.; Meyer, B.; Niessner, W.; Schalch, D.; Scharmann, A., Tungsten and fluorine co-doping of VO 2 films. *Thin Solid Films* **2002,** *402* (1), 226-231.
73. Zhou, J.; Gao, Y.; Liu, X.; Chen, Z.; Dai, L.; Cao, C.; Luo, H.; Kanahira, M.; Sun, C.; Yan, L., Mg-doped VO 2 nanoparticles: hydrothermal synthesis, enhanced visible transmittance and decreased metal–insulator transition temperature. *Physical Chemistry Chemical Physics* **2013,** *15* (20), 7505-7511.
74. Nishikawa, M.; Nakajima, T.; Kumagai, T.; Okutani, T.; Tsuchiya, T., Ti-doped VO2 films grown on glass substrates by excimer-laser-assisted metal organic deposition process. *Japanese Journal of Applied Physics* **2011,** *50* (1S2), 01BE04.
75. Lu, Z.; Li, C.; Yin, Y., Synthesis and thermochromic properties of vanadium dioxide colloidal particles. *Journal of Materials Chemistry* **2011,** *21* (38), 14776-14782.
76. Mlyuka, N.; Niklasson, G. A.; Granqvist, C.-G., Mg doping of thermochromic VO 2 films enhances the optical transmittance and decreases the metal-insulator transition temperature. *Applied physics letters* **2009,** *95* (17), 171909.
77. Dietrich, M. K.; Kramm, B. G.; Becker, M.; Meyer, B. K.; Polity, A.; Klar, P. J., Influence of doping with alkaline earth metals on the optical properties of thermochromic VO2. *Journal of Applied Physics* **2015,** *117* (18), 185301.
78. Du, J.; Gao, Y.; Chen, Z.; Kang, L.; Zhang, Z.; Luo, H., Enhancing thermochromic performance of VO 2 films via increased microroughness by phase separation. *Solar Energy Materials and Solar Cells* **2013,** *110*, 1-7.
79. Koo, H.; Xu, L.; Ko, K.-E.; Ahn, S.; Chang, S.-H.; Park, C., Effect of oxide buffer layer on the thermochromic properties of VO2 thin films. *Journal of materials engineering and performance* **2013,** *22* (12), 3967-3973.
80. Granqvist, C. G., Transparent conductors as solar energy materials: A panoramic review. *Solar energy materials and solar cells* **2007,** *91* (17), 1529-1598.
81. Kang, L.; Gao, Y.; Luo, H.; Wang, J.; Zhu, B.; Zhang, Z.; Du, J.; Kanehira, M.; Zhang, Y., Thermochromic properties and low emissivity of ZnO: Al/VO 2 double-layered films with a lowered phase transition temperature. *Solar Energy Materials and Solar Cells* **2011,** *95* (12), 3189-3194.
82. Chen, Z.; Gao, Y.; Kang, L.; Du, J.; Zhang, Z.; Luo, H.; Miao, H.; Tan, G., VO 2-based double-layered films for smart windows: optical design, all-solution preparation and improved properties. *Solar Energy Materials and Solar Cells* **2011,** *95* (9), 2677-2684.
83. Zheng, J.; Bao, S.; Jin, P., TiO 2 (R)/VO 2 (M)/TiO 2 (A) multilayer film as smart window: Combination of energy-saving, antifogging and self-cleaning functions. *Nano Energy* **2015,** *11*, 136-145.

84. 康利涛; 高彦峰; 陈长; 杜靖; 张宗涛; 罗宏杰, Pt/VO2 double-layered films combining thermochromic properties with low emissivity. **2010**.
85. Li, M.; Magdassi, S.; Gao, Y.; Long, Y., Hydrothermal Synthesis of VO2 Polymorphs: Advantages, Challenges and Prospects for the Application of Energy Efficient Smart Windows. *Small* **2017**.
86. Whittaker, L.; Jaye, C.; Fu, Z.; Fischer, D. A.; Banerjee, S., Depressed phase transition in solution-grown VO2 nanostructures. *Journal of the American Chemical Society* **2009,** *131* (25), 8884-8894.
87. Whittaker, L.; Velazquez, J. M.; Banerjee, S., A VO-seeded approach for the growth of star-shaped VO 2 and V 2 O 5 nanocrystals: facile synthesis, structural characterization, and elucidation of electronic structure. *CrystEngComm* **2011,** *13* (17), 5328-5336.
88. Whittaker, L.; Wu, T.-L.; Stabile, A.; Sambandamurthy, G.; Banerjee, S., Single-Nanowire Raman Microprobe Studies of Doping-, Temperature-, and Voltage-Induced Metal–Insulator Transitions of WxV1–xO2 Nanowires. *ACS Nano* **2011,** *5* (11), 8861-8867.
89. Wu, C.; Zhang, X.; Dai, J.; Yang, J.; Wu, Z.; Wei, S.; Xie, Y., Direct hydrothermal synthesis of monoclinic VO 2 (M) single-domain nanorods on large scale displaying magnetocaloric effect. *Journal of Materials Chemistry* **2011,** *21* (12), 4509-4517.
90. Mutta, G. R.; Popuri, S. R.; Vasundhara, M.; Maciejczyk, M.; Racu, A. V.; Banica, R.; Robertson, N.; Wilson, J. I.; Bennett, N. S., Facile hydrothermal synthesis of economically viable VO2 (M1) counter electrode for dye sensitized solar cells. *Materials Research Bulletin* **2016,** *83*, 135-140.
91. Zhang, Y.; Zhang, J.; Zhang, X.; Mo, S.; Wu, W.; Niu, F.; Zhong, Y.; Liu, X.; Huang, C.; Liu, X., Direct preparation and formation mechanism of belt-like doped VO2 (M) with rectangular cross sections by one-step hydrothermal route and their phase transition and optical switching properties. *Journal of Alloys and Compounds* **2013,** *570*, 104-113.
92. Zhang, Y.; Zhang, X.; Huang, Y.; Huang, C.; Niu, F.; Meng, C.; Tan, X., One-step hydrothermal conversion of VO2 (B) into W-doped VO2 (M) and its phase transition and optical switching properties. *Solid State Communications* **2014,** *180*, 24-27.
93. Chen, R.; Miao, L.; Cheng, H.; Nishibori, E.; Liu, C.; Asaka, T.; Iwamoto, Y.; Takata, M.; Tanemura, S., One-step hydrothermal synthesis of V 1− x W x O 2 (M/R) nanorods with superior doping efficiency and thermochromic properties. *J. Mater. Chem. A* **2015,** *3* (7), 3726-3738.
94. Lv, W.; Huang, D.; Chen, Y.; Qiu, Q.; Luo, Z., Synthesis and characterization of Mo–W co-doped VO2 (R) nano-powders by the microwave-assisted hydrothermal method. *Ceramics International* **2014,** *40* (8), 12661-12668.
95. Wang, N.; Duchamp, M.; Xue, C.; Dunin‐Borkowski, R. E.; Liu, G.; Long, Y., Single‐Crystalline W‐Doped VO2 Nanobeams with Highly Reversible Electrical and Plasmonic Responses Near Room Temperature. *Advanced Materials Interfaces* **2016,** *3* (15).
96. Alie, D.; Gedvilas, L.; Wang, Z.; Tenent, R.; Engtrakul, C.; Yan, Y.; Shaheen, S. E.; Dillon, A. C.; Ban, C., Direct synthesis of thermochromic VO2 through hydrothermal reaction. *Journal of Solid State Chemistry* **2014,** *212*, 237-241.
97. Ji, S.; Zhang, F.; Jin, P., Preparation of high performance pure single phase VO2 nanopowder by hydrothermally reducing the V2O5 gel. *Solar Energy Materials and Solar Cells* **2011,** *95* (12), 3520-3526.
98. Gao, Y.; Cao, C.; Dai, L.; Luo, H.; Kanehira, M.; Ding, Y.; Wang, Z. L., Phase and shape controlled VO 2 nanostructures by antimony doping. *Energy & Environmental Science* **2012,** *5* (9), 8708-8715.
99. Li, W.; Ji, S.; Li, Y.; Huang, A.; Luo, H.; Jin, P., Synthesis of VO 2 nanoparticles by a hydrothermal-assisted homogeneous precipitation approach for thermochromic applications. *Rsc Advances* **2014,** *4* (25), 13026-13033.
100. Chen, Z.; Gao, Y.; Kang, L.; Cao, C.; Chen, S.; Luo, H., Fine crystalline VO 2 nanoparticles: synthesis, abnormal phase transition temperatures and excellent optical properties of a derived VO 2 nanocomposite foil. *J. Mater. Chem. A* **2014,** *2* (8), 2718-2727.
101. Li, W.; Ji, S.; Sun, G.; Ma, Y.; Guo, H.; Jin, P., Novel VO 2 (M)–ZnO heterostructured dandelions with combined thermochromic and photocatalytic properties for application in smart coatings. *New Journal of Chemistry* **2016,** *40* (3), 2592-2600.
102. Song, Z.; Zhang, L.; Xia, F.; Webster, N. A. S.; Song, J.; Liu, B.; Luo, H.; Gao, Y., Controllable synthesis of VO2(D) and their conversion to VO2(M) nanostructures with thermochromic phase transition properties. *Inorganic Chemistry Frontiers* **2016,** *3* (8), 1035-1042.
103. Zhang, Z.; Gao, Y.; Chen, Z.; Du, J.; Cao, C.; Kang, L.; Luo, H., Thermochromic VO2 thin films: solution-based processing, improved optical properties, and lowered phase transformation temperature. *Langmuir* **2010,** *26* (13), 10738-10744.
104. Zhang, H.; Wu, Z.; Wu, X.; Yang, W.; Jiang, Y., Transversal grain size effect on the phase-transition hysteresis width of vanadium dioxide films comprising spheroidal nanoparticles. *Vacuum* **2014,** *104*, 47-50.
105. Chen, Z.; Cao, C.; Chen, S.; Luo, H.; Gao, Y., Crystallised mesoporous TiO 2 (A)–VO 2 (M/R) nanocomposite films with self-cleaning and excellent thermochromic properties. *J. Mater. Chem. A* **2014,** *2* (30), 11874-11884.
106. Yang, Y.; Lee, K.; Zobel, M.; Maćković, M.; Unruh, T.; Spiecker, E.; Schmuki, P., Formation of highly ordered VO2 nanotubular/nanoporous layers and their supercooling effect in phase transitions. *Adv Mater* **2012,** *24* (12), 1571-1575.
107. Zhang, Y.; Zheng, J.; Hu, T.; Tian, F.; Meng, C., Synthesis and supercapacitor electrode of VO2(B)/C core–shell composites with a pseudocapacitance in aqueous solution. *Applied Surface Science* **2016,** *371*, 189-195.

108. Chen, Y.; Zeng, X.; Zhu, J.; Li, R.; Yao, H.; Cao, X.; Ji, S.; Jin, P., High Performance and Enhanced Durability of Thermochromic Films Using VO2@ ZnO Core–Shell Nanoparticles. *ACS applied materials & interfaces* **2017,** *9* (33), 27784-27791.
109. Tong, K.; Li, R.; Zhu, J.; Yao, H.; Zhou, H.; Zeng, X.; Ji, S.; Jin, P., Preparation of VO2/Al-O core-shell structure with enhanced weathering resistance for smart window. *Ceramics International* **2017,** *43* (5), 4055-4061.
110. Wang, M.; Tian, J.; Zhang, H.; Shi, X.; Chen, Z.; Wang, Y.; Ji, A.; Gao, Y., Novel synthesis of pure VO2@SiO2 core@shell nanoparticles to improve the optical and anti-oxidant properties of a VO2 film. *RSC Advances* **2016,** *6* (110), 108286-108289.
111. Mondal, T.; Pant, K. K.; Dalai, A. K., Catalytic oxidative steam reforming of bio-ethanol for hydrogen production over Rh promoted Ni/CeO2–ZrO2 catalyst. *international journal of hydrogen energy* **2015,** *40* (6), 2529-2544.
112. Mortensen, P. M.; de Carvalho, H. W.; Grunwaldt, J.-D.; Jensen, P. A.; Jensen, A. D., Activity and stability of Mo2C/ZrO2 as catalyst for hydrodeoxygenation of mixtures of phenol and 1-octanol. *Journal of Catalysis* **2015,** *328*, 208-215.
113. Neumann, N.; Leion, H.; Zhao, D.; Wokon, M.; Linder, M. P., Particle stability investigation of Mn-Fe oxides supported by TiO2, ZrO2 or CeO2 as thermochemical energy storage materials. **2016**.
114. Evangelista, V.; Acosta, B.; Miridonov, S.; Smolentseva, E.; Fuentes, S.; Simakov, A., Highly active Au-CeO2@ ZrO2 yolk–shell nanoreactors for the reduction of 4-nitrophenol to 4-aminophenol. *Applied Catalysis B: Environmental* **2015,** *166*, 518-528.
115. Li, L.; Mao, D.; Yu, J.; Guo, X., Highly selective hydrogenation of CO2 to methanol over CuO–ZnO–ZrO2 catalysts prepared by a surfactant-assisted co-precipitation method. *Journal of Power Sources* **2015,** *279*, 394-404.
116. Mortensen, P. M.; de Carvalho, H. W. P.; Grunwaldt, J.-D.; Jensen, P. A.; Jensen, A. D., Activity and stability of Mo2C/ZrO2 as catalyst for hydrodeoxygenation of mixtures of phenol and 1-octanol. *Journal of Catalysis* **2015,** *328*, 208-215.
117. Li, L.; Zhang, N.; Huang, X.; Liu, Y.; Li, Y.; Zhang, G.; Song, L.; He, H., Hydrothermal stability of core-shell Pd@ Ce0. 5Zr0. 5O2/Al2O3 catalyst for automobile three-way reaction. *ACS Catalysis* **2018**.
118. Armstrong, T. R.; Buchanan, R. C., Influence of Core‐Shell Grains on the Internal Stress State and Permittivity Response of Zirconia‐Modified Barium Titanate. *Journal of the American Ceramic Society* **1990,** *73* (5), 1268-1273.
119. Yin, J.; Qian, X.; Yin, J.; Shi, M.; Zhang, J.; Zhou, G., Preparation of polystyrene/zirconia core-shell microspheres and zirconia hollow shells. *Inorganic Chemistry Communications* **2003,** *6* (7), 942-945.
120. Yang, X.; Wang, X.; Gao, G.; Liu, E.; Shi, Q.; Zhang, J.; Han, C.; Wang, J.; Lu, H.; Liu, J., Nickel on a macro-mesoporous Al2O3@ ZrO2 core/shell nanocomposite as a novel catalyst for CO methanation. *International Journal of Hydrogen Energy* **2013,** *38* (32), 13926-13937.
121. Du, J.; Zhang, J.; Liu, Z.; Han, B.; Jiang, T.; Huang, Y., Controlled synthesis of Ag/TiO2 core− shell nanowires with smooth and bristled surfaces via a one-step solution route. *Langmuir* **2006,** *22* (3), 1307-1312.
122. Menzies, D. B.; Cervini, R.; Cheng, Y.-B.; Simon, G. P.; Spiccia, L., Nanostructured ZrO2-Coated TiO2 Electrodes for Dye-Sensitised Solar Cells. *J Sol-Gel Sci Technol* **2004,** *32* (1), 363-366.
123. Chappel, S.; Chen, S.-G.; Zaban, A., TiO2-coated nanoporous SnO2 electrodes for dye-sensitized solar cells. *Langmuir* **2002,** *18* (8), 3336-3342.
124. Palomares, E.; Clifford, J. N.; Haque, S. A.; Lutz, T.; Durrant, J. R., Control of charge recombination dynamics in dye sensitized solar cells by the use of conformally deposited metal oxide blocking layers. *Journal of the American Chemical Society* **2003,** *125* (2), 475-482.
125. Jiang, H.-L.; Akita, T.; Ishida, T.; Haruta, M.; Xu, Q., Synergistic catalysis of Au@ Ag core− shell nanoparticles stabilized on metal− organic framework. *Journal of the American Chemical Society* **2011,** *133* (5), 1304-1306.
126. Liu, M.; Guyot-Sionnest, P., Synthesis and optical characterization of Au/Ag core/shell nanorods. *The Journal of Physical Chemistry B* **2004,** *108* (19), 5882-5888.
127. Shankar, S. S.; Rai, A.; Ahmad, A.; Sastry, M., Rapid synthesis of Au, Ag, and bimetallic Au core–Ag shell nanoparticles using Neem (Azadirachta indica) leaf broth. *Journal of colloid and interface science* **2004,** *275* (2), 496-502.
128. Ma, Y.; Li, W.; Cho, E. C.; Li, Z.; Yu, T.; Zeng, J.; Xie, Z.; Xia, Y., Au@ Ag core− shell nanocubes with finely tuned and well-controlled sizes, shell thicknesses, and optical properties. *ACS nano* **2010,** *4* (11), 6725-6734.
129. Huang, C.-C.; Yang, Z.; Chang, H.-T., Synthesis of dumbbell-shaped Au− Ag core− shell nanorods by seed-mediated growth under alkaline conditions. *Langmuir* **2004,** *20* (15), 6089-6092.
130. Dhanalekshmi, K. I.; Meena, K. S., DNA intercalation studies and antimicrobial activity of Ag@ZrO2 core–shell nanoparticles in vitro. *Materials Science and Engineering: C* **2016,** *59*, 1063-1068.
131. Chang, I.; Lee, J.; Lee, Y.; Lee, Y. H.; Ko, S. H.; Cha, S. W., Thermally stable Ag@ZrO2 core-shell via atomic layer deposition. *Materials Letters* **2017,** *188*, 372-374.
132. Li, J.; Hu, Y.; Yang, J.; Wei, P.; Sun, W.; Shen, M.; Zhang, G.; Shi, X., Hyaluronic acid-modified Fe3O4@ Au core/shell nanostars for multimodal imaging and photothermal therapy of tumors. *Biomaterials* **2015,** *38*, 10-21.
133. Lin, L.-S.; Cong, Z.-X.; Cao, J.-B.; Ke, K.-M.; Peng, Q.-L.; Gao, J.; Yang, H.-H.; Liu, G.; Chen, X., Multifunctional Fe3O4@ polydopamine core–shell nanocomposites for intracellular mRNA detection and imaging-guided photothermal therapy. *ACS nano* **2014,** *8* (4), 3876-3883.

134. Brollo, M.; Orozco-Henao, J.; López-Ruiz, R.; Muraca, D.; Dias, C.; Pirota, K.; Knobel, M., Magnetic hyperthermia in brick-like Ag@ Fe3O4 core–shell nanoparticles. *Journal of Magnetism and Magnetic Materials* **2016,** *397*, 20-27.
135. Sharma, R.; Monga, Y.; Puri, A., Magnetically separable silica@ Fe3O4 core–shell supported nano-structured copper (II) composites as a versatile catalyst for the reduction of nitroarenes in aqueous medium at room temperature. *Journal of Molecular Catalysis A: Chemical* **2014,** *393*, 84-95.
136. Jiang, M.; Liu, W.; Yang, X.; Jiang, Z.; Yao, T.; Wei, S.; Peng, X., Pt/Fe3O4 Core/Shell Triangular Nanoprisms by Heteroepitaxy: Facet Selectivity at the Pt–Fe3O4 Interface and the Fe3O4 Outer Surface. *ACS nano* **2015,** *9* (11), 10950-10960.
137. Li, Y.; Leng, T.; Lin, H.; Deng, C.; Xu, X.; Yao, N.; Yang, P.; Zhang, X., Preparation of Fe3O4@ZrO2 Core−Shell Microspheres as Affinity Probes for Selective Enrichment and Direct Determination of Phosphopeptides Using Matrix-Assisted Laser Desorption Ionization Mass Spectrometry. *Journal of Proteome Research* **2007,** *6* (11), 4498-4510.
138. Wang, W.; Zhang, H.; Zhang, L.; Wan, H.; Zheng, S.; Xu, Z., Adsorptive removal of phosphate by magnetic Fe3O4@C@ZrO2. *Colloids and Surfaces A: Physicochemical and Engineering Aspects* **2015,** *469*, 100-106.
139. Watanabe, T.; Nakajima, A.; Wang, R.; Minabe, M.; Koizumi, S.; Fujishima, A.; Hashimoto, K., Photocatalytic activity and photoinduced hydrophilicity of titanium dioxide coated glass. *Thin Solid Films* **1999,** *351* (1), 260-263.
140. Chen, D.-H.; He, X.-R., Synthesis of nickel ferrite nanoparticles by sol-gel method. *Materials Research Bulletin* **2001,** *36* (7-8), 1369-1377.
141. Jagadale, T. C.; Takale, S. P.; Sonawane, R. S.; Joshi, H. M.; Patil, S. I.; Kale, B. B.; Ogale, S. B., N-doped TiO2 nanoparticle based visible light photocatalyst by modified peroxide sol− gel method. *The journal of physical chemistry C* **2008,** *112* (37), 14595-14602.
142. Zhang, J.; Gao, L., Synthesis and characterization of nanocrystalline tin oxide by sol–gel method. *Journal of solid state chemistry* **2004,** *177* (4-5), 1425-1430.
143. Xu, J.; Yang, H.; Fu, W.; Du, K.; Sui, Y.; Chen, J.; Zeng, Y.; Li, M.; Zou, G., Preparation and magnetic properties of magnetite nanoparticles by sol–gel method. *Journal of Magnetism and magnetic Materials* **2007,** *309* (2), 307-311.
144. Yuranova, T.; Mosteo, R.; Bandara, J.; Laub, D.; Kiwi, J., Self-cleaning cotton textiles surfaces modified by photoactive SiO2/TiO2 coating. *Journal of Molecular Catalysis A: Chemical* **2006,** *244* (1), 160-167.
145. Hirakawa, T.; Kamat, P. V., Charge separation and catalytic activity of Ag@ TiO2 core− shell composite clusters under UV− irradiation. *Journal of the American Chemical Society* **2005,** *127* (11), 3928-3934.
146. Law, M.; Greene, L. E.; Radenovic, A.; Kuykendall, T.; Liphardt, J.; Yang, P., ZnO− Al2O3 and ZnO− TiO2 core− shell nanowire dye-sensitized solar cells. *The Journal of Physical Chemistry B* **2006,** *110* (45), 22652-22663.
147. Hwang, Y. J.; Boukai, A.; Yang, P., High density n-Si/n-TiO2 core/shell nanowire arrays with enhanced photoactivity. *Nano letters* **2008,** *9* (1), 410-415.
148. Greene, L. E.; Law, M.; Yuhas, B. D.; Yang, P., ZnO− TiO2 core− shell nanorod/P3HT solar cells. *The Journal of Physical Chemistry C* **2007,** *111* (50), 18451-18456.
149. Chen, C.-T.; Chen, Y.-C., Fe3O4/TiO2 core/shell nanoparticles as affinity probes for the analysis of phosphopeptides using TiO2 surface-assisted laser desorption/ionization mass spectrometry. *Analytical chemistry* **2005,** *77* (18), 5912-5919.
150. Liu, S.; Zhang, N.; Tang, Z.-R.; Xu, Y.-J., Synthesis of one-dimensional CdS@ TiO2 core–shell nanocomposites photocatalyst for selective redox: the dual role of TiO2 shell. *ACS applied materials & interfaces* **2012,** *4* (11), 6378-6385.
151. Ni, M.; Leung, M. K. H.; Leung, D. Y. C.; Sumathy, K., A review and recent developments in photocatalytic water-splitting using TiO2 for hydrogen production. *Renewable and Sustainable Energy Reviews* **2007,** *11* (3), 401-425.
152. Antolini, E.; Cardellini, F., Formation of carbon supported PtRu alloys: an XRD analysis. *Journal of Alloys and Compounds* **2001,** *315* (1-2), 118-122.
153. Nayak, P. S.; Singh, B., Instrumental characterization of clay by XRF, XRD and FTIR. *Bulletin of Materials Science* **2007,** *30* (3), 235-238.
154. Bertaux, J. L.; Korablev, O.; Perrier, S.; Quemerais, E.; Montmessin, F.; Leblanc, F.; Lebonnois, S.; Rannou, P.; Lefèvre, F.; Forget, F., SPICAM on Mars Express: Observing modes and overview of UV spectrometer data and scientific results. *Journal of Geophysical Research: Planets* **2006,** *111* (E10).
155. Carver, A.; Hennessy, J.; Wilson, D.; Jewell, A.; Mouroulis, P.; Nikzad, S., Advanced Ultraviolet Imaging Spectrometer for Planetary Studies. *Bulletin of the American Physical Society* **2018**.
156. Goldstein, J. I.; Newbury, D. E.; Michael, J. R.; Ritchie, N. W.; Scott, J. H. J.; Joy, D. C., *Scanning electron microscopy and X-ray microanalysis*. Springer: 2017.
157. Yamazaki, M.; Kazumi, H.; Sasaki, Y.; Suzuki, M., Scanning electron microscope. Google Patents: 2015.
158. Wen, J. G., Transmission electron microscopy. In *Practical Materials Characterization*, Springer: 2014; pp 189-229.
159. Pol, E.; Coumans, F.; Grootemaat, A.; Gardiner, C.; Sargent, I.; Harrison, P.; Sturk, A.; Leeuwen, T.; Nieuwland, R., Particle size distribution of exosomes and microvesicles determined by transmission electron microscopy, flow cytometry, nanoparticle tracking analysis, and resistive pulse sensing. *Journal of Thrombosis and Haemostasis* **2014,** *12* (7), 1182-1192.
160. Chenet, D. A.; Aslan, O. B.; Huang, P. Y.; Fan, C.; van der Zande, A. M.; Heinz, T. F.; Hone, J. C., In-plane anisotropy in mono-and few-layer ReS2 probed by Raman spectroscopy and scanning transmission electron microscopy. *Nano letters* **2015,** *15* (9), 5667-5672.

161. Zhang, Y., VO2(B) conversion to VO2(A) and VO2(M) and their oxidation resistance and optical switching properties. In *Materials Science-Poland*, 2016; Vol. 34, p 169.
162. Son, J.-H.; Wei, J.; Cobden, D.; Cao, G.; Xia, Y., Hydrothermal synthesis of monoclinic VO2 micro-and nanocrystals in one step and their use in fabricating inverse opals. *Chemistry of Materials* **2010,** *22* (10), 3043-3050.
163. Preiss, H.; Schultze, D.; Szulzewsky, K., Carbothermal synthesis of vanadium and chromium carbides from solution-Derived precursors. *Journal of the European Ceramic Society* **1999,** *19* (2), 187-194.
164. Chen, Z.; Gao, Y.; Kang, L.; Cao, C.; Chen, S.; Luo, H., Fine crystalline VO2 nanoparticles: synthesis, abnormal phase transition temperatures and excellent optical properties of a derived VO2 nanocomposite foil. *J. Mater. Chem. A* **2014,** *2* (8), 2718-2727.
165. Lee, J.; Yang, J.; Kwon, S. G.; Hyeon, T., Nonclassical nucleation and growth of inorganic nanoparticles. *Nature Reviews Materials* **2016,** *1* (8), 16034.
166. Kang, L.; Gao, Y.; Zhang, Z.; Du, J.; Cao, C.; Chen, Z.; Luo, H., Effects of Annealing Parameters on Optical Properties of Thermochromic VO2 Films Prepared in Aqueous Solution. *The Journal of Physical Chemistry C* **2010,** *114* (4), 1901-1911.
167. Li, D. X.; Huang, W. X.; Song, L. W.; Shi, Q. W. In *The Stability Study on Vanadium Dioxide*, Advanced Materials Research, Trans Tech Publ: 2015; pp 158-167.
168. Cho, W.; Kim, S.-M.; Song, J. H.; Yim, T.; Woo, S.-G.; Lee, K.-W.; Kim, J.-S.; Kim, Y.-J., Improved electrochemical and thermal properties of nickel rich LiNi0. 6Co0. 2Mn0. 2O2 cathode materials by SiO2 coating. *Journal of Power Sources* **2015,** *282*, 45-50.
169. Wu, S.; Sun, A.; Lu, Z.; Cheng, C.; Gao, X., Magnetic properties of iron-based soft magnetic composites with SiO2 coating obtained by reverse microemulsion method. *Journal of Magnetism and Magnetic Materials* **2015,** *381*, 451-456.
170. Yuan, L.; Han, C.; Pagliaro, M.; Xu, Y.-J., Origin of enhancing the photocatalytic performance of TiO2 for artificial photoreduction of CO2 through a SiO2 coating strategy. *The Journal of Physical Chemistry C* **2015,** *120* (1), 265-273.
171. Li, H.; Wang, D.; Chen, C.; Weng, F., Effect of CeO2 and Y2O3 on microstructure, bioactivity and degradability of laser cladding CaO–SiO2 coating on titanium alloy. *Colloids and Surfaces B: Biointerfaces* **2015,** *127*, 15-21.
172. Prasanna, K.; Kim, C.-S.; Lee, C. W., Effect of SiO2 coating on polyethylene separator with different stretching ratios for application in lithium ion batteries. *Materials Chemistry and Physics* **2014,** *146* (3), 545-550.
173. Wong, Y. J.; Zhu, L.; Teo, W. S.; Tan, Y. W.; Yang, Y.; Wang, C.; Chen, H., Revisiting the stober method: inhomogeneity in silica shells. *Journal of the American Chemical Society* **2011,** *133* (30), 11422-11425.
174. Shen, R.; Camargo, P. H.; Xia, Y.; Yang, H., Silane-based poly (ethylene glycol) as a primer for surface modification of nonhydrolytically synthesized nanoparticles using the stober method. *Langmuir* **2008,** *24* (19), 11189-11195.
175. Wang, X.; Zhang, Y.; Luo, W.; Elzatahry, A. A.; Cheng, X.; Alghamdi, A.; Abdullah, A. M.; Deng, Y.; Zhao, D., Synthesis of ordered mesoporous silica with tunable morphologies and pore sizes via a nonpolar solvent-assisted stober method. *Chemistry of Materials* **2016,** *28* (7), 2356-2362.
176. Kobayashi, Y.; Misawa, K.; Takeda, M.; Ohuchi, N.; Kasuya, A.; Konno, M., Preparation and Properties of Silica-Coated AgI Nanoparticles with a Modified Stober Method. *MRS Online Proceedings Library Archive* **2008,** *1074*.
177. Liu, J.; Qiao, S. Z.; Liu, H.; Chen, J.; Orpe, A.; Zhao, D.; Lu, G. Q. M., Extension of the Stöber method to the preparation of monodisperse resorcinol–formaldehyde resin polymer and carbon spheres. *Angewandte Chemie International Edition* **2011,** *50* (26), 5947-5951.
178. Bagwe, R. P.; Yang, C.; Hilliard, L. R.; Tan, W., Optimization of dye-doped silica nanoparticles prepared using a reverse microemulsion method. *Langmuir* **2004,** *20* (19), 8336-8342.
179. Yang, Y.; Gao, M., Preparation of fluorescent SiO2 particles with single CdTe nanocrystal cores by the reverse microemulsion method. *Adv Mater* **2005,** *17* (19), 2354-2357.
180. Koole, R.; van Schooneveld, M. M.; Hilhorst, J.; de Mello Donegá, C.; Hart, D. C. ’.; van Blaaderen, A.; Vanmaekelbergh, D.; Meijerink, A., On the incorporation mechanism of hydrophobic quantum dots in silica spheres by a reverse microemulsion method. *Chemistry of Materials* **2008,** *20* (7), 2503-2512.
181. Lee, M. S.; Park, S. S.; Lee, G.-D.; Ju, C.-S.; Hong, S.-S., Synthesis of TiO2 particles by reverse microemulsion method using nonionic surfactants with different hydrophilic and hydrophobic group and their photocatalytic activity. *Catalysis Today* **2005,** *101* (3-4), 283-290.
182. Jing, L.; Yang, C.; Qiao, R.; Niu, M.; Du, M.; Wang, D.; Gao, M., Highly fluorescent CdTe@ SiO2 particles prepared via reverse microemulsion method. *Chemistry of Materials* **2009,** *22* (2), 420-427.
183. Ding, H. L.; Zhang, Y. X.; Wang, S.; Xu, J. M.; Xu, S. C.; Li, G. H., Fe3O4@SiO2 Core/Shell Nanoparticles: The Silica Coating Regulations with a Single Core for Different Core Sizes and Shell Thicknesses. *Chemistry of Materials* **2012,** *24* (23), 4572-4580.
184. 胡永红; 容建华; 刘应亮; 满石清. SiO2/Ag 核壳结构纳米粒子的制备及表征. 2005.
185. Dani, R.; Wang, H.; Bossmann, S.; Wysin, G.; Chikan, V., *Faraday rotation enhancement of gold coated Fe2O3 nanoparticles: Comparison of experiment and theory*. 2011; Vol. 135, p 224502.
186. Dabbousi, B. O.; Rodriguez-Viejo, J.; Mikulec, F. V.; Heine, J. R.; Mattoussi, H.; Ober, R.; Jensen, K. F.; Bawendi, M. G., (CdSe) ZnS core− shell quantum dots: synthesis and characterization of a size series of highly luminescent nanocrystallites. *The Journal of Physical Chemistry B* **1997,** *101* (46), 9463-9475.

187. Lu, X.; Xiao, X.; Cao, Z.; Zhan, Y.; Cheng, H.; Xu, G., A novel method to modify the color of VO 2-based thermochromic smart films by solution-processed VO 2@ SiO 2@ Au core–shell nanoparticles. *RSC Advances* **2016,** *6* (53), 47249-47257.
188. Li, R.; Ji, S.; Li, Y.; Gao, Y.; Luo, H.; Jin, P., Synthesis and characterization of plate-like VO2(M)@SiO2 nanoparticles and their application to smart window. *Materials Letters* **2013,** *110*, 241-244.
189. Huang, A.; Zhou, Y.; Li, Y.; Ji, S.; Luo, H.; Jin, P., Preparation of VxW1-xO2(M)@SiO2 ultrathin nanostructures with high optical performance and optimization for smart windows by etching. *J. Mater. Chem. A* **2013,** *1* (40), 12545-12552.
190. Peng, H.; Zhou, M.; Peng, J., A highly sensitive resonance rayleigh scattering method for the determination of vitamin c based on the formation of zirconium hexacyanoferrate (II) nanoparticles. *Food Analytical Methods* **2016,** *9* (4), 942-949.
191. Fang, M.; Kaschak, D. M.; Sutorik, A. C.; Mallouk, T. E., A "mix and match" ionic− covalent strategy for self-assembly of inorganic multilayer films. *Journal of the American Chemical Society* **1997,** *119* (50), 12184-12191.
192. Li, M.; Feng, Z.; Xiong, G.; Ying, P.; Xin, Q.; Li, C., Phase transformation in the surface region of zirconia detected by UV Raman spectroscopy. *The Journal of Physical Chemistry B* **2001,** *105* (34), 8107-8111.
193. Kim, J. M.; Chang, S. M.; Kim, S.; Kim, K.-S.; Kim, J.; Kim, W.-S., Design of SiO2/ZrO2 core–shell particles using the sol–gel process. *Ceramics International* **2009,** *35* (3), 1243-1247.
194. Cairns, J.; Baglin, J. E.; Clark, G.; Ziegler, J., Strong metal-support interactions for Pt and Rh on Al2O3 and TiO2: Application of nuclear backscattering spectrometry. *Journal of Catalysis* **1983,** *83* (2), 301-314.
195. Colmenares, J. C.; Lisowski, P.; Łomot, D.; Chernyayeva, O.; Lisovytskiy, D., Sonophotodeposition of bimetallic photocatalysts Pd–Au/TiO2: application to selective oxidation of methanol to methyl formate. *ChemSusChem* **2015,** *8* (10), 1676-1685.
196. Kuang, D.; Brillet, J.; Chen, P.; Takata, M.; Uchida, S.; Miura, H.; Sumioka, K.; Zakeeruddin, S. M.; Grätzel, M., Application of highly ordered TiO2 nanotube arrays in flexible dye-sensitized solar cells. *ACS nano* **2008,** *2* (6), 1113-1116.
197. Paulose, M.; Shankar, K.; Varghese, O. K.; Mor, G. K.; Grimes, C. A., Application of highly-ordered TiO2 nanotube-arrays in heterojunction dye-sensitized solar cells. *Journal of Physics D: Applied Physics* **2006,** *39* (12), 2498.
198. Tang, Y.-B.; Lee, C.-S.; Xu, J.; Liu, Z.-T.; Chen, Z.-H.; He, Z.; Cao, Y.-L.; Yuan, G.; Song, H.; Chen, L., Incorporation of graphenes in nanostructured TiO2 films via molecular grafting for dye-sensitized solar cell application. *Acs Nano* **2010,** *4* (6), 3482-3488.
199. Gondikas, A. P.; Kammer, F. v. d.; Reed, R. B.; Wagner, S.; Ranville, J. F.; Hofmann, T., Release of TiO2 nanoparticles from sunscreens into surface waters: a one-year survey at the old Danube recreational Lake. *Environmental science & technology* **2014,** *48* (10), 5415-5422.
200. Peter, L.; Wijayantha, K., Intensity dependence of the electron diffusion length in dye-sensitised nanocrystalline TiO2 photovoltaic cells. *Electrochemistry communications* **1999,** *1* (12), 576-580.
201. Lai, Y.; Lin, L.; Pan, F.; Huang, J.; Song, R.; Huang, Y.; Lin, C.; Fuchs, H.; Chi, L., Bioinspired patterning with extreme wettability contrast on TiO2 nanotube array surface: a versatile platform for biomedical applications. *Small* **2013,** *9* (17), 2945-2953.
202. Oh, H.-J.; Lee, J.-H.; Kim, Y.-J.; Suh, S.-J.; Lee, J.-H.; Chi, C.-S., Surface characteristics of porous anodic TiO2 layer for biomedical applications. *Materials Chemistry and Physics* **2008,** *109* (1), 10-14.
203. Konstantinou, I. K.; Albanis, T. A., TiO2-assisted photocatalytic degradation of azo dyes in aqueous solution: kinetic and mechanistic investigations: a review. *Applied Catalysis B: Environmental* **2004,** *49* (1), 1-14.
204. Mahmoodi, N. M.; Arami, M.; Limaee, N. Y.; Tabrizi, N. S., Kinetics of heterogeneous photocatalytic degradation of reactive dyes in an immobilized TiO2 photocatalytic reactor. *Journal of colloid and interface Science* **2006,** *295* (1), 159-164.
205. Akpan, U.; Hameed, B., Parameters affecting the photocatalytic degradation of dyes using TiO2-based photocatalysts: a review. *Journal of hazardous materials* **2009,** *170* (2-3), 520-529.
206. Fernandez, A.; Lassaletta, G.; Jimenez, V.; Justo, A.; Gonzalez-Elipe, A.; Herrmann, J.-M.; Tahiri, H.; Ait-Ichou, Y., Preparation and characterization of TiO2 photocatalysts supported on various rigid supports (glass, quartz and stainless steel). Comparative studies of photocatalytic activity in water purification. *Applied Catalysis B: Environmental* **1995,** *7* (1-2), 49-63.
207. Zhang, L.; Kanki, T.; Sano, N.; Toyoda, A., Development of TiO2 photocatalyst reaction for water purification. *Separation and Purification Technology* **2003,** *31* (1), 105-110.
208. Xu, C.; Cui, A.; Xu, Y.; Fu, X., Graphene oxide–TiO2 composite filtration membranes and their potential application for water purification. *Carbon* **2013,** *62*, 465-471.
209. Liu, S.; Chen, A., Coadsorption of horseradish peroxidase with thionine on TiO2 nanotubes for biosensing. *Langmuir* **2005,** *21* (18), 8409-8413.
210. Tasviri, M.; Rafiee-Pour, H.-A.; Ghourchian, H.; Gholami, M. R., Amine functionalized TiO2 coated on carbon nanotube as a nanomaterial for direct electrochemistry of glucose oxidase and glucose biosensing. *Journal of Molecular Catalysis B: Enzymatic* **2011,** *68* (2), 206-210.
211. Chen, J.; Xu, L.; Xing, R.; Song, J.; Song, H.; Liu, D.; Zhou, J., Electrospun three-dimensional porous CuO/TiO2 hierarchical nanocomposites electrode for nonenzymatic glucose biosensing. *Electrochemistry Communications* **2012,** *20*, 75-78.

212. Chen, X.; Selloni, A., Introduction: Titanium Dioxide (TiO2) Nanomaterials. *Chemical Reviews* **2014,** *114* (19), 9281-9282.
213. Buyuktas, B. S., Investigation of the complexation and hydrolysis–condensation of titanium(IV) n-butoxide [Ti(OBun)4] with some unsaturated mono and dicarboxylic acids. *Transition Metal Chemistry* **2006,** *31* (6), 786-791.